

Untangling the signals: Investigating accretion and photometric variability in young stars

An observational analysis

Darryl Sergison

Submitted by Darryl Sergison to the University of Exeter as a thesis for the degree of Doctor of Philosophy in Physics, June 2015.

This thesis is available for Library use on the understanding that it is copyright material and that no quotation from the thesis may be published without proper acknowledgement.

I certify that all material in this thesis which is not my own work has been identified and that no material has previously been submitted and approved for the award of a degree by this or any other University.

Signed:

In the condition where Darryl Sergison is brought together with thesis

Date:

Abstract

In this thesis, an assessment is made of the value of optical CMDs as a useful diagnostic of the accretion properties of young stars. An analysis has been made of the phenomena that we observe and their effect on the position of stars in the CMD. Limitations and potential biases have been identified and evaluated.

Variability causes some luminosity spread at a given colour in optical CMDs. A detailed characterisation of variability has been performed which places strong constraints on the magnitudes and the timescales on which the variability is seen. On timescales $\lesssim 15$ minutes, almost no variability is detected (at levels greater than $\approx 0.2\%$) in the i band for a sample of ≈ 700 disc-bearing young stellar objects (YSOs). This suggests that the variability predicted by some accretion shock models is either very weak or not present. On hours to days timescales the optical variability in most stars is well described by a simple power law. The amplitude of the variability, $a \propto f^{-k}$, where f is the frequency of the variability in days. Disc-bearing and discless YSOs exhibit median values of k of 0.85 ± 0.02 and 0.95 ± 0.03 respectively, the uncertainty being the error on the median. The power law is valid up to a certain timescale (t_{\max}) at which point the variability amplitude does not increase any further. t_{\max} is found to be 1.50 ± 0.07 days and 1.41 ± 0.10 days for disc-bearing and discless stars respectively. Disc-bearing stars show greater variability amplitudes than the discless stars. However, it is notable that the variability timescale and power spectrum exponent are remarkably similar. This implies that the amplitude of the variability is driven by the physics of the underlying process, but that the timescales are instead driven by geometric effects.

For disc-bearing stars, the highest amplitude variables are the accreting stars, which often appear to vary in the CMD along lines that correspond to changes in accretion luminosity. Four disc-bearing stars (approximately 0.5% of the disc-bearing sample) in Cep OB3b show extreme variability on timescales of years. Three (possible EXor candidates), show long-timescale changes that have a dramatic effect on their CMD position. However their small numbers mean that the overall impact on the CMDs of young associations is small. Variability on timescales of the rotational period and shorter adds uncertainty to age estimates of individual stars that are calculated by comparison with PMS models.

Having provided a detailed description of variability and its impact on the CMD, it is clear that there are further significant mechanisms that affect the positions of YSOs in the CMD. I show that the spread in luminosity seen in the Orion Nebula Cluster and NGC 2264 could not be explained by accretion at rates of $\dot{M} \geq 5 \times 10^{-4} M_{\odot} \text{ yr}^{-1}$ occurring within the protostellar phase of YSO evolution. Thus it appears that CMDs are not a useful diagnostic for study of the accretion histories of YSOs.

The wavelength dependence of the extinction by dust within the inner regions of YSO discs is shown to differ from that seen in the ISM. Typically the wavelength dependence of the extinction is given by $R_V \approx 5 - 8$, compared with the value of $R_V \approx 3.1$ typical of the ISM. The interpretation is that grain growth has occurred. The location of this material within the ‘snow line’ implies that

grains have coalesced rather than simply gaining an ice mantle. This is evidence for the beginning of planet formation. The effect of the high value of R_V on the CMD is to add additional uncertainty of $\lesssim 0.1$ mag to photometric measurements that have been corrected for the effects of extinction.

Accretion luminosity is shown to be the dominant signal in the luminosity spread seen in CMDs of young associations. Stars which exhibit excess flux in the U band or $H\alpha$ are displaced in CMD space. The accretion vector is shown to be a significant blueward shift in colour accompanied by a modest brightening in the $g, g - i$ CMD. Accretion results in a luminosity spread as stars are displaced blueward below the PMS locus. This effect is not seen in non-accreting disc-bearing stars. Examination of the underlying excess luminosity spectrum for 15 accreting stars shows that the colour of the emission excess is not consistent across the sample. Thus to quantify the effect of accretion luminosity on CMD positions for individual stars, moderate resolution spectra are required with a large range in wavelength. This accretion luminosity may systematically bias estimates of PMS ages. A simple mitigation is to exclude accreting stars from age analysis. U band and $H\alpha$ flux excesses are shown to vary independently by ≈ 1 dex on timescales shorter than the rotation period of the star. The relation between U band flux excess and veiling at 7000\AA also appears to be variable. This implies that single epoch measurements of these parameters will add an uncertainty of ≈ 1 dex on accretion rates derived from them. Accretion rates derived from either U or $H\alpha$ excess should be calculated from a mean of several photometric measurements, separated by significant fractions of the rotation period of the star. In most stars, the veiling at 7000\AA is shown not to be a good measure for the calculation of the accretion rate.

Despite providing a detailed characterisation of phenomena that influence the positions of YSOs in the CMD, there exists some residual luminosity spread at a given T_{eff} that cannot be explained by variability on any timescale, extinction uncertainties or accretion luminosity. This residual spread should provide an opportunity to study an as-yet uncharacterised aspect of young stars.

Contents

1	Introduction	26
1.1	Star Formation - Clouds to Cores	26
1.2	Young low-mass stars ($< 2 M_{\odot}$)	29
1.2.1	Angular momentum evolution	31
1.2.2	Circumstellar discs	31
1.2.3	Accretion	33
1.3	Classification schemes	36
1.3.1	T Tauri stars: $H\alpha$ emission	36
1.3.2	YSO Classifications: mid-IR emission	37
1.3.3	YSO Classifications: nomenclature used in this study	39
1.4	Measuring accretion rates	39
1.4.1	UV photometry	42
1.4.2	Emission line flux	43
1.4.3	Veiling	44
1.5	Young star variability	46
1.6	The ages of young stars	52
1.6.1	Colour-magnitude diagrams	52
1.6.2	Lithium derived (nuclear) ages	54
1.7	The structure of this thesis	55
2	Using Lithium to probe the accretion history of young stars	57
2.1	Introduction	57
2.2	Theory and target selection	60
2.2.1	Theoretical lithium depletion	60
2.2.2	Target selection	63
2.3	Observations and data reduction	63
2.4	Analysis	64
2.4.1	Radial velocity and binary stars	65
2.4.2	Accretion veiling and $v \sin i$	68
2.4.3	Lithium equivalent width versus colour	69
2.5	Discussion	70
2.5.1	Accretion veiling	70

2.5.2	EW[Li] distribution, age spreads and correlation with CMD position . . .	70
2.5.3	Depleted lithium members	74
2.5.4	Isochronally old stars	76
2.6	Summary	77
3	Characterising YSO variability	79
3.1	Introduction	79
3.2	Data	80
3.2.1	Observations	80
3.2.2	Reduction	82
3.3	Analysis	85
3.3.1	Source classification	85
3.3.2	Characterising the lightcurve variability	85
3.3.3	Constructing the structure functions for YSOs in Cep OB3b	87
3.4	Discussion	91
3.4.1	Population-level variability statistics	91
3.4.2	Sub-hour timescale variability	96
3.5	Summary	99
4	Performing simultaneous multi-colour photometry and spectroscopy to explore young star variability	102
4.1	Introduction	102
4.2	Sample selection	103
4.3	Data collection	108
4.3.1	Photometric observations	108
4.3.2	Image reduction and optimal photometry	110
4.3.3	Profile correction	110
4.3.4	Correction of lightcurve systematics	111
4.3.5	Absolute calibration of photometry	112
4.3.6	Spectroscopic observations	112
4.3.7	Reduction and wavelength calibration	114
4.3.8	Flux calibration and removal of night-sky and nebular contamination	114
5	Young star multi-colour photometric variability	118
5.1	Introduction	118
5.2	Variability in $g, g - i$	118
5.2.1	Variability trends	119
5.3	What contribution does variability make to the ‘age spread’ in the $g, g - i$ diagram for the ONC?	121
5.3.1	Motivation	121
5.3.2	Analysis	122
5.4	Summary	125

6	Dust within the inner regions of YSO discs	128
6.1	Introduction	128
6.2	Extinction driven variables as probes of inner-disc dust	129
6.2.1	Selection of purely extinction variability stars	129
6.2.2	Analysis of variability in the SED	130
6.2.3	Measurement of R_V	132
6.3	Discussion	136
6.3.1	The location of the extinguishing material	136
6.3.2	Grain growth	137
6.3.3	Photometric extinction correction	139
6.4	Summary	140
7	Spectral typing, extinction and veiling estimates for spectroscopic target stars	142
7.1	Introduction	142
7.2	Discless templates	143
7.2.1	De-reddening of template stars - the TiO bandhead index vs. $g - i$ for discless stars.	143
7.2.2	Rejection of anomalous templates	144
7.3	Deriving the fundamental parameters	145
7.3.1	Fitting procedure	147
7.4	Results	150
7.5	Summary	150
8	How does accretion affect the colours of young stars?	152
8.1	Introduction	152
8.2	The $g, g - i$ colour-magnitude diagram	153
8.3	Identifying accreting stars	153
8.3.1	H α emission line excess	155
8.3.2	Ultraviolet excess	157
8.3.3	Comparison of accretion diagnostics	158
8.4	Accretion induced luminosity spreads in the CMD	160
8.5	What is the physical mechanism for this blueward shift?	162
8.5.1	'Grey' extinction	162
8.5.2	Accretion luminosity	162
8.6	Discussion	164
8.6.1	Ages of young star-forming regions	164
8.6.2	Angular momentum evolution	167
8.6.3	Correlations between Lithium depletion and apparent age	168
8.7	Summary	169

9	Comparing accretion diagnostics and exploring the nature of veiling	171
9.1	Introduction	171
9.2	The accretion luminosity model	172
9.3	Comparison of accretion diagnostics	172
9.3.1	U band flux vs. $H\alpha$	173
9.3.2	U band flux and veiling	174
9.4	Analysis of correlation between U excess and veiling	176
9.4.1	Measurement of the luminosity excess spectrum	178
9.4.2	Comparing the luminosity excess with SED time-variability	179
9.4.3	Comparing stars with ‘correlated’ and ‘uncorrelated’ U band excess and veiling behaviour	182
9.5	Mass accretion rates	184
9.6	Summary	184
10	Long-timescale high-amplitude variability	186
10.1	Introduction	186
10.2	The evolution of V733 Cep	187
10.3	Detection of long-timescale variables	189
10.3.1	What is causing the extreme variability in these stars?	195
10.4	Summary	199
11	Conclusions and Future work	201
11.1	Conclusions	201
11.1.1	Photometric variability	201
11.1.2	Other physical processes that influence CMDs of young stars	203
11.2	Further work	206
11.2.1	Exploring ‘old’ stars in young clusters	206
11.2.2	Searching for ‘minutes’ timescale accretion shock variability	206
11.2.3	Long-timescale episodic accretion	207
11.2.4	The effect of spots on PMS evolution	208
	Appendices	222
A	The variability of spectroscopic target stars in CMD space	223

List of Figures

1.1	A VISTA near-Infrared image of the Orion Nebula with the Trapezium OB stars at its core. Credit: ESO/J. Emerson/VISTA & R.Gendler. Acknowledgment: Cambridge Astronomical Survey Unit	27
1.2	Theoretical evolutionary tracks for stars with masses between 7.0 to 0.1 M_{\odot} for solar metallicity PMS stars. Isochrones at 1, 10 and 100 Myr are also shown (dashes). Credit: Siess et al. (2000).	30
1.3	Histograms showing the period distribution for ONC stars with masses exceeding 0.25 M_{\odot} (top) and with masses below 0.25 M_{\odot} . It is clear that the higher mass stars exhibit a bi-modal period distribution and that the lower mass stars rotate faster and exhibit a unimodal distribution. Credit: Herbst et al. (2002).	32
1.4	Resolved observations of circumstellar discs around PMS stars. Left: ALMA sub-mm observations of the disc surrounding the young star HL Tauri. Credit: ALMA (ESO/NAOJ/NRAO). Right: <i>HST</i> WFPC2 image of HH30, an edge-on PMS system. The central star is hidden from view, but its light is visible, scattered off the upper and lower surfaces of the disk. A bipolar outflow is also seen. Credit: Chris Burrows (STScI), the WFPC2 Science Team and NASA/ESA.	32
1.5	Fractions of stars with circumstellar discs as a function of cluster age. Credit: Bell et al. (2013).	33
1.6	A schematic of the accretion shock models of Matsakos et al. (2013). A strong magnetic field penetrates the chromosphere and confines the plasma in flux tubes. The accretion stream impacts on the surface and pushes the chromosphere down to the point where the ram pressure is equal to the stellar pressure. The black dashes show the region of interest in shock simulations by Sacco et al. (2008); Orlando et al. (2010); Matsakos et al. (2013). Credit: Matsakos et al. (2013).	34
1.7	3D MHD models of stable (left) and unstable (right) magnetospheric accretion. Red lines are sample magnetic field lines. The green surface is a constant-density surface showing the distribution of accreting gas. The black arrows indicate the rotational and magnetic field axes. Credit: Romanova et al. (2008).	35
1.8	Simulated lightcurves provided by models of accretion in which gravitational instability (top), planet induced thermal instability (middle) and inner-disc thermal instability (lower) cause episodic bouts of accretion to occur between quiescent phases. Credit: Audard et al. (2010).	36

- 1.9 IPHAS colours of known T Tauri stars in IC 1396. Green squares are identified CTTS. Red triangles are WTTS. The solid line shows the simulated main-sequence curve at the mean reddening of the cluster ($A_V = 1.56$). Dashed lines show the position of stars at increasing levels of $H\alpha$ emission as predicted by Drew et al. (2005). Grey dots show field stars in the region. The arrow shows the reddening shift for an M0V object being reddened from $A_V = 0$ to $A_V = 1.56$. Credit: Barentsen et al. (2011). 37
- 1.10 A representation of the YSO classification scheme. Left panels show the ideal SED for YSOs at each stage of the scheme. Right panels show a schematic of the morphology of the YSO at each stage. Credit: Andre (2011). 40
- 1.11 IRAC and IRAC-2MASS colour-colour diagrams used to identify young stellar objects in the star-forming regions of Orion (upper panels) and reference fields (lower panels). The coloured markers show identified protostars (Class 0, I and flat-spectrum sources) in red and Class II YSOs in green and blue. Blue markers in the Class II sample indicate possible ‘transition’ objects, which may exhibit disc truncation at a larger radius than typical of Class IIs. This may be indicative of disc clearing and reaching the end of the Class II phase. Black points are stars that do not exhibit IR excess. Further details of the classification cuts may be found in Gutermuth et al. (2008, 2009). Credit: Megeath et al. (2012). 41
- 1.12 The relationship between traditional young star classifications and the nomenclature used in this thesis. 41
- 1.13 $U - V, V - I$ colour-colour diagram of stars in the Orion flanking-fields. Note the population of stars with $U - V$ colours that are far above the main population and the ZAMS model. These U band excesses cannot be explained by extinction and reddening as shown by the extinction vector (arrow) corresponding to $A_I = 0.25$. Credit Rebull et al. (2000). 43
- 1.14 Mass accretion rates calculated from U band fluxes in the nearby star forming regions σ Ori (left) and NGC 2264 (right). In the left panel the different colours represent different disc classifications. Red dots are Class IIs, green triangles are ‘Transition-discs’ and blue squares are ‘Evolved-discs’ (see Hernández et al. 2007, for more details on these classifications), arrows show upper limits. In the right panel, orange dots and green triangles show stars identified by Stauffer et al. (2014) whose variability is dominated by stochastic accretion bursts and variable extinction respectively. Black dots are all other objects in the sample, arrows show upper limits. Credit: Rigliaco et al. (2011) [left panel], Venuti et al. (2014)[right panel]. 44
- 1.15 A comparison of $\text{Pa}\beta$ and $\text{Br}\gamma$ emission line equivalent widths with accretion rate. Filled circles are accretion rates from blue spectra, crosses are from U band photometry. Credit Muzerolle et al. (1998). 45

1.16	Spectra for RU Lup at two epochs with different levels of veiling. In the most veiled phase, photospheric lines are noticeably weaker. Certain lines (marked with arrows) appear to show line-filling as well as the addition of the continuum flux. Credit Gahm et al. (2008).	45
1.17	Non-exhaustive list of theoretical physical mechanisms that may be associated with variability in YSOs.	47
1.18	Lightcurve morphology classes, based on periodicity (Q) and flux asymmetry (M) metrics for optical light curves from <i>CoRoT</i> in a disc-bearing sample. Colour coding indicates the variability classification chosen by eye, before statistical assessment. The eclipsing binary is not strictly periodic because its lightcurve contains aperiodic fluctuations out of eclipse. Credit: Cody et al. (2014).	50
1.19	B band photometry of the outburst of FU Ori. Credit: Hartmann & Kenyon (1996)	51
1.20	A CMD of the Pleiades cluster compared with a simulated model population. Both the data (red dots) and the model (black points) are by Bell et al. (2012). The model age is 135Myr, is comprised of both single and binary stars and is corrected to a distance modulus of 5.61mag.	53
1.21	A V , $V - I$ CMD of the ONC is compared with ZAMS, 0.1Myr, 1Myr and 10Myr isochrones by D'Antona & Mazzitelli (1994) Filled circles indicate proper motion members. Crosses are proper option non members. Open circles are stars without proper motion data. Credit: Hillenbrand (1997).	54
2.1	Colour-magnitude diagrams of target cluster members in the Orion Nebula Cluster (top) and NGC 2264 (bottom) compared with isochrones from Siess et al. (2000). Medium orange (light grey) filled circles are confirmed single star members for which I have established veiling and EW[Li]. Large green (dark grey) filled circles are spectroscopic binary stars (and confirmed members) for which I have EW[Li] lower limits. Red crosses depict stars that I observed but were identified as radial velocity non-members. The limits of the plot represent the photometric limits imposed on my sample by (i) the sensitivity of the observations (ii) the T_{eff} cuts applied for the mass range of interest. Note: The three members that appear fainter than the 10 Myr isochrone in the ONC are numbered, these are discussed in Section 2.5.4. ONC photometry from Hillenbrand (1997), NGC 2264 photometry from Mayne et al. (2007).	58
2.2	Evolution of radius (upper panel) and photospheric lithium abundance (lower panel) as a function of time for Baraffe & Chabrier (2010) models with episodic accretion and reaching a final mass of $1 M_{\odot}$. Short dash (red): $M_{\text{init}} = 1 M_{\text{jup}}$, $\dot{M}_{\text{burst}} = 1 \times 10^{-4} M_{\odot}\text{yr}^{-1}$, $N_{\text{burst}} = 100$; dot (green): $M_{\text{init}} = 10 M_{\text{jup}}$, $\dot{M}_{\text{burst}} = 5 \times 10^{-4} M_{\odot}\text{yr}^{-1}$, $N_{\text{burst}} = 20$; dash-dot (black): $M_{\text{init}} = 20 M_{\text{jup}}$, $\dot{M}_{\text{burst}} = 5 \times 10^{-4} M_{\odot}\text{yr}^{-1}$, $N_{\text{burst}} = 20$; long dash (blue): $M_{\text{init}} = 30 M_{\text{jup}}$, $\dot{M}_{\text{burst}} = 5 \times 10^{-4} M_{\odot}\text{yr}^{-1}$, $N_{\text{burst}} = 20$; solid line (black) is a non-accreting model for a $1 M_{\odot}$ star. All calculations are made with $\Delta t_{\text{burst}} = 100$ yr and $\Delta t_{\text{quiet}} = 1000$ yr. The grey shaded region encompasses age estimates for the clusters studied in this paper	61

- 2.3 Predicted evolution of the 6708 Å lithium line strength as a function of age and colour in non-accreting models of PMS stars. The (red) hatched region is where I expect to find no stars that are younger than 20 Myr, thus defining a ‘forbidden zone’ in the clusters based on current age estimates. Stellar interior models are from Baraffe et al. (2002) and Siess et al. (2000), T_{eff} to $(V - I_c)_0$ from Kenyon & Hartmann (1995), curves of growth from Jeffries et al. (2003), $A(\text{Li}) = 3.3$ from Anders & Grevesse (1989). 62
- 2.4 Histogram of radial velocities for stars in the ONC (top) and NGC 2264 (bottom) relative to the median of the respective samples. Inset shows the entire sample including radial velocity outliers. 66
- 2.5 Example velocity cross-correlation function (CCF) plots, showing single star (top left), and close and wide line separation binary stars (top right and bottom). . . . 67
- 2.6 Spectrum of object RA = 05 35 15.47 Dec = -05 27 22.7 in the ONC. The thin black line is the object spectrum. The dotted line is the template showing significantly deeper photospheric absorption lines. The green (light grey) broad line is the broadened and veiled template that best fits the object spectrum ($r_\lambda = 0.69$). The template spectrum has a greater SNR than the target one (SNR of 58 per pixel as opposed to 38 per pixel). The broadening kernel and the addition of the smooth veiling model are also likely to make the model spectrum appear more smooth outside of the line regions than the target spectrum. 69
- 2.7 A comparison of 6708 Å lithium line equivalent width measurements for stars in the ONC (top) and NGC 2264 (bottom) plotted as a function of intrinsic $(V - I_c)_0$. Red points are unveiled single star measurements, black triangles are lower limits for spectroscopic binaries which are left as veiled (raw) measurements. The 0 Myr, 10 Myr and 20 Myr isochrones are based on models by Baraffe et al. (2002). Solid lines indicate models using a convective mixing length parameter (α) of 1.9. Dotted lines indicate $\alpha = 1.0$. Blue triangles are data from Palla et al. (2005) which are cited as having depleted lithium. These points have been calculated using $n(\text{Li})$ to EW[Li] conversion from curves of growth in Table 1 of Palla et al. (2007). The conversion from T_{eff} to intrinsic $(V - I_c)_0$ colour for the Palla et al. (2005) data have been made using the relation defined by Kenyon & Hartmann (1995). 71
- 2.8 Comparison of the EW[Li] data for bright and faint sub-samples in each cluster. In both clusters the population of faint stars shows a systematic decrease in lithium line strength. 72
- 2.9 Evolution of the surface lithium abundance divided by initial Li abundance for a selection of models producing stars in the range $0.7 - 1 M_\odot$ (from Baraffe & Chabrier 2010). Solid lines (blue) are those using accretion burst rates $\dot{M} = 5 \times 10^{-4} M_\odot \text{yr}^{-1}$. Dashed (red) lines are those using $\dot{M} = 1 \times 10^{-4} M_\odot \text{yr}^{-1}$. For model details see Table 3. Shaded grey region encompasses age estimates for the clusters in this study. 75

- 3.1 $V, V - I$ CMD of Cep OB3b. The black dots are all sources in the Cep OB3b field. The blue dots are sources classified as pre-MS using *Spitzer* infrared colours (left panel) and detection in X-rays (right panel). The dashed white and black line is the ZAMS of Siess et al. (2000) and the region defined by the black curve represents the PMS locus. The black arrow corresponds to 1 mag of extinction using the reddening law of Rieke & Lebofsky (1985). Credit: Allen et al. (2012). 81
- 3.2 INT WFC field-of-view (blue lines) overlaid on a Digitized Sky Survey red image of Cep OB3b. Circles denote the locations of periodic association members. The black boxes denote the field-of-view of observations made using the Faulkes telescope that were not used in this study. Credit: Littlefair et al. (2010). 81
- 3.3 Seeing and transparency plots for the observations made in 2013 Nov. Top panels show seeing conditions on the night of Nov 9 (left) and Nov 10 (right). Lower panels show the relative transparency on Nov 9 (left) and Nov 10 (right). The horizontal dashed lines show cuts made in seeing and transparency to reject the poorest data. 83
- 3.4 Examples of subsets of INT WFC i lightcurve data collected for a single disc-bearing source in Cep OB3b. The top panel shows data collected at a cadence of 1 minute on a single night in 2013 November. The middle panel is data collected over 16 nights in 2004 September. The lower panel is data collected over a period of 68 nights in 2005 August to November. Additional data was also collected in 2007 October. 84
- 3.5 $r, r - i$ CMDs showing the classification of sources in Cep OB3b. The left panel shows the disc-bearing sample (red crosses) overlaid on the photometry for all stars (black dots). The PMS locus is clearly visible, offset from the field stars. The right panel shows the X-ray identified discless sources (blue crosses) on the same CMD. The green box bounds the region from which the ‘Field’ population was selected. The region was selected to be wider in colour at brighter magnitudes to reduce the numerical bias toward fainter stars 85
- 3.6 An Ideal structure function, illustrating the main regimes. (See text for detail). Credit: Paltani (1999) 87
- 3.7 The structure function for BL-Lac object PKS 2155-304. The solid line is a fitted model of a power-law-shaped PSD. Credit: Paltani (1999) 88
- 3.8 A comparison of mean fluxes measured for individual field stars in data collected on 2013 Nov 10 and 2007 Oct 21 - 24. The data for 2013 Nov 10 have been corrected with a single scaling factor (of $\approx 10\%$) for each CCD, bringing the fluxes for all field stars into agreement within better than a few percent across the majority of the field. The left panel shows flux residuals as a function of x-position on each CCD. The right panel shows the same as a function of y-position. 89

3.9	Example noise model for field stars on CCD 2. Each point represents a slice of 51 stars in a given SF time-lag bin. The x-axis shows the mean flux for the stars in each slice. The y-axis is the (\log_{10}) mean fractional variability for all of the stars in that flux bin. The circles are the measured values, the lines are the best-fit analytical model described by Equation 3.3. The different colours represent different time-lags, calculated as part of the structure functions. Each CCD and time-lag have their own defined analytical coefficients that allow precise subtraction of non-astrophysical contributions to stellar variability.	90
3.10	Histograms showing $S(\tau)$ on short timescales for disc-bearing stars in Cep OB3b. Note that $S(\tau)$ is on a linear scale rather than the previous log scale examples. The top three panels show the variability on timescales of ≈ 1 minute, ≈ 5 minutes and ≈ 0.5 hours respectively. The lower panel shows the mean photometric uncertainty on a single lightcurve point for the same stars.	92
3.11	Example structure functions for disc-bearing YSOs in this analysis. A range of variability amplitudes and characteristic timescales are shown. Circles are the ‘field subtracted’ structure function for the target star. The dotted line shows the structure function for the subtracted ‘non-stellar’ variability. The red points are those which only use the high cadence data from 2013 Nov 10. The blue points are calculated using the years-timescale lightcurves.	93
3.12	Structure functions for a selection of discless YSOs in this study. Detail as per Fig. 3.11	94
3.13	PDFs of intrinsic stellar variability for disc-bearing (left) and discless YSOs (right) respectively.	96
3.14	Histograms of derived parameters for YSOs in Cep OB3b. The top left panel compares $S(\tau)$ when $\tau > t_{\max}$, for stars in the disc-bearing and discless samples. The top right panel compares the exponent of the variability power-law (k) for the samples. The lower panel compares t_{\max}	97
3.15	t_{\max} is compared with the rotation periods of periodic stars from Littlefair et al. (2010). Blue diamonds are discless stars. Red circles are disc-bearing stars.	98
3.16	Short-timescale transient events seen in the i lightcurves of two discless stars. The lightcurves are normalised so that their quiescent magnitude is zero.	99
3.17	Structure functions for the stars exhibiting short-timescale ‘flaring’ transient events. Details as in Fig. 3.11. As the flare events are ‘one off’ events that only occur within the minutes timescale dataset, the SF on longer timescales appears lower than on short timescales.	100
3.18	INT WFC i band images of star 4-1660 before (left) and during (right) the flare event shown in Fig. 3.16. These images were taken ≈ 5 minutes apart at BJD 2456607.49479 and 2456607.49820 respectively.	100

- 4.1 Literature variability parameters for all spectroscopic target stars. The left panel shows a histogram of variability amplitudes measured in the optical catalogues of Rebull (2001) and Herbst et al. (2002) and the near-IR catalogue of Wolk et al. (2014). Where a star appears in both the optical and near-IR catalogues, its optical variability amplitude is used. The right panel shows periods and variability amplitudes of stars in the spectroscopic sample where literature values exist. Circles (green) are from Rebull (2001), crosses (blue) are from Herbst et al. (2002) and diamonds (red) are from Wolk et al. (2014). 104
- 4.2 CMD comparing the positions of the spectroscopic sample (red circles) with the ONC population (black crosses) in the photometric dataset used to select the spectroscopic targets. Photometry from Hillenbrand (1997). 105
- 4.3 2MASS J-band image of the Orion Nebula Cluster region with my three INT WFC fields of view overlaid. Fields 1, 2 and 3 are represented by black, blue and purple CCD mosaics respectively. The positions of stars simultaneously monitored using the AF2/WYFFOS spectrograph are marked with red squares. 109
- 4.4 The two principal elements of the profile correction model for the g band photometry. Left panel: The relation between the square of the seeing (in pixels) and the measured profile correction for all bright, unsaturated stars in all g band frames. The blue points represent the difference in measured magnitude for a given star in a given frame using optimal and large-aperture (10 pixel radius) photometry. The linear fit (solid black line) shows the derived relation of $-0.002501 \text{ mag/arcsec}^2$. This seeing component is removed prior to the subsequent fitting of tilts and radial aberrations. Right panel: The ‘tilted plane’ components of the four CCD chips in the camera. 111
- 4.5 Theoretical relations for $r - i$ vs. $r - H\alpha$ and $r - i$ vs. $r - n_{6800}$ derived for main sequence stars in the mass range $0.1 - 7 M_{\odot}$. Interior models are from Siess et al. (2000) and atmospheres are from Allard et al. (2011). 113
- 4.6 Histogram of airmass differences between target and telluric star observations for the entire set of spectra. The mean of the modulus of the difference in airmass is 0.047. 114
- 4.7 Examples of individual (single epoch) spectra collected using AF2/WYFFOS. Spectra are flux calibrated using n_{6800} photometry. Important atomic and molecular lines are labeled. All stars display the presence of lithium, evidence of their youth. Star 95 shows weak photospheric absorption lines, broad $H\alpha$ emission and strong He I emission, all indicators of accretion. 116
- 4.8 An example of a composite photometric/spectroscopic SED for star 95 at a single epoch. The (coloured) diamonds are photometric measurements in U , g , r , n_{6800} and i bands. the (black) solid line is the spectrum. The horizontal error bars on the photometric points indicate the nominal bandwidth of the filters. 117

- 5.1 $g, g - i$ colour-magnitude diagrams for a selection of target stars showing how their position varies in CMD space over the course of one week. The black points are the mean colours and magnitudes for all stars with clean photometry in this study. The red (grey) points are the positions at different epochs for the target star in question. The inset is a close-up of the positions of the target star, coloured to represent the epoch and highlighting the photometric uncertainties. Extinction vectors corresponding to $A_V = 1.0$ are shown for $R_V = 3.1$ and 5.5. A range of movement is seen in this diagram, the physical nature of this is investigated in later sections of this thesis. 120
- 5.2 A comparison of variability vectors for disc-bearing (left panel) and discless (right panel) stars in the ONC. Each circular data point marks the mean $g, g - i$ position for a given star. The line running through each data point is a linear fit through the variability locus for that star. The length of the line represents the rms variability with respect to the mean position. The points are coloured to show whether they are identified as being in the ‘accreting disc-bearing’ (blue), ‘non-accreting disc-bearing’ (red) or ‘discless’ samples as identified in Chapter 8. The discless sample only shows stars which have membership probabilities $> 95\%$ from Hillenbrand (1997). 122
- 5.3 The amplitude of the variability vectors shown in Fig 5.2 are presented for the accreting (top left), non-accreting disc-bearing (top right) and discless (lower middle) stars as a function of CMD position. The diameter of each symbol corresponds linearly with the length of the variability vector in Fig 5.2. In addition to the CMD position differences between the populations, it is clear that the accreting population exhibits significantly greater variability. The non-accreting disc-bearing and discless populations are indistinguishable. 123
- 5.4 The synthetic model population, constructed and compared with the real data for the ONC. The left panel shows the real ONC data (black circles) overlaid with the model locus (red line). The central panel shows a synthetic model population of stars with binary fraction 0.5 displaced equally about the model locus (red dots). The real data is compared (grey dots). The right panel shows the synthetic population dispersed by the variability measured from my real lightcurve data (red dots) and compared with the real data (grey dots). It is clear that the spread in the model population which simulates the effects of binarity, variability and photometric uncertainties is insufficient to explain the full luminosity spread in the data. 125
- 5.5 Histograms to show the spread in $g - i$ present in the model (blue) and real (green) CMD data for the ONC. Each histogram is contracted by binning the deviations in $g - i$ shown for all stars in a sample about the model PMS locus. The real data is clearly spread more widely than the model dataset, implying that a source of spread is present in addition to the binarity, variability and photometric variability modelled in this analysis. 126

- 6.1 n_{6800} flux plotted against EW_{TiO} for four stars which show flux variability without apparent changes in the EW of the photospheric lines. The blue points are the measurements for the star at epochs over 7 nights of observations. The black dotted lines are vectors along which the star should move if the line EW was ‘veiled’ by an amount corresponding to the change in flux in the n_{6800} band. As these stars move vertically in this plot, the flux changes that we see are likely to be driven by occultation/extinction of the star rather than changes in the accretion luminosity or cool-spot coverage. Fig 6.2 shows the equivalent plot for two stars which show photometric modulation that is attributed to changes in accretion luminosity and cool spots. 131
- 6.2 For comparison with Fig. 6.1, the same data is plotted for a star that shows significant accretion luminosity changes (left panel) and brightness changes that are attributed to change in cool-spot area (right panel). They are clearly distinguishable from the stars in 6.1 as they show significant changes in EW_{TiO} as the n_{6800} flux varies. The black dotted lines are vectors along which the star should move if the line EW was ‘veiled’ by an amount corresponding to the change in flux in the n_{6800} band. 132
- 6.3 The mean spectrum (black) compared with the FPC (red) for each of the ‘extinction’ driven variable stars. In each case the FPC has been scaled by its mean amplitude from the seven nights of observations. The FPCs describe almost all of the variability ($> 96\%$) for each star. Each FPC also appears to be essentially a scaled version of the mean spectrum, supporting the assertion that extinction changes are driving the variability in these stars. 133
- 6.4 Normalised extinction curves for the YSO variability are compared with ISM models. The black points are the extinction curves calculated for each star, coloured lines are models of extinction from Cardelli et al. (1989), using $R_V = 3.1, 5.0$ and 7.0 . It is clear that the circumstellar extinction is ‘greyer’ than that typically seen in the ISM, implying that grain growth has occurred. 135
- 6.5 Calculated orbital radii of material in Keplerian orbits about stars with mass $0.1, 0.5, 1.0$ and $2.0 M_{\odot}$ as a function of period. The radii calculated are typical of quasi-static structures in the inner-discs of ‘AA Tau analogue’ systems found in NGC 2264 by Alencar et al. (2010). 137
- 6.6 The Keplerian velocity of material orbiting stars of mass $0.1, 0.5, 1.0$ and $2.0 M_{\odot}$ as a function of orbital radius (black solid lines). The black dotted line shows the lower limit of orbital velocity required to occult a star of radius $1R_{\odot}$ in 1 day. The dotted line places upper limits on the orbital radius of clumps that could provide the variable extinction that I measure in Section 6.2.3. For comparison Mercury, Earth, Jupiter and Neptune (black crosses) and some extra-solar planets (labelled black circles) are shown. The inner radius of the measurement by Throop et al. (2001) of outer disc dust is shown by the black dashed line, indicating the regions probed in this study are between 1 and 2 orders of magnitude closer to the star. . . 138

- 7.1 Relationship between TiO spectral index and measured $g - i$ for discless template stars. The (blue) circles are stars with $A_V < 0.05$ according to Hillenbrand (1997). The black line is a second order polynomial fit to these points. The (red) crosses are stars with $A_V > 0.05$. The dashed lines are the measured $g - i$ colour excesses which are attributed to extinction-reddening. Stars which show a $g - i$ excess are corrected for extinction and reddening using the wavelength dependent extinction relation of Fitzpatrick (1999). 144
- 7.2 The spectra of the selected discless template stars are shown, corrected for reddening and normalised to 1.0 at 7000\AA . The correlation between the depth of TiO absorption bands with the gradient of the spectra (increasing with reducing T_{eff}) is clear. The range of spectra shown here correspond to $1.26 < (g - i)_0 < 3.06$ 145
- 7.3 $g, g - i$ colour-magnitude diagram showing the positions of the template stars (red circles) compared with the rest of the ONC population (grey dots). The templates have been corrected for the effects of extinction and reddening, based on their spectroscopic TiO index. The black dashed line is a linear fit to the template stars. 146
- 7.4 A grid of values showing the χ^2 fitting statistic as a function of template and extinction, (A_i) for one example star in my sample (Star 50). The y-axis shows the iterative step in A_i running from -0.5 (top) to 4.0 (bottom). The x-axis corresponds to the template number, running from hotter (left) to cooler (right). White areas show regions of the χ^2 space that return negative veiling, an un-physical situation that rules them out of the fitting. The colour scaling corresponds to $\log_{10}\chi^2$. Visually this reduces the contrast between good and poor fits, however it is necessary to illustrate the large range of χ^2 values returned. The best-fit solution in this case is template 79 ($g - i = 1.83$), $A_i = 0.3$ and a veiling flux at 6805\AA of $1.41 \times 10^{-25} \text{ erg cm}^{-2} \text{ s}^{-1} \text{ Hz}^{-1}$ 148
- 7.5 ‘Best-fitting’ models of template, extinction and veiling for four target stars. The dark blue line is the target spectrum, the green line is the best-fit template spectrum. The light-blue line is the residual (assumed to be the accretion spectrum) and the black line is the boxcar smoothed residual against which χ^2 is measured. The red line is the complete model spectrum, comprising the extinguished template plus the smoothed accretion spectrum. The top two panels show stars which show optical veiling and also show accretion luminosity excess in their photometry (left panel - star 14, right panel - star 50) . The lower two panels show stars with discs which do not have photometric excesses consistent with accretion (left panel - star 62, right panel - star 155). 149
- 8.1 $g, g - i$ CMD of all stars in our field of view with clean photometry (unflagged and $S/N \geq 10$). The black (solid) lines show 1, 10 and 100 Myr isochrones from the models of Bell et al. (2014). Red (dashed) lines show (from right to left) evolutionary tracks for single stars of mass 0.1, 0.2, 0.3, 0.4, 0.5, 0.6, 0.8, 1.0, 1.5 and $2.0 M_{\odot}$. The sample is limited at the faintest g magnitudes by S/N and at the brightest magnitudes by saturation. 154

- 8.2 $r - i$, $r - H\alpha$ colour-colour plot for stars that are likely members of the ONC and that do not exhibit Mid-IR evidence of an accretion disc. Black points (with error-bars) are all stars in the sample. Red (light grey) diamonds are the median colours in 20 star wide bins in $r - i$. A 2σ clipping routine has been applied in $r - H\alpha$ to reduce the influence of the few contaminating stars that exhibit $H\alpha$ excess or strong extinction. The solid line is a quadratic function fitted to the median colour points and defines the locus for non-accreting stars. A (dashed) line shows the expected $r - H\alpha$ excess corresponding to an equivalent width of 10 \AA above the non-accreting locus. 156
- 8.3 $U - g$, $g - i$ colour-colour plot for stars that are likely members of the ONC and that do not exhibit mid-IR evidence of an accretion disc or evidence of active accretion via $H\alpha$ excess. Black points (with error-bars) are all stars in the sample. Red (light grey) diamonds are the median colours in 20 star wide bins in $g - i$. The solid line is a quadratic function fitted to the median colour points and defines the locus for non-accreting stars. 157
- 8.4 $U - g$ excess plotted against $r - H\alpha$ excess for the discless stars (left panel) and disc-bearing stars (right panel) identified by Megeath et al. (2012). The correlation between U excess and $H\alpha$ is strong, although scatter about this correlation is ≈ 1 mag in either colour. The dotted lines show the adopted cuts made to identify accreting stars. The upper right quadrant is the accreting star population. The lower left quadrant is the non-accreting sample. The other two quadrants contain stars with ambiguous accretion status. The green points highlight stars for which spectral time-series were collected. An extinction vector corresponding to $R_V = 3.1$ is shown. 159
- 8.5 A $U - g$, $g - i$ plot comparing the positions of the accreting (red) and non-accreting (blue) samples. The accreting stars show significant excess in U compared with the non-accreting stars. 160
- 8.6 g , $g - i$ colour magnitude diagrams showing the samples containing only accreting stars (upper left), non-accreting disc-bearing stars (upper right) and discless stars (lower). The discless sample comprises stars with membership probability $> 95\%$ and $A_V < 1.0$ in Hillenbrand (1997). All stars in these diagrams have photometry which is unflagged and has $S/N > 10$ in both g and i 161

- 8.7 A comparison of the non-accreting disc-bearing and accreting disc-bearing stars based on *Spitzer* IRAC colours. A histogram (left panel) compares the α IRAC index for the accreting (blue-dotted) and non-accreting (red-hatched) stars. The histograms are normalised as a probability distribution function so that the area under the curve equals one. The vertical dotted lines denote the empirical disc classifications of Lada et al. (2006). NP: Naked photosphere, AD: Anaemic disc, TD: Thick disc, FS: Flat spectrum, CI: Class I. The right panel shows a *Spitzer* colour-colour diagram with the limit defined by Gutermuth et al. (2009) to classify Class II YSOs. Circles (red) denote non-accreting disc-bearing stars, Diamonds (blue) denote accreting disc-bearing stars. Faint (black) dots denote all stars in Cep OB3b with *Spitzer* photometry. Data from Megeath et al. (2012). 163
- 8.8 $g, g - i$ CMDs for accreting stars with spectra. For each accreting star the CMD position of the best-fit template star found in Chapter 7 is shown by the green box. The bounds of the green box are defined by the discrete colours of the template stars and their intrinsic luminosity spread. The extent of the green box defines the region in which we should find the intrinsic ‘photosphere only’ position for the accreting star. The blue box is the region in which a star within the green box will reside once its photospheric colours have been subject to extinction and reddening corresponding to the spectroscopically measured extinction of the accreting star. The red diamond is the mean CMD position for the accreting star. Extinction and accretion-luminosity vectors are shown with black arrows. 165
- 8.9 Accretion luminosity vectors calculated for all accreting stars within the spectroscopic sample (black arrows) compared with the CMD (black dots). The picture shown is clear, accretion luminosity moves stars blue-ward in the CMD, spreading stars away from the PMS locus. Extinction vectors corresponding to $A_V = 1$ are shown for comparison. 166
- 8.10 A comparison of accretion induced g band magnitude changes with mean values of veiling at 6800 \AA for the accreting stars. 166
- 8.11 A comparison of $V, V - I$ CMDs for YSOs in Cep OB3b. Disc-bearing stars (left panel) are identified from *Spitzer* colours, Discless stars (right panel) are identified using *Spitzer* colours and X-ray flux (Allen et al. 2012). Optical photometry is from Mayne et al. (2007), as used in the Littlefair et al. (2011) study. 168
- 8.12 $g, g - i$ CMD (left panel) and $U - g, g - i$ colour-colour diagram (right panel) of the six stars identified in Palla et al. (2007) (red points) as having H-R diagram and/or lithium derived ages > 10 Myr. The CMD shows these stars compared with the general ONC population (black dots) and isochrones at 1, 10 and 100 Myr from Bell et al. (2014). In the colour-colour diagram, these stars are compared with the general ONC population (black dots) and the empirically defined PMS locus. The position of these stars in the colour-colour diagram implies that they have a large U excess and hence are heavily-accreting objects. 169

- 9.1 The accretion luminosity models of Calvet & Gullbring (1998) for a selection of stellar masses, radii and accretion energy fluxes \mathcal{F} . The dotted line is optically thin emission from the preshock (plus attenuated post-shock emission), the dashed line is the emission from the heated photosphere, and the solid line is the total emission. 172
- 9.2 Empirical relation between L_{acc} and $L_{\text{H}\alpha}$. From: Manara et al. (2012). 173
- 9.3 A comparison of H α and U band excess fluxes as a function of time for accreting disc-bearing stars in the spectroscopic sample. The (red) crosses show measurements made at different epochs over the seven nights for a given star. The black circles are mean measurements (over the seven nights) for all available stars in the ONC dataset. The spread seen in the black circles is comparable to the spread seen in single epoch data by Manara et al. (2012). An extinction vector corresponding to $A_V = 1$ is shown. No correction for extinction has been made. 175
- 9.4 A comparison of veiling and U band excess fluxes as a function of time for accreting disc-bearing stars in the spectroscopic sample. The points show measurements made at different epochs over the seven nights for a given star. Changes in extinction will move points vertically in this diagram. No correction for extinction has been made. 177
- 9.5 A comparison of intrinsic photospheric SEDs with observed SEDs for accreting stars. The dashed black line is the extinction-free best-fit photospheric template SED found for each star using the spectroscopic analysis in Chapter 7. The (black) circles represent the template after application of the extinction measured for each accreting star in the spectroscopic analysis. Uncertainties on the template SED caused by uncertainties in the adopted value of R_V are indicated by the black error bars, which are computed assuming $R_V = 6$ rather than the nominal $R_V = 3.1$. Where error bars are not visible, they are smaller than the markers. The (grey) shaded region represents the uncertainty on the photospheric SED due to uncertainty on the intrinsic radius of the templates. The (red) diamonds represent the measured SED for each accreting star. The peak in the SEDs at 6568Å is the flux measurement in the narrow-band H α filter. 180
- 9.6 The luminosity excess flux calculated as a function of wavelength for 15 accreting stars in the ONC (red circles). The grey shaded region shows the uncertainty on the excess. The dashed lines show black-body functions with temperatures of 5000 K, 7500 K, 10 000 K and 50 000 K, normalised to the data at the wavelength of the g band. The excess in the narrowband H α filter is omitted as it is likely that multiple sources of non-thermal flux are present and thus any measurement of luminosity excess is considered unreliable. 181
- 9.7 Comparison of photometric SED variability with the excess luminosity for accreting stars. The black points show the measured luminosity excess. The red points show the first principal component. The excess luminosity SED had been normalised to the variability SED at the n_{6800} wavelength to allow for comparison. 183

10.1	INT WFC images of V733 Cep (star 2-336) taken using the <i>i</i> filter. Image scale is $0.333 \text{ \AA pixel}^{-1}$. Upper left and right are taken in August and September 2004. Lower left was taken in 2007 and lower right in 2013. The brightening event detected in the photometry is clearly evident.	188
10.2	The INT lightcurve (left panel) and SED (right panel) for V733 Cep (star 2-336). The SEDs are from the <i>SDSS</i> and Bell et al. (2013), taken in 2003 and 2007 respectively.	188
10.3	Long-term lightcurve for V733 Cep (star 2-336). Data is compiled from Reipurth et al. (2007); Peneva & Semkov (2008); Abazajian et al. (2009); Peneva et al. (2010); Barentsen et al. (2014). Measurements made by Abazajian et al. (2009), Barentsen et al. (2014) and this study use a <i>SDSS</i> based filter bandpass which adds an additional systematic error of ≈ 0.3 magnitudes when compared with photometry using the Johnson/Cousins filter systems of the other observers. It is clear though that the large amplitude of variability seen means that this systematic does not have any impact on conclusions drawn from these observations.	189
10.4	Close-up of the region of the combined structure function where stars may show long-timescale variability in excess of that seen on rotation timescales. The blue crosses are individual points in the structure functions of all stars in the disc-bearing sample. On timescales $\gtrsim 1$ year, a few stars exhibit variability that is greater than that seen on timescales of a few days where variability saturates for most disc-bearing stars.	190
10.5	<i>SDSS</i> r-band image showing the locations of the disc-bearing YSOs identified by Allen et al. (2012) (red circles). The blue points show the location of the four high-amplitude variables identified in Section 10.3. Star 2-336 is V733 Cep. Image created using <i>Aladin</i> (Bonnarel et al. 2000).	191
10.6	INT WFC images of star 1-3653 taken using the <i>i</i> filter. Image scale is $0.333 \text{ \AA pixel}^{-1}$. Upper left and right are taken in August and September 2004. Lower left was taken in 2007 and lower right in 2013. The brightening event detected in the photometry is clearly evident.	192
10.7	Lightcurve (left panel) and <i>u, g, r, i, z</i> , photometric SED (right panel) for star 1-3653. The SEDs are from the <i>SDSS</i> and Bell et al. (2013), taken in 2003 and 2007 respectively.	192
10.8	Images of star 4-4327. Details as per Fig. 10.6. The bright phase in 2007 is evident compared with the other epochs.	193
10.9	Lightcurve (left panel) and SED (right panel) for star 4-4327. Details as per Fig. 10.7.	193
10.10	Images of star 4-7279. Details as per Fig. 10.6. The 2007 and 2013 epochs clearly show the star in a brighter state.	194
10.11	Lightcurve (left panel) and SED (right panel) for star 4-7279. Details as per Fig. 10.7.	194

10.12	Zero point corrections between photometry in the INT WFC system and <i>SDSS</i> for 182 PMS stars from Bell et al. (2013).	196
10.13	<i>SDSS</i> $i, g - i$ (left), $i, i - z$ (right) and $g, g - i$ (lower), CMDs of Cep OB3b. Black points are all stars within the INT field of view that appear in the <i>SDSS</i> . The four long-timescale variables have two epochs of photometry plotted (red points connected with lines) taken from observations in 2003 and 2007 showing how they move in CMD space. Numbers correspond to ccd number and ID for each star.	197
10.14	A <i>Spitzer</i> colour-colour diagram comparing the mid-IR SEDs of the long-timescale variables (yellow dots) with the Cep OB3b population. Star 2-336 is the FUor candidate V733 Cep. Green crosses are Class I YSOs (embedded protostars), blue crosses are Class II YSOs (disc-bearing), black crosses are Class IIIs (discless). The red crosses are ‘transition-disc’ objects. Photometry from Allen et al. (2012).	198
10.15	Photometry of previously studied EXors from the literature. The crosses (red) are photometry of the EXor candidate showing the brightness and colour evolution from quiescence to outburst. The stars V1118 Ori and V1647 Ori are compared with $V, V - I$ photometry of the ONC by Hillenbrand (1997). XZ Tau N is compared with photometry of Taurus by Kenyon & Hartmann (1995). The other stars do not have available photometry of associated star forming regions so they are compared with photometry of Cep OB3b from Littlefair et al. (2010) which have been corrected to the distance modulus of each EXor. The (blue) ‘plus’ symbols are PMS members in the associated regions. In Cep OB3b photometry these are those identified by Bell et al. (2013). EXor Data are from Audard et al. (2010) [V1118 Ori], Kun et al. (2011a) [V1180 Cas], Kóspál et al. (2013) [V2492 Cyg], Kóspál et al. (2011) [VSX J205126.1+440523], Coffey et al. (2004) [XZ Tau N], Kun et al. (2011b) [PV Cep].	200

List of Tables

2.1	Key parameters for clusters selected in this study.	62
2.2	Parameters for accreting models plotted in Fig. 2.9	74
3.1	Summary of observations made and collated as part of this study.	82
3.2	Variability parameters derived through model fitting of YSO population SF data. See section 3.4.1 for details. Note that t_{\max} has been converted to days and c is expressed as $S(\tau)$ (not $\log_{10}S(\tau)$ as shown in the plots).	96
4.1	Star ID numbers assigned in this study, stellar coordinates and literature YSO classifications (from Megeath et al. 2012) for all stars in the spectroscopic sample. N: Naked photosphere, D: Circumstellar Disc, P: Protostar.	106
4.2	Central coordinates in each field of view for INT pointings	108
4.3	Filters and exposure times used for each of the cycled INT pointings	109
5.1	Derived parameters for CMD variability for stars in the ONC. Each parameter has a mean value quoted with its standard error. The standard deviations of each parameter across the samples are also shown.	121
6.1	Key parameters for stars which show variability in extinction. A_i is that measured in Chapter 7 at a single epoch and varies from this value. Spectral types are from Hillenbrand et al. (2013). The fraction of the SED variability described by the FPC is shown in column 6. In all of these stars, the variability due to the FPC is dominant, comprising > 96% of the variability observed.	132
6.2	Derived extinction parameters for ‘variable extinction’ stars. A_V and A_B are found by linear interpolation of extinctions in the INT WFC filters. Note that all of the R_V values are ‘greyer’ than that typically adopted for the ISM ($R_V \approx 3.1$).	134
6.3	Comparison of the spectroscopically derived A_i with the Peak-to-peak inner-disc extinction for the four ‘extinction variable’ stars. For stars 62 and 66, the overall extinction for the star can be entirely explained by the circumstellar material. For stars 133 and 152, approximately 25% of the observed extinction can be attributed to inner circumstellar material, the rest being due to the ISM or the outer circumstellar regions.	140

7.1	Best-fit parameters determined for stars with discs in the ONC based on the spectroscopic fitting procedure. The last column defines the accretion status of each star based on U band and $H\alpha$ excess flux found in Chapter 8. ‘acc’ denotes accreting stars, ‘non-acc’ denotes non-accreting stars.	151
8.1	Mean colour excess and 1σ limits for all discless stars in our sample	159
9.1	Key parameters for stars showing correlated U excess and veiling behaviour . . .	178
9.2	Key parameters for stars showing uncorrelated U excess and veiling behaviour . .	178
9.3	Estimated stellar masses and accretion rates for stars with extracted excess luminosity SEDs.	184

Declaration

This thesis contains work published or pending publication as papers. The results and techniques of Chapter 2 have been published in MNRAS, Volume 434, Issue 2, pp. 966-977. Chapters 3 to 10 contain work that will be published in the near future.

The photometric observations taken with the Wide-Field Camera on the *Isaac Newton* Telescope and the spectroscopic observations taken with AF2/WYFFOS on the *William Herschel* Telescope were obtained by Nathan Mayne, Tim Naylor, Jon Rees and myself. The rest of the work presented in this thesis is my own.

The *Isaac Newton* Telescope and the *William Herschel* Telescope are both operated on the island of La Palma by the *Isaac Newton* Group (ING) in the Spanish Observatorio del Roque de los Muchachos of the Instituto de Astrofísica de Canarias.

Acknowledgements

Matthew Bate once made a comment which went something along the lines of “A PhD is all done in the last 6 months anyway”. As I sit here in June adding the finishing touches prior to submission, it certainly feels like that comment has some truth. Particularly as the reduction of the simultaneous photometry and spectroscopy seemed to spring no-end of awkward challenges to test the student.

Fortunately, I have had the support of an excellent supervisor. Tim Naylor has been constantly supportive, particularly as I undertook my PhD whilst I and my family live 70 miles away in Cornwall. Tim’s ability to ask the question that instantly illuminates the solution to a problem has saved me from myself on many occasions. I offer him my most sincere thanks, both for giving this ‘mature student’ an opportunity to fulfil a longstanding dream of studying for a PhD and for letting me have the freedom to really find my own way through this project.

I also offer my thanks to the various scientists with which I have had the great fortune to work. In no particular order, Nathan Mayne, Rob Jeffries, Cameron Bell and Jon Rees have been a source of great inspiration and intellectual support. My thanks also go to all of the staff and students at the Astrophysics department of Exeter University for their friendship and help.

On a more personal level, I have to thank my Mum and Dad, not least for the number of times that they have stepped into the breach, looking after the girls so that I could concentrate on my work. Also to my dearest wife Amy, who gave me the push to give up my perfectly good job to become a student again, then supported me throughout. During the course of my PhD she also gave me a second beautiful daughter and did me the greatest honour of becoming my wife. Finally, I would like to dedicate this thesis to my two beautiful daughters, Eva and Flo, a constant source of inspiration and mischief!

Darryl Sergison
Exeter, U.K.
8th June 2015

Chapter 1

Introduction

1.1 Star Formation - Clouds to Cores

Young stars are typically found associated with regions of cold and dense molecular gas. These ‘molecular clouds’ are found on a variety of scales from giant star forming complexes of $\sim 10^6 M_{\odot}$ and diameter 100 pc to clouds of $< 1 M_{\odot}$ and < 1 pc and smaller (Hartmann 1998). A significant nearby example is the Orion nebula (Fig. 1.1) where an estimated $10^5 M_{\odot}$ of molecular hydrogen, helium and a small fraction of heavier elements is found within a region of diameter ≈ 10 pc. Being only 400 pc from the Earth (Menten et al. 2007) allows study of the Orion nebula in greater detail than most other star formation regions. At the centre of the molecular cloud is a large cavity which contains a young star cluster containing more than 2000 stars within the central 0.15 pc (Hartmann 1998). At the centre of the cluster is found the trapezium group of OB stars. The cluster has an estimated age of between of 2 and 6 Myr (Mayne & Naylor 2008; Da Rio et al. 2010b; Bell 2012). As a result of its youth, most stars in the cluster are pre-main sequence stars (Hillenbrand 1997) and the majority have dusty circumstellar discs (Haisch et al. 2001).

Giant molecular clouds (GMCs) probably form and evolve dynamically from compression of the interstellar medium (ISM) by kinematic motions driven by gravity and turbulence (Bergin et al. 2004; Dobbs et al. 2006; Dobbs & Bonnell 2007). The clumps and cores that form stars also appear to be dynamic and evolving objects that behave somewhere between waves and discreet objects (Vazquez-Semadeni et al. 1996). H_2 molecules are believed to form in the ISM by catalysed combination of hydrogen atoms on the surface of interstellar dust grains (Hollenbach & Salpeter 1971). H_2 will dissociate again through thermal collisions or exposure to ionising radiation. The rate of H_2 production compared with its dissociation reaches an equilibrium that depends on the local conditions within the cloud. A density increase caused by dynamical compression of the cloud will increase the collision probability between hydrogen atoms and dust grains, thus shifting the equilibrium in favour of the production of H_2 . The molecules can only survive for any significant time within the interiors of dark and translucent interstellar clouds (and possibly the deep interior of diffuse clouds), which are simultaneously shielded from radiative dissociation by external UV photons and are cold enough ($\lesssim 20$ K, e.g. Wilson et al. 1997) to avoid collisional dissociation (Shull & Beckwith 1982). The observed low temperatures of molecular regions are explained as the result of a thermal balance between heating by cosmic rays and cooling by molecular line



Figure 1.1: A VISTA near-Infrared image of the Orion Nebula with the Trapezium OB stars at its core. Credit: ESO/J. Emerson/VISTA & R.Gendler. Acknowledgment: Cambridge Astronomical Survey Unit

emission, the rate of which increases steeply with increasing temperature (de Jong et al. 1980). If the density of the cloud falls, so will the collision probability between grains and atoms. Thus the rate of dissociation will become larger than recombination and the equilibrium will favour production of neutral hydrogen. As a result, the dynamic nature of cloud compression and the resulting H_2 production means that GMCs are relatively short lived. Observational evidence suggests that clouds appear, form stars and disperse on dynamical timescales of just a few million years (Elmegreen 2000).

The high density and low temperatures found in the cores of molecular clouds are essential for the gas to collapse under gravity to form stars. The gas will be prevented from collapse as long as its internal pressure is in balance with the gravitational force acting on the cloud. This balance is described by the virial theorem which states that in static equilibrium

$$2E_k + E_g = 0 \quad (1.1)$$

where E_k is the internal energy of the gas and E_g is the gravitational potential energy of the system. In the case where

$$E_k < -\frac{1}{2}E_g \quad (1.2)$$

the cloud will collapse. For a spherical cloud containing N particles, of total mass M , temperature T , and with mean radius $\langle R \rangle$, if the gas is considered ideal and the density is uniform then the condition for collapse becomes

$$\frac{3}{2}NkT < \frac{GM^2}{\langle R \rangle}, \quad (1.3)$$

where k is the Boltzmann constant. This is known as the Jeans' condition (Jeans 1902). For a given temperature and density, the minimum mass required for a cloud to collapse is

$$M_J = \left(\frac{3NkT\langle R \rangle}{G} \right)^{\frac{1}{2}}. \quad (1.4)$$

This is known as the Jeans' mass. The number of atoms in a Jeans' mass is

$$N = \frac{M_J}{m_p \mu} \quad (1.5)$$

where m_p is the atomic mass unit and μ is the mean molecular weight of the gas. The density of the cloud is defined as

$$\rho = \frac{4}{3}\pi\langle R \rangle^3 \quad (1.6)$$

Substituting Equations 1.5 and 1.6 into Equation 1.4 gives

$$M_J = \rho^{-\frac{1}{2}} T^{\frac{3}{2}} \left(\frac{5k}{G\mu m_p} \right)^{\frac{3}{2}} \left(\frac{3}{4\pi} \right)^{\frac{1}{2}} \quad (1.7)$$

It is clear from this equation that both an increase in density or a decrease in temperature will reduce the mass required for gravitational collapse. This explains why the cool, dense cores of molecular clouds are the preferred regions for star formation. This equation also suggests that as the cloud collapses (assuming the collapse is isothermal) its rising density means that the Jeans' mass within the cloud will fall, leading to fragmentation and the possible formation of many smaller cores from the initial larger cloud.

Protostellar formation

(Larson 1969) conducted some of the first successful 1D simulations of the collapse of molecular clouds into protostars. Since 1969, star formation theory has developed significantly and now includes more complex physics such as magnetic fields and angular momentum evolution. However, to provide a basic outline of protostellar formation, the results of the early work are outlined here.

As a cloud collapses, it will be heated by its own liberated gravitational energy. Initially the heated gas is cooled through line and then dust continuum emission and will remain essentially isothermal. As the collapse progresses, pressure gradients cause the density of the cloud to increase preferentially toward the centre. As the density rises the gas becomes increasingly opaque and enters a more adiabatic phase, which slows the rate of cooling and collapse. Fortunately, the increasing density heats the dust in the cloud through collisions, allowing it to radiate and permit further cooling and contraction. Eventually collapse in the centre of the cloud is halted by the thermal pressure and it approaches hydrostatic equilibrium. This results in the formation of the first hydrostatic core with a predicted temperature of $\approx 170\text{K}$ and a radius of $\approx 4\text{ AU}$. Further accretion and the development of shocks from infalling material cause the core to continue to be

heated until the temperature reaches ≈ 2000 K, at which point the H_2 molecules begin to dissociate. This process cools the cloud and permits its further collapse on timescales commensurate with the free-fall time. The contracting core of the cloud dissociates its H_2 and reaches temperatures high enough to ionise hydrogen and helium gas, both of these processes further cool the cloud and permit further collapse. Once the core of the cloud reaches a temperature of ≈ 20000 K it once again reaches hydrostatic equilibrium with a radius close to that of a star. Accretion continues both directly from its collapsing cloud and via a forming circumstellar disc onto the central object which is now classified as a protostar.

Star formation timescales

The timescales for converting ISM material into new stars has been the focus of much research, yet is still not well constrained and observational estimates are contradictory. The picture so far described in this introduction of dynamic molecular cloud formation is principally based on theoretical models and observations of GMCs. It suggests that star formation is a rapid process, occurring in a given region on timescales commensurate with the sound crossing-time (which might be ~ 1 Myr for a region such as the ONC). This is a picture that is supported by studies such as Elmegreen (2000), Hartmann et al. (2001), Ballesteros-Paredes & Hartmann (2007) and Jeffries (2007) who infer rapid cloud evolution and cessation of star formation. However, this view of rapid star formation in a given GMC is not one that is universally observed. Blitz et al. (2007) find that molecular clouds in the Large Magellanic Cloud have lifetimes of 20 - 30 Myr and that star formation could continue in a given cloud for ≈ 10 Myr. Populations of stars that appear to be older than 8 Myr have been found in the Eagle nebula, apparently co-located with stars of age 1 Myr (De Marchi et al. 2013), implying an extended star formation history. Extended periods of star formation have also been suggested in NGC 6306 (Correnti et al. 2012) and other nearby associations (Palla & Stahler 2000, 2002). Elmegreen (2007) suggests that the discrepancy may be due to there being a two stage process where initial rapid star formation and subsequent feedback from ionising radiation and supernovae leads to fragmentation of the clouds, which then continue to form stars at a slower rate.

1.2 Young low-mass stars ($< 2 M_{\odot}$)

The newly formed protostars described in Section 1.1 are thought to be enshrouded in their accreting envelopes for timescales of $\sim 5 \times 10^5$ years (Feigelson & Montmerle 1999; Hatchell et al. 2007). During this time they slowly contract as thermal energy is radiated away. Finally, the infall slows as the environment around the protostar becomes depleted in gas and the photosphere of the young star becomes visible, surrounded by an orbiting circumstellar disc. At this stage the star is referred to as a pre-main-sequence (PMS) star.

The emerging star has a radius and luminosity that are significantly greater than its main sequence counterpart of similar mass. For instance, a $1 M_{\odot}$ star at an age of 1 Myr is predicted to have a radius of $2.6 R_{\odot}$ and a bolometric luminosity of $2.3 L_{\odot}$ (Siess et al. 2000). At this stage, the energy source of the star is gravitational contraction, as opposed to the hydrogen burning seen

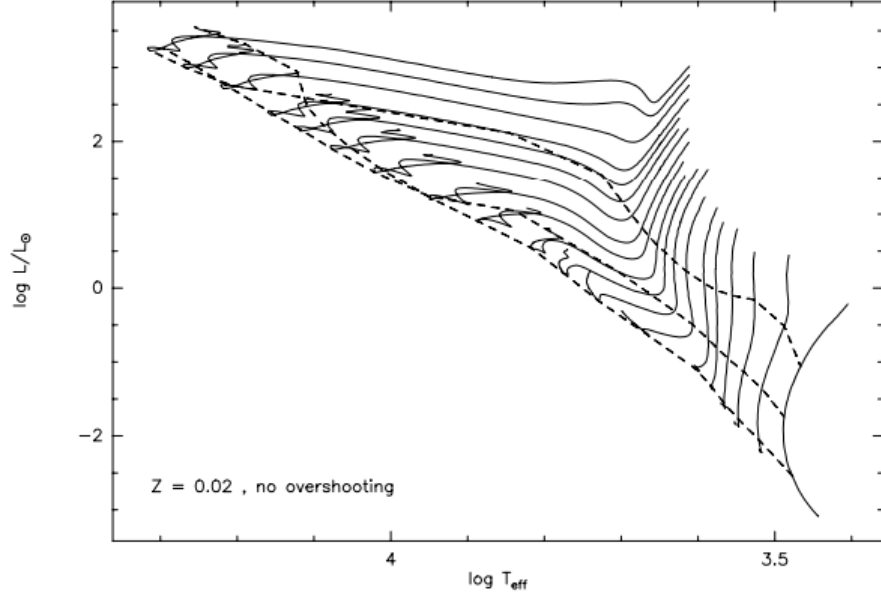


Figure 1.2: Theoretical evolutionary tracks for stars with masses between 7.0 to $0.1 M_{\odot}$ for solar metallicity PMS stars. Isochrones at 1 , 10 and 100 Myr are also shown (dashes). Credit: Siess et al. (2000).

in main sequence stars. Once PMS stars become optically visible, theoretical models suggest that they slowly contract whilst their surface temperature remains broadly stable. The timescale for the contraction is defined by the Kelvin-Helmholtz timescale

$$t_{\text{KH}} \approx \frac{\text{total gravitational energy}}{\text{rate of energy loss}} \approx \frac{GM^2}{RL}. \quad (1.8)$$

For a $1 M_{\odot}$ star at an age of 1 Myr, this corresponds to a timescale of ≈ 30 Myr. The contraction causes the luminosity to decrease, whilst the colours remain broadly unchanged. On the Hertzsprung-Russell (H-R) or colour-magnitude diagram (CMD) this contraction follows a vertical Hayashi track (Hayashi 1961). Stars of mass $\lesssim 0.5 M_{\odot}$ will continue on Hayashi tracks, eventually reaching the zero-age main sequence (ZAMS) and the commencement of hydrogen burning. More massive PMS stars will develop a radiative core prior to reaching the ZAMS and will turn onto a horizontal Henyey track (Henyey et al. 1955), across the convective-radiative gap (Mayne 2010). These evolutionary paths are shown in an H-R diagram in Fig. 1.2.

All PMS stars of less than $2 M_{\odot}$ are expected to be fully convective at ages less than 10 Myr (e.g. Siess et al. 2000; Baraffe et al. 2002). They also appear to exhibit very strong (kG) yet variable magnetic fields, often with strong dipolar components (e.g. Johns-Krull 2007; Donati et al. 2007; Yang & Johns-Krull 2011; Donati et al. 2013). The magnetic field reaches out into the inner regions of the circumstellar disc and controls the final trajectory of material accreting onto the star (see Section 1.2.3 for further discussion on accretion).

The presence of a strong magnetic field also results in cool spots on the surface of the star where convection is locally suppressed by flux tubes emerging from the stellar surface. Large cool

spots are observed that cover up to $\approx 40\%$ of the surface of the star and with temperatures between 500 and 1500 K cooler than the surrounding photosphere (Bouvier et al. 1986b, 1995; Bary & Petersen 2014).

1.2.1 Angular momentum evolution

It has long been known that PMS stars rotate remarkably slowly ($\lesssim 10\%$) compared with their break-up velocity (Vogel & Kuhl 1981; Bouvier et al. 1986a; Hartmann & Kenyon 1996). This is contrary to the expectation that these stars might rotate close to breakup velocity, having recently contracted from molecular clouds with much higher intrinsic angular momentum. Thus they appear to have shed large amounts of angular momentum in the protostellar phase. The primary candidate mechanism for the removal of angular momentum is magnetic disc-locking between the rotating star and its orbiting circumstellar disc (Koenigl 1991; Shu et al. 1994). In this scenario, the magnetic field lines of the star thread the inner regions of the disc and magnetically couple the star to orbiting material. The resulting torque prevents continued accretion from increasing the rotational velocity of the star. The additional interaction of an accretion-driven wind may also moderate the rotational velocity of the star (Fendt 2007; Romanova et al. 2008). The result is a period distribution that ranges from approximately 2 to 10 days (Fig. 1.3). PMS stars that still have their circumstellar discs tend toward the longer periods. Stars without discs are seen to have ‘spun-up’ and exhibit rotational periods at the lower end of this range (Rebull et al. 2006; Davies et al. 2014). Whilst this model appears to describe the behaviour of higher mass PMS stars ($> 0.25M_{\odot}$), there is a curious trend for lower mass stars to exhibit significantly higher rotational velocities, even when they exhibit a significant circumstellar disc. (Choi & Herbst 1996; Stassun et al. 1999; Herbst et al. 2002; Irwin et al. 2007). Following the dispersal of their discs, stars continue to increase their rotational velocity until they reach the ZAMS and the onset of hydrogen burning halts further contraction (see Bouvier et al. 2014, and references therein).

1.2.2 Circumstellar discs

A large fraction of the PMS stars in young clusters exhibit strong emission at mid-infrared wavelengths, $\lambda \gtrsim 2\mu\text{m}$ (e.g. Mendoza V. 1966; Lada & Wilking 1984; Lada et al. 2006; Megeath et al. 2012). Theoretical models (e.g. Whitney et al. 2003; Robitaille et al. 2006) and resolved observations at many wavelengths (e.g. Burrows et al. 1996; O’dell & Wong 1996; Dutrey et al. 1996, and Fig. 1.4) suggest that this emission is caused by dust within a cool orbiting circumstellar disc.

During the protostellar phase, the infalling material possesses angular momentum. Thus material does not generally fall directly onto the surface of the young star but to conserve angular momentum it forms a dusty, gaseous rotating disc which orbits the young star. Buckle et al. (2015) find that the median disc mass is $\lesssim 1\%$ of the mass of the star at ages beyond $\sim 10^5$ yr. Many observed discs have radii of several hundred AU (e.g. Burrows et al. 1996). The most successful SED models suggest that discs are ‘flared’ with a scale height that increases with distance from the star (e.g. Robitaille et al. 2006). The inner edge is typically truncated at a few stellar radii from the star, and significant evidence exists that the inner edge is ‘puffed-up’ through heating by the

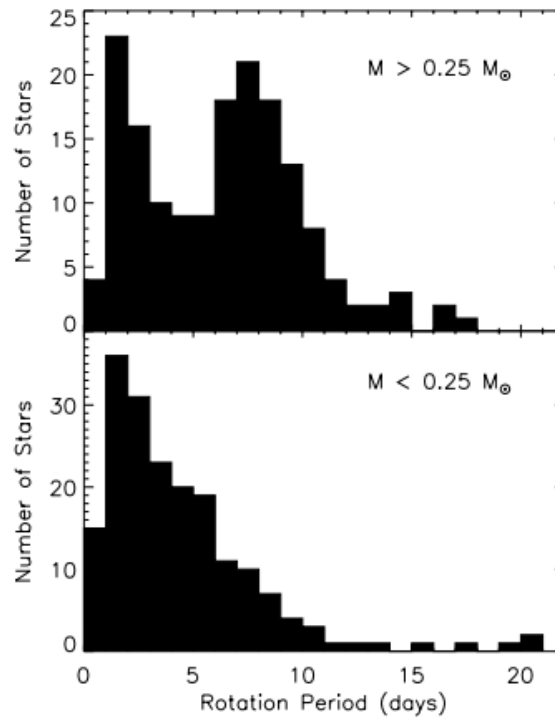


Figure 1.3: Histograms showing the period distribution for ONC stars with masses exceeding $0.25M_{\odot}$ (top) and with masses below $0.25M_{\odot}$. It is clear that the higher mass stars exhibit a bi-modal period distribution and that the lower mass stars rotate faster and exhibit a unimodal distribution. Credit: Herbst et al. (2002).

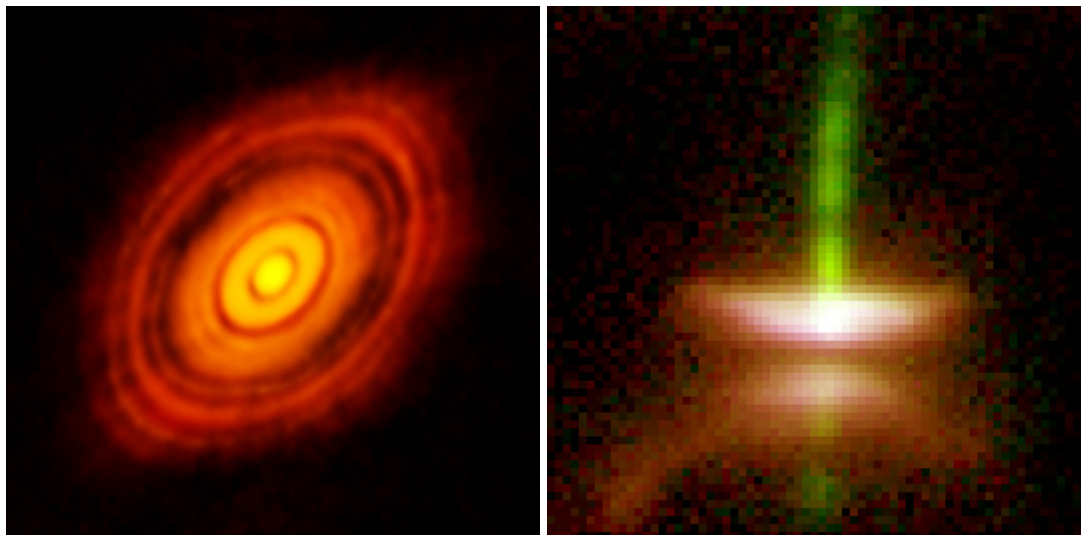


Figure 1.4: Resolved observations of circumstellar discs around PMS stars. Left: ALMA sub-mm observations of the disc surrounding the young star HL Tauri. Credit: ALMA (ESO/NAOJ/NRAO). Right: *HST* WFPC2 image of HH30, an edge-on PMS system. The central star is hidden from view, but its light is visible, scattered off the upper and lower surfaces of the disk. A bipolar outflow is also seen. Credit: Chris Burrows (STScI), the WFPC2 Science Team and NASA/ESA.

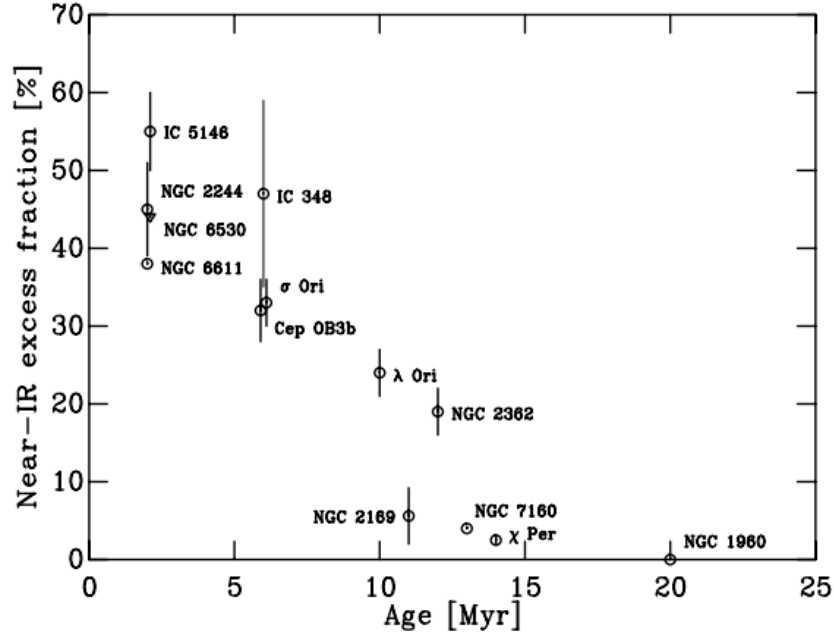


Figure 1.5: Fractions of stars with circumstellar discs as a function of cluster age. Credit: Bell et al. (2013).

star (Kraus et al. 2009). Within the disk, collisional growth of small dust grains can occur, these grains may eventually form into planetesimals and lead to the formation of planets (see Chambers 2010, for a review).

Fig 1.5 shows that $\approx 80\%$ of discs are found to have dispersed on timescales of $\approx 10 - 12$ Myr. Bell et al. (2013) finds a disc half-life of $\approx 5 - 6$ Myr. Disc dispersal is driven by a combination of photo-ablation, accretion onto the central star and planet formation (Hollenbach et al. 2000; Meyer et al. 2007). The local star-formation environment may be significant in disc dispersal, the presence of nearby OB stars likely increasing erosion by strong UV flux and winds (e.g. Henney & O’Dell 1999; Clarke 2007).

1.2.3 Accretion

Active accretion is one of the key defining processes in young PMS stars. Material that has collected in the disc is subject to viscous forces which cause it to fall inward through the disc toward the star. Models and observations suggest that the accretion rate declines as a function of age, typical rates of $\dot{M} \sim 10^{-7} - 10^{-8} M_{\odot}\text{yr}^{-1}$ at 1 Myr, tail off to $\dot{M} \sim 10^{-9} M_{\odot}\text{yr}^{-1}$ or less after several Myr (Gullbring et al. 1998; Hartmann et al. 1998; Barentsen et al. 2013; Venuti et al. 2014). The mass accretion rate is also seen to vary with stellar mass as $\dot{M} \propto M_{\star}^2$, albeit with a large spread in \dot{M} at any given mass (Muzerolle et al. 2003; Mohanty et al. 2005; Natta et al. 2006).

Gravitational potential energy liberated during the accretion process is observed in continuum emission from soft-X-rays through to UV and optical wavelengths (e.g. Hartigan et al. 1989; Gullbring et al. 2000; Kastner et al. 2002). Strong emission lines (such as $H\alpha$ and Ca I) are also observed in accreting YSOs, often with strong inverse-P-Cyg profiles, indicative of infalling gas

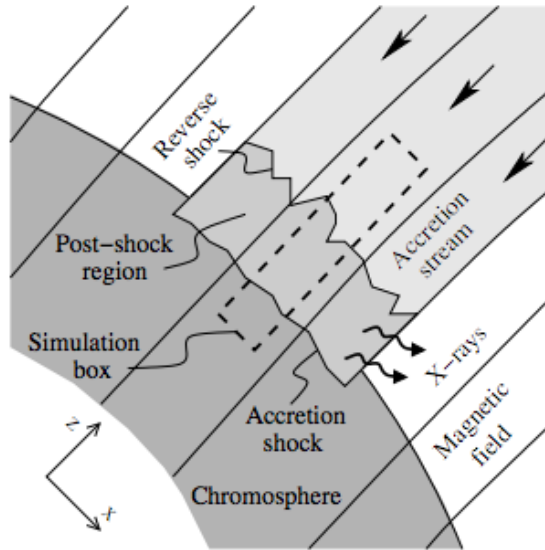


Figure 1.6: A schematic of the accretion shock models of Matsakos et al. (2013). A strong magnetic field penetrates the chromosphere and confines the plasma in flux tubes. The accretion stream impacts on the surface and pushes the chromosphere down to the point where the ram pressure is equal to the stellar pressure. The black dashes show the region of interest in shock simulations by Sacco et al. (2008); Orlando et al. (2010); Matsakos et al. (2013). Credit: Matsakos et al. (2013).

(Reipurth et al. 1996).

The current paradigm that explains the wide range of YSO observations is magnetospheric accretion. In this model the rotating magnetic field of the star disrupts ionised material in the inner disc, causing the disc to become truncated at a distance of a few stellar radii (e.g. Koenigl 1991; Shu et al. 1994; Romanova et al. 2002). Material disrupted at the inner edge of the disc becomes channeled by the magnetic field and falls along field lines onto the surface of the star. The free-falling material impacts the surface at velocities of up to several hundred km s^{-1} , shock-heating the gas to temperatures of $\sim 10^6$ K (Calvet & Gullbring 1998, see Fig. 1.6). Magnetic confinement of the flow may cause the shocked gas to build into columns that rise several thousand km above the chromosphere, periodically collapsing as opacity changes modulate the cooling rate (Sacco et al. 2008; Orlando et al. 2010; Matsakos et al. 2013). Infalling material upstream of the shock is heated by X-ray emission from the shock, and more importantly by adiabatic compression due to the converging nature of the flow (Martin 1996). Emission from this optically thin infalling gas is principally in the Balmer and Paschen continuum and lines. The high velocity of the gas relative to the photosphere explains in-part the complex line morphologies (including inverse-P Cyg profiles) observed (Walker 1972; Edwards et al. 1994; Kurosawa et al. 2006). X-ray emission from the shock is also likely to heat the post-shock gas and the surrounding photosphere, leading to thermal continuum emission with a characteristic temperature of $T_{\text{eff}} \approx 6000 - 10000\text{K}$ (Calvet & Gullbring 1998; Gullbring et al. 2000).

The magnetic field entrains the infalling gas, confining its impact to relatively small regions of the stellar surface (e.g. Romanova et al. 2002, 2008). Depending on the strength of the stellar

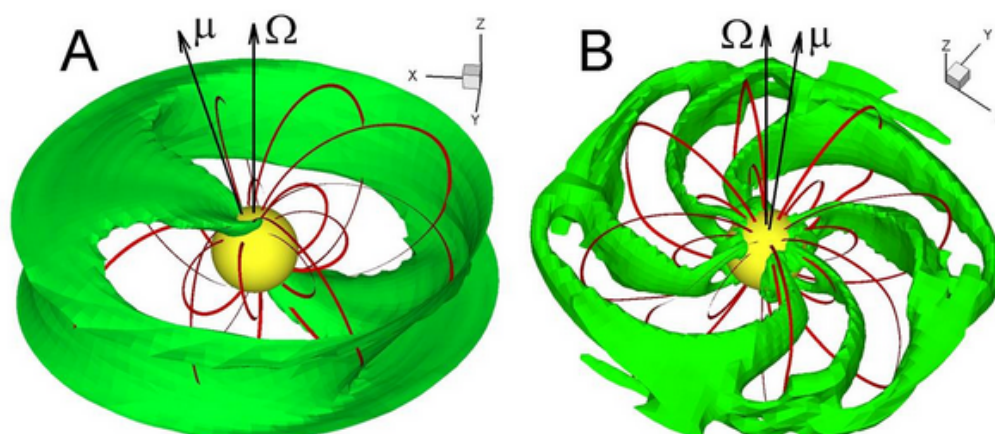


Figure 1.7: 3D MHD models of stable (left) and unstable (right) magnetospheric accretion. Red lines are sample magnetic field lines. The green surface is a constant-density surface showing the distribution of accreting gas. The black arrows indicate the rotational and magnetic field axes. Credit: Romanova et al. (2008).

magnetic field, its alignment with the magnetic poles and its morphology, the accretion flows may be stable and quasi-static on the surface of the star, or may alternatively be unstable and sweep across the surface of the star in multiple streams. Fig. 1.7 shows 3D MHD models of these unstable and stable configurations.

Many observations and models suggest that $\approx 10\%$ of the accretion energy is ejected via winds and outflows that occur along open magnetic field lines (Hartigan et al. 1995). The wind launching mechanism is relatively poorly understood. If open field lines occur in the disc, close to the co-rotation radius an X-wind Shu et al. (1994) may result. If the open field lines are located over a wider area of the disc, a disc wind similar to that of Konigl & Pudritz (2000) is produced. Jets and winds are sometimes observed as Herbig-Haro objects (see Fig. 1.4) and also contribute significantly to modification of emission line profiles.

YSO accretion rate variability on days-to-weeks timescales is observed in $H\alpha$ line emission (Costigan et al. 2014) and broadband flux (Venuti et al. 2014). This variability is attributed to the interaction between the rotating magnetic field of the star and that of the disc (termed ‘magnetorotational disc instability’). Field lines connecting the star to the disc ‘wind-up’ on rotational timescales before reconnection events accelerate material along the field lines to accrete onto the star (e.g. Romanova et al. 2011). On long timescales ($\tau \gg$ rotation period), it is not clear whether the majority of accretion occurs via a broadly smooth progression of material through the disc or whether relatively quiescent periods are punctuated by episodes of high accretion rate. High-rate bursts are certainly predicted from theory (see Fig. 1.8). Proto-planets within the disc are predicted to trigger instabilities that may lead to an ‘avalanche’ of material accreting onto the star (e.g. Lodato & Clarke 2004). Planets may also cause dynamical modulation of accreting material through the disc (e.g. Nayakshin & Lodato 2012). Gravitational and magneto-rotational instability of the disc is also predicted to occur, both within dense regions of the outer disc and within shielded regions of the inner disc (e.g. Gammie 2001; Vorobyov & Basu 2005; Martin et al. 2012;

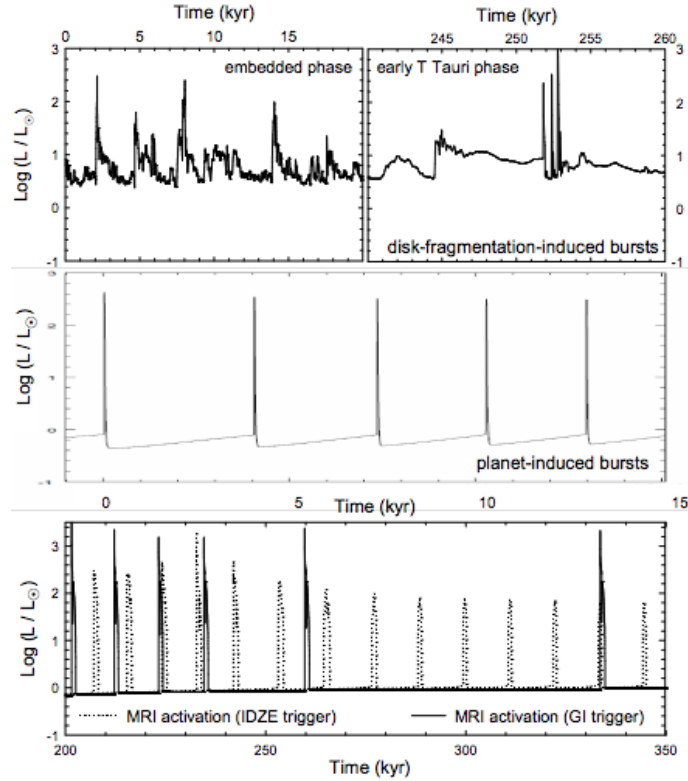


Figure 1.8: Simulated lightcurves provided by models of accretion in which gravitational instability (top), planet induced thermal instability (middle) and inner-disc thermal instability (lower) cause episodic bouts of accretion to occur between quiescent phases. Credit: Audard et al. (2010).

Vorobyov & Basu 2015). These and other mechanisms that are predicted to occur within the disc, strongly suggest that accretion on long-timescales should be highly variable. Despite this, evidence for variability on year and longer timescales is weak. Costigan et al. (2012) and Grankin et al. (2007) study changes in spectral-line and broad-band emission respectively, but they find little evidence of long-term accretion changes. However, when one moves to timescales of decades and longer, a small number of YSOs (‘FUors’ and ‘EXors’) do exhibit large-amplitude variability. Unfortunately though, these objects are largely discovered by chance. When statistics on high-amplitude long-timescale variability have been obtained (Scholz et al. 2013; Contreras Peña et al. 2014) they have been from IR data, which will be significantly biased toward deeply embedded systems in the protostellar phase (ages $< 1\text{Myr}$), have consisted of only two widely separated epochs, and sampled only extreme variability.

1.3 Classification schemes

1.3.1 T Tauri stars: $H\alpha$ emission

Optically visible young stars with masses $M_{\star} < 2M_{\odot}$ are often referred to as T Tauri stars after the prototype of the class. T Tauri stars have traditionally been subdivided into two subclasses based on the strength of $H\alpha$ emission in their spectra. Classical T Tauri stars (CTTS) display a

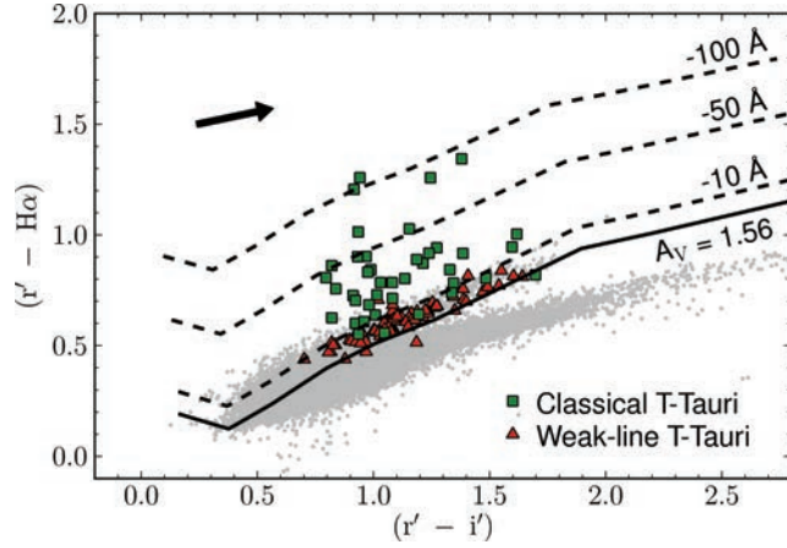


Figure 1.9: IPHAS colours of known T Tauri stars in IC 1396. Green squares are identified CTTS. Red triangles are WTTS. The solid line shows the simulated main-sequence curve at the mean reddening of the cluster ($A_V = 1.56$). Dashed lines show the position of stars at increasing levels of $H\alpha$ emission as predicted by Drew et al. (2005). Grey dots show field stars in the region. The arrow shows the reddening shift for an M0V object being reddened from $A_V = 0$ to $A_V = 1.56$. Credit: Barentsen et al. (2011).

strong $H\alpha$ emission line with an equivalent width defined as $EW_{H\alpha} > 10\text{\AA}$. T Tauri stars with $EW_{H\alpha} < 10\text{\AA}$ are referred to as weak-lined T Tauri stars (WTTS). CTTS have traditionally been discovered through objective prism surveys (e.g. Herbig 1958; Babcock & Weaver 2000). More recently, $H\alpha$ narrowband surveys have been very successful in identifying emission line stars and classifying them as CTTS (see Barentsen et al. 2011, and Fig. 1.9). WTTS have traditionally been more difficult to identify, however the advent of X-ray surveys has allowed identification of these stars based on their high levels of coronal activity and hence X-ray emission (e.g. Montmerle et al. 1983; Getman et al. 2005). The two classifications are thought to broadly correspond to accreting and non-accreting YSOs respectively, although the distinction is probably a poor one as stars will fall onto a spectrum of accretion behaviour and hence the strict delineation is probably inappropriate. Unfortunately for a given star, the $H\alpha$ line is composed of emission and absorption from many sources including the photosphere, chromosphere, accretion flows, winds and nebular emission. Thus whilst useful for identifying populations of young stars, the $EW_{H\alpha}$ of a given star is a relatively poor descriptor of the individual properties of a system. Also, there is some evidence that stars can change their spectral signatures significantly so as to change from WTTS to CTTS on decade timescales (Littlefair et al. 2004; Hillenbrand et al. 2013).

1.3.2 YSO Classifications: mid-IR emission

Lada (1987) first proposed a classification scheme for young stars based on the slope of the spectral energy distribution (SED) in the wavelength range 2.2 to 20 μm . This slope is determined by

thermal emission from the circumstellar disc or infalling envelope, making it a powerful diagnostic for the evolutionary status of young stars. He proposed a scheme of Class I, II and III YSOs based on the spectral index α , defined as

$$\alpha = \frac{d \log(\lambda f_\lambda)}{d \log(\lambda)} \quad (1.9)$$

where λ is the wavelength and f_λ is the flux density. Andre et al. (1993) and Greene et al. (1994) added the additional Class 0 and ‘Flat spectrum’ classifications. The classification scheme is broadly considered to be an evolutionary progression. A summary, including model SEDs are shown in Fig. 1.10.

Class 0: Undetectable at $\lambda < 10\mu\text{m}$

Class 0 sources are very young ($< 10^4$ yr) objects where the bulk of the final mass has not yet been assembled. They feature strong sub-mm emission and remain undetected at $\lambda < 10\mu\text{m}$, hence the α index is not strictly applicable to this class. These objects are still deeply embedded within their infalling molecular envelope, however theory suggests that even at this early stage a disc has formed and the core will be driving powerful bipolar outflows (e.g. Machida et al. 2006, 2010; Bate 2011).

Class I: $\alpha > 0.3$

As the infalling molecular envelope depletes in mass, the protostar begins to become visible in the mid-IR. The peak of the SED is still at $\sim 100\mu\text{m}$ and is dominated by emission from the envelope. At the Class I stage, the star is thought to have accreted most of its mass, however a remnant envelope still exists. Class I spectra are broadly featureless due to the strong continuum veiling from the envelope dust emission. Strong bipolar outflows are a feature at this stage. The Class I stage is thought to last for ~ 0.5 Myr (e.g. Hatchell et al. 2007), although the revised Class II lifetimes found by Naylor (2009) and Bell et al. (2013) may indicate that it is closer to 1 Myr.

Flat spectrum: $-0.3 < \alpha < 0.3$

Flat spectrum sources are thought to have broadly cleared their infalling envelopes, however their spectra are strongly veiled at near-IR wavelengths due to the presence of hot circumstellar dust (Greene & Lada 2000). At this and later stages, accretion proceeds via the disc.

Class II: $-1.6 < \alpha < -0.3$

Class II YSOs are dominated by photospheric emission that broadly approximates to a black-body. In addition, a significant flux contribution is made by dust in the circumstellar disc at wavelengths $\lambda \gtrsim 2\mu\text{m}$. The YSO is typically modelled as an optically visible star surrounded by an optically thick circumstellar disc. Evidence of outflow is still seen, however the infalling envelope that dominates earlier phases has dissipated. At this stage the extinction to the star can be low so UV flux from accretion hot-spots may become visible. Veiling (see Section 1.4.3) is often observed both at optical wavelengths by accretion luminosity and at IR wavelengths by dust emission from the disc. Class II YSOs share many

characteristics with CTTS. The Flat-spectrum and Class II stages combined are thought to last for $\sim 10^6 - 10^7$ yr

Class III: $\alpha < -1.6$

Flux from Class III YSOs is essentially limited to photospheric emission with a small contribution from the highly active chromosphere. There is possible evidence for some weak contribution from optically thin gas in the disc but IR emission from dust is all but absent. At this stage the disc has dissipated and the remaining PMS star is possibly surrounded by a planetary system and debris leftover from the planet forming process. Class III YSOs share many characteristics with WTTS.

With the advent of large ground and space based IR surveys, comprehensive classification schemes have been developed to identify and characterise YSOs using combined photometry at wavelengths from $1 - 24\mu\text{m}$. Gutermuth et al. (2008, 2009) present one notable example, whereby YSOs are distinguished from contaminating sources such as nebular knots and background galaxies, whilst differentiating between evolutionary phases within the YSO classification scheme. Some example classification cuts are shown in Fig. 1.11 for stars within the Orion star-forming regions.

1.3.3 YSO Classifications: nomenclature used in this study

The classification schemes discussed here have dealt with young stars on the basis of their observable parameters. As there now exists a significant understanding of the drivers of these observational phenomena, I have chosen to use terminology in this thesis that relates to the physical mechanisms rather than the observable traits. There is a traditional view that Class II and Class III YSOs are equivalent to CTTS and WTTS respectively. However, a significant number of Class II YSOs have been found that do not show evidence of accretion (e.g. Teixeira et al. 2012). There also appears to be some evidence of ongoing accretion in a small subsample of Class III YSOs (e.g. Rebull et al. 2002; Littlefair et al. 2004). This presumably implies that significant accretion rates can still occur from dust-free circumstellar discs or that some substantial discs (possibly with large central holes) remain undetected in near-IR photometric surveys. To clarify the physical nature of the stars studied in this thesis I have referred to WTTS or CTTS stars as ‘non-accreting’ or ‘accreting’ stars respectively. Similarly, I have referred to flat-spectrum and Class II YSOs in this thesis as ‘disc-bearing’ (although ‘dusty-disc-bearing’ might be more accurate) and Class III YSOs are referred to as discless (after Cody et al. 2014). In the rare event that I describe a Class I object, it will be referred to as ‘disc-bearing’, however a comment will be made on the protostellar nature of the object if it is pertinent to the discussion. Fig. 1.12 illustrates the relationship between the classifications and nomenclature that I have used in this thesis.

1.4 Measuring accretion rates

Understanding accretion rates is crucial to understanding how young stars are built and evolve. No single method is entirely satisfactory when attempting to measure accretion rates as each method

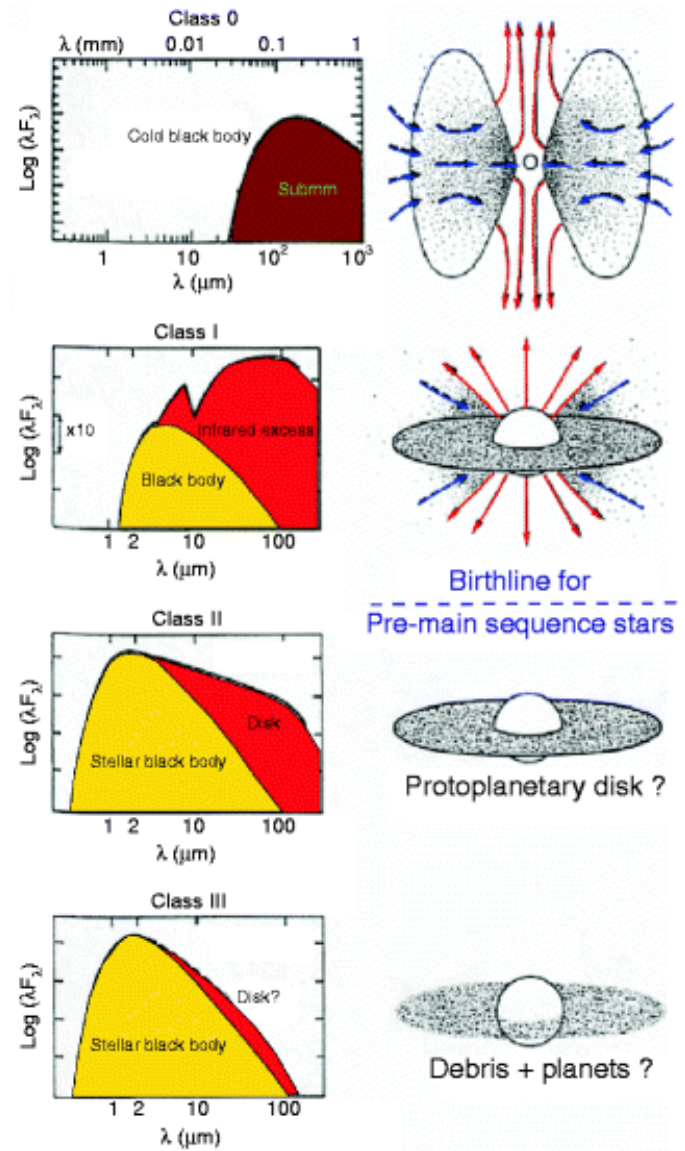


Figure 1.10: A representation of the YSO classification scheme. Left panels show the ideal SED for YSOs at each stage of the scheme. Right panels show a schematic of the morphology of the YSO at each stage. Credit: Andre (2011).

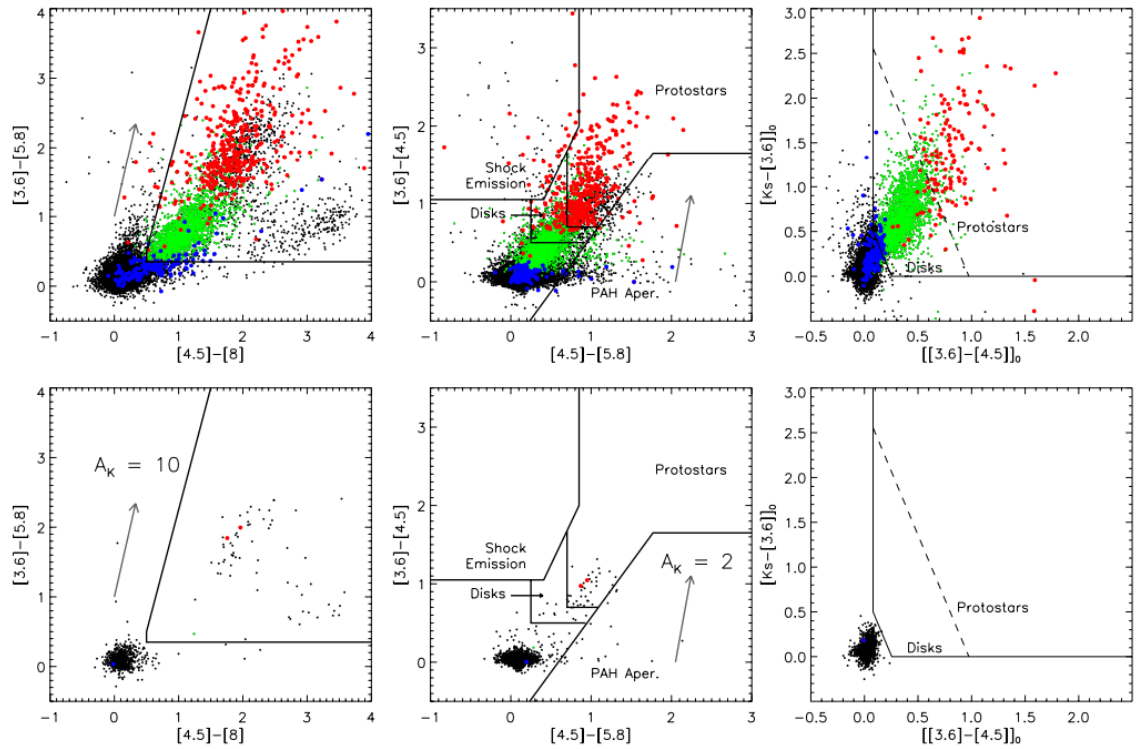


Figure 1.11: IRAC and IRAC-2MASS colour-colour diagrams used to identify young stellar objects in the star-forming regions of Orion (upper panels) and reference fields (lower panels). The coloured markers show identified protostars (Class 0, I and flat-spectrum sources) in red and Class II YSOs in green and blue. Blue markers in the Class II sample indicate possible ‘transition’ objects, which may exhibit disc truncation at a larger radius than typical of Class IIs. This may be indicative of disc clearing and reaching the end of the Class II phase. Black points are stars that do not exhibit IR excess. Further details of the classification cuts may be found in Gutermuth et al. (2008, 2009). Credit: Megeath et al. (2012).

T Tauri stars

	Classical T Tauri star	Weak T Tauri star
YSOs		
Class II	<i>"Disc-bearing accretor"</i>	<i>"Disc-bearing non-accretor"</i>
Class III	<i>"Discless accretor"</i>	<i>"Discless non-accretor"</i>

Figure 1.12: The relationship between traditional young star classifications and the nomenclature used in this thesis.

employed has limitations and model dependencies. Circumstantial accretion indicators such as the presence of mid-IR disc emission are sometimes used as a proxy for classifying the accretion status of YSOs (e.g. Littlefair et al. 2011). However, it is not clear that disc presence alone is a guarantee that accretion is ongoing (see Teixeira et al. 2012, and Chapter 8 of this thesis) and no quantitative estimate of accretion rate may be made.

To obtain quantitative measures of accretion rate, three principal observational tools are available for PMS stars at the Class II stage. Broadband UV flux may be measured in a wavelength region that is typically dominated by accretion luminosity in low mass YSOs and may be achieved through photometric measurements. The flux in emission lines such as $H\alpha$ or $Ca II$, which is associated with accretion flows and shocks are also valuable measures of accretion rate, although calibration is required through modelling or comparison with other accretion measures. As well as spectroscopic measurement of these line fluxes, $H\alpha$ flux may be measured through the use of narrowband photometry. A further estimate of broad-band accretion luminosity in the Paschen continuum may be made by comparing the depths of photospheric absorption lines to that of a template which is assumed to be free of accretion luminosity, a quantity known as *veiling*. These quantitative accretion measures are discussed further in the following sections.

1.4.1 UV photometry

Much of the energy in the accretion flows that is thermalised in shocks near the stellar surface is re-emitted as a hot $\approx 6000 - 10000$ K thermal continuum and in Balmer emission (Hartigan et al. 1991; Calvet & Gullbring 1998). This flux is most effectively detected and measured using U band photometry, as that is where its SED is intrinsically brightest. For low mass stars, the photospheric luminosity in U is lower than at redder wavelengths, thus U band measurements provide a greater contrast between the accretion luminosity (L_{acc}) and photospheric luminosity (L_{phot}) than measurements at longer wavelengths. Fig. 1.13 shows a population of objects that are anomalously bright in the U band compared with the main population in the Orion star forming region.

L_{acc} may be used to calculate the mass accretion rate, \dot{M} , by simple energy arguments

$$\dot{M} = \left(1 - \frac{R_{\star}}{R_{trunc}}\right)^{-1} \frac{L_{acc} R_{\star}}{GM_{\star}} \sim 1.25 \frac{L_{acc} R_{\star}}{GM_{\star}}. \quad (1.10)$$

The factor $\left(1 - \frac{R_{\star}}{R_{trunc}}\right)^{-1}$ is estimated to be ~ 1.25 by assuming that the accreting gas falls onto the star from the truncation radius of the disc at $R_{trunc} \approx 5R_{\star}$ (Hartmann et al. 1998). This method also relies on an estimate of the bolometric correction for the accretion luminosity to derive L_{acc} from the U band flux. Gullbring et al. (1998) found a relation between L_{acc} and U band luminosity (L_U) defined by

$$\log\left(\frac{L_{acc}}{L_{\odot}}\right) = 1.09^{+0.04}_{-0.18} \log\left(\frac{L_U}{L_{\odot}}\right) + 0.98^{+0.02}_{-0.07}. \quad (1.11)$$

Venuti et al. (2014) derive a similar relation which estimates L_{acc} to be a factor of ≈ 2 to 4 greater. This corresponds to a difference of ≈ 0.2 dex at the highest \dot{M} rates ($\sim 10^{-7} M_{\odot} \text{yr}^{-1}$) and ≈ 0.6 dex at the lowest \dot{M} rates ($\sim 10^{-10} M_{\odot} \text{yr}^{-1}$). Uncertainties in U band flux estimates of \dot{M} also hinge

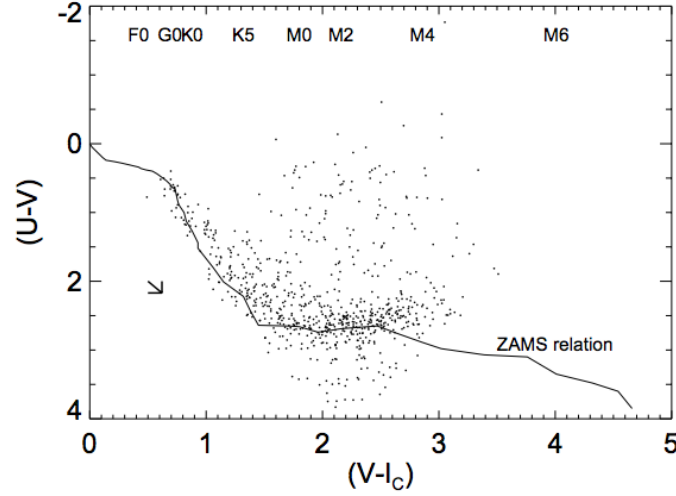


Figure 1.13: $U - V, V - I$ colour-colour diagram of stars in the Orion flanking-fields. Note the population of stars with $U - V$ colours that are far above the main population and the ZAMS model. These U band excesses cannot be explained by extinction and reddening as shown by the extinction vector (arrow) corresponding to $A_I = 0.25$. Credit Rebull et al. (2000).

on uncertainties in extinction and distance. Whilst in a given star forming association, the distance is often well constrained, the extinction for individual stars is often difficult to calculate from photometry due to degeneracy in the signatures of accretion luminosity and reddening. Spectra that are simultaneously collected with U band photometry can break this degeneracy if a robust estimate of T_{eff} and extinction can be made from fluxes in the photospheric spectral lines. Fig 1.14 shows that in a given star forming region, accretion rates derived from U band fluxes are seen to scatter by at least 2 orders of magnitude at a given mass. This scatter is likely to be the result of both intrinsic accretion rate spreads, variability in accretion rate (~ 0.5 dex according to Venuti et al. 2014) and also uncertainties due to poor extinction correction.

1.4.2 Emission line flux

Muzerolle et al. (2003) developed models to measure \dot{M} from high-resolution $H\alpha$ line profiles for low-mass stars and brown dwarfs in the range $M_{\star} \approx 0.02 - 0.14 M_{\odot}$. The models varied parameters such as stellar mass and radius, viewing inclination, and accretion rate. The accretion rates modelled ranged from $10^{-12} < \dot{M} < 10^{-9} M_{\odot} \text{yr}^{-1}$. At higher accretion rates, strong stellar outflows contaminate the line profile and bias the result (Muzerolle et al. 2001; Kurosawa et al. 2006). The use of spectroscopic line profiles in this way is useful as the results are not compromised by uncertainties in extinction and distance.

Empirical relations between emission line fluxes and accretion rates derived using UV excess have also been found. Muzerolle et al. (1998) derive relations between \dot{M} and the equivalent width of $\text{Br}\gamma$ and $\text{Pa}\beta$ lines of hydrogen (see Fig. 1.15). Similar relations are found for other lines of hydrogen and other elements such as Ca II and Na I (e.g. Muzerolle et al. 2001). Barentsen et al. (2011) derive a relation between spectroscopically derived $L_{H\alpha}$ and L_{acc} . This relation is

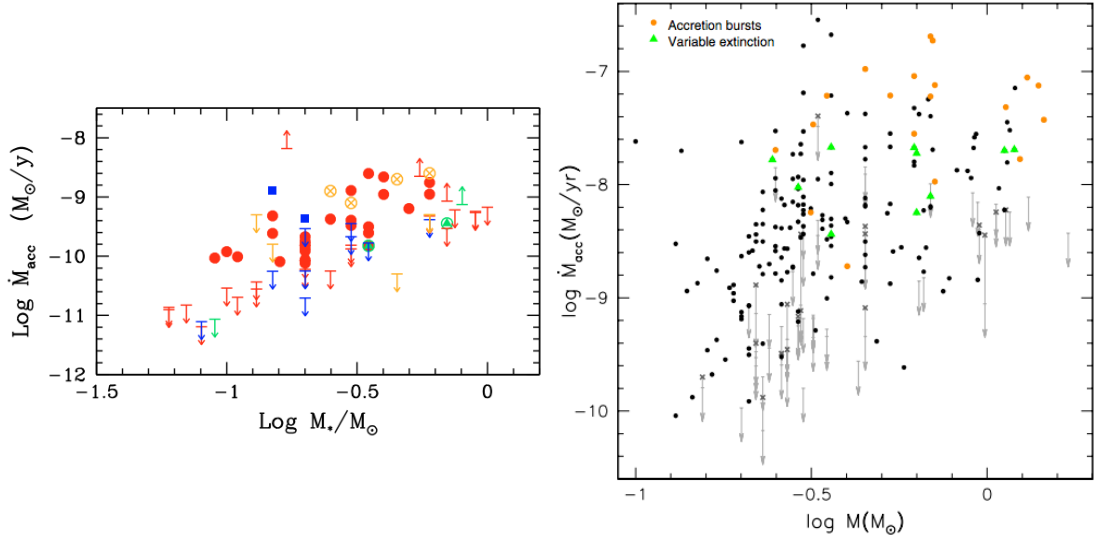


Figure 1.14: Mass accretion rates calculated from U band fluxes in the nearby star forming regions σ Ori (left) and NGC 2264 (right). In the left panel the different colours represent different disc classifications. Red dots are Class IIs, green triangles are ‘Transition-discs’ and blue squares are ‘Evolved-discs’ (see Hernández et al. 2007, for more details on these classifications), arrows show upper limits. In the right panel, orange dots and green triangles show stars identified by Stauffer et al. (2014) whose variability is dominated by stochastic accretion bursts and variable extinction respectively. Black dots are all other objects in the sample, arrows show upper limits. Credit: Rigliaco et al. (2011) [left panel], Venuti et al. (2014)[right panel].

then used with photometrically derived $L_{H\alpha}$ measurements from *IPHAS* survey data to estimate \dot{M} using equation 1.10. Manara et al. (2012) define a relation between U band derived L_{acc} and $L_{H\alpha}$ using photometry of the ONC from Da Rio et al. (2009).

1.4.3 Veiling

The addition of a smooth continuum to a stellar photospheric spectrum results in a reduction of the equivalent width of photospheric absorption lines. This phenomenon is called veiling and makes the lines appear weaker (see Hartigan et al. 1989, and Fig. 1.16). In YSOs a smooth continuum is thought to result from accretion hot-spots ($\lambda \lesssim 1\mu\text{m}$) and thermal emission from the circumstellar disc ($\lambda \gtrsim 2\mu\text{m}$). There is also evidence of an additional (and unidentified) source of veiling at wavelengths around $\lambda \approx 1\mu\text{m}$ (Fischer et al. 2011).

The veiling at a given wavelength is defined as

$$r_\lambda = \frac{f_{\text{veil}}}{f_{\text{phot}}}, \quad (1.12)$$

where f_{veil} is the flux from the veiling continuum and f_{phot} is the flux from the photosphere. The veiling at optical wavelengths can be measured if the photospheric line flux (or equivalent width) is compared with synthetic or observed templates of similar spectral type and surface gravity. For measurement to be possible, the veiling continuum must be assumed to be smooth and free from line emission. If the veiling continuum flux can be measured and is assumed to be entirely due to accretion luminosity (as is often assumed at optical wavelengths), then a bolometric correction

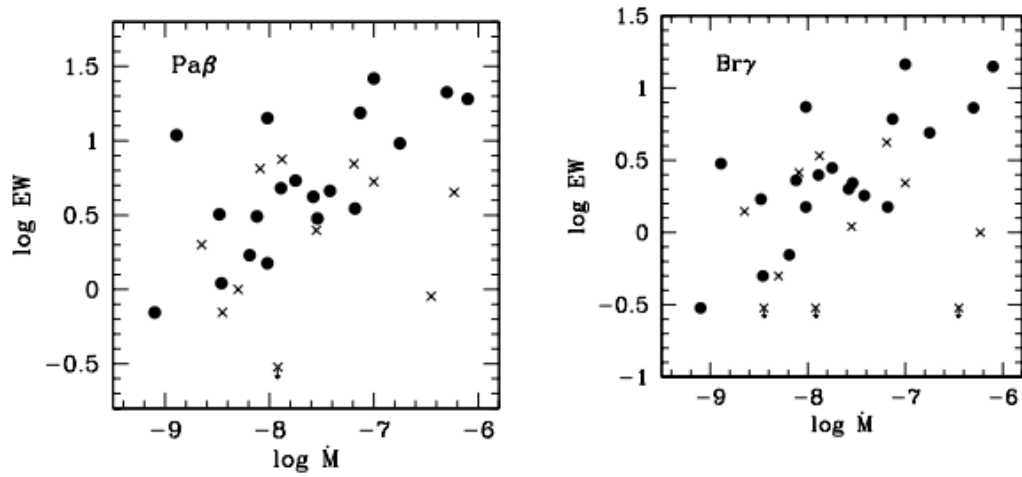


Figure 1.15: A comparison of Pa β and Bry emission line equivalent widths with accretion rate. Filled circles are accretion rates from blue spectra, crosses are from U band photometry. Credit Muzerolle et al. (1998).

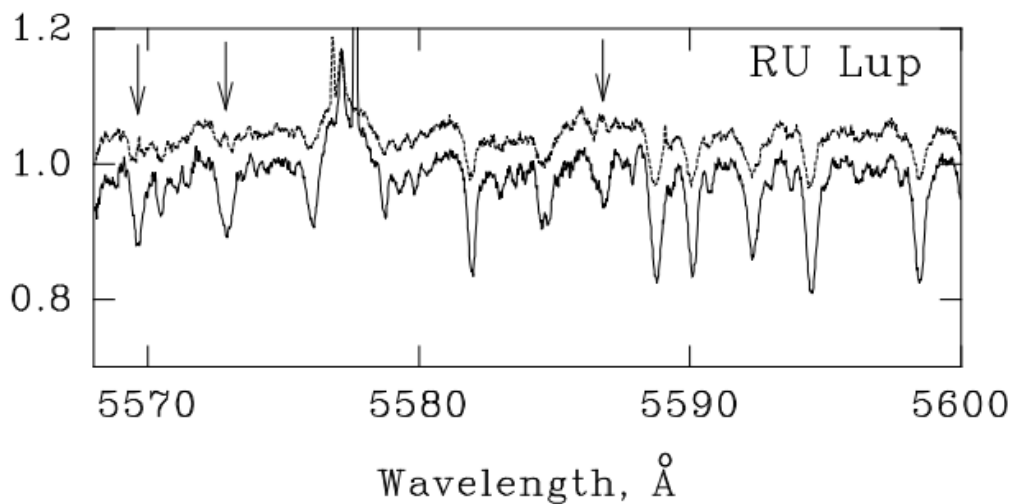


Figure 1.16: Spectra for RU Lup at two epochs with different levels of veiling. In the most veiled phase, photospheric lines are noticeably weaker. Certain lines (marked with arrows) appear to show line-filling as well as the addition of the continuum flux. Credit Gahm et al. (2008).

can be applied to correct for unseen emission, providing an estimate of L_{acc} and hence \dot{M} (e.g. Hartigan et al. 1991; White & Basri 2003; White & Hillenbrand 2004). Unfortunately, the shape of the accretion SED is poorly understood, with ‘hot slab’ models appearing to underestimate the veiling at 7000\AA by factors of ~ 2 . Herczeg & Hillenbrand (2008) estimate that a factor two error in the bolometric correction could lead to an overall error in \dot{M} of 0.3 dex. Veiling measurements are complicated by the fact that at high accretion rates, the accretion continuum is unlikely to be smooth and certain photospheric lines will be preferentially filled by line emission (Gahm et al. 2008; Dodin & Lamzin 2012a). In addition, one must be very careful when selecting templates for PMS stars as the surface gravity is significantly different from (and in between) that of field dwarfs and giants. Surface gravity differences have a significant impact on both continuum shape and line depths, thus biasing veiling measurements.

1.5 Young star variability

Young stars show photometric variability at all wavelengths and on all timescales that have been observed (e.g. Joy 1945; Montmerle et al. 1983; Bouvier et al. 1993; Herbst et al. 1994; Burningham et al. 2005; Morales-Calderón et al. 2011; Cody et al. 2014; Rice et al. 2015). The variability arises from a wide range of physical processes occurring on the stellar surface, within the magnetosphere, and in the disc and outflows. Fig. 1.17 shows a non-exhaustive selection of theoretically postulated physical mechanisms that have been associated with YSO variability. Ultimately, a full understanding of the time-domain behaviour of young stars is needed to inform models of their interaction with surrounding discs, the accretion process, and the structure and geometry of star-disc systems.

In Class III YSOs, the absence of a significant disc or accretion means that the optical and near-IR variability is dominated by changing viewing angles of irregular distributions of cool spots (similar to solar sunspots) on the surface of the rotating star (e.g. Bouvier et al. 1986b; Stassun et al. 1999; Saunders et al. 2009). In addition, contributions to variability at optical and shorter wavelengths have been attributed to chromospheric activity such as flares, analogous to those seen on the Sun (Gahm et al. 1995; Guenther & Ball 1998; Uzawa et al. 2011). In Class IIIs, the physical mechanisms driving the variability are located on or close to the surface of the star. Thus the variability timescales found have typically been commensurate with the rotation period of the star or shorter. It is likely though that some longer timescale variability may be associated with Class III YSOs. Decade timescale magnetic cycles have long been studied on the Sun and are now being identified and studied in other active stars (Lanza 2010). Whilst no photometric evidence of magnetic cycles has been found for YSOs, magnetic field evolution on timescales of years has been detected in spectropolarimetric observations of CTTS (Donati et al. 2012, 2011). In addition, some evidence of significant spectroscopic changes have been observed in four WTTS stars between observations made two decades apart (Littlefair et al. 2004). These observations are explained through changes in accretion rate, despite their being little evidence of a circumstellar disc in these stars.

In Class II YSOs the variability picture is far more complex. Fortunately however, this

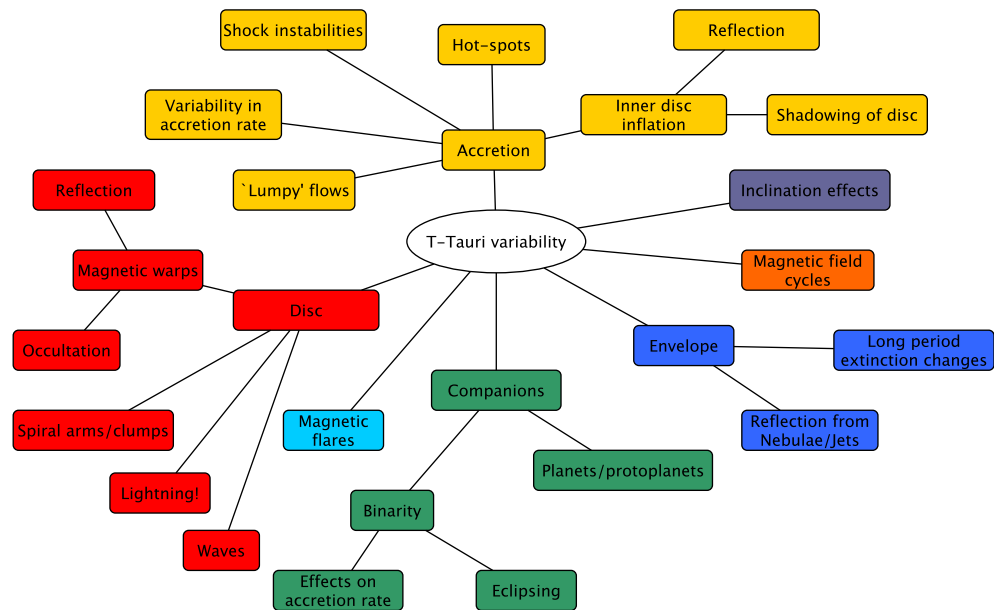


Figure 1.17: Non-exhaustive list of theoretical physical mechanisms that may be associated with variability in YSOs.

complexity allows variability to be used as a diagnostic tool in investigating the nature of Class II stars and their environments. Herbst et al. (1994) used *UBVRI* photoelectric monitoring data for ≈ 80 young stars collected over ~ 10 years to characterise YSO variability. The sample included stars brighter than $V \approx 14$, thus limiting it to nearby stars of spectral type earlier than $\approx M2$. They summarised some basic features of YSO variability and defined three main categories.

Type I: Cool spots

Type I variability is essentially that described for Class III YSOs, cool magnetically induced spots rotating into and out of view. These variability events were often periodic and showed typical amplitudes of a few tenths of a mag in V . Stars were seen to redden as they faded. Lightcurve shapes were seen to change as spot patterns evolved but periods remained stable over months or years.

Type II: Changes in veiling continuum

Type II variability was only seen in CTTS and generally showed irregular variability on timescales as short as hours. Amplitudes were typically less than 1 mag in V , however occasional events of up to 2.6 mag were observed. Periodicity was sometimes present with this behaviour but was not as persistent as in Type I. The cause of the variability was attributed to changes in accretion rate and small (0.3% of stellar surface) hot spots with temperatures $\sim 10\,000\text{K}$ rotating into and out of view. The origin of the spots was attributed to magnetically channelled accretion.

Type III: Unknown origin (but probably variable circumstellar obscuration)

Type III behaviour was generally irregular variations on timescales of days to weeks. The

minima appeared to be asymmetric with faster declines than recoveries. Amplitudes were typically less than 1 mag but variations as great as 2.8 mag were seen. Spectroscopically the photospheric lines remained unchanged, however strengthening H α was seen during fades. Typically colours became redder during fade events, however in extreme fade events a colour reversal towards the blue was seen. Linear polarisation was anti-correlated with brightness.

The observationally based classifications defined by Herbst et al. (1994) have been investigated by many authors to further develop models of the underlying physical processes. However, most studies have either focussed on detailed measurements of individual objects, (perhaps using a wide wavelength or cadence range) or more limited observations of larger stellar samples.

Bouvier et al. (1999) performed a one-month campaign, observing the CTTS AA Tau in *BVRI* bands and with low-resolution spectra on timescales ranging from hours to weeks. AA Tau exhibited deep quasi-periodic fading events that were accompanied by an increase in the equivalent widths of the Balmer lines of hydrogen. The fades were interpreted as occultation events caused by the presence of an orbiting magnetically induced disc-warp. The Balmer line EW increases were attributed to suppression of the continuum rather than an increase in line flux.

Grankin et al. (2007) improved the long-baseline observational sample by collecting *UBVR* lightcurves for 72 disc-bearing YSOs over ~ 20 years. The variability that was observed strongly implied that the vast majority of variability occurs on timescales shorter than one month, with only smooth low-amplitude variations (possibly associated with changes in extinction) seen on longer timescales.

Rucinski et al. (2008) dramatically increased the cadence range observed in a given object with observations of TW Hya on timescales from 30 seconds to 8 years using broad-band space and ground based monitoring. Some evidence of periodic behaviour with a period of 3.56 days was identified at one epoch, however at later epochs a spectrum of unstable periods within the range of 2 to 9 days was observed. The detected periods had a tendency to progressively shorten with time and the overall power spectrum of the variability suggest a combination of several mechanisms dominated by accretion processes.

Alencar et al. (2010) studied high precision ‘white-light’ lightcurves of 83 CTTS stars in NGC 2264 collected continuously for 23 days by the *CoRoT* satellite with a cadence of ≈ 8 minutes. The unbroken nature of these observations were instrumental in providing detailed morphological classifications for lightcurves on much shorter timescales than were previously possible. 61% of stars in of the sample exhibited some kind of periodic behaviour, 25% of which were quasi-sinusoidal and attributed to modulation by cool spots (similar to Herbst et al. 1994, Type I). Between 24 and 34% of stars in the sample exhibited quasi-periodic dips in their lightcurves, analogous to those seen in AA Tau. Interestingly, stars with spot modulated lightcurves had a similar distribution of periods to the AA Tau analogues. This is a curious result as the standard disc locking paradigm might imply that stars with less accretion activity (and hence cool spot dominated lightcurves) should be less likely to be disc locked and thus might be expected to rotate more quickly than stars where the magnetosphere is able to actively disrupt the inner disc to create an obscuring disc warp.

Costigan et al. (2012) used high resolution spectroscopic time-series of 10 accreting stars in the Chameleon I star forming region to investigate changes in accretion rate that might occur over the course of 15 months. They derived accretion rates using equivalent widths of H α and Ca II emission lines. It appeared that the maximum variability in \dot{M} was on the order of 0.37dex, far below the scatter seen in typical accretion rate vs. stellar mass relations (Fig. 1.15). A major portion of the variability was seen on timescales shorter than ≈ 10 days.

Cody et al. (2014) undertook a further 40 day set of *CoRoT* observations of NGC 2264 in 2011/2012. They observed 489 high-probability members of which 162 were ‘disc-bearing’ stars. A simultaneous campaign was undertaken for 29 days during this period using the 3.6 μ m and 4.5 μ m channels on the *Spitzer* telescope. They developed two metrics to describe the degree of periodicity (Q) and the flux asymmetry (M) within each lightcurve. They computed Q by first searching for the strongest period present in the lightcurve using the autocorrelation technique defined by McQuillan et al. (2013). They then folded the lightcurve on the strongest period and assessed how close the lightcurve points were to the systematic noise floor before and after the phased trend was subtracted

$$Q = \frac{rms_{\text{resid}}^2 - \sigma^2}{rms_{\text{raw}}^2 - \sigma^2}, \quad (1.13)$$

where rms_{raw} and rms_{resid} are the rms values of the raw lightcurve and σ is the estimated uncertainty. A low value of Q ($\lesssim 0.15$) is associated with well defined periodicity, such as an eclipsing binary. A high value of Q (0.6 - 1) describes no detectable periodicity. Intermediate values of Q describe quasi-periodic behaviour such as rotationally modulated accretion bursts or occultation by disc warps. In addition, Cody et al. (2014) observed that many lightcurves are asymmetric with respect to a reflection along the magnitude axis. Some stars show prominent downward flux dips, while others have abrupt increases. The flux asymmetry metric (M) quantifies this asymmetry, and was defined by first selecting the 10% highest and 10% lowest magnitude values in each lightcurve, after removal of 5σ outliers. M was then calculated as

$$M = (\langle d_{10\%} \rangle - d_{\text{med}}) / \sigma, \quad (1.14)$$

where $\langle d_{10\%} \rangle$ is the mean of all data in the top and bottom decile of the lightcurve, d_{med} is the median of the entire light curve and σ is its overall rms. Negative values of M indicate a lightcurve which is predominantly in a faint state but brightens in bursts. Positive values of M indicate a lightcurve that is predominantly bright but appears to experience fading behaviour. $M \approx 0$ indicates no preference for a bright or faint state. Fig. 1.18 compares the measured Q and M metrics for disc-bearing stars in the sample and classifies them as ‘periodic’, ‘quasi-periodic’ and ‘aperiodic’, and also classifies them as ‘bursting’, ‘symmetric’ and ‘dipping’. 21% of the disc-bearing stars are found to be ‘dipping’ variables at optical wavelengths, slightly more than the 15% predicted by analysis of hydrostatic disc models by Bertout (2000). Whilst this study provided a robust analytical method of classifying lightcurves using high-quality data, further follow-up is required to interpret these classifications.

Stauffer et al. (2014) makes a thorough analysis of 23 stars which fall in the ‘bursting’

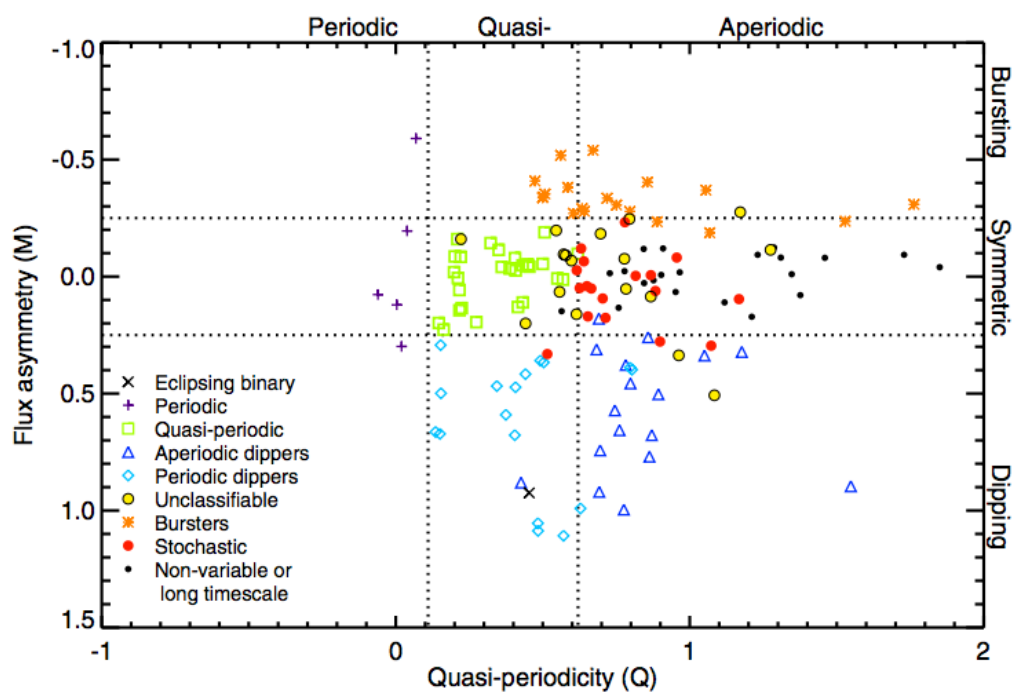


Figure 1.18: Lightcurve morphology classes, based on periodicity (Q) and flux asymmetry (M) metrics for optical light curves from *CoRoT* in a disc-bearing sample. Colour coding indicates the variability classification chosen by eye, before statistical assessment. The eclipsing binary is not strictly periodic because its lightcurve contains aperiodic fluctuations out of eclipse. Credit: Cody et al. (2014).

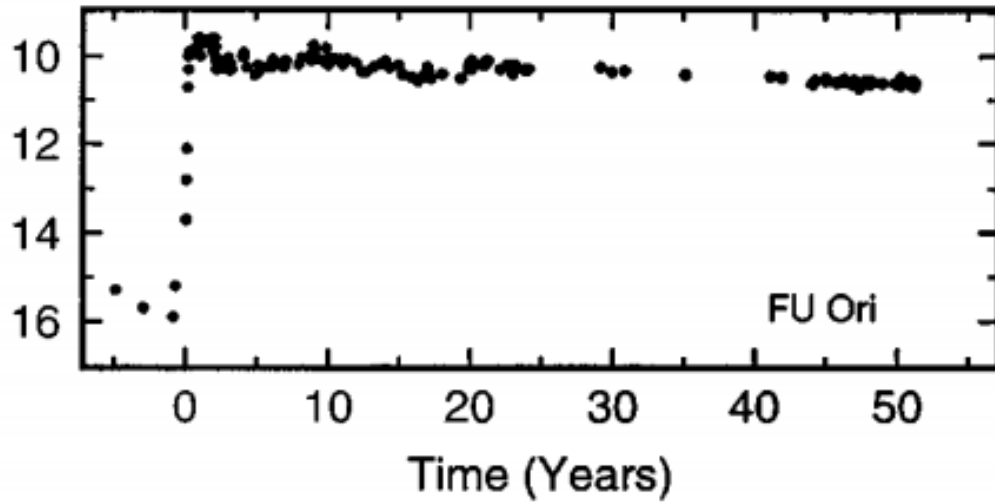


Figure 1.19: *B* band photometry of the outburst of FU Ori. Credit: Hartmann & Kenyon (1996)

category from the Cody et al. (2014) classifications. These light curves show many short (hours timescale) brightenings with amplitudes generally in the range of 5% to 50% of the quiescent level. These bursts appear in stochastic sequences and are found to appear most often in stars with large *UV* excess. Thus these bursts are attributed to increases in mass accretion rates. This lightcurve morphology is predicted for stars whose accretion is modulated by Rayleigh-Taylor or magneto-rotational instabilities in the inner disk. (e.g. Romanova et al. 2012; Kurosawa & Romanova 2013). They also find that lightcurve morphologies suggestive of stable funnel-flow accretion occur only about 1/3 as often as light curves dominated by short-duration accretion bursts and that the spectroscopic $H\alpha$ profiles for these stars are generally centrally peaked (class I in the scheme of Reipurth et al. 1996).

Long term, high-amplitude variability

The studies discussed so far have all found little evidence of significant variability on timescales much longer than the typical rotation periods of young stars (~ 10 days). This contrasts with the behaviour observed for a small number (≈ 20) of YSOs which are classed as FUor or EXor outbursting stars. FUors are believed to undergo accretion outbursts during which the accretion rate typically increases from $\dot{M} \sim 10^{-7} M_{\odot}\text{yr}^{-1}$ to $\dot{M} \sim 10^{-4} M_{\odot}\text{yr}^{-1}$ and remains at a high level on timescales of decades. The prototype of this class, FU Ori, brightened in magnitude from $B \approx 16.0$ to 9.7 in 1937 and has since faded only very slowly (see Kenyon et al. 2000, and Fig. 1.19). During their outbursts, classical FUors have bolometric luminosities of 100 - 300 L_{\odot} and exhibit F/G supergiant spectral types but with broad absorption lines compared with CTTS, and with little indication of accretion. The two FUor objects with pre-outburst spectra appear to be similar to CTTS in quiescence (Herbig 1977).

EXors are a loosely defined class of PMS stars that exhibit shorter (often repeating) outbursts, and appear to be associated with lower accretion rates. Outburst luminosities peak at a few

tens of L_{\odot} , and the colour evolution suggests that the brightening is due to a combination of emission from circumstellar dust that has been heated by accretion emission (Lorenzetti et al. 2012) and clearing of circumstellar material (Kóspál et al. 2013). In quiescence, EXors display spectra that are similar to CTTS (Parsamian & Mujica 2004; Herbig 2008).

The relationship between the two classes, and broader PMS evolution, is unclear. Theory suggests that accretion may proceed in ‘episodic’ bursts on long timescales (see Section 1.2.3), however current observations cannot tell us whether FUor and EXor phenomena are triggered by the same physical mechanism or even occur within the same evolutionary phase.

1.6 The ages of young stars

A wide range of key properties of young stars are believed to evolve as a function of time. Thus, being able to robustly measure the ages of young stars is critical to understanding physical processes such as their internal structure, the evolution of circumstellar discs and the formation of planets. Two key methods are available to estimate the ages of optically visible (principally Class II and Class III) stars, both involving comparison of observations with theoretical models of stellar evolution. The observable parameters that are predicted and used in age estimation are the colours and magnitudes (as proxies for T_{eff} and L_{bol} respectively), and abundance of Lithium in the stellar photosphere.

1.6.1 Colour-magnitude diagrams

Colour-magnitude diagrams (CMDs) are the observer’s equivalent of the Hertzsprung-Russell diagram. Instead of deriving astrophysical parameters (T_{eff} and L_{bol}) from observed parameters, we plot the observed colours and magnitudes and then compare them with theoretical model data that has been transformed into the observational plane. Interior models are able to simulate the evolution of young stars and predict T_{eff} and L_{bol} at any given age (e.g. D’Antona & Mazzitelli 1994; Baraffe et al. 1998; Siess et al. 2000; Dotter et al. 2008). Stellar atmosphere models (e.g. Castelli & Kurucz 2004; Allard et al. 2011) combined with filter and instrument system responses then allow the prediction of photometric colours and magnitudes. Improvements to these models can also be made through calibration of isochrones against well characterised datasets, thus overcoming some shortfalls known to exist in stellar atmosphere models (e.g. Bell et al. 2012). Isochrones are then created which show the relation between colour and magnitude at a given age. Systematic correction must be made to the models to allow for distance, binarity and interstellar extinction and reddening. Often these parameters may simultaneously be derived as part of the fitting process (Jeffries et al. 2007; Naylor 2009; Bell et al. 2013). Comparison of isochrones of different ages with a stellar association that is assumed to be co-eval allows an estimate of the age of the association to be made. Fig. 1.20 shows a CMD for the Pleiades compared with model isochrones.

Many physical mechanisms can affect the colours of a star so that its position in the CMD does not represent the intrinsic properties of the star. Improper extinction correction, cool spots on the surface, an intrinsic radius difference, accretion luminosity, and contamination from additional

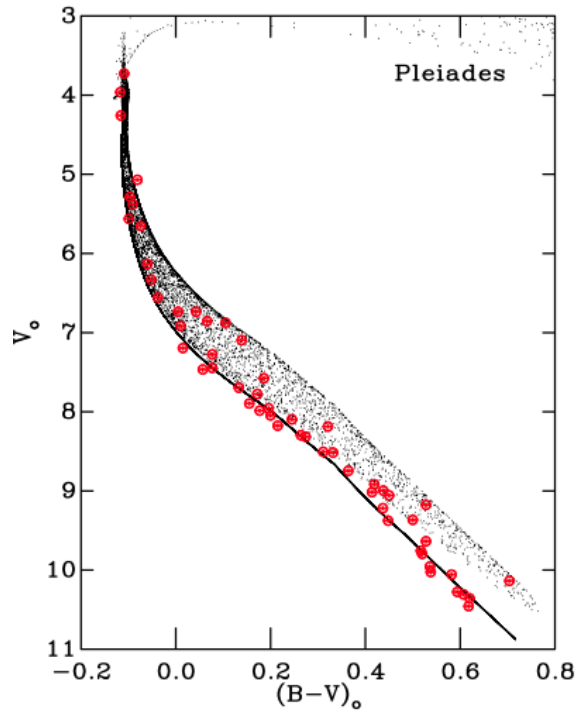


Figure 1.20: A CMD of the Pleiades cluster compared with a simulated model population. Both the data (red dots) and the model (black points) are by Bell et al. (2012). The model age is 135Myr, is comprised of both single and binary stars and is corrected to a distance modulus of 5.61mag.

sources of emission may all affect the CMD position. The perturbing effects are particularly potent in the youngest clusters ($< 10\text{Myr}$) as at this stage the stars may still be embedded within the precursor cloud and surrounded by accretion discs. The effect of these factors on a population of stars causes a spread in positions about the nominal PMS. Fig. 1.21 shows an example CMD for the ONC, where considerable scatter is evident, some apparent members are even seen to be fainter than the ZAMS. It is not clear whether all of the luminosity spread seen in young clusters is due to contaminating effects or whether a real luminosity spread is in fact present. The confirmation of a genuine luminosity spread in a PMS population would be important as it would imply that the stars in a given region displayed a range of intrinsic radii. A radius spread that could explain the luminosity spread in a cluster such as the ONC would have important ramifications for our understanding of star formation and stellar evolution. It could imply that stars in a given region have a significant range of ages and thus star formation had been proceeding in a given cloud for an extended period of time (Palla & Stahler 1999). Alternatively, some theories suggest that episodic bouts of accretion at high rates ($\dot{M} \gtrsim 10^{-4}M_{\odot}\text{yr}^{-1}$) in the protostellar phase could reduce the radius of a star, leaving it smaller and fainter throughout the PMS contraction phase (e.g. Baraffe & Chabrier 2010).

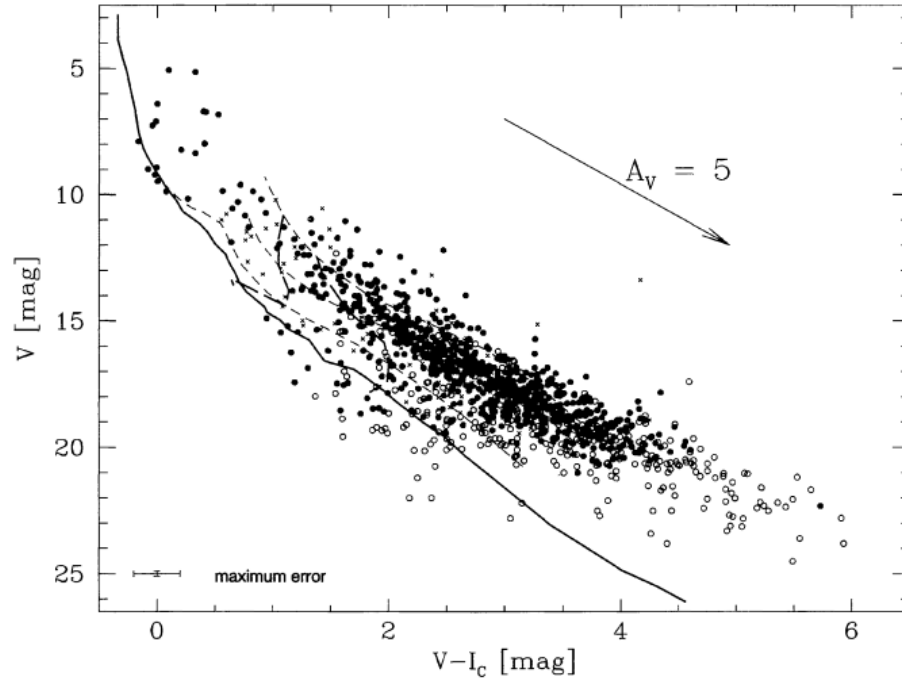


Figure 1.21: A V , $V - I$ CMD of the ONC is compared with ZAMS, 0.1 Myr, 1 Myr and 10 Myr isochrones by D'Antona & Mazzitelli (1994). Filled circles indicate proper motion members. Crosses are proper motion non members. Open circles are stars without proper motion data. Credit: Hillenbrand (1997).

1.6.2 Lithium derived (nuclear) ages

In low-mass stars, photospheric lithium depletion can be used as an alternative method of age estimation to CMDs. Unfortunately though, lithium depletion ages do have the disadvantage that they are only effective in stars older than ≈ 15 Myr.

Lithium depletion occurs as the abundance of lithium in the photosphere is a sensitive function of the temperature at the core of a fully convective star. PMS contraction causes the temperature in the core of the star to slowly increase as the star evolves along its Hayashi track. Once core temperatures exceed $\sim 2.5 \times 10^6$ K (slightly below that required for hydrogen burning), lithium is swiftly depleted via ${}^7\text{Li} + \text{p} \rightarrow {}^4\text{He} + \alpha$ reactions. Depletion is predicted to begin at an age of ~ 10 Myr in stars of mass $M_{\star} \approx 0.6 M_{\odot}$. By the time that a coeval association reaches ≈ 15 Myr there is a sharp transition between faint stars that retain their initial lithium and only slightly more luminous stars that are depleted. This boundary then steadily progresses to stars with lower masses at greater ages. Measurement of the luminosity at which this 'lithium depletion boundary' is found can then be used to estimate the age of the association (Bildsten et al. 1997). Lithium depletion ages are thought to be less model dependent than CMD ages as stellar atmospheric models are not required to convert stellar parameters into the observational plane. However, at young ages veiling can be a problem and must be carefully measured and accounted for to prevent over-estimation of lithium depletion.

1.7 The structure of this thesis

Colour-magnitude diagrams are widely used and powerful tools for the study of young stars. If we are to make use of CMDs to study the underlying physical phenomena, it is important that we fully understand how different physical processes drive the position of stars in the CMD. It is also crucial that any limitations and potential biases are fully understood. In this context, the aim of this thesis is defined as.

Aim: *To explore poorly understood behaviours that are seen in colour-magnitude diagrams of young star forming regions and use this new information to characterise the physical processes that occur in the formation and evolution of young stars.*

This thesis is the result of three distinct datasets, two of which explore different aspects of time-series variability in young stars. The multi-epoch nature of these observations reflect the dynamic and varying nature of the young stars under study and have been absolutely essential for characterising the behaviour and physics that occur. To achieve the stated aim, the thesis has been split into chapters that address the following aspects:

Chapters 3, 5 and 10 provide a thorough characterisation of photometric variability in YSOs and investigates the effect that it has on the interpretation of physical phenomena and the positions of stars in the CMD. Variability in the i band is shown to be dominated by processes that occur on timescales shorter than the rotation periods of YSOs ($\lesssim 10$ days). However, almost no variability is detected (at levels above $\approx 0.2\%$) on timescales shorter than 30 minutes. Optical variability is also shown to be strongly dominated by phenomena that are directly related to accretion luminosity (rather than the presence of discs alone). I identify four high-amplitude long-timescale variable stars which do show significant variability on timescales longer than the rotation period. One of these stars is a known FUor. The other three are likely to be EXor outbursting stars. The frequency of these stars within the sample imply that episodic accretion events may occur for a given disc-bearing star on timescales of ≈ 2000 years.

Chapter 6 shows that models for ISM dust are unsuitable for correcting for the extinction of YSOs with discs. The chromatic dependence of the extinction (R_V) measured in four YSOs imply that dust grains within the inner regions the circumstellar disc have coagulated to form larger grains. Extinction corrections made using values for R_V typical of the ISM, would underestimate the V band luminosity of these stars by between 0.05 and 0.1 mag, making them appear fainter in the CMD.

Chapter 2 shows that the spread in luminosity seen at a given T_{eff} in many young associations cannot be explained by episodic accretion at high-rates occurring within the protostellar phase of YSO evolution. It is clear that the CMD is not a useful tool for examining the accretion history of young stars. This chapter almost entirely comprises Sergison et al. (2013).

Chapter 8 shows that accretion luminosity significantly shifts the positions of YSOs blueward in the $g, g - i$ CMD. This effect causes stars to appear older than they really are when compared with non-accreting models and explains the presence of cluster members which fall below the ZAMS in CMDs.

Chapter 9 assesses the limitations of accretion rate diagnostics by comparing simultaneous measurements of U band excess, $H\alpha$ excess and veiling at 7000\AA for 15 stars in the ONC. Some evidence is found for the presence of ‘cool’ veiling sources which may contaminate veiling measurements that are used to estimate accretion rates.

Chapter 2

Using Lithium to probe the accretion history of young stars

2.1 Introduction

The radius and luminosity of a pre-main-sequence (PMS) star are determined by the balance between its Kelvin-Helmholtz (K-H) contraction timescale and accretion activity. If accretion increases the mass of the star more rapidly than the K-H timescale allows energy to be radiated away, it will displace the star from thermal equilibrium and cause it to exhibit a radius and luminosity that is inconsistent with non-accreting models (Tout et al. 1999; Baraffe et al. 2009; Hartmann et al. 2011). As the age of a T Tauri star ($\sim 2 - 5$ Myr) can be less than the K-H timescale, its radius and luminosity may still exhibit the influence of its prior accretion history in the embedded phase.

The core conditions of an embedded protostar are potentially dependent on its mass accretion rate. Accretion of material with low internal energy ('cold' accretion), at rates in excess of $\dot{M} \geq 10^{-4} M_{\odot} \text{ yr}^{-1}$ may gravitationally compress the star, increasing its core temperature and triggering the early onset of lithium burning (see Baraffe & Chabrier 2010, and Section 1.6.2). Efficient large-scale convection (seen in PMS stars) would then rapidly deplete lithium throughout the star. Observationally, this mechanism may be apparent in the later T Tauri phase as a surface lithium abundance that is much lower than that expected for a given age. In order for lithium to be depleted, a star must be radially compressed and hence the luminosity must be affected. As a result, lithium abundance in combination with luminosity may be a powerful observational signature of heavy accretion during the early evolution of PMS stars.

Current support for past accretion at high rates in early stellar evolution stems from three key observations.

1. Kenyon et al. (1990) find observational evidence for accretion at high rates contributing a significant fraction of a star's mass during the early 'assembly phase' of star formation. Angular momentum conservation indicates that infall must proceed first onto a circumstellar disc. Some of this material may then fall onto the star in bursts, perhaps through gravitational instability. Models by Vorobyov & Basu (2005) predict heavy bouts ($\dot{M} \geq$

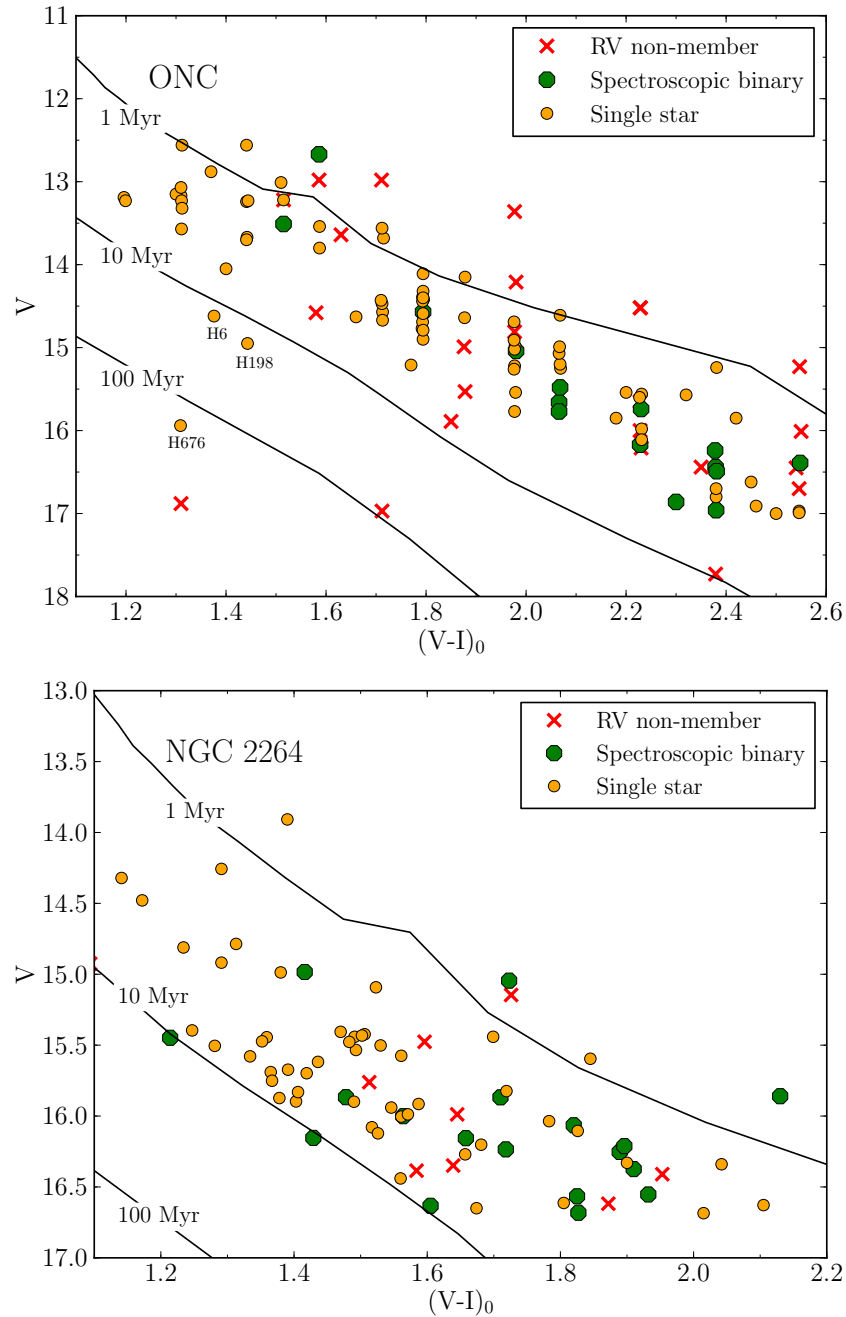


Figure 2.1: Colour-magnitude diagrams of target cluster members in the Orion Nebula Cluster (top) and NGC 2264 (bottom) compared with isochrones from Siess et al. (2000). Medium orange (light grey) filled circles are confirmed single star members for which I have established veiling and $EW[Li]$. Large green (dark grey) filled circles are spectroscopic binary stars (and confirmed members) for which I have $EW[Li]$ lower limits. Red crosses depict stars that I observed but were identified as radial velocity non-members. The limits of the plot represent the photometric limits imposed on my sample by (i) the sensitivity of the observations (ii) the T_{eff} cuts applied for the mass range of interest. Note: The three members that appear fainter than the 10 Myr isochrone in the ONC are numbered, these are discussed in Section 2.5.4. ONC photometry from Hillenbrand (1997), NGC 2264 photometry from Mayne et al. (2007).

$10^{-4} M_{\odot} \text{ yr}^{-1}$) of accretion lasting ≤ 100 years, between quiescent periods ($\dot{M} \leq 10^{-6} M_{\odot} \text{ yr}^{-1}$) lasting 1–3 kyr. These timescales fit with current observations of YSOs, explaining both the large population of low-luminosity class I sources and the small fraction of very luminous sources (Enoch et al. 2009).

2. Many observations of both star-forming regions (see Elmegreen 2000, for a review) and local molecular clouds (Ballesteros-Paredes & Hartmann 2007) appear to support the idea that star formation occurs on the order of one to a few dynamical crossing times, which is no more than a few Myr for a cluster such as the Orion Nebula Cluster (ONC) (e.g. Tan et al. 2006; Jeffries et al. 2011). If this is true then the CMD luminosity dispersion observed in young clusters (see Fig. 2.1 and McNamara 1976; Palla & Stahler 2000; Da Rio et al. 2010a), that is sometimes attributed to an age spread ≥ 10 Myr, may simply be evidence of variation in radius (and potentially early accretion history) within a coeval population. Jeffries (2007) find strong evidence for this in the ONC through statistical comparison of rotational periods and $v \sin i$.
3. Stars that are unusually depleted in lithium have been reported in the young clusters σ Ori and the ONC (Palla et al. 2005, 2007; Sacco et al. 2007). Some of these lithium depleted objects are also faint compared with the main cluster population. These characteristics are explained by invoking ages that are at least 10 Myr older than the main cluster population. However, past accretion at high rates may also be a consistent explanation and does not need to invoke an age spread that is at odds with observations of star formation on a dynamical crossing time.

Accreting material adds gravitational and thermal energy to the stellar interior at a rate defined by Hartmann et al. (1997) as

$$\frac{dE_{acc}}{dt} = \alpha \epsilon \frac{G M_{\star} \dot{M}}{R_{\star}} \quad (2.1)$$

where $\epsilon \leq 1$ for material falling from within the star's potential well and $\epsilon \leq 0.5$ for material accreted through a boundary layer from a thin disc. α is the fraction of the accretion luminosity absorbed by the star. Hartmann et al. (1997) suggest that $\alpha \ll 1$, providing the fraction of the stellar surface that accretion occurs over is small.

These qualitative ideas are supported by the results of numerical simulations, such as those by Tout et al. (1999), Baraffe et al. (2009), Baraffe & Chabrier (2010), Hosokawa et al. (2011) and Baraffe et al. (2012). Baraffe & Chabrier (2010) find that in the limit where $\alpha \lesssim 0.2$ (termed 'cold' accretion) additional mass added to the star causes gravitational contraction, reducing overall luminosity and increasing core temperature and pressure (see Fig. 2.2). They also find that this process significantly depletes lithium abundance in very young stars (from $\lesssim 1$ Myr) with $M_{\star} < 2 M_{\odot}$. The models suggest that a threshold accretion rate exists whereby detectable lithium

depletion occurs if the accretion rate during bursts exceeds $\dot{M} \geq 5 \times 10^{-4} M_{\odot} \text{ yr}^{-1}$ and the initial core mass of the proto-star has a mass $\leq 0.03 M_{\odot}$ (see Fig. 2.2). For a $1 M_{\odot}$ star, cold accretion that is able to measurably change a star's luminosity is found to always cause a measurable depletion in lithium. In contrast, non-accreting models suggest that lithium depletion will occur much later in the star's evolution. Siess et al. (2000) and Baraffe et al. (2002) predict less than 20 per cent lithium depletion for stars of age $< 10 \text{ Myr}$ at masses above $0.6 M_{\odot}$. Cold accretion models make two clear predictions which I have tested by observation.

1. If accretion occurs at $\dot{M} \geq 5 \times 10^{-4} M_{\odot} \text{ yr}^{-1}$, some highly lithium depleted stars should be found that cannot be explained by non-accreting evolutionary models.
2. In the cold accretion model, lithium depletion and low luminosity result from the same mechanism, hence observed lithium depletion should correlate with the appearance of old age in the CMD.

Section 2.2 describes the theoretical models and target selection. Section 2.3 details the observations and data reduction process. Section 2.4 presents the results, including radial velocity, binarity, accretion veiling, $v \sin i$, and lithium equivalent width. In Section 2.5, I discuss the lithium and veiling results for each cluster and show that there is some correlation between lithium abundance and CMD position. In Section 2.6, I conclude that there is no evidence for past episodes of cold accretion at very high rates.

2.2 Theory and target selection

2.2.1 Theoretical lithium depletion

Fig. 2.3 shows simulated lithium isochrones based on several different interior models (Baraffe et al. 2002; Siess et al. 2000) and illustrates the predicted equivalent width of the 6708 \AA lithium line ($\text{EW}[\text{Li}]$) as a function of $(V - I_c)_0$ colour. The isochrones were derived using a colour – T_{eff} relation defined by observations of main-sequence stars (Kenyon & Hartmann 1995), curves of growth from Jeffries et al. (2003) and an assumed initial lithium abundance of $A(\text{Li}) = 3.3$ on the logarithmic scale of Anders & Grevesse (1989).

These models suggest that lithium depletion can be used as a sensitive indicator of age in the mass range $0.4 < M_{\star} < 0.6 M_{\odot}$ ($3400 < T_{\text{eff}} < 3800 \text{ K}$, $1.2 < (V - I_c)_0 < 2.6$). Outside this range, PMS stars of lower mass than $0.4 M_{\odot}$ reach the temperature for lithium burning too slowly to show depletion in young ($< 10 \text{ Myr}$) clusters. Stars of mass $> 0.6 M_{\odot}$ develop a radiative core early and the base of the convective zone rises to regions of cooler temperature before all lithium can be destroyed (Pinsonneault 1997), rendering lithium depletion ineffective as an age indicator in young clusters.

Studies by Palla et al. (2005), Palla et al. (2007) and Sacco et al. (2007) derive ages based on $\text{EW}[\text{Li}]$ for individual stars in the ONC and $\sigma \text{ Ori}$. They compare lithium depletion ages for each

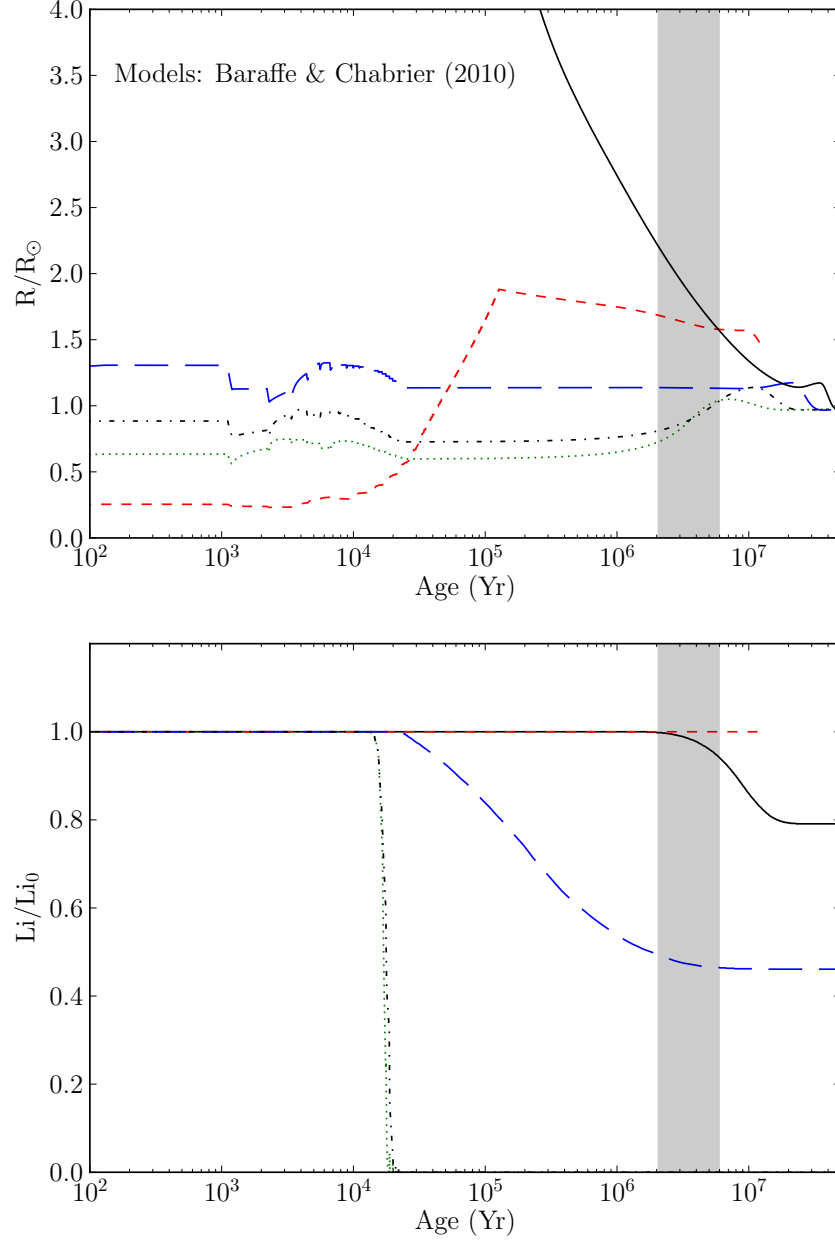


Figure 2.2: Evolution of radius (upper panel) and photospheric lithium abundance (lower panel) as a function of time for Baraffe & Chabrier (2010) models with episodic accretion and reaching a final mass of $1 M_{\odot}$. Short dash (red): $M_{\text{init}} = 1 M_{\text{jup}}$, $\dot{M}_{\text{burst}} = 1 \times 10^{-4} M_{\odot} \text{yr}^{-1}$, $N_{\text{burst}} = 100$; dot (green): $M_{\text{init}} = 10 M_{\text{jup}}$, $\dot{M}_{\text{burst}} = 5 \times 10^{-4} M_{\odot} \text{yr}^{-1}$, $N_{\text{burst}} = 20$; dash-dot (black): $M_{\text{init}} = 20 M_{\text{jup}}$, $\dot{M}_{\text{burst}} = 5 \times 10^{-4} M_{\odot} \text{yr}^{-1}$, $N_{\text{burst}} = 20$; long dash (blue): $M_{\text{init}} = 30 M_{\text{jup}}$, $\dot{M}_{\text{burst}} = 5 \times 10^{-4} M_{\odot} \text{yr}^{-1}$, $N_{\text{burst}} = 20$; solid line (black) is a non-accreting model for a $1 M_{\odot}$ star. All calculations are made with $\Delta t_{\text{burst}} = 100$ yr and $\Delta t_{\text{quiet}} = 1000$ yr. The grey shaded region encompasses age estimates for the clusters studied in this paper

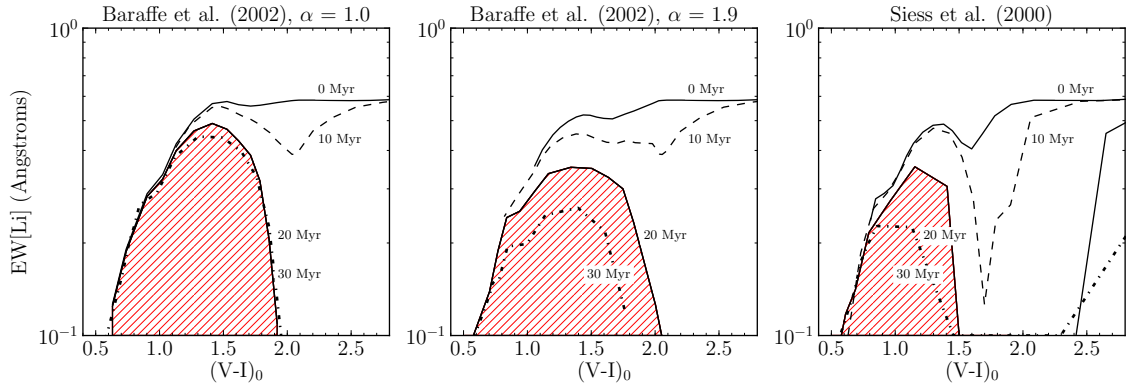


Figure 2.3: Predicted evolution of the 6708 Å lithium line strength as a function of age and colour in non-accreting models of PMS stars. The (red) hatched region is where I expect to find no stars that are younger than 20 Myr, thus defining a ‘forbidden zone’ in the clusters based on current age estimates. Stellar interior models are from Baraffe et al. (2002) and Siess et al. (2000), T_{eff} to $(V - I_c)_0$ from Kenyon & Hartmann (1995), curves of growth from Jeffries et al. (2003), $A(\text{Li}) = 3.3$ from Anders & Grevesse (1989).

Table 2.1: Key parameters for clusters selected in this study.

Cluster	Age (Myr)	Distance modulus	Number of selected targets	Supporting catalogues
Orion Nebula Cluster	2 ⁽¹⁾	8.08±0.04 ⁽²⁾	115	Hillenbrand (1997)
NGC 2264	3 ⁽¹⁾	9.37 ^{+0.15} _{-0.11} ⁽¹⁾	88	Mayne et al. (2007)

¹Mayne & Naylor (2008)

²Menten et al. (2007)

star with that found using isochrone fitting in the CMD. A small number of objects are identified in each cluster with anomalously low lithium line strength and in a few cases these correlate with an older CMD age. The lithium-derived age spread found within the clusters is proposed to support a slow star formation model. However, a small number of stars in the very low mass regime ($\lesssim 0.25 M_{\odot}$) are found in both the ONC and σ Ori with lithium depletion significantly greater than expected from their CMD age.

Lithium depletion predicted from simulations of cold accretion may occur throughout the mass range (see examples in Baraffe & Chabrier 2010, of stars with mass 0.1 and 1 M_{\odot}) providing the mass accretion rate during bursts $\dot{M} \geq 5 \times 10^{-4} M_{\odot} \text{ yr}^{-1}$. Conversely, age related depletion is highly sensitive to mass and is shown by some stellar interior models to be suppressed in the range 0.6 – 2 M_{\odot} due to the onset of the radiative core. As a result, the region in EW[Li] vs. colour space between $0.5 > (V - I_c)_0 > 1.6$ and below a EW[Li] of 0.35 Å is a ‘forbidden zone’ (shown in Figure 3) where low lithium objects should not exist according to non-accreting models. Confirmed young cluster members found in the forbidden zone would offer strong support to cold accretion theories, even if combined with modest age spreads.

2.2.2 Target selection

The constraints established in Section 2.2 lead me to require nearby young clusters with ages < 10 Myr, where lithium depletion may identify PMS members with a high accretion rate history or greater age. I also required comprehensive literature photometry and spectroscopy to characterise the observed stars and allow construction of CMDs for isochronal age determination. The clusters selected were the ONC and NGC 2264. Key parameters for these clusters are shown in Table 2.1. Whilst previous age estimates for these clusters are around 2-3 Myr, recent work by Naylor (2009) and Bell et al. (2013) suggest that PMS ages are underestimated by a factor 2, hence the clusters may in reality be closer to 4-6 Myr.

To ensure a high fraction of stars studied were cluster members, indicators of youth such as X-ray luminosity (Flaccomio et al. 1999, 2002), $H\alpha$ emission (Dahm & Simon 2005) and optical variability (Herbst et al. 2002; Lamm et al. 2004) were used in conjunction with position in colour-magnitude space to select target stars. Importantly, photometric selection did not exclude members with low luminosity. Instrumental constraints meant that selection was also weighted toward the cluster centre, thus preferring a smaller number of objects close to the cluster core over a larger number further out. This led to the selection of fewer stars per field, although those selected had a higher probability of cluster membership. The final selection criteria for target stars was a cut in T_{eff} (determined via the colour - T_{eff} relation of Kenyon & Hartmann 1995) in the range 3400-4900 K, approximately corresponding to mass range $0.3 - 1.9 M_{\odot}$ on the isochrones of Siess et al. (2000) at an age of 3 Myr.

For the ONC, the selection deliberately targeted 7 literature cluster members that appear to be fainter than the main population in the CMD. Since low-luminosity objects could result from cold accretion, I shall investigate whether these objects also exhibit depleted lithium. Alternative theories proposed to explain them include an age spread (Palla & Stahler 2000), as gravitationally captured field stars (Pflamm-Altenburg & Kroupa 2007) or unusually blue objects exhibiting heavy accretion veiling (Hillenbrand 1997). I shall refer to this population in the rest of the chapter as the ‘low luminosity group’ (LLG).

2.3 Observations and data reduction

The observations were made on the nights of 2011 November 20, 21 using the AF2/WYFFOS multi-object fibre-fed spectrograph on the 4.2 m *William Herschel* Telescope. The small fibres module contains 150 fibres, each with a diameter of 1.6 arcsec. To avoid potentially damaging fibre collisions, not all of the fibres may be placed on target stars in any given configuration, thus limiting the actual number of targets to significantly less than 150 per field. This was an important limiting factor in these observations due to the centrally condensed nature of the clusters studied. I used an echelle grating and order sorting filter, centered at 6545 \AA with a range of $\sim 390 \text{ \AA}$. This covered the wavelength range including $H\alpha$ and the lithium doublet at 6708 \AA . The signal-to-noise (SNR) obtained ranged from 10-60 per 0.22 \AA wavelength step with a resolution, $R \sim 10\,000$.

Time, weather and observability constraints meant that for the ONC two ‘bright’ (1 x 2700 sec) and one ‘faint’ (4 x 2700 sec) setups were obtained and for NGC 2264 three ‘bright’

(1 x 2700 sec) setups. The longer exposure times for the ONC were offset by the greater levels of extinction to that cluster ($A_v \sim 1.5 - 6$, Hillenbrand 1997) as compared with NGC 2264 ($A_v = 0.37$, Mayne et al. 2007). As a result, the limiting magnitude (corrected for extinction) for both clusters was $V_0 \geq 17$. 115 stars were observed in the ONC and 88 in NGC 2264 (see Fig. 2.1).

Science frames were bias corrected using a median of 5 bias frames, with bad pixels identified from dark frames and subsequently masked. Tungsten lamp flat-fields were obtained before each science exposure and used to trace the positions of spectra on the CCDs. Flat-field images were also used to construct a weighting function for the optimal extraction routine. Arc lamp exposures before and after each science frame were used to provide wavelength calibration. Sky signal was subtracted using a minimum of 30 randomly placed sky fibres. The spectra were extracted and calibrated using an IDL based software pipeline provided by the *Issac Newton* Group and optimised for the AF2/WYFFOS instrument¹. Spectra were extracted using an optimal routine (see Horne 1986) which helps to minimise statistical noise. Once calibration and reduction were complete the data were then interpolated and re-binned onto 10 000 logarithmically placed wavelength steps.

2.4 Analysis

The 6708 Å lithium line equivalent width (EW[Li]) was measured with respect to a pseudo-continuum. A wavelength step integration of the spectral line was performed between upper and lower line limits defined to exclude other lines and to incorporate the entire line irrespective of rotational broadening or binarity. At the resolution of my spectra, contamination of up to 20 mÅ is likely to be present from a weak Fe I line at 6707.4 Å. Uncertainties due to the definition of the pseudo-continuum and line limits were determined through repeat measurements to be ± 10 mÅ. Photon noise in the signal contributes a further $\pm 10 - 60$ mÅ, dependent on the SNR of the spectrum. The three uncertainties are combined in quadrature with that described in Section 2.4.2 for accretion veiling.

As I am trying to measure the intrinsic EW[Li] for these stars, I must account for ‘veiling’ of spectral lines by continuum emission from magnetospheric accretion regions on the surface of the star. This ‘veiling’ effect is well studied (eg. Gahm et al. 2008; Dodin & Lamzin 2012b) and its effect has been corrected through the use of techniques outlined in Hartigan et al. (1989). The accretion veiling contamination is visible as a weakening of absorption lines and hence has a significant effect on the measurement of photospheric features such as the 6708 Å lithium line. The effect of accretion veiling is to reduce measured EWs, hence without careful consideration this could affect the apparent lithium abundance in the objects being studied. A correction for the veiling flux is made assuming that it is a smoothly varying continuum over the spectral range from 6390 to 6710 Å. Within the narrow range specified this is probably a reasonable assumption as determined by Hartigan et al. (1989) and Guenther & Hessman (1994). Before determining and correcting for veiling, an assessment of radial velocity and $v \sin i$ must first be made between the

¹<http://www.ing.iac.es/astronomy/instruments/af2/reduction.html>

object and template stars in order to correct for wavelength and line profile differences. Typically the unveiling process contributes an uncertainty of similar magnitude to the combination of the other measurement uncertainties and is combined with them to provide an uncertainty estimate for the final measurements.

2.4.1 Radial velocity and binary stars

Radial velocities (RVs) were determined using cross-correlation of spectral lines in the range 6385 – 6510 Å between each star and an arbitrary (low $v \sin i$) single star reference in the field. No absolute RV standards were measured as relative velocities are sufficient for veiling analysis and cluster membership verification. Fig. 2.4 shows histograms of the derived radial velocity distributions for both clusters.

The ONC displays a clear velocity grouping with a range of $\pm 10 \text{ km s}^{-1}$ about the sample median, this is consistent with previous RV studies of this cluster (e.g. Biazzo et al. 2009). 21 objects were identified with velocities outside the range specified and hence were removed from further analysis of the sample. Many of these objects are likely to be unequal mass spectroscopic binary cluster members that are unresolved from their cross-correlation function (CCF), however without multi-epoch measurements I cannot be clear as to which objects fall into this category. As a result I reject all stars with $|\text{RV}| > 10 \text{ km s}^{-1}$.

The NGC 2264 RV histogram shows that this cluster exhibits a non-Gaussian velocity dispersion with a range of $\pm 9 \text{ km s}^{-1}$ about the median. This is consistent with previous measurements by Fűrész et al. (2006). Nine objects in the NGC 2264 sample exhibit RV with magnitudes outside the range defined above and hence have also been removed from further analysis.

Some of the identified RV outliers exhibit lithium absorption and H α emission, so are likely to actually be cluster members. I have been deliberately cautious in excluding potential non-members though, as my aim was to set up a robust sample of members that does not use lithium detection as a criterion. Exclusion of some stars which are actually members only affects the result by reducing the sample size. Conversely, including a star that was not a member could seriously bias the result.

Binary stars with resolved splitting in spectral lines cause significant difficulties with accretion spectrum fitting. Potential binaries were identified since they exhibit multiple peaks in the CCF and were removed from the data set before the veiling analysis. Examples showing single and binary star CCFs are shown in Fig. 2.5. Multiple peaks in a broad CCF could also be due to noise overlaid on highly rotationally broadened spectra. This is difficult to confirm or refute on a star by star basis, however unveiled Li[EW] measurements for these stars were included in the analysis as veiled lower limits in EW[Li].

Four of the seven stars in the ONC ‘LLG’ (see Section 2.2) were identified as having RVs that are inconsistent with the cluster. As a result they are removed from the sample and their faint nature may be explained as being characteristic of main-sequence or post-main-sequence stars from the galactic field that are moving through or behind the cluster. These objects are marked by red crosses in Fig. 2.1.

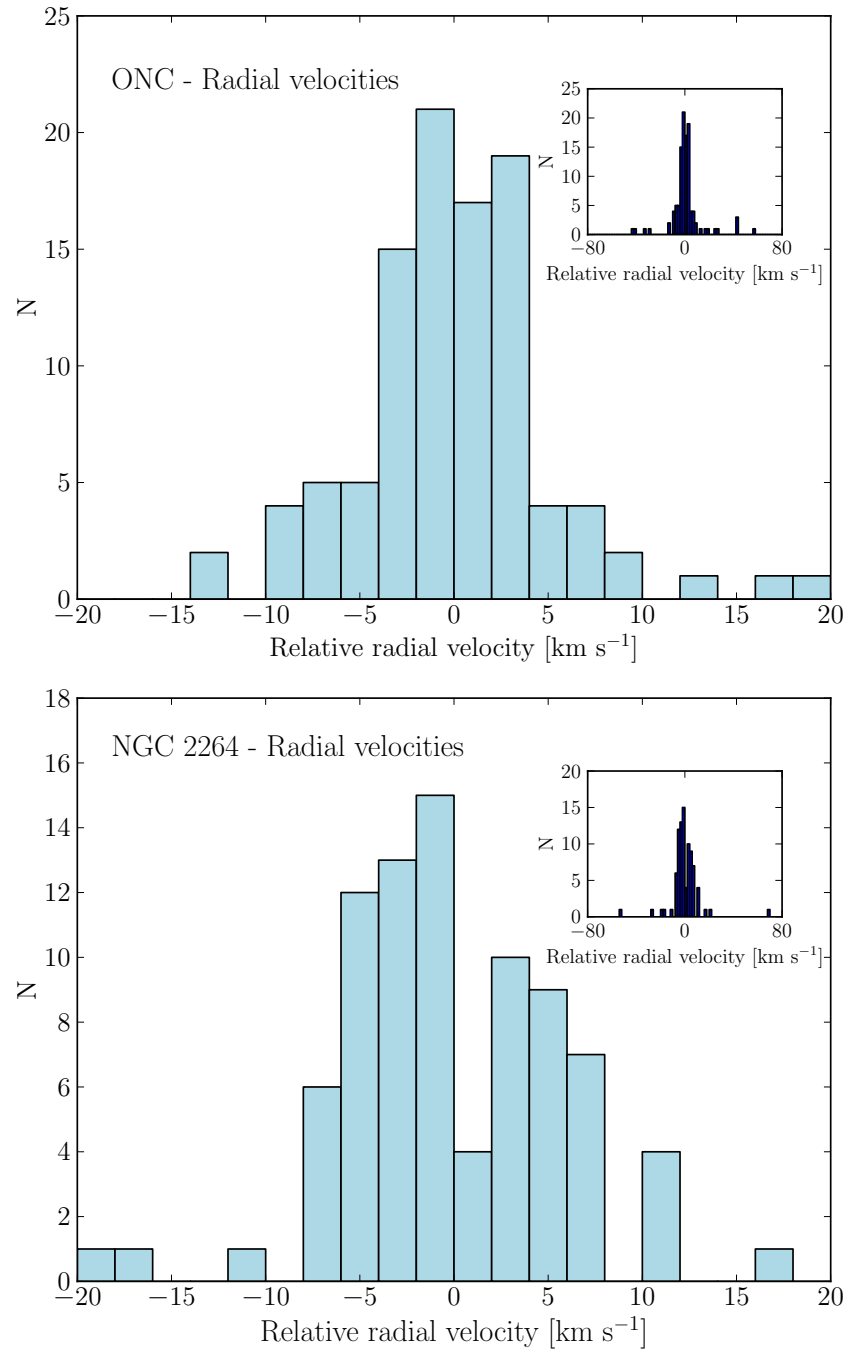


Figure 2.4: Histogram of radial velocities for stars in the ONC (top) and NGC 2264 (bottom) relative to the median of the respective samples. Inset shows the entire sample including radial velocity outliers.

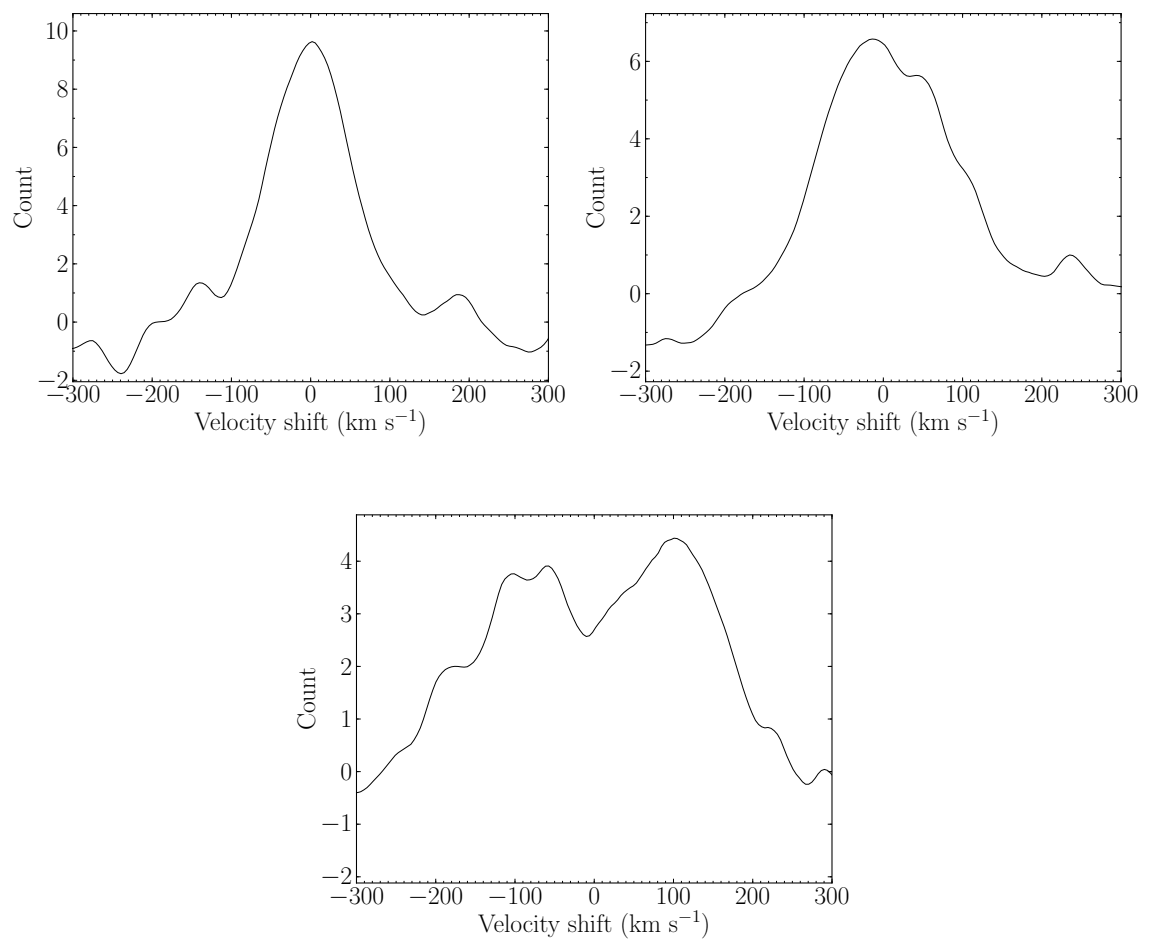


Figure 2.5: Example velocity cross-correlation function (CCF) plots, showing single star (top left), and close and wide line separation binary stars (top right and bottom).

2.4.2 Accretion veiling and $v \sin i$

In Section 1.4.3, the veiling for a given object at a given wavelength was defined as:

$$r_\lambda = \frac{f_{\text{veil}}}{f_{\text{phot}}} \quad (2.2)$$

where r_λ is the flux ratio of the accretion veiling continuum (f_{veil}) to the stellar photospheric continuum (f_{phot}).

To estimate the veiling continuum flux, a set of template stars have been selected for each cluster from their own populations (9 for the ONC and 8 for NGC 2264) across the full colour range. Selected template stars form the upper envelope of the EW[Li] vs. $(V - I_c)_0$ diagram and exhibit $v \sin i$ limited by the instrumental FWHM. Hence these objects should be amongst those with the lowest veiling and intrinsic $v \sin i$ within my sample. The templates were first offset in wavelength to compensate for the difference in RV between template and object. They were then rotationally broadened (using a kernel with limb darkening coefficient of 0.5; van Hamme 1993) and normalised to a similar flux as that of the object spectrum to produce reference templates.

The templates were then subtracted from the object spectrum to leave residuals which are assumed to represent the accretion spectrum. I varied the normalisation of the templates and examined the residuals using a χ^2 test, performed between the residuals and (30 Å boxcar average) smoothed versions of themselves. Adopted $v \sin i$ and veiling values were identified using the residuals with minimum χ^2 . The parameter search space was defined by $v \sin i$, from 0–100 km s⁻¹ with a resolution of 1 km s⁻¹ and veiling ratio of 0–5 in steps of 0.01 of the photospheric continuum. Fig. 2.6 shows an example of an object spectrum, template and best fitting broadened and veiled model template.

This process was repeated as it was found that a considerably stronger CCF was obtained if the RV cross correlation is performed against an appropriately broadened template. Thus the first iteration identifies approximate RV and $v \sin i$, the second iteration improves the RV and hence $v \sin i$ as the fitted RV template has a more similar shaped line profile.

Fitting of templates was performed in two wavelength regions, the first between 6390 and 6500 Å, in a region containing 7 photospheric absorption lines (Fe I 6393.6 Å, Ne II 6407.9 Å, Fe I 6411.7 Å, Fe I 6421.3 Å, Fe I 6431.0 Å, Ca I 6439.1 Å, Ca I 6450.0 Å, Ca I 6462.5 Å and Fe I 6495 Å). The second was between 6610 and 6675 Å, containing three lines (V I 6624.8 Å, Ni I 6643.6 Å and Fe I 6663.4 Å). These regions are free from contamination by H α or significant sky and nebular line emission.

Analysis of sky and nebular lines indicate that the spectrograph was operating with a resolution of $R \sim 10\,000$. Comparison with literature (see Rhode et al. 2001; Baxter et al. 2009) indicate that the corresponding limit in $v \sin i$ resolution is $\sim 20 - 30$ km s⁻¹, depending on target SNR.

The veiling for each star was calculated as the weighted mean across the cluster template set based on the inverse of the difference in $(V - I_c)_0$ colour between each template star and the object. To avoid overweighting when the template and object colours were very close, a

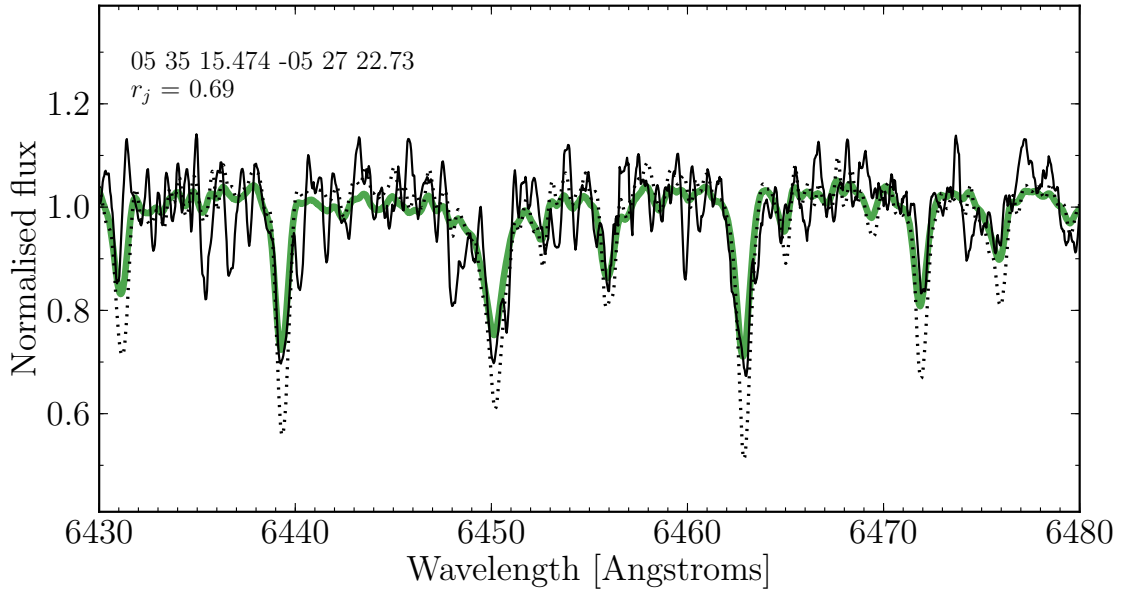


Figure 2.6: Spectrum of object RA = 05 35 15.47 Dec = -05 27 22.7 in the ONC. The thin black line is the object spectrum. The dotted line is the template showing significantly deeper photospheric absorption lines. The green (light grey) broad line is the broadened and veiled template that best fits the object spectrum ($r_\lambda = 0.69$). The template spectrum has a greater SNR than the target one (SNR of 58 per pixel as opposed to 38 per pixel). The broadening kernel and the addition of the smooth veiling model are also likely to make the model spectrum appear more smooth outside of the line regions than the target spectrum.

minimum $\Delta(V - I_c)_0$ of 0.1 was placed on the weighting algorithm. The aim of this process is to use multiple templates to provide reliability of fit, without introducing errors from large template-to-star colour differences. It should be noted that although great care was taken to ensure that the veiling was derived from templates of similar colour, in practice the veiling measured was found to be surprisingly insensitive to template colour for any given star. The range of fractional uncertainty due to template mismatch was measured to be $\sim 0.05-0.3$ across the sample. Template to template variations appear to dominate, possibly caused by differences in the template line profiles due to rotation, binarity, and chromospheric activity.

Uncertainties in veiling were derived by analysing the range in veiling estimates returned by all of the fits from the full template set. The standard deviation (also weighted as a function of template to star colour difference) of the set of veiling values was calculated and adopted as the uncertainty in the veiling measurement. As the method used here analyses lines over a narrow spectral range, it is independent of reddening and extinction and hence is robust in dusty regions of new star formation such as the clusters studied in this paper. Measured values of r_λ vary from 0 to 4.0.

2.4.3 Lithium equivalent width versus colour

Once the magnitude of the veiling continuum had been established for each star, a correction was applied to the raw measured lithium EW to quantify the unveiled EW. The uncertainty in

the corrected EW[Li] was calculated by combining uncertainties in the raw line measurements with the uncertainty in veiling. Fig. 2.7 shows veiling corrected lithium EWs and associated uncertainties plotted as a function of dereddened $(V - I_c)_0$ colour. Most of the data points lie slightly above the undepleted model isochrone. Reasons for this may include uncertainties in molecular line strengths in stars with $T_{\text{eff}} < 4000\text{K}$, causing difficulty in definition of the pseudo-continuum around the lithium line. In the hotter stars a lack of inclusion of NLTE effects may cause uncertainties in the modelled curves of growth (e.g. Carlsson et al. 1994). Theoretical 0 (undepleted), 10 and 20 Myr isochrones (Baraffe et al. 2002) are also shown. Dereddened $(V - I_c)_0$ colours for the ONC are from Hillenbrand (1997). It should be noted that the dereddening method used for the ONC was performed on a star-by-star basis and groups objects into bins by spectral class. Hence $(V - I_c)_0$ colours are not continuous. Dereddened colours for NGC 2264 were derived in Mayne et al. (2007) using a single global solution of $E(V - I_c) = 0.15$, based on a mean measured $(V - I_c)$ excess for main-sequence stars. Accurate unveiling of spectroscopic binaries is a very difficult and uncertain process, so these points have been left in their raw measured (veiled) values and are displayed as lower limits in EW[Li].

2.5 Discussion

2.5.1 Accretion veiling

The data show that the sample of stars in the ONC exhibit greater accretion veiling than the sample in NGC 2264. The mean r_λ and standard deviation have been calculated for all stars in both clusters and for a subset in both clusters that cover a common colour range ($1.2 < (V - I_c)_0 < 2.0$). All measured stars in the ONC exhibit a mean $r_\lambda = 0.48$ with a standard deviation (σ) of 0.37 dex. This compares with mean $r_\lambda = 0.16$, $\sigma = 0.34$ dex for all measured stars in NGC 2264. The subset with colour range $1.2 < (V - I_c) < 2.0$ in the ONC exhibit a mean $r_\lambda = 0.44$, $\sigma = 0.41$ dex and in NGC 2264 the mean $r_\lambda = 0.15$, $\sigma = 0.34$ dex. It is notable that whilst the absolute levels of veiling differ, the ratio of σ/r_λ is similar in both clusters.

If NGC 2264 is older than the ONC as suggested through studies of young main-sequence stars (Mayne & Naylor 2008) then my finding is consistent with models of decreasing disc fraction (and hence accretion) with age. If however, the ages of the clusters are indistinguishable from each other as suggested by main-sequence turn-off ages (see Naylor 2009) then the difference in apparent accretion luminosity may suggest an environmental difference between the two clusters such that stars in the ONC accrete more vigorously or for longer than NGC 2264.

2.5.2 EW[Li] distribution, age spreads and correlation with CMD position

Both clusters appear to exhibit lithium equivalent widths that are approximately consistent with their CMD derived ages (< 10 Myr). It is also apparent that no highly lithium depleted stars are seen with $\text{EW}[\text{Li}] \lesssim 0.4 \text{ \AA}$. NGC 2264 appears to show a slightly greater spread in EW[Li] at higher masses than the ONC.

The observed dispersion in EW[Li] might imply an age spread that is similar in magni-

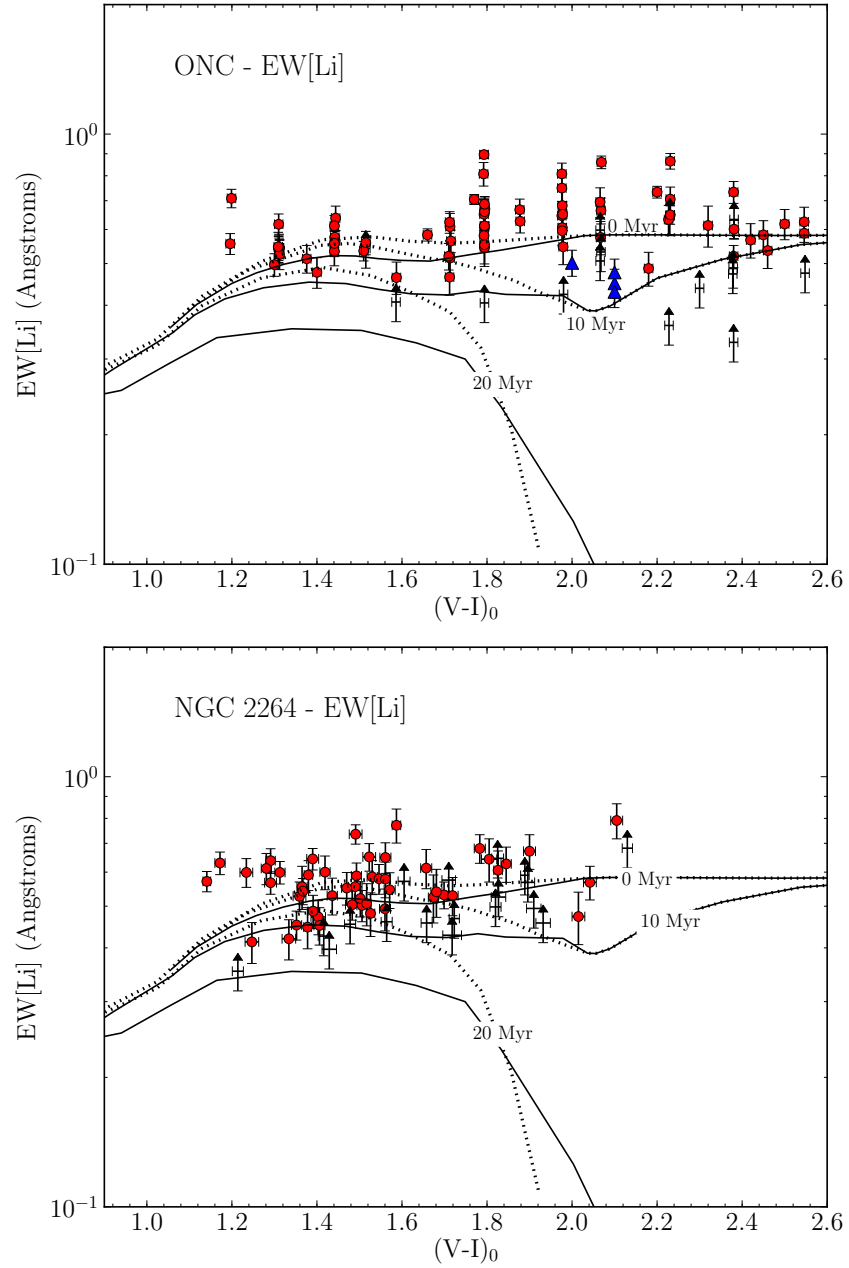


Figure 2.7: A comparison of 6708 Å lithium line equivalent width measurements for stars in the ONC (top) and NGC 2264 (bottom) plotted as a function of intrinsic $(V - I_c)_0$. Red points are unveiled single star measurements, black triangles are lower limits for spectroscopic binaries which are left as veiled (raw) measurements. The 0 Myr, 10 Myr and 20 Myr isochrones are based on models by Baraffe et al. (2002). Solid lines indicate models using a convective mixing length parameter (α) of 1.9. Dotted lines indicate $\alpha = 1.0$. Blue triangles are data from Palla et al. (2005) which are cited as having depleted lithium. These points have been calculated using $n(\text{Li})$ to $\text{EW}[\text{Li}]$ conversion from curves of growth in Table 1 of Palla et al. (2007). The conversion from T_{eff} to intrinsic $(V - I_c)_0$ colour for the Palla et al. (2005) data have been made using the relation defined by Kenyon & Hartmann (1995).

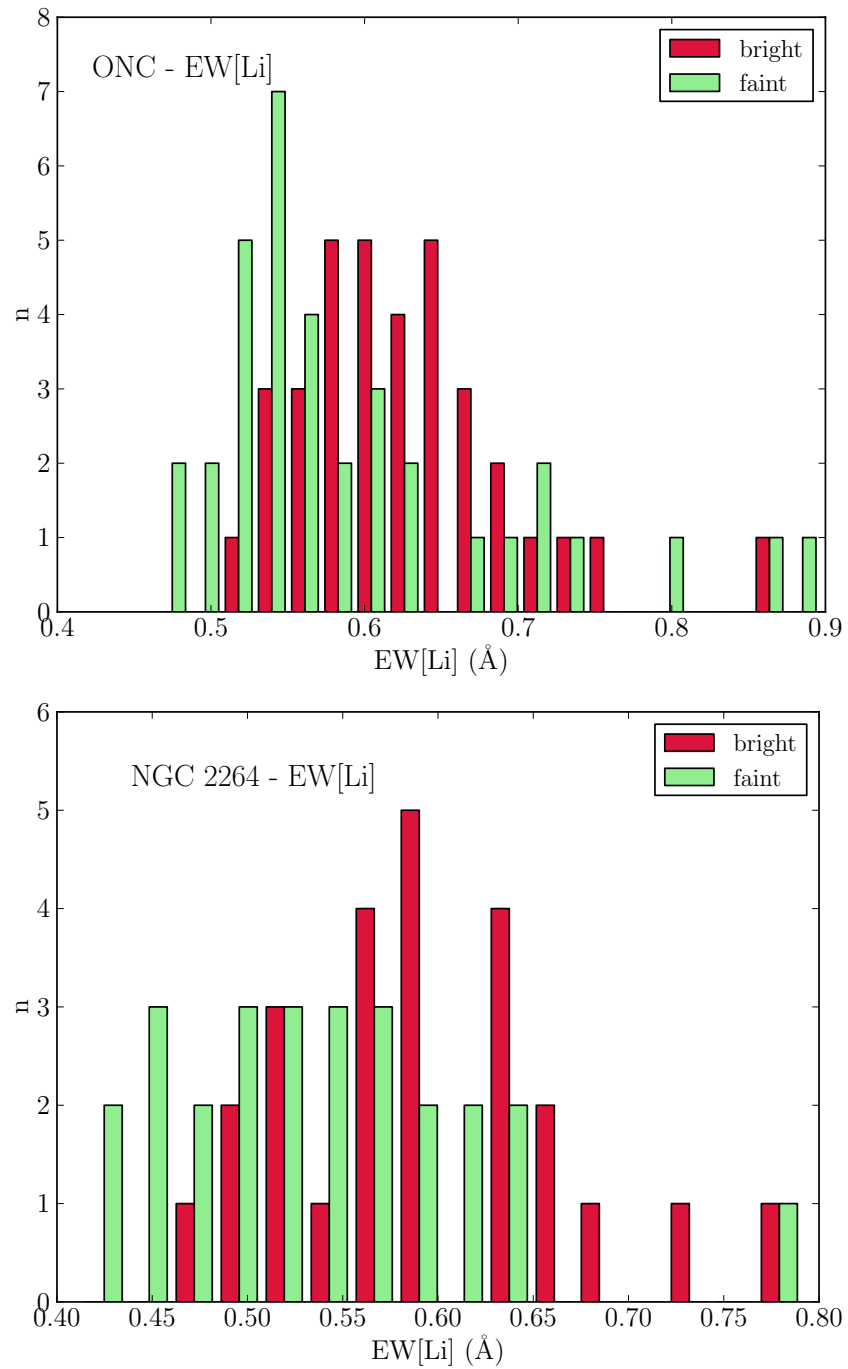


Figure 2.8: Comparison of the EW[Li] data for bright and faint sub-samples in each cluster. In both clusters the population of faint stars shows a systematic decrease in lithium line strength.

tude to the apparent age spread implied by the luminosity dispersion seen in CMD space. To test whether this really could be an age spread, I looked for disagreement between the EW[Li] seen in bright and faint sub-populations of stars. Each cluster was split onto two sub-samples representing the bright and faint populations using the following method. First I calculated the median dereddened colour in 0.1 mag. wide magnitude bins, and a straight line was fitted to define the median magnitude as a function of colour. These lines may be seen plotted over the data in Fig. 2.1. Stars with magnitudes brighter than this were assigned to the bright sub-sample and vice-versa. If an age spread explanation were to be plausible, the bright sample should be the youngest and ages should increase as one moves to fainter magnitudes. This should be evident as a depletion in lithium in the faint population.

I compared the sub-populations for each cluster using the 2 sample K-S test. The ONC shows evidence for the two samples being drawn from different populations with the null hypothesis that they are from the same population being rejected at the 99.8 per cent confidence level. The bright population exhibits median EW[Li] = 0.63 Å and the faint population median EW[Li] = 0.56 Å. A similar trend is shown in NGC 2264, the bright population exhibits median EW[Li] = 0.59 Å and the faint population EW[Li] = 0.54 Å with the null hypothesis being rejected at the 98.2 per cent confidence level. These findings are illustrated in Fig. 2.8.

I have considered whether this trend in EW[Li] is a systematic effect of the unveiling process. Although there is a weak correlation between EW[Li] and veiling, this cannot be the cause of the correlation of CMD position with Li[EW] since there is not the correlation between veiling and position in the CMD which would be required to translate this into the observed effect. It should be noted that if there is a veiling related systematic error, one would expect its effect to be most apparent in the ONC where veiling is strongest. In practice the ONC shows no correlation between veiling and CMD position, yet the EW[Li] vs. CMD position correlation is significant.

I have also considered whether this trend in EW[Li] may be due to differences in surface gravity, however the correlation is in the opposite sense to that found in simulations by Zapatero Osorio et al. (2002) and Palla et al. (2005) as a function of $\log g$. Another consideration is whether the observed depletion (either real or a systematic measurement error) is related to rotation rate. Studies such as Viallet & Baraffe (2012) suggest that rotationally induced mixing can deplete lithium on timescales of just a few Myr. I find no correlation when EW[Li] is plotted against measured $v \sin i$ or rotation period. The depletion I see would also conflict with the rotation rate vs. CMD position correlation seen by Littlefair et al. (2011) if rotationally induced mixing were responsible.

Interpreting this trend in luminosity and EW[Li] is critically dependent on the adopted value of the convective mixing length (α). In the model where $\alpha = 1.9$, the EW[Li] trend is compatible with an evolution where ageing stars are slowly depleting lithium across the ($V - I_c$) colour range as they contract toward the zero age main-sequence (ZAMS). This model agrees with Jeffries (2007) who finds a statistical decrease in radius as one moves from bright to faint objects at a given colour in the CMD. Importantly, if α is closer to 1.0 then I would expect to see a difference in dispersion with colour if a large (≥ 10 Myr) age spread were present as at ($V - I_c$) ≈ 2.2 the uncertainties in EW[Li] are less than the depletion predicted by the 10 Myr isochrone. My data

Table 2.2: Parameters for accreting models plotted in Fig. 2.9

Ref	M_{init} (M_{\odot})	\dot{M} ($M_{\odot}\text{yr}^{-1}$)	No. bursts	T_{quiet} (yr)	Time to complete accretion (yr)	Final mass (M_{\odot})
1	0.001	1×10^{-4}	100	10^3	1.1×10^5	1.0
2	0.01	1×10^{-4}	99	10^3	1.1×10^5	1.0
3	0.01	1×10^{-4}	69	10^3	7.6×10^4	0.7
4	0.01	5×10^{-4}	14	10^3	1.5×10^4	0.7
5	0.01	5×10^{-4}	16	10^3	1.8×10^4	0.8
6	0.01	5×10^{-4}	20	10^3	2.2×10^4	1.0
7	0.01	5×10^{-4}	14	10^4	1.4×10^5	0.7
8	0.02	5×10^{-4}	20	10^3	2.2×10^4	1.0
9	0.03	5×10^{-4}	20	10^3	2.2×10^4	1.0

appear inconsistent with an age spread of this magnitude.

Whilst it is tempting to consider the link between EW[Li], luminosity and radius as confirmation of an age spread, it is evident from Fig. 2.2 that cold accretion can ‘accelerate’ the evolution of a star making it appear in all observable ways older. Thus the EW[Li], luminosity and radius trends are the expected outcomes of either an age spread or cold accretion; my data do not allow me to differentiate.

2.5.3 Depleted lithium members

It should be noted that not all cold accretion scenarios will show detectable lithium depletion in young stars in the mass ($0.3 < M_{\star} < 1.9 M_{\odot}$) and age range (2 – 6 Myr) that I consider in this Section. Fig. 2.9 shows a range of accreting models from Baraffe & Chabrier (2010) with a selection of starting and accretion parameters that are summarised in Table 2.2. My data place limits on the levels of lithium depletion seen in my sample. I observe up to ≈ 10 per cent depletion in EW[Li] which corresponds to a factor of $\lesssim 2$ in lithium abundance for stars within the colour range defined by the forbidden zone. Thus, my observations exclude the possibility that the objects have experienced past accretion with $\dot{M} \geq 5 \times 10^{-4} M_{\odot} \text{yr}^{-1}$. The only exception might be in the case of an extremely high-mass initial core ($M_{\text{init}} > 0.03 M_{\odot}$). An initial core mass $> 0.03 M_{\odot}$ is at least an order of magnitude larger than expected from calculations (see Baraffe et al. 2012, and references therein) of collapse from first to second Larson core (Larson 1969). Also, these high initial mass models do not explain the full range of luminosities seen in the CMD and thus do not help to explain the observed luminosity dispersion.

The lack of strongly lithium depleted members in the sample is consistent with the findings of Palla et al. (2005) for the ONC in my mass range, and with the only available literature sample for NGC 2264 (King 1998). The Palla et al. (2005) sample has 82 stars in the ONC, in the mass range $0.4\text{--}1 M_{\odot}$. Significant lithium depletion is cited for 4 of these stars, however (as may be seen in Fig. 2.7) these depleted objects are found to be broadly consistent with the spread in EW[Li] seen in my data. The levels of depletion identified are far less than expected for cold accretion at high rates and no stars are shown to fall within the forbidden zone.

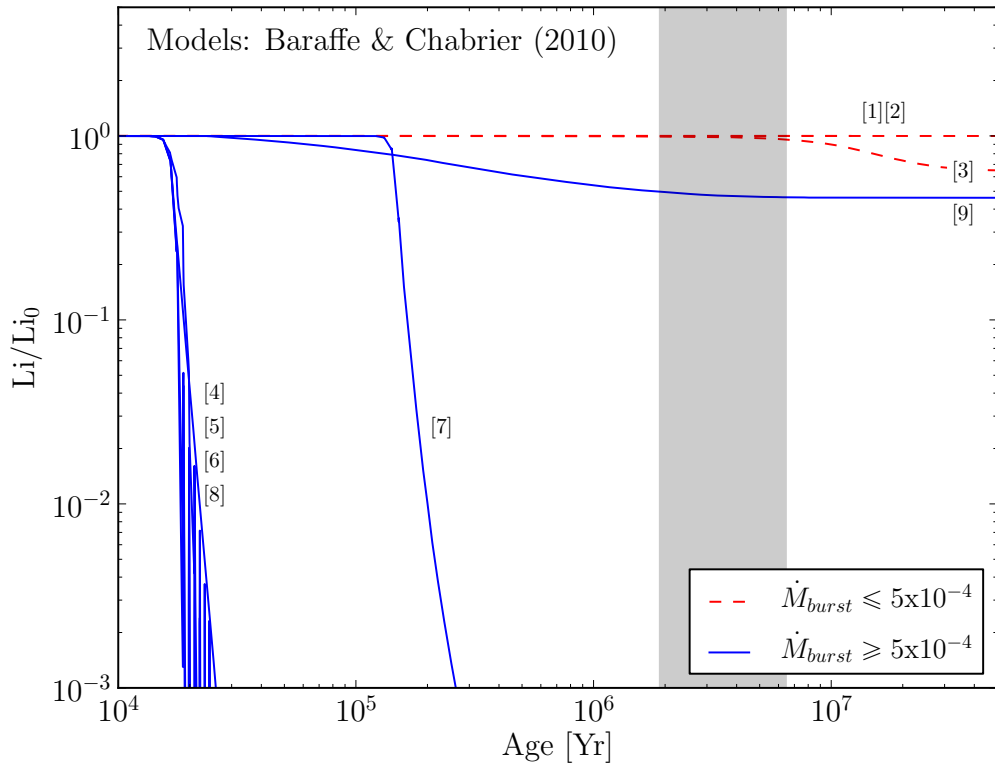


Figure 2.9: Evolution of the surface lithium abundance divided by initial Li abundance for a selection of models producing stars in the range $0.7 - 1 \text{ M}_{\odot}$ (from Baraffe & Chabrier 2010). Solid lines (blue) are those using accretion burst rates $\dot{M} = 5 \times 10^{-4} \text{ M}_{\odot} \text{ yr}^{-1}$. Dashed (red) lines are those using $\dot{M} = 1 \times 10^{-4} \text{ M}_{\odot} \text{ yr}^{-1}$. For model details see Table 3. Shaded grey region encompasses age estimates for the clusters in this study.

King (1998) finds that lithium abundance is indistinguishable from meteoritic values in a sample of 12 stars of spectral type range G0V to K3V in NGC 2264. The 3 stars closest in spectral type to my sample (K3V) exhibit EW[Li] ranging from 0.49 - 0.75 Å, which falls firmly within the range observed in my data.

Below the mass range that I explore, Palla et al. (2007) present lithium measurements for 4 objects of $M_{\star} < 0.3 M_{\odot}$. Their EW[Li] measurements range between 0.3 – 0.44 Å, implying lithium depletion of 1 to 2 orders of magnitude, and ages of 15-30 Myr according to non-accreting models. Objects as old as this in the mass range I explore would exhibit levels of lithium far below that which I observe.

2.5.4 Isochronally old stars

In Section 2.2 I described the selection of seven stars that appear faint with respect to the ONC cluster CMD and referred to these as the LLG. These stars could be interpreted as being older than the bulk of the population if their CMD position was considered a reliable diagnostic of age. However, four of these stars were shown in Section 2.4 to be non-members based on their RV. Of the remaining three, two lie below the 10 Myr isochrone and one lies below the 100 Myr isochrone. Whilst in CMD space these objects appear old, their measured EW[Li] and veiling ratio are entirely consistent with the other apparently younger measured stars in the cluster. If the apparently oldest star has an age that is genuinely > 100 Myr, then I would expect its EW[Li] to have depleted by approximately two thirds, which I do not see. Thus the lithium age and CMD age are in conflict. I now discuss these three stars, reconcile their photometric and EW[Li] properties and show that none are likely to be genuinely ‘old’ compared with the rest of the cluster.

H676. In CMD space, this star is apparently far older than the rest of the cluster with an isochronal age of > 100 Myr. *Hubble* Space Telescope (HST) images (Smith et al. 2005) reveal an edge-on massive flared disc and accompanying Herbig-Haro jet. Its exhibited low luminosity appears to be a function of disc extinction due to the geometry of the system. It is clear from studies by Walker et al. (2004) and Mayne & Harries (2010) that circumstellar disc and accretion structures associated with young PMS stars can have a significant impact on the position of an object in CMD space. The disc is a clear indicator of youth and thus the age of the object should be considered consistent with its EW[Li] age of < 10 Myr.

H198. This object sits below the 10 Myr isochrone in the CMD and yet has an unveiled EW[Li] of 0.57 ± 0.03 Å, which is consistent with a star that is undepleted in lithium. HST imagery (Bally et al. 2000) reveals a resolved proto-planetary disc, visible in $H\alpha$ emission. It also exhibits strong evidence of interaction with a fast wind and strong UV flux from the star Θ^1 Ori C. This is evident from the strong bow shock where the T Tauri wind interacts with the wind from the O-star. The intense UV irradiation may cause the disc to be heated, increase in thickness and photo-ablate (Johnstone et al. 1998). An inflated disc and downstream flow of dusty ablating material may be obscuring the central star and decreasing its

apparent luminosity.

- H6.** This object also sits below the 10 Myr isochrone in the CMD and has an unveiled EW[Li] which is consistent with a star that is undepleted in lithium. It is found to be highly extinguished in photometry by both Hillenbrand (1997) and Da Rio et al. (2009). A_V values are 3.96 and 5.30 respectively, measured at the two epochs which are separated by over a decade. Infrared colour indices $(J - H) = 1.32$ and $(J - K) = 2.12$ also indicate strong reddening, suggesting that this object is deeply embedded within its envelope or within the OMC1 molecular cloud. When subject to dereddening and extinction correction by Hillenbrand (1997), it appears that the luminosity may be underestimated. Dereddening vectors typically lie almost parallel to the PMS in M_V vs. $(V - I_c)$ if the ratio of total to selective extinction is the typical interstellar value of $R_V \approx 3.1$ (Bessell et al. 1998). In Chapter 6 of this thesis, I show that dust within the inner disc of YSOs in the ONC exhibits $5 < R_V < 8$. A higher value of R_V steepens the reddening vector in M_V vs. $(V - I_c)_0$. Thus for a given correction in $(V - I_c)_0$, a greater value of R_V would give an intrinsically brighter star once corrected for extinction.

2.6 Summary

I have performed a spectral analysis of two young clusters, NGC 2264 and the Orion Nebula Cluster around the 6708Å lithium doublet at a resolution of $R \sim 10\,000$. Correction has been made for accretion veiling, yielding estimates of the EW of the lithium line for 94 stars (76 single and 18 binary) in the ONC field and 74 stars (54 single and 20 binary) in the NGC 2264 field. Comparison has been made between measured EW[Li] and theory. I draw the following conclusions from my analysis.

1. No evidence is found in 168 stars (130 unveiled stars and 38 spectroscopic binaries with lower limits) for objects with $\text{EW}[\text{Li}] < 0.4 \text{ \AA}$. This finding is consistent with that of King (1998) for 12 stars in NGC 2264 and 82 stars in the ONC of Palla et al. (2005), but I have now almost tripled the available sample. The 262 stars now observed in the two clusters place limits on cold accretion models, indicating that burst accretion rates of $\dot{M} \geq 5 \times 10^{-4} M_\odot \text{ yr}^{-1}$ occur in less than 0.5 per cent of $0.3 \leq M_\star \leq 1.9 M_\odot$ stars. This mass accretion rate can only be exceeded without depleting lithium if the initial core mass is $> 0.03 M_\odot$, however such models seem incapable of producing the luminosity dispersion seen in CMDs. This initial core mass is also at least an order of magnitude larger than predicted by theory (see Baraffe et al. 2012, and references therein).
2. Approximately 10 per cent depletion in EW[Li] is seen between the brighter and fainter populations in both clusters and the depletion appears to be broadly independent of mass. This could be due to an age spread if the convective mixing length parameter (α) is close to

1.9. The scatter in age implied by the scatter in EW[Li] is similar to the small age spread implied by the scatter in CMD position. If α is closer to 1.0 then a large age spread (> 10 Myr) is inconsistent with my observations and another explanation must be sought. The spread in EW[Li] is also consistent with the accelerated evolution of stellar radius and lithium abundance described by models of past cold accretion at rates of $\dot{M} < 5 \times 10^{-4} M_{\odot} \text{ yr}^{-1}$. I cannot tell which of the above scenarios are preferred as the data and models do not allow me to distinguish between the age spread and accretion mechanisms.

3. I targeted seven previously identified members in the ONC whose position in the CMD indicated they may be old. Four turned out to be radial velocity non-members. The other three objects exhibit EW[Li] consistent with very young stars but are also found to be directly associated with circumstellar discs or strong extinction. Whilst in each case I cannot be sure that these features are the reason for the discrepant luminosity, it adds weight to the idea that discs and extinction contribute to the observed luminosity dispersion in PMS CMDs. No correlation is apparent between extinction corrected V magnitudes and derived A_V across the population as a whole.
4. The median accretion veiling found for single stars in the ONC ($r_{\lambda} = 0.24$) is greater than than seen in NGC 2264 ($r_{\lambda} = 0.13$). In addition, the ONC displays 9 highly veiled objects ($r_{\lambda} > 1$) whereas none are seen in NGC 2264. The highest veiling ratio seen in the ONC is 4.0 and in NGC 2264 is 1.0.
5. When establishing membership lists for young clusters (< 10 Myr), lithium detection is a necessary requisite for membership confirmation in the mass range $0.3 \leq M_{\star} \leq 1.9 M_{\odot}$. If lithium is not detected, a star must have less than 0.5 per cent chance of being a young cluster star.

Chapter 3

Characterising YSO variability

3.1 Introduction

Photometric variability on a wide variety of timescales is a key characteristic of YSOs. Joy (1945) observed brightness fluctuations in emission line objects near molecular clouds. Since then, YSO variability has been associated with many physical processes operating at the stellar surface, in its nearby environment and within the orbiting circumstellar disc. The amplitudes, timescales and wavelength dependence of the variability are important clues to understanding the underlying physics, and are therefore key to the study of young stars.

Until recently, most work on young star variability has concentrated on searches for periodicity (e.g. Herbst et al. 2002; Lamm et al. 2004; Rebull et al. 2006; Littlefair et al. 2010), typically using frequency analysis to identify dominant periods.(e.g. Lomb 1976; Scargle 1982). Most authors draw conclusions based on the assumption that the observed periodic signal reflects the rotation period of the star. Roughly one-third of YSOs appear to exhibit behaviour that is broadly periodic. Herbst et al. (2002) found 25-40% of stars in the ONC to offer convincing periods, Littlefair et al. (2010) found 25-30% in Cep OB3b. Periodic variability is often attributed to the presence of cool (e.g. Bouvier et al. 1986b) or hot (e.g. Kenyon et al. 1994) spots on the surface of the rotating star. In addition, many stars exhibit quasi-periodic lightcurve behaviour (e.g. Bouvier et al. 2003; Cody et al. 2014). Alencar et al. (2010) find that $28 \pm 6\%$ of stars monitored in NGC 2264 using the *CoRoT* spacecraft exhibit quasi-periodic fading behaviour.

This leaves roughly half to two-thirds of the variable stars in star-forming regions without well-defined periods, and this aperiodic variability may provide a window on different physical phenomena to those associated with periodic variability. Aperiodic variability has often been noted and catalogued but until recently has been relatively uninterpreted within the YSO literature. Many stars slip between periodic and aperiodic variability at different epochs (Herbst et al. 1994; Rucinski et al. 2008). Aperiodic or quasi-periodic variability in YSOs has been attributed to a number of mechanisms, including obscuration by circumstellar material (Herbst et al. 1994; Chelli et al. 1999; Alencar et al. 2010), accretion shock instability (Sacco et al. 2008; Matsakos et al. 2013), unsteady accretion (Fernandez & Eiroa 1996; Scholz et al. 2009; Stauffer et al. 2014; Venuti et al. 2014) and instabilities within the circumstellar disc (Bouvier et al. 2007; Romanova et al. 2008, 2011).

It is important to distinguish between phenomena that occur on different timescales. Many studies to-date have concentrated on timescales of days to a few years (e.g. Bouvier et al. 1993; Herbst et al. 1994; Grankin et al. 2007; Wolk et al. 2013). However there is significant evidence that we should see important variability on a much wider range of timescales. For example Sacco et al. (2008) and Matsakos et al. (2013) propose that accretion shock instabilities at the surface of the star may show variability on timescales of minutes. In contrast, long-term outbursting behaviour such as that seen in EXor (Herbig 2007, 2008) and FUor (Reipurth 1990) stars may support models of accretion rate variability that is predicted to occur on timescales of years to thousands of years (e.g. Vorobyov & Basu 2005; D’Angelo & Spruit 2012). Thus, several important questions concerning YSO variability are outstanding.

- What is the full range of timescales on which we observe YSO variability?
- Can we quantitatively characterise the aperiodic-variability more robustly?
- What range of variability amplitudes do we see as a function of timescale?

I have compiled a set of *SDSS-i* (hereafter ‘*i*’) photometric observations for ≈ 1100 YSOs in the young OB association Cep OB3b. The observations are all made using the Wide Field Camera (WFC) on the 2.5m *Issac Newton* telescope (INT) and provide well-sampled monitoring with a cadence ranging from 1 minute to 10 years (a dynamic range of ≈ 7 dex). This unique dataset provides variability monitoring data that is capable of providing useful statistics on variability events occurring with duty cycles of up to ≈ 10000 years and allows us to begin to answer the questions outlined above.

3.2 Data

The time-series photometric measurements have been compiled using data from several observing campaigns, performed between 2004 and 2013. The subject is Cep OB3b which is an OB association containing more than 3000 X-ray and infrared identified PMS stars (Allen et al. 2012). It is similar in membership and overall size to the ONC, however Cep OB3b appears older and more evolved. Bell et al. (2013) assigns Cep OB3b an age of ≈ 6 Myr (similar to σ Ori and IC 348) and distance of 570 ± 20 pc. Allen et al. (2012) measure an average disk fraction in the region as $33 \pm 2\%$. The CMD for the association is shown in Fig. 3.1.

3.2.1 Observations

I used INT photometry taken with the Wide-Field Camera (WFC) which consists of four EEV 2k x 4k CCDs, providing a 34×34 arcmin² field of view. The CCDs are arranged in an ‘L’ shape with a small square region missing from the top-right corner and small gaps between CCDs. The image scale is $0.33''$ per pixel. A single field was observed centred on $\alpha = 22^{\text{h}} 55^{\text{m}} 43^{\text{s}}.3, \delta = +62^{\text{d}} 40^{\text{m}} 13^{\text{s}}$ J2000.0, this region is shown in Fig. 3.2.

The observations were made at several different epochs by different observers. A summary of the observations are shown in Table 3.1. Observations made during 2004 Sep 21- Oct 6 were a

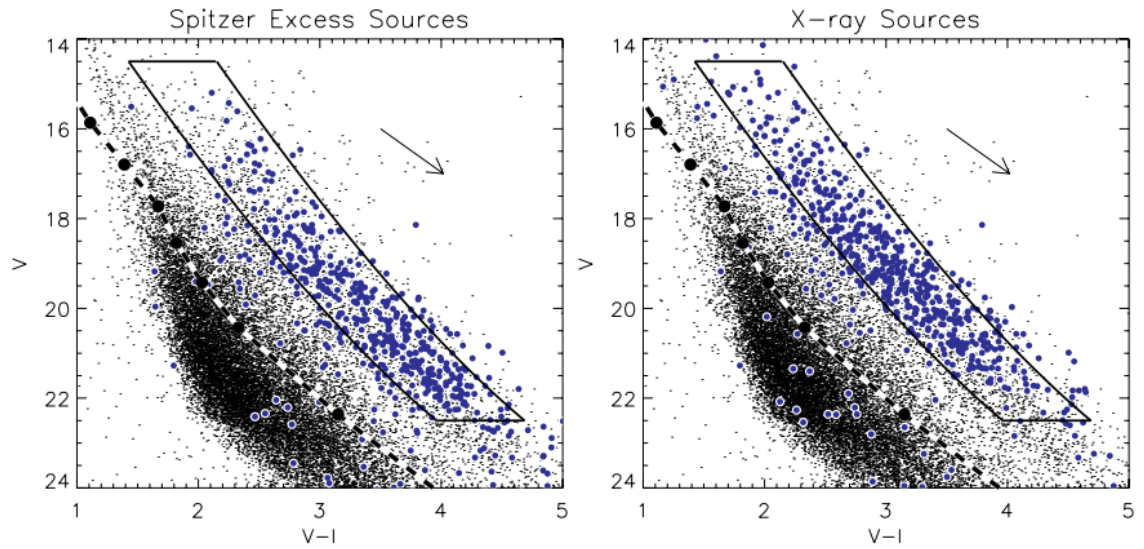


Figure 3.1: $V, V-I$ CMD of Cep OB3b. The black dots are all sources in the Cep OB3b field. The blue dots are sources classified as pre-MS using *Spitzer* infrared colours (left panel) and detection in X-rays (right panel). The dashed white and black line is the ZAMS of Siess et al. (2000) and the region defined by the black curve represents the PMS locus. The black arrow corresponds to 1 mag of extinction using the reddening law of Rieke & Lebofsky (1985). Credit: Allen et al. (2012).

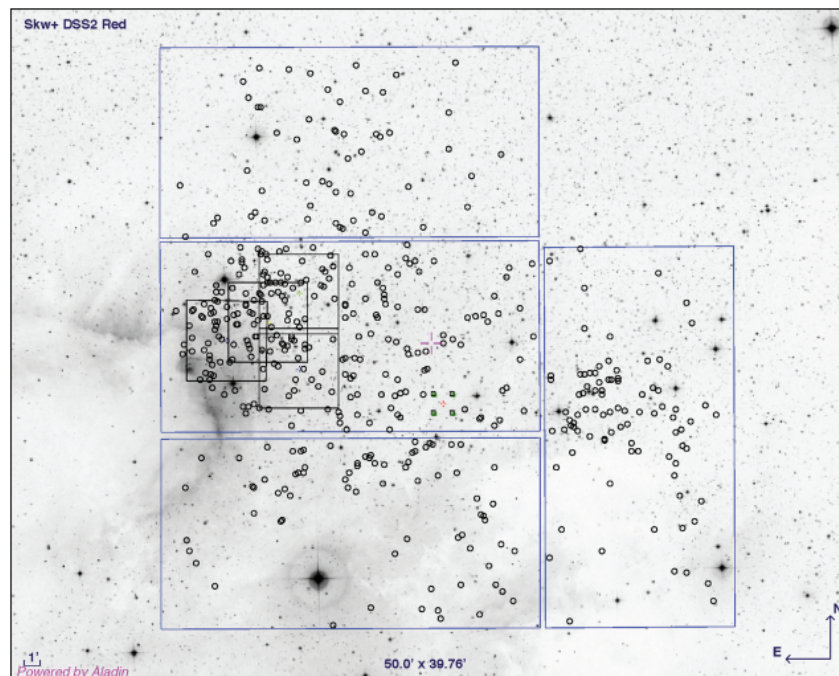


Figure 3.2: INT WFC field-of-view (blue lines) overlaid on a Digitized Sky Survey red image of Cep OB3b. Circles denote the locations of periodic association members. The black boxes denote the field-of-view of observations made using the Faulkes telescope that were not used in this study. Credit: Littlefair et al. (2010).

Table 3.1: Summary of observations made and collated as part of this study.

Date	Number of observations	Filter	Exposure time	Publication reference Publication reference
2004 Sep 21- Oct 6	617	<i>i</i>	300s	Littlefair et al. (2010)
2005 Aug 23 - Nov 1	41	<i>i</i>	300s	Littlefair et al. (2010)
2007 Oct 21 - 24	5	<i>i</i>	100-500s	Bell et al. (2013)
2013 Nov 9 - 10	175	<i>i</i>	30s	-

time series taken throughout the 16 nights with a cadence of ≈ 8 minutes. Some breaks occurred due to poor weather, however observations were made for at least 2 hours on most nights. Observations made between 2005 Aug 23 - Nov 1 typically consisted of one or two exposures per night. Some nights in this period were missed due to weather or telescope scheduling constraints. Full details of the observing campaigns for these two runs are given by Littlefair et al. (2010). Stuart Littlefair provided the reduced lightcurves and photometric catalogues for all stars within the field of view. The observations made on 2007 Oct 21 - 24 also consisted of one or two exposures per night. Full details of these observations and subsequent reduction are given in Bell et al. (2012) and Bell et al. (2013). Cameron Bell again provided the reduced lightcurves and photometric catalogues for all stars within the field of view.

The final set of observations were taken specifically for this study. I performed the observations on 2013 Nov 9 - 10 and they consisted of 174 observations taken in two approximately 90 minute blocks (one on each night) with a cadence of ≈ 1 minute. Conditions during the night of Nov 9 were clear but with some patchy cirrus. Frames that required a correction for changes in atmospheric transparency greater than 0.1 mag have been rejected. The seeing ranged from 1.6 to 3.0 arcsec with a median seeing of 2.0 arcsec. The night of Nov 10 was photometric, the seeing ranged from 0.9 to 1.3 arcsec with a median of 1.1 arcsec. Fig. 3.3 shows the seeing and transparency for the observations on these two nights and highlights the quality cuts in seeing and transparency made during the reduction process.

3.2.2 Reduction

The reduction details in this section are for the dataset collected in 2013 November. They are however almost identical to those for the other datasets. Specific details for the reduction of the 2004, 2005 and 2007 datasets are detailed in Littlefair et al. (2010) and Bell et al. (2012) respectively.

WFC frames were first bias subtracted using a median stack of bias frames. To mitigate for non-linearity in the response of the CCDs, linearity tests were performed by comparing counts in the vignetted corner of CCD 3 with the rest of the mosaic. As the corner is vignetted, its count values are much lower than the rest of the CCDs and can provide a linear reference level from which non-linearity at high counts on the other regions of the detector may be measured. The derived CCD dependent non-linearity corrections were then applied to the data before further processing.

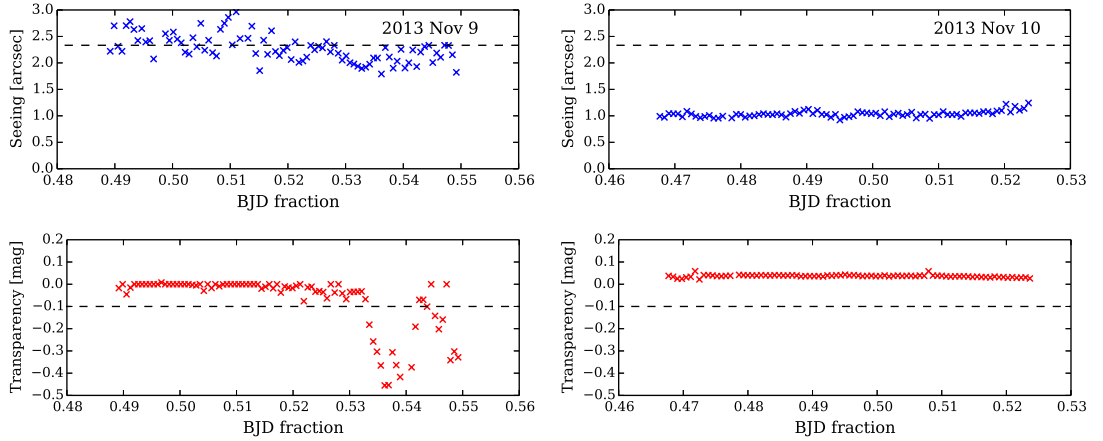


Figure 3.3: Seeing and transparency plots for the observations made in 2013 Nov. Top panels show seeing conditions on the night of Nov 9 (left) and Nov 10 (right). Lower panels show the relative transparency on Nov 9 (left) and Nov 10 (right). The horizontal dashed lines show cuts made in seeing and transparency to reject the poorest data.

Twilight flat frames were constructed using frames taken during bright sky conditions, with detector count levels between 30 000 and 40 000. Application of the flat frames allowed pixel-to-pixel sensitivity variations and vignetting effects to be corrected. A bad pixel mask constructed by Littlefair et al (2010) was used. De-fringing was performed by scaling library fringe frames to match the amplitude of the fringes in the target exposures.

The data were analyzed using the `CLUSTER` software package described in detail by Naylor et al. (2002), Burningham et al. (2003) and Jeffries et al. (2004). Star positions were measured from a stack of 10 frames with seeing < 1 arcsec, airmass < 1.4 and good transparency.

Optimal photometry was performed, fixed on the measured positions, providing a flux for each object in each frame. The fluxes were then ‘profile corrected’ (analogous to an aperture correction in aperture photometry) using a spatially varying polynomial function, calculated using bright unsaturated stars. The photometric measurements were then adjusted for any difference in the airmass and transparency for each frame, by determining a relative transparency correction from an ensemble of bright stars which showed no evidence of variability in a chi-squared (χ^2) test. An additional statistical uncertainty (0.013 and 0.007mag on Nov 09 and Nov 10 respectively) was added to each measurement at this stage to ensure that the distribution of χ^2 for all stars was independent of signal-to-noise ratio. This uncertainty reflects uncertainties in the flat-fields and profile corrections. Positions from the Two Micron All Sky Survey (2MASS; Cutri et al. 2003) were used to provide an astrometric solution with a precision ≈ 0.1 arcsec. Lightcurves were constructed in each dataset by collating all reduced measurements for each star. An example set of lightcurves for one star is shown in Fig. 3.4. The lightcurves from the four individual datasets were merged to create a single lightcurve for each star. Each star had different identification number in each of the individual datasets, so cross matching was performed on an astrometric coordinate basis to guard against mis-matches. The final identification numbers assigned to each star were those from Littlefair et al. (2010). Typically each star has ≈ 840 points in its final lightcurve.

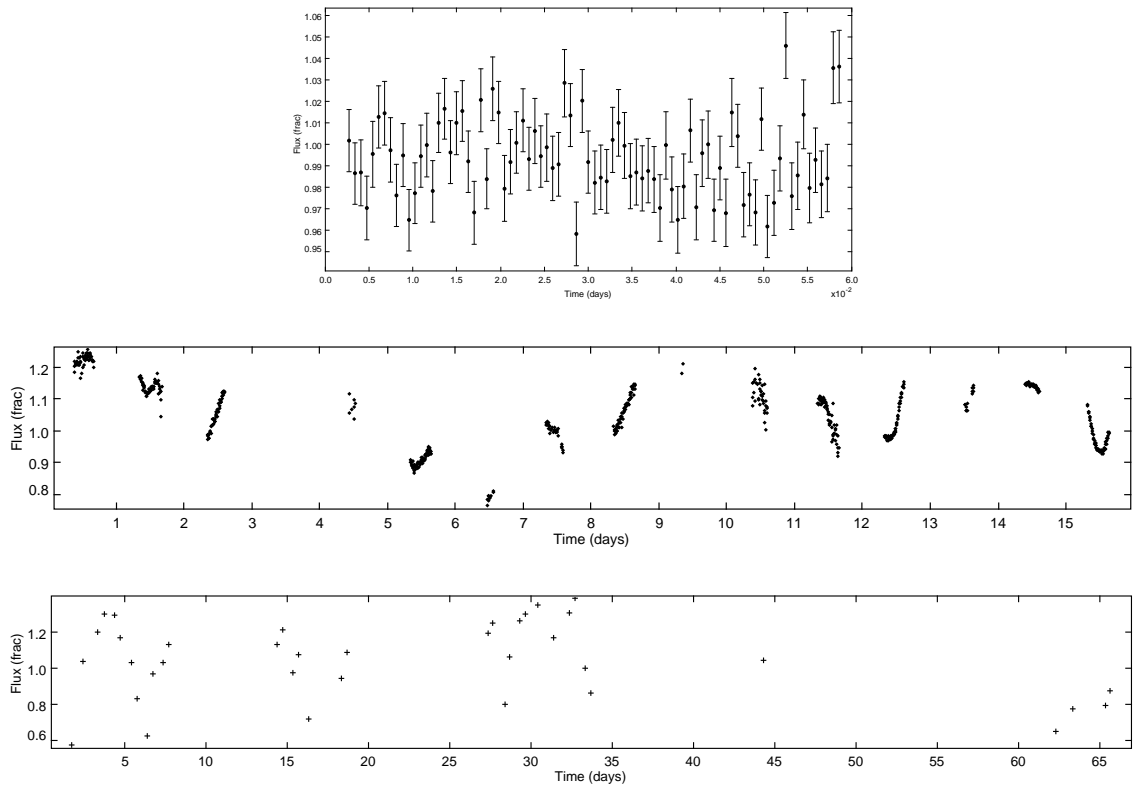


Figure 3.4: Examples of subsets of INT WFC *i* lightcurve data collected for a single disc-bearing source in Cep OB3b. The top panel shows data collected at a cadence of 1 minute on a single night in 2013 November. The middle panel is data collected over 16 nights in 2004 September. The lower panel is data collected over a period of 68 nights in 2005 August to November. Additional data was also collected in 2007 October.

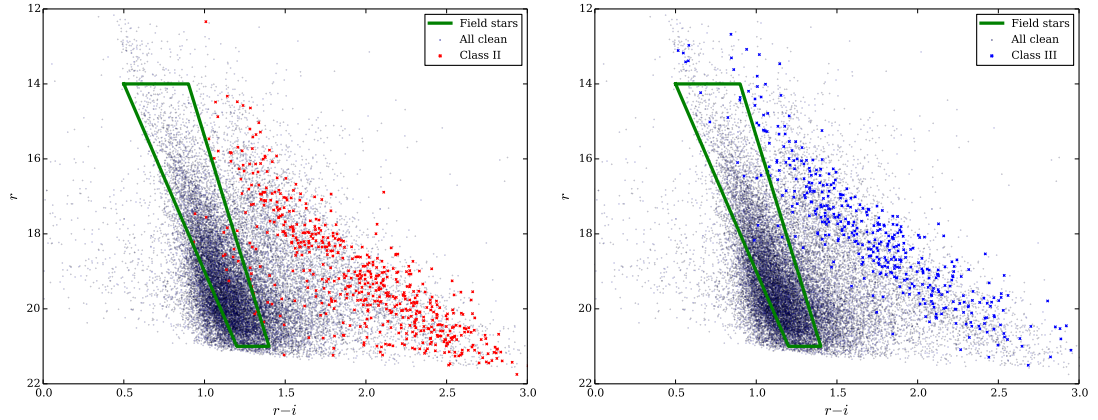


Figure 3.5: $r, r-i$ CMDs showing the classification of sources in Cep OB3b. The left panel shows the disc-bearing sample (red crosses) overlaid on the photometry for all stars (black dots). The PMS locus is clearly visible, offset from the field stars. The right panel shows the X-ray identified discless sources (blue crosses) on the same CMD. The green box bounds the region from which the ‘Field’ population was selected. The region was selected to be wider in colour at brighter magnitudes to reduce the numerical bias toward fainter stars

3.3 Analysis

3.3.1 Source classification

Sources in the i band catalogue were cross matched against the catalogue of Allen et al. (2012) using a matching radius of 1 arcsec. The sample was then divided into three subgroups. The first two subgroups contained stars which Allen et al. (2012) classified using *Spitzer* colours and X-ray fluxes as Class II and Class III YSOs respectively. Importantly, for Class III objects to be included within the sample they had to show increased X-ray flux compared with the main-sequence or post-main-sequence populations of similar optical colours. This minimised contamination from foreground dwarfs or background giants and ensured that the statistics were not significantly biased by inclusion of many non-PMS stars. A final subgroup was defined from stars that were not identified as YSOs and that fell within a defined region of the $r, r-i$ CMD that is well below the identified PMS locus (see Fig. 3.5). This final subgroup is ‘Field’ stars which as an ensemble should exhibit low intrinsic photometric variability. This control group allows precise measurement of the noise at all epochs and allows the robust combination of data-sets which have been collected many years apart. As outlined in Section 1.3.3, The Class II sample will be described as the ‘disc-bearing’ sample and the Class III sample will be called the ‘discless’ sample. 758 stars were identified in the disc-bearing sample, 448 in the discless sample and 6614 stars were found in the ‘Field’ sample.

3.3.2 Characterising the lightcurve variability

Characterising aperiodic variability is a challenge for statistical techniques. Lomb-Scargle periodograms are successful in characterising the presence of periodic components in lightcurves, however they are ineffective in analysing aperiodic signals. No standard metric analogous to the

periodogram exists for characterising aperiodic signals. Autocorrelation functions are a useful tool for finding repeating patterns in signals and may be of use in systems where cyclical physical behaviour occurs. However, they require that the sampling is regular and uninterrupted, a situation that is very rarely achievable in astronomical data-sets. A tool that is useful for studying aperiodic signals is the Structure Function (Simonetti et al. 1985; Hughes et al. 1992; de Vries et al. 2003).

Structure functions - Theory

Structure functions (SF) are a method of measuring the time dependence of both periodic and aperiodic variability in a lightcurve that is relatively insensitive to sampling cadence and aliasing. This makes it particularly useful in analysing data such as YSO lightcurves, where the sampling is by necessity discrete, sometimes sparse and on a wide variety of cadence scales. Structure functions provide an effective tool for quantifying aperiodic variability power spectra. Upper and lower limits on the timescales of physical phenomena within the system may be determined, providing the amplitude of the variability is at least comparable to the photometric uncertainties. Another useful feature is that variability resulting from systematic errors in the data (for instance photometric zero-point errors in observations made at different epochs) may be removed from the target SF by characterising the structure function of a sample on non-varying stars in the field and subtracting that structure function from that of the target (e.g de Vries et al. 2003).

The SF adopted here provides a measure of root-mean-squared (rms) variability as a function of sampling timescale. I calculate the SF in discrete logarithmically spaced time-lag bins by first taking all $N(\tau_1, \tau_2)$ data points in a given bin, where

$$\tau_1 < \tau_i - \tau_j < \tau_2. \quad (3.1)$$

τ_1 and τ_2 are the lower and upper timescale limits for each bin. The SF is then calculated in each bin as

$$S(\tau = \tau_1 \rightarrow \tau_2) = \left(\frac{1}{N(\tau_1, \tau_2)} \sum [f_i - f_j]^2 \right)^{\frac{1}{2}}. \quad (3.2)$$

The summation is made for $N(\tau_1, \tau_2)$ pairs of data points, each with a time separation $\tau = \tau_i - \tau_j$, $\tau > 0$ so that each pair of points is measured only once. The uncertainty is calculated as the standard deviation of the measurements in each bin divided by \sqrt{N} . The resulting SF provides a method for assessing the power spectrum of the variability, however in contrast with Fourier techniques it has the advantage that it is calculated in the time domain, and thus the dependence on the sampling is much reduced. Gaps in the sampling have little impact on the SF, as long as a statistically meaningful number of time differences exist within a each bin. It also has the advantage that it is sensitive to all variability, unlike a Fourier analysis which is preferentially sensitive to periodic signals.

SFs have been widely used in the study of active galactic nuclei, where stochastic lightcurves (similar to those often seen in YSOs) are common (e.g. Kawaguchi et al. 1998; Hawkins 2002; de Vries et al. 2003; Wilhite et al. 2008; MacLeod et al. 2012). Fig. 3.6 shows an ideal structure

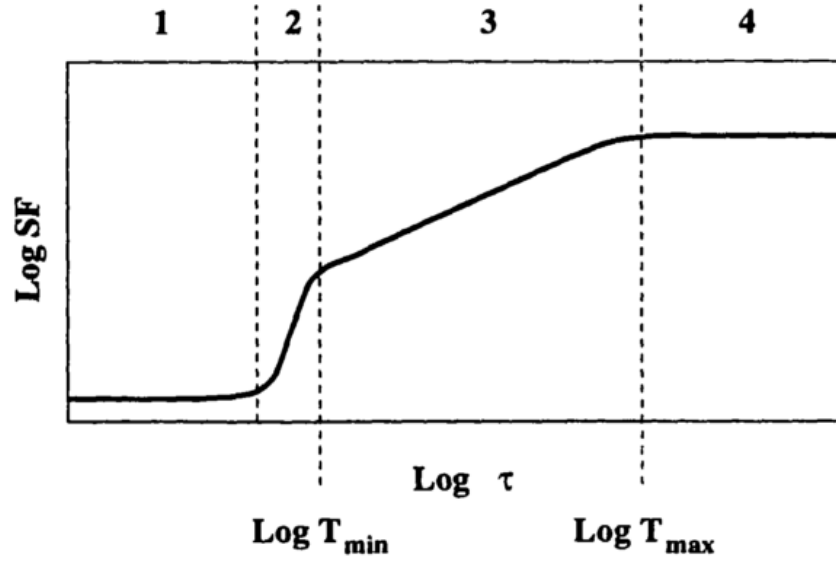


Figure 3.6: An Ideal structure function, illustrating the main regimes. (See text for detail). Credit: Paltani (1999)

function and highlights the four main regimes that can be identified.

Region 1 is at a timescale where any intrinsic variability within the lightcurve is much smaller than the measurement uncertainties on the data points. This region provides an independent estimate of the short-timescale photometric uncertainty.

Region 2 sees the SF rise above the uncertainty level, increasing as τ^2 while $\tau \ll t_{min}$, the minimum timescale on which the target lightcurve exhibits real variability.

Region 3 sees the SF increase, but less steeply than τ^2 . The gradient is determined by the variability power spectrum exhibited by the target. It is possible to see plateaux in this region if the variability power spectrum contains discreet low and high frequency components.

Region 4 is beyond t_{max} , the point at which the variability power spectrum tends to zero. i.e. at timescales longer than t_{max} , no additional intrinsic variability, beyond that seen on shorter timescales is present.

Fig. 3.7 shows an example structure function for BL-Lac object PKS 2155-304.

3.3.3 Constructing the structure functions for YSOs in Cep OB3b

Structure functions were created for each star with logarithmically spaced time-lag bins in the range 0.0005 to 3796 days (≈ 45 seconds to ≈ 10.4 years). Each bin has an upper limit that is 1.5 times greater than that of the previous bin. Importantly, the structure functions calculated for the very shortest time-lag bins ($\tau < 5$ min) were constructed only using data from the night of 2013 Nov 10. While the data from the night of 2013 Nov 9 was sampled at a high enough cadence to contribute to these bins, the relatively poor observing conditions added significantly to

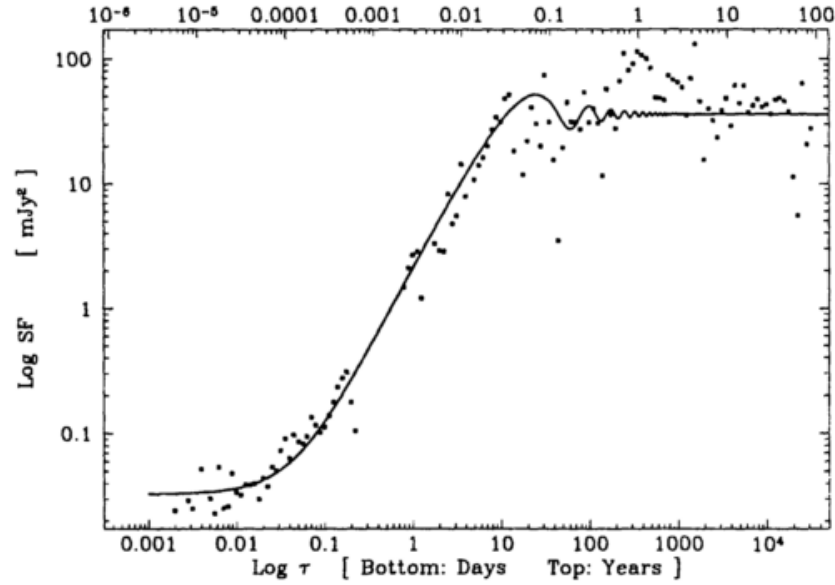


Figure 3.7: The structure function for BL-Lac object PKS 2155-304. The solid line is a fitted model of a power-law-shaped PSD. Credit: Paltani (1999)

the uncertainty on those measurements. As the shortest time lag bins are intrinsically measuring the smallest variability amplitudes, only using the highest quality photometry will increase the sensitivity of the experiment to any low amplitude variability present. The data from 2013 Nov 9 were of sufficient quality to contribute to the calculation of SFs on multi-year timescales.

The SF points for the longest timescales (> 1 year) were constructed by combing the datasets taken by different observers at different epochs. Great care was taken to ensure that variability was not introduced through calibration and zero point errors between observations made so far apart in time. A comparison was made between the mean fluxes of the individual field stars in each reduction. A multiplicative correction was made on a CCD by CCD basis to each data-set so that the mean flux across the field star population was constant across all epochs and agreed with the fluxes measured by Bell et al. (2013). Once these bulk ‘flux zero point’ corrections had been made, the residual systematic flux discrepancies were at a level $< \text{few}\%$ and are probably due to a combination of scattered light within the flat fields and discrepancies in the profile correction polynomials at the extreme corners of the field (see Fig. 3.8). A systematic at this level is far below any significance threshold for studying long-term ($> \text{years}$) variability, thus it was considered acceptable.

Modelling and subtraction of non-stellar variability

The structure functions for the YSOs were corrected for variability resulting from processes unrelated to the stellar variability through analysis of the field star population. Structure functions were calculated for > 5000 ‘field’ stars over the field of view. This large sample allowed the creation of an analytical model of the noise on each SF measurement. Once the non-stellar signal was quantified it was subtracted from the SF for each YSO, leaving a SF that represents only the

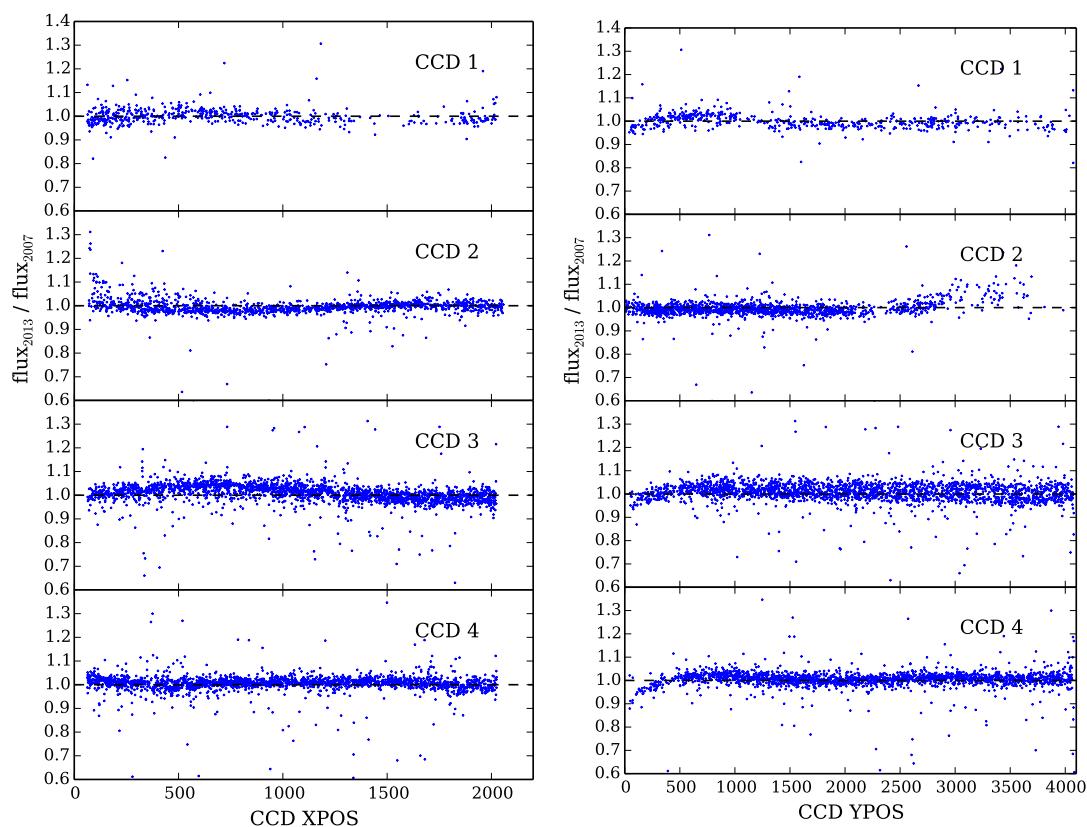


Figure 3.8: A comparison of mean fluxes measured for individual field stars in data collected on 2013 Nov 10 and 2007 Oct 21 - 24. The data for 2013 Nov 10 have been corrected with a single scaling factor (of $\approx 10\%$) for each CCD, bringing the fluxes for all field stars into agreement within better than a few percent across the majority of the field. The left panel shows flux residuals as a function of x-position on each CCD. The right panel shows the same as a function of y-position.

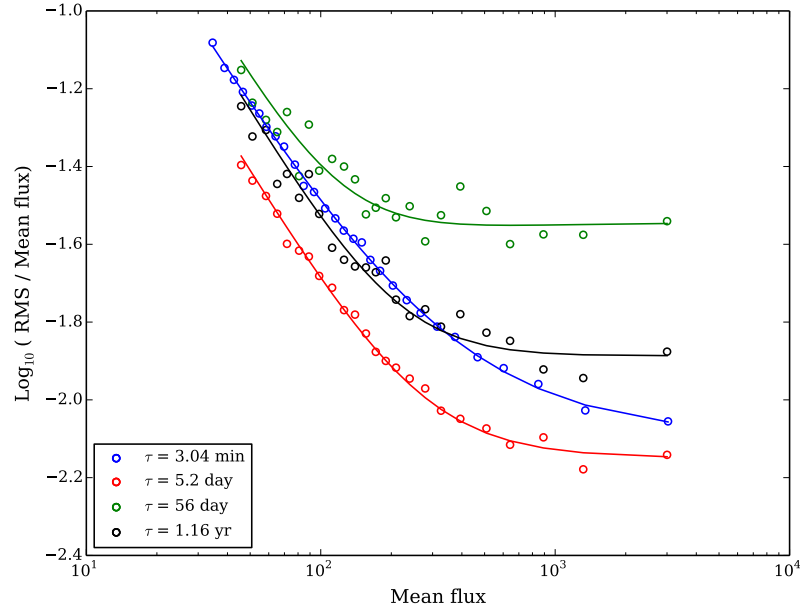


Figure 3.9: Example noise model for field stars on CCD 2. Each point represents a slice of 51 stars in a given SF time-lag bin. The x-axis shows the mean flux for the stars in each slice. The y-axis is the (\log_{10}) mean fractional variability for all of the stars in that flux bin. The circles are the measured values, the lines are the best-fit analytical model described by Equation 3.3. The different colours represent different time-lags, calculated as part of the structure functions. Each CCD and time-lag have their own defined analytical coefficients that allow precise subtraction of non-astrophysical contributions to stellar variability.

intrinsic stellar variability signal.

To do this, the structure functions for the field stars on each CCD were ordered by mean flux and then sliced into groups of 51 stars. Each of these 51 star ‘magnitude slices’ then had its median SF calculated. Thus for each small magnitude slice on each CCD I had a empirical median structure function. Then, for each time-lag bin the variability as a function of flux was fitted with an analytical model of the form

$$\sigma = \sqrt{S^2 + K_1^2 f_\star + (K_2 f_\star)^2} \quad (3.3)$$

where S is the sky noise in the frame (a fitted parameter that is constant across the CCD), f_\star is the measured stellar flux and K_1 and K_2 are empirically derived constants. Examples of the empirical relations and analytical fits are shown in Fig. 3.9. Once the model was fitted, the non-astrophysical SF for each target star was precisely characterised as a function of time-lag, CCD and stellar flux. This non-astrophysical component was then subtracted. Any error within the model left a residual within the calculated intrinsic stellar SF. If the process is working effectively, the distribution of these residuals should be centred about zero, providing that the intrinsic stellar variability is negligible. It appears that on the shortest timescales ($\tau \lesssim 10$ mins) this is true. Fig. 3.10 shows the distribution of intrinsic SFs for disc-bearing stars on three timescales, all shorter than ≈ 30

min. The SF distribution (having had the systematic non-stellar component subtracted) peaks within $< 0.1\%$ of zero and has a residual scatter of approximately $\pm 0.2\%$. The peak is actually very slightly negative and this probably reflects intrinsic variability (e.g. eclipsing binaries or pulsating variables) within the field stars causing a slight over-estimation of the non-astrophysical SF. This illustrates that the systematic model subtraction appears to be both highly effective and robust. The resulting SFs allow the detection of variability that is statistically significant, at levels below the photometric noise level. Examples of the calculated SFs may be seen in Fig. 3.11 for disc-bearing stars and in Fig. 3.12 for discless stars.

It is expected that the SF should always increase as the sampling timescale increases. However, in some cases the SF is seen to reduce slightly. There are two reasons for this behaviour. Firstly, in a small fraction of stars, a difference in the short term variability at different long-term epochs means that less variability is seen on the longer timescales than shorter ones. This is real and tells us that the short-term variability that we measure can change with time. Secondly, for very regular and periodic lightcurves, an effect akin to aliasing within periodic signals is seen where the sampling timescale is close to an integer number of half periods. This effect is mitigated by the discrete bin-widths employed. Thus in a given SF we may see points with reduced RMS in a certain bin followed by an increase corresponding to this ‘aliasing’ effect.

3.4 Discussion

3.4.1 Population-level variability statistics

It is immediately clear that the SFs of almost all YSOs have an upper variability timescale (t_{\max}) that is on the order of days. It is also apparent that almost no variability (where $S(\tau) \gtrsim 0.2\%$) appears in the SFs on timescales shorter than ≈ 10 minutes. Probability distribution functions (PDFs) of the measured $S(\tau)$ were constructed by combining all of the SF measurements for all stars in a given source category. The density of points was measured by binning the individual points in $S(\tau)$ vs. τ space into bins of size 0.3 in $\log_{10} S(\tau)$. The measurements are already binned in $\log_{10} \tau$ as part of the SF measurement process. The numbers of stars in each bin were then normalised so that the sum of the probability in each $\log_{10} \tau$ column equals unity. The resulting PDFs, describing the variability behaviour of the disc-bearing and discless populations are shown in Fig. 3.13.

This basic analysis allows several important conclusions to be drawn. As expected, the disc-bearing stars show greater variability amplitude on all timescales than the discless sample. The fact the the SF PDF flattens indicates that variability saturates for all YSOs on timescales $t_{\max} >$ few days. Beyond this timescale, little (if any) extra variability is seen. At timescales $< t_{\max}$, the variability power spectrum appears linear (in log-log space) whilst above the measurement noise floor.

The PDFs suggest that the structure function, $S(\tau)$ is well modelled by

$$\begin{aligned} S(\tau) &= k\tau & \tau < t_{\max} \\ S(\tau) &= c & \tau > t_{\max} \end{aligned} \tag{3.4}$$

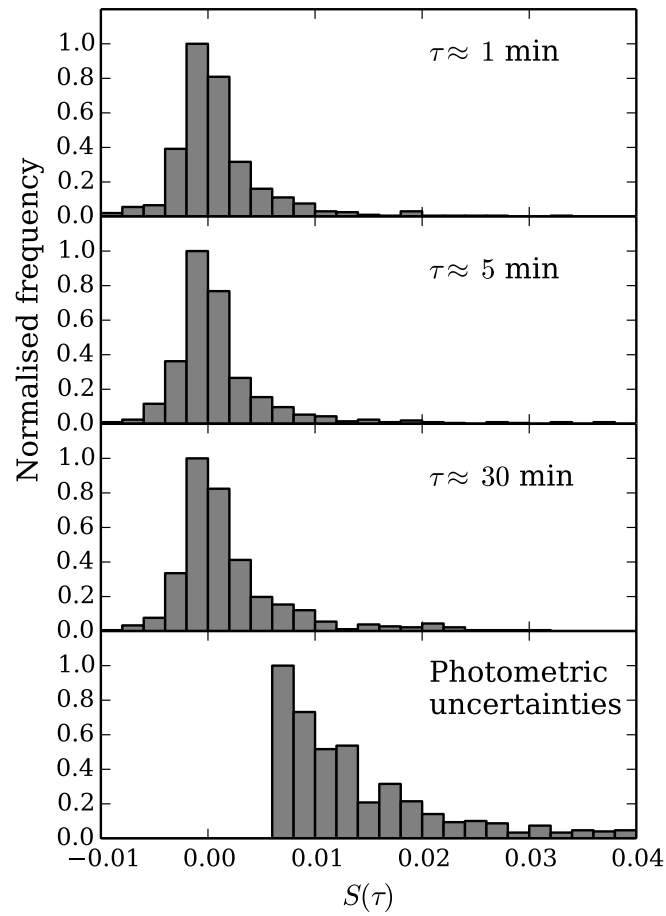


Figure 3.10: Histograms showing $S(\tau)$ on short timescales for disc-bearing stars in Cep OB3b. Note that $S(\tau)$ is on a linear scale rather than the previous log scale examples. The top three panels show the variability on timescales of ≈ 1 minute, ≈ 5 minutes and ≈ 0.5 hours respectively. The lower panel shows the mean photometric uncertainty on a single lightcurve point for the same stars.

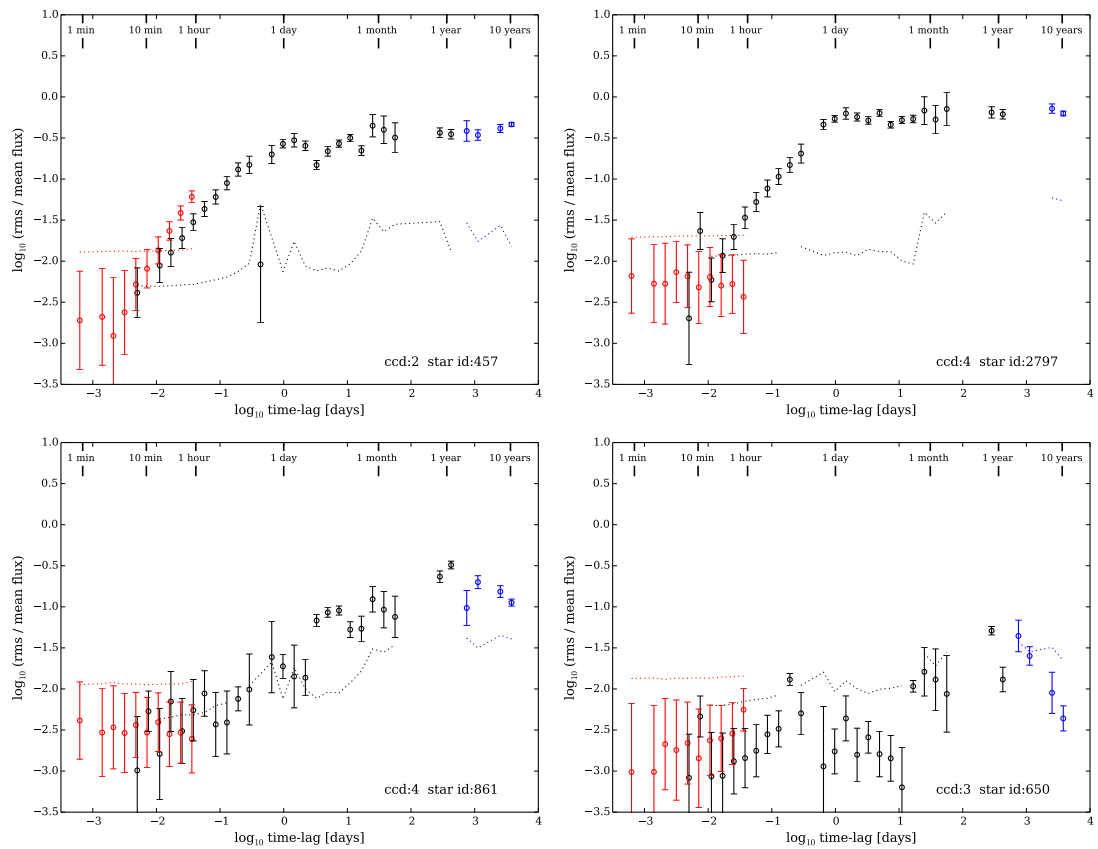


Figure 3.11: Example structure functions for disc-bearing YSOs in this analysis. A range of variability amplitudes and characteristic timescales are shown. Circles are the ‘field subtracted’ structure function for the target star. The dotted line shows the structure function for the subtracted ‘non-stellar’ variability. The red points are those which only use the high cadence data from 2013 Nov 10. The blue points are calculated using the years-timescale lightcurves.

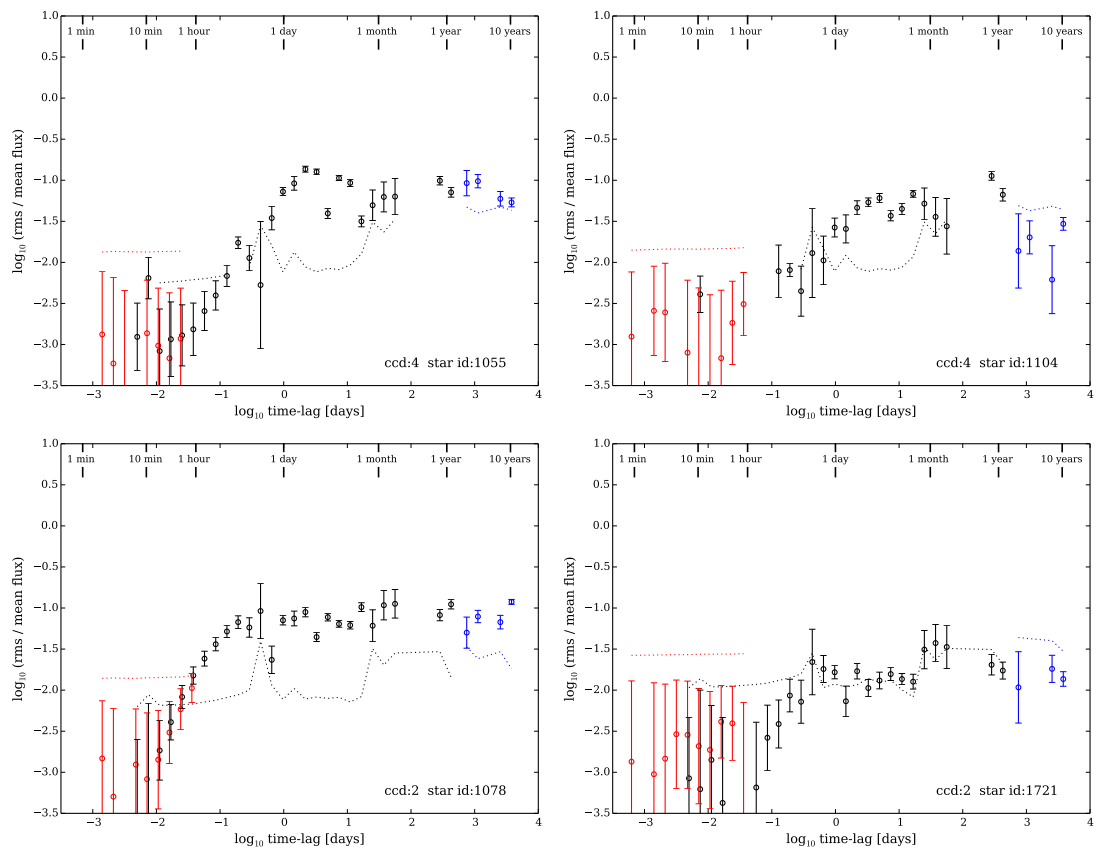


Figure 3.12: Structure functions for a selection of discless YSOs in this study. Detail as per Fig. 3.11

where k and c are constants describing the gradient and saturation level respectively. The fact that $S(\tau) = k\tau$ when $\tau < t_{\max}$ means that the intrinsic variability power spectrum is well described by a simple power law. The gradient k , becomes the exponent of the power law if we describe the amplitude of the variability as a function of frequency.

$$a \propto f^{-k} \quad (3.5)$$

where a is the amplitude of the variability and f is the frequency in cycles per day. I measured k , c and t_{\max} for each star by fitting the function described in Equation 3.4 to the individual SFs. The fitting was performed using a simple routine which minimises χ^2 . Fig. 3.14 compares histograms of the derived parameters for the disc-bearing and discless samples. The median of each of these parameters was calculated for each sample. The uncertainties on the median values were calculated by first creating a model sample of 1000 points drawn randomly from the observed distribution. The median of this sample was calculated. This process was repeated 1000 times, providing a sample of calculated medians. The standard deviation of the sample of median values was adopted to represent the uncertainty on the median for the real data sample. Table 3.2 shows the measured parameters.

Variability amplitudes

Parameter c is found to be ≈ 2.3 times larger in disc-bearing stars than discless stars. Disc-bearing stars show a median variability rms (when $\tau > t_{\max}$) of $8.3 \pm 0.3\%$. For discless stars it is $3.6 \pm 0.1\%$.

Variability timescales

The disc-bearing population is found to show a median t_{\max} that is slightly greater than that of the discless population. However, considering the overlapping uncertainties, the significance of this difference is weak. A longer t_{\max} possibly reflects the longer rotation periods typically found in disc-bearing stars. It is interesting to explore whether t_{\max} really does describe the rotational timescale of these stars. Fig 3.15 shows a comparison of t_{\max} against the rotational periods of periodic stars found by Littlefair et al. (2010). It is clear that t_{\max} correlates strongly with rotational period although the value of t_{\max} is $\sim 1/4$ of the period for any given star. If this relation between t_{\max} and rotation period holds for all stars then the similarity in the distributions of t_{\max} that is seen between periodic and non-periodic stars implies that the rotational period distribution described by periodic stars is representative of the population as a whole.

Variability power spectra

Notably, the median gradient k , where $\tau < t_{\max}$ appears to be very similar for the two populations. The power law exponent describing the variability power-spectrum for the discless stars is slightly greater than in the more-variable disc-bearing stars. Considering the different physical mechanisms at-play in the two populations, this might appear surprising. The actual values (0.85 ± 0.02 and 0.95 ± 0.03 for disc-bearing and discless respectively) are close to the value of ~ 1 found by Cody et al. (2014) in a sample of stochastically varying stars in NGC 2264. Similar behaviour was

Table 3.2: Variability parameters derived through model fitting of YSO population SF data. See section 3.4.1 for details. Note that t_{\max} has been converted to days and c is expressed as $S(\tau)$ (not $\log_{10}S(\tau)$ as shown in the plots).

Sample	t_{\max} (days)	k	c
Disc-bearing	1.50 ± 0.07	0.85 ± 0.02	0.083 ± 0.003
Discless	1.41 ± 0.10	0.95 ± 0.03	0.036 ± 0.001

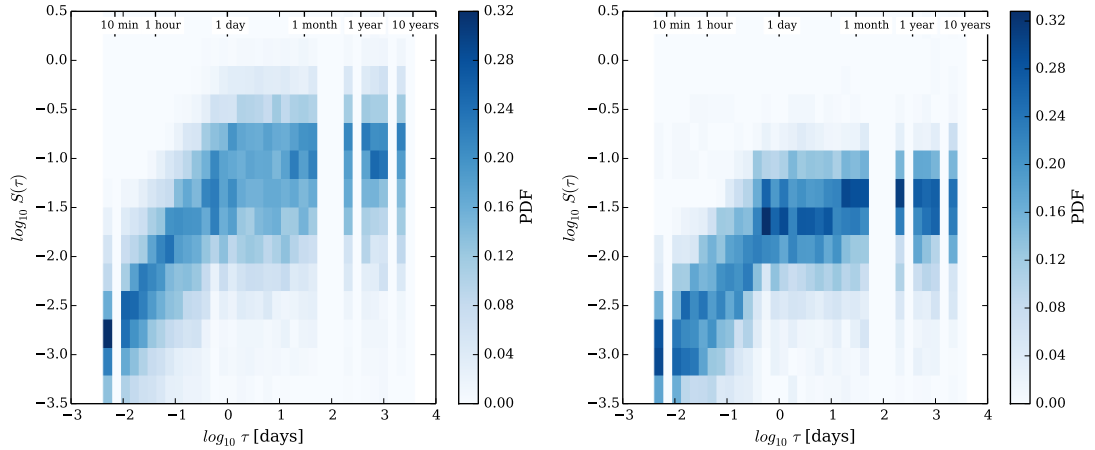


Figure 3.13: PDFs of intrinsic stellar variability for disc-bearing (left) and discless YSOs (right) respectively.

also detected in a Herbig Ae stars by Rucinski et al. (2010). This is in contrast to the $a \propto 1/\sqrt{f}$ ‘flicker noise’ spectrum found in photometric data of TW Hya by Rucinski et al. (2008), although the distribution of k that is shown in Fig. 3.14 certainly includes many stars with values of k consistent with this lower value. Objects with a higher value of k display greater amplitudes at lower frequencies than expected for standard $a \propto 1/\sqrt{f}$ flickering (Press 1978).

3.4.2 Sub-hour timescale variability

Analysis of the high-cadence dataset shows that variability on timescales of less than 0.5 hours is almost entirely dominated by residual noise from the subtraction of the non-astrophysical SF model. Fig. 3.10 compares the variability observed across the entire disc-bearing sample on three different timescales of $\lesssim 0.5$ hours. The longer (0.5 hours) timescale appears to show a weak tail of variability at the 1 to 2% level when compared with the shorter timescale. This is probably real and is the tail of the power spectrum that we see at hour timescales and longer. All variability on sub-hour timescales appear to be dominated by variability that is significantly below the photometric uncertainties. This implies that both of these timescales are still within Region 1 of Fig. 3.6, where the variability is dominated by the measurement uncertainty. Thus, the vast majority of variability occurring in the disc-bearing sample on timescales less than ≈ 1 hour exhibits amplitudes comparable-to or less-than our measurement noise threshold ($\gtrsim 0.7\%$). The discless sample shows almost the same result, except for two stars which do exhibit some

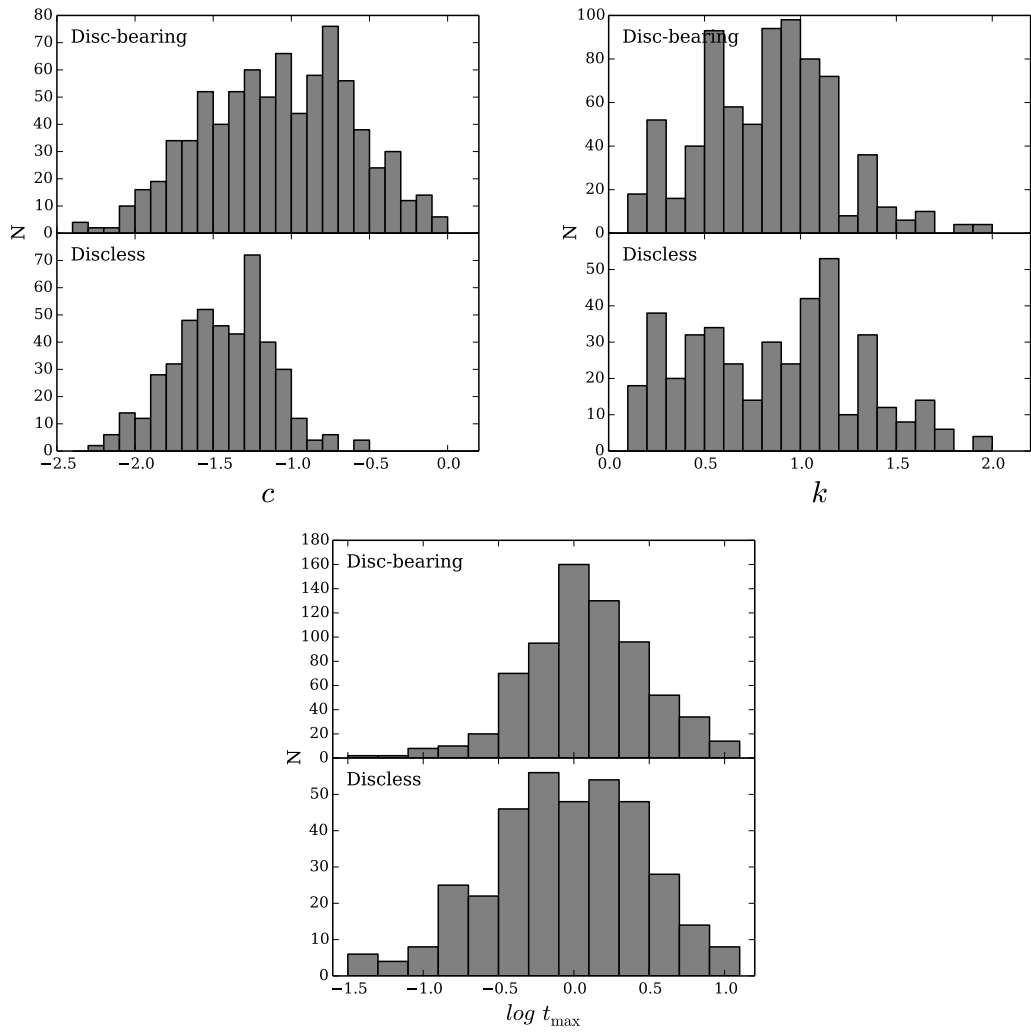


Figure 3.14: Histograms of derived parameters for YSOs in Cep OB3b. The top left panel compares $S(\tau)$ when $\tau > t_{\max}$, for stars in the disc-bearing and discless samples. The top right panel compares the exponent of the variability power-law (k) for the samples. The lower panel compares t_{\max} .

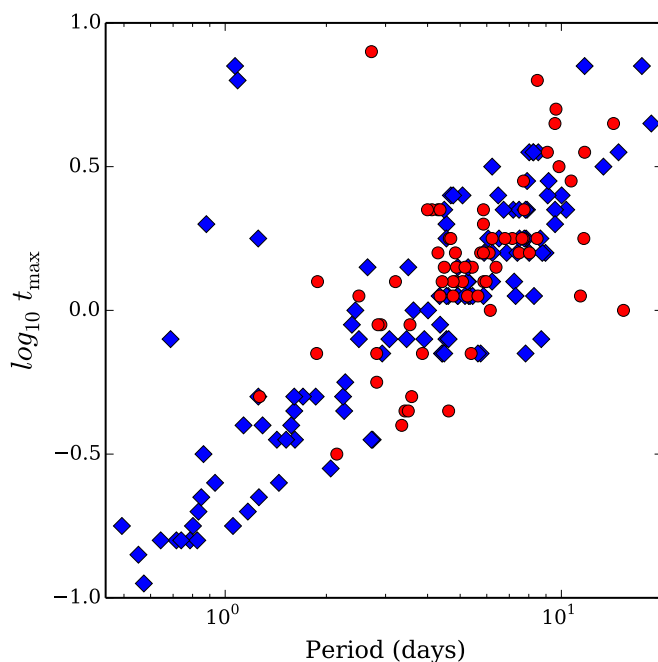


Figure 3.15: t_{\max} is compared with the rotation periods of periodic stars from Littlefair et al. (2010). Blue diamonds are discless stars. Red circles are disc-bearing stars.

short timescale variability that may be associated with chromospheric magnetic activity.

Disc-bearing stars

I do not observe the short-timescale variability that is predicted to result from instability in accretion shocks. Thus it is either very weak or not present in this sample. It may be that the emission from the accretion shock is simply too hot to contribute significantly in the i -band, or it may be that the quasi-periodicity that is predicted in the oscillation of the shock-front is in some way disrupted (e.g. Matsakos et al. 2013). Alternatively, it may be that gas in the shock region is optically thin and thus any quasi-periodic emission from the shock-heated gas is emitted in the Balmer continuum and lines.

Discless stars

In contrast to the disc-bearing stars, two individual discless sources in my sample do show bona-fide short timescale variability. This is in the form of short brightening events which exhibit amplitudes of 0.6 and 0.25 mag respectively. One of these brightenings appears to be a discreet transient ‘flash’ with a total duration of less than 10 minutes. The other has a similarly fast rise-time but then appears to decay more slowly. Fig. 3.16 shows the lightcurves of these events and Fig 3.18 compares images taken before and during one of the events. The other was also inspected and was confirmed to be real in the raw images.

T Tauri stars have long been known to exhibit flares, analogous to magnetic reconnection events seen on the Sun. Guenther & Ball (1998) estimate a rate of 0.015 - 0.04 flares per hour

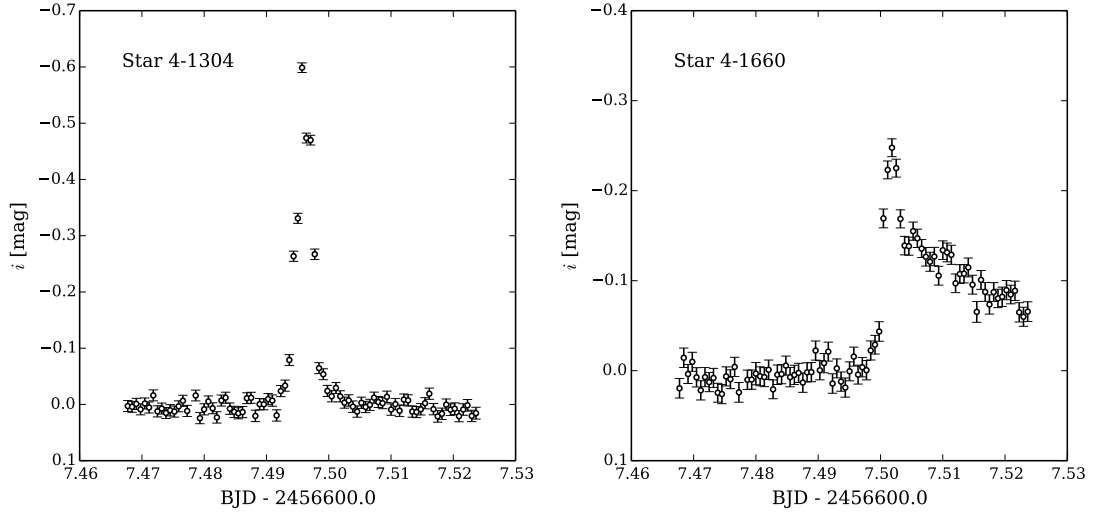


Figure 3.16: Short-timescale transient events seen in the i lightcurves of two discless stars. The lightcurves are normalised so that their quiescent magnitude is zero.

for WTTS based on 7250 spectroscopic observations of young stars in the Taurus and Chameleon star-forming regions. I have 417 discless stars with high-cadence monitoring, each of which was observed for 1.34 hours. The detection of two flares implies a flare-rate of 0.0036 ± 0.0014 flares per hour. This is significantly less than the rate seen by Guenther & Ball (1998). The two studies do however use different techniques. My data rely on changes within the continuum emission, whereas the study by Guenther & Ball (1998) detect changes in emission lines such as $H\alpha$. It is expected that much weaker flare events would be visible in optically thin emission than in the continuum, thus the lower flare detection rate in my data may be explained by the different observing technique. Alternatively, the relatively low flare rate that I see may be explained if stars in Cep OB3b are systematically older than those in Taurus and Chameleon and if their magnetic activity reduces as function of time.

3.5 Summary

Analysing the i band variability of 755 disc-bearing and 445 discless sources on timescales between 1 minute and ≈ 10 years gave this study a uniquely large sample of data from which to characterise population scale YSO variability. The key results are as follows.

- On timescales $\lesssim 15$ minutes, almost no variability is detected (at levels greater than $\approx 0.2\%$).
- Two discless stars show variability on minutes timescales, these are individual events that appear to be ‘flare’ like activity.
- On timescales between ≈ 30 minutes and 1 week, the variability for both disc-bearing and discless stars is entirely dominated by a power-law spectrum where the amplitude, $a \propto f^{-0.85 \pm 0.02}$ for disc-bearing stars and $a \propto f^{-0.95 \pm 0.03}$ for discless stars. It is notable that these

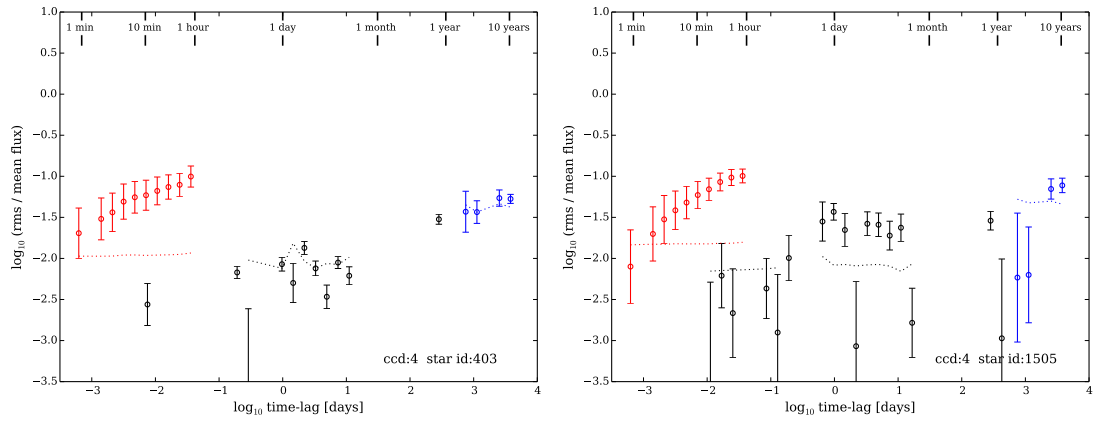


Figure 3.17: Structure functions for the stars exhibiting short-timescale ‘flaring’ transient events. Details as in Fig. 3.11. As the flare events are ‘one off’ events that only occur within the minutes timescale dataset, the SF on longer timescales appears lower than on short timescales.

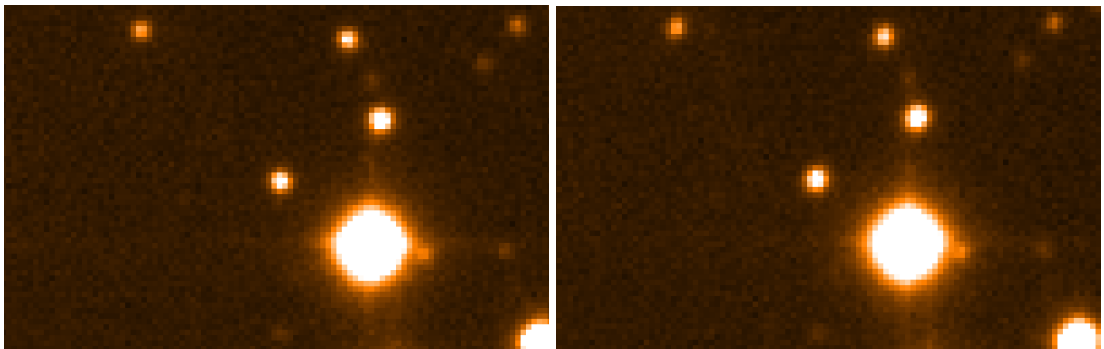


Figure 3.18: INT WFC *i* band images of star 4-1660 before (left) and during (right) the flare event shown in Fig. 3.16. These images were taken ≈ 5 minutes apart at BJD 2456607.49479 and 2456607.49820 respectively.

exponents are quite similar for both populations and close to $a \propto 1/f$ found for stochastic stars in NGC 2264 by Cody et al. (2014).

- Variability typically saturates on timescales on the order of the rotation period (disc-bearing: $t_{\max} = 1.50 \pm 0.07$ days, discless: $t_{\max} = 1.41 \pm 0.10$ days). Whilst longer term variability is observed (such as the years timescale modulation seen by Grankin et al. 2007), the amplitude of the long timescale variability is less than that seen on timescales less than t_{\max} .
- The median S_{τ} when $\tau > t_{\max}$ is 0.083 ± 0.003 for disc-bearing stars and 0.036 ± 0.001 for discless objects (note the uncertainties are the standard error on the median).

Whilst as expected the disc-bearing stars exhibit greater variability amplitude than discless stars at all timescales larger than 1 hour, it is notable that other parameters are very similar. Whilst different physical mechanisms may drive the observed variability in disc-bearing and discless stars, the similarity in t_{\max} and k indicate that the timescales that these processes exhibit are remarkably similar. t_{\max} appears to correlate well with the rotational timescale of periodic stars and the distributions of t_{\max} seen imply that this holds true for the entire population. The close link between t_{\max} and rotation periods is probably no coincidence as optical variability is most-likely either driven by the transit of cool or hot spots across the disc of the star as it rotates, or by accretion flows and inner-disc structures that are coupled to the magnetic field of the star. On timescales longer than the rotation period, it is striking that little additional variability appears in the structure function analysis on timescales of up to 10 years. This implies that almost the full range of variability that we might observe for a given star may be characterised by observing it for just a single rotation period. In discless stars, ‘flare’ events appear to occur at a rate of 0.0036 ± 0.0014 per hour (roughly 1 every 12 days). In the sample of two flare events seen in Cep OB3b, the duration of the brightenings range from ≈ 10 minutes to 1 hour.

Chapter 4

Performing simultaneous multi-colour photometry and spectroscopy to explore young star variability

4.1 Introduction

Understanding the circumstellar environment and accretion process in Young Stellar Objects (YSOs) is crucial for the study of the formation of stars and planetary systems. Protostellar evolution, disc dissipation and planet formation all hinge on the mass, energy and angular momentum exchange that is regulated by the infall of material onto the surface of a young star. The central AU in these systems is currently unresolved in any waveband, so I have used the time-domain to provide a window on this highly dynamic and variable region. I have chosen principally to study disc-bearing YSOs as they show strong signs of accretion and a circumstellar disc (e.g. Ménard & Bertout 1999), yet the dusty envelopes that conceal very young stars have dissipated. Disc-bearing YSOs can show complex variability in their optical photometric lightcurves with amplitudes up to several magnitudes (e.g. Herbst et al. 2002; Alencar et al. 2010; Cody et al. 2014; Stauffer et al. 2014). Similarly complex and variable behaviour are also seen in spectral lines (particularly emission lines), which betray the presence of dynamic processes both in the disc and the stellar atmosphere (e.g. Herbig 1962; Kenyon et al. 1994; Alencar & Basri 2000; Kurosawa et al. 2006).

Many previous approaches to the study of the central AU have concentrated on particular spectral lines. However, spectra alone cannot discriminate between variability caused by changes in flux from accretion related thermal continuum sources, changes in emission line flux, and extinction from the inner disc. For example, an increase in the equivalent width of the $H\alpha$ emission line could be due to an intrinsic change in $H\alpha$ line flux caused by an increase in accretion rate. Conversely however, the same equivalent width increase of the $H\alpha$ line could be caused by a reduction in the continuum flux caused by dust obscuration of the photosphere that does not effect the $H\alpha$ flux from wind emission. Flux calibration of the spectra is required to break the degeneracy between these two very different physical phenomena.

Both slit and fibre-fed spectrographs suffer from losses at the slit or fibre aperture. Changes

in the seeing and transparency vary the fraction of the light from the star that reaches the detector. Thus accurate flux calibration of ground-based spectra is most simply achieved though obtaining simultaneous photometry of the targets and using this photometry to correct the spectra for the seeing losses and transparency variations. Simultaneous photometry also has the distinct advantage that the optical SED can be characterised over a very wide wavelength range (in this study it is from 3500 to 8000 Å), while monitoring a small region at higher resolution with the spectrograph. Whilst it is possible to monitor a wide spectral range at high-resolution for a single target using some spectrographs (e.g. Echelle instruments), flux calibration across the wavelength range is difficult and only one target may be measured at a given time. The advantage of my observations is that I have been able to study a sample of 67 stars simultaneously, allowing analysis of a wide range of variability behaviour across a range in mass, T_{eff} and accretion rate.

In Chapter 3 I showed that monitoring on timescales of the rotation period is sufficient to characterise almost all of the i band variability that we see in young stars. Thus this study monitors YSOs in the Orion Nebula Cluster (ONC) over the course of seven nights. Typical rotation periods for stars in the ONC range from two to ten days (Stassun et al. 1999; Herbst et al. 2002). Stars of mass less than $0.25 M_{\odot}$ and discless stars tend to have rotation periods at the lower end of this scale. In those cases the monitoring will cover more than one full rotation of the star. Higher-mass disc-bearing stars tend to have longer rotation periods and my seven nights will typically cover greater than half of one rotation cycle.

The result of this monitoring is a large database of variability events in which I understand the flux contributions to the lightcurve from the photosphere, accretion continuum and circumstellar extinction. This information, in combination with physical parameters from the literature provides an opportunity to understand and characterise the underlying physical processes that drive the variability.

4.2 Sample selection

The science goals demand a target sample of disc-bearing YSOs that exhibit a wide range of periodic and irregular lightcurves covering a wide range of periods and amplitudes. The ONC contains > 1000 variable disc-bearing stars with measured photometric lightcurves, showing rotation rates in the range 2 - 10 days and with variability ΔI_c of up to 2 magnitudes. Disc-bearing targets for spectroscopy were selected using the optical variability catalogues of Rebull (2001) and Herbst et al. (2002), as well as the near-IR catalogue of Wolk et al. (2014). I collected photometric variability data for ≈ 3000 stars in the ONC region, however the spectroscopic sample was much smaller

The AF2/WYFFOS spectrograph uses 150 movable science fibres on a field plate at the prime focus of the *William Herschel* Telescope. As the fibres may not cross and the positioning buttons have a finite size, not all of the fibres may be placed on target stars in any given configuration, thus limiting the actual number of targets to significantly less than 150 per field. The fibre setup was configured to maximise the number of cluster members observed, whilst being weighted toward stars with the highest amplitude variability. High amplitude variables are more rare, but are

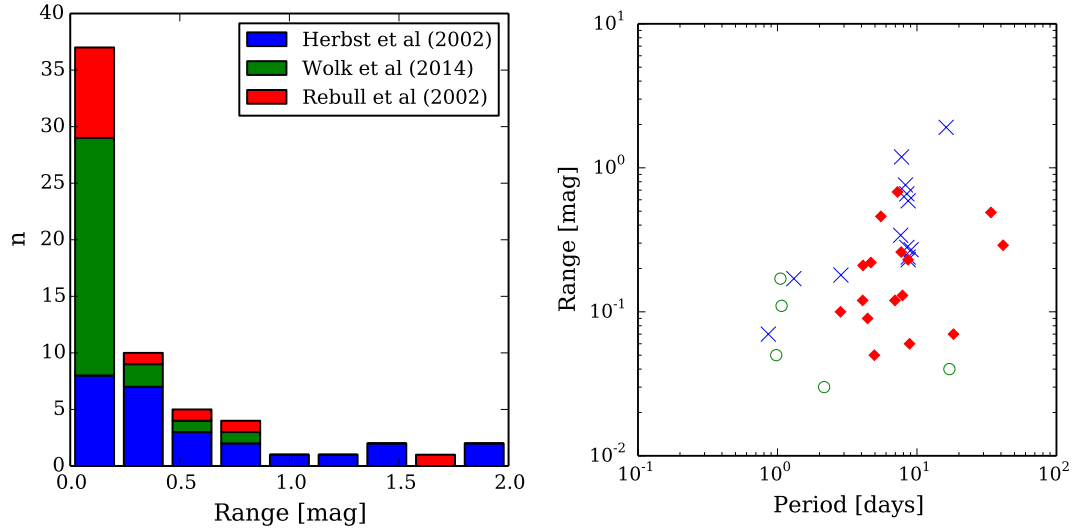


Figure 4.1: Literature variability parameters for all spectroscopic target stars. The left panel shows a histogram of variability amplitudes measured in the optical catalogues of Rebull (2001) and Herbst et al. (2002) and the near-IR catalogue of Wolk et al. (2014). Where a star appears in both the optical and near-IR catalogues, its optical variability amplitude is used. The right panel shows periods and variability amplitudes of stars in the spectroscopic sample where literature values exist. Circles (green) are from Rebull (2001), crosses (blue) are from Herbst et al. (2002) and diamonds (red) are from Wolk et al. (2014).

probably the most useful for studying the physics of YSOs. Thus this weighting scheme was used to provide a sample which contained a higher fraction of high-amplitude variables than the general population and provided effective sampling of the entire variability parameter space. Within these selection constraints, the number of spectroscopic targets that I observed was therefore limited to 66, in-part due to the centrally condensed nature of the Orion Nebula Cluster. Once the science target fibres had been configured, 22 spare unused fibres were placed randomly within the field of view. These fibres were exposed concurrently with the science targets, allowing simultaneous measurement of the spectrum of the sky. These sky spectra were later used to subtract atmospheric emission lines from the science target spectra. Fig. 4.1 shows a histogram of literature variability amplitudes (irrespective of periodicity) as well as the periods and amplitudes for known periodic stars in the spectroscopic sample.

I wished to ensure that the monitoring cadence was less than 0.5 hours as the work detailed in Chapter 3 suggested that this was the shortest timescale on which significant variability behaviour might be seen. This cadence, when combined with the sensitivity of the spectrograph determined that a brightness limit of $V = 18$ ($I \approx 15$) was required for all targets. A CMD comparing the target stars with the whole ONC population is shown in Fig. 4.2.

To understand the spectroscopic veiling, luminosity excess and photospheric characteristics of the disc-bearing stars, it was important that I also observed a selection of discless stars in the ONC. Whilst providing an interesting sample in themselves, these stars also provided spectral templates of approximately the same age, metallicity and surface gravity. Thus the disc-bearing targets were supplemented with a sample of 21 discless stars in the field. The final field configu-

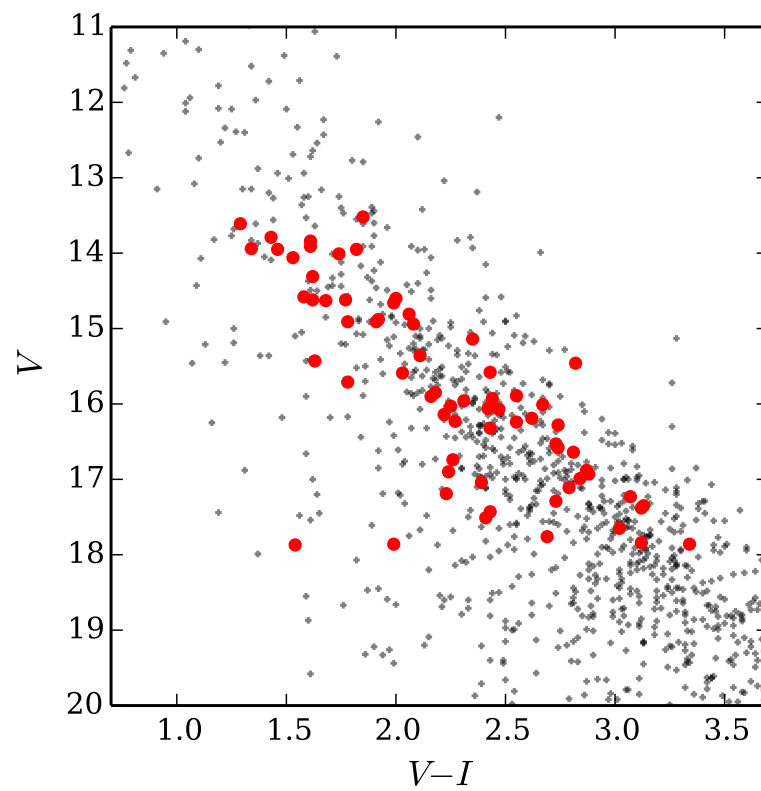


Figure 4.2: CMD comparing the positions of the spectroscopic sample (red circles) with the ONC population (black crosses) in the photometric dataset used to select the spectroscopic targets. Photometry from Hillenbrand (1997).

ration consisted of 67 stars. Details of these objects are shown in Table 4.1.

Table 4.1: Star ID numbers assigned in this study, stellar coordinates and literature YSO classifications (from Megeath et al. 2012) for all stars in the spectroscopic sample. N: Naked photosphere, D: Circumstellar Disc, P: Protostar.

Star ID	RA (J2000.0) <i>hh mm ss.sss</i>	Dec (J2000.0) <i>dd mm ss.ss</i>	YSO classification
3	05 35 18.986	-05 37 36.76	N
4	05 35 20.294	-05 30 39.52	D
6	05 35 27.508	-05 35 19.47	N
8	05 35 35.602	-05 39 08.19	D
10	05 35 27.974	-05 29 31.10	D
13	05 35 44.311	-05 37 33.54	D
14	05 35 36.354	-05 31 37.87	D
20	05 36 00.305	-05 34 23.50	N
23	05 36 07.044	-05 34 18.27	D
24	05 35 30.277	-05 25 51.62	N
26	05 36 03.861	-05 30 18.81	D
30	05 35 54.628	-05 27 07.56	D
36	05 36 14.590	-05 25 49.83	N
40	05 35 44.845	-05 24 34.48	N
42	05 35 46.614	-05 22 24.32	D
45	05 36 08.688	-05 21 02.16	N
49	05 36 10.494	-05 19 44.91	D
50	05 35 35.289	-05 21 27.15	D
58	05 35 50.773	-05 16 29.18	D
59	05 35 26.169	-05 20 06.05	D
62	05 35 52.760	-05 12 59.01	D
66	05 35 46.123	-05 10 51.78	D
70	05 35 54.056	-05 04 14.76	D
71	05 35 32.443	-05 15 06.90	D
72	05 35 43.555	-05 05 41.46	D
74	05 35 37.686	-05 06 32.10	D
75	05 35 38.529	-04 59 41.15	D
77	05 35 25.231	-05 15 35.83	D
79	05 35 23.442	-05 10 51.78	N
81	05 35 12.819	-05 15 24.03	N
84	05 35 09.140	-05 06 47.16	N
85	05 35 06.828	-05 10 38.53	N
88	05 35 01.426	-05 09 32.61	N

90	05 34 47.949	-05 04 55.01	D
92	05 35 04.762	-05 17 42.17	D
95	05 34 45.190	-05 10 47.65	D
98	05 34 54.941	-05 17 01.79	D
101	05 34 30.248	-05 11 48.20	D
104	05 34 29.260	-05 14 39.75	D
107	05 35 02.438	-05 20 46.58	N
108	05 34 07.316	-05 13 45.47	N
110	05 33 48.222	-05 13 26.21	D
111	05 34 42.958	-05 20 06.99	N
115	05 34 52.163	-05 22 31.95	N
118	05 33 44.719	-05 21 04.08	N
119	05 34 46.570	-05 23 25.61	D
121	05 33 41.675	-05 24 04.26	D
124	05 33 47.652	-05 25 48.58	N
126	05 34 28.520	-05 24 57.89	D
127	05 34 26.164	-05 26 30.40	D
130	05 35 00.468	-05 25 14.31	D
133	05 34 19.548	-05 30 19.86	D
134	05 34 17.485	-05 31 58.63	D
135	05 34 00.346	-05 35 43.45	N
137	05 34 03.003	-05 36 57.28	D
139	05 34 52.759	-05 27 54.58	D
141	05 34 47.894	-05 30 46.57	D
143	05 34 37.468	-05 34 51.95	D
146	05 34 27.852	-05 41 37.81	N
149	05 34 48.309	-05 37 22.82	N
150	05 34 45.875	-05 41 09.70	D
152	05 34 41.179	-05 46 11.64	D
153	05 34 49.098	-05 46 05.00	D
155	05 34 54.911	-05 46 43.93	D
157	05 35 06.445	-05 33 35.19	P
158	05 35 12.210	-05 30 32.91	D

Table 4.2: Central coordinates in each field of view for INT pointings

Field No.	RA (J2000.0)	Dec. (J2000.0)
1	05 ^h 35 ^m 26 ^s .64	-05°30′03″.6
2	05 ^h 35 ^m 12 ^s .48	-05°15′39″.6
3	05 ^h 35 ^m 31 ^s .68	-05°25′51″.6

4.3 Data collection

Simultaneous photometric and spectroscopic observations were made using the 2.5-m *Isaac Newton* Telescope (INT) and the 4.2-m *William Herschel* Telescope (WHT) respectively. Both telescopes are located at the Observatorio del Roque de los Muchachos on La Palma and, importantly, co-location practically guaranteed simultaneous temporal coverage of the targets. Observations were performed on seven consecutive nights during 2013 November 7-13. Time-series photometry was collected continuously for between 5 and 7 hours, on every night. Spectral time-series were collected for ~ 6 hours on the nights of November 11-12 and for 2-3 hours per night on the other five nights.

4.3.1 Photometric observations

INT photometry was performed using the Wide-Field Camera (see Chapter 3 for details of the instrument). RGO-*U* (centred at 3630 Å) and *g*, *r* and *i* broad-band filters with similar bandpasses to the *Sloan Digital Sky Survey* (SDSS) filters were used. In addition, observations were made with a 95 Å wide, narrow-band H α filter centred on 6568 Å. I also observed using a 92 Å wide narrowband filter centred on 6800 Å (n_{6800}) which was entirely encompassed by the wavelength range of the WHT spectra. This photometry allowed me to flux calibrate the spectra (see Section 4.3.8). The seeing throughout the seven nights varied in *i* between 0.9 and 4 arcsec with a median and standard deviation of 1.6 and 0.7 arcsec respectively. In *g*, the seeing varied between 1.1 and 6.1 arcsec with a median and standard deviation of 1.8 and 0.9 arcsec. The nights of the 7th to the 9th of November were affected by thin cirrus cloud, though typically extinctions were less than 0.5 magnitudes. The nights of the 10th to the 12th of November were photometric. The final night was affected by cloud and so only n_{6800} and *U* observations were made when possible.

To cover the same field-of-view as the spectroscopic observations, I cycled between three overlapping fields with the INT. The offsets between fields also provided coverage in regions where gaps between the CCDs and bad pixel columns prevented data collection. Field centres are detailed in Table 4.2. Each field was observed with the full set of broad and narrow filters using the exposure times detailed in Table 4.3. The total observing time (including CCD readout and filter changes) for each field was ≈ 20 minutes. Lightcurve cadence for a given star was then determined by whether it fell in one, two or three of the INT fields, resulting in 20, 30 or 60 minute mean cadence respectively. In addition to the time series monitoring, four fields in stripe 82 of the SDSS were used as photometric standards and were observed on three different nights.

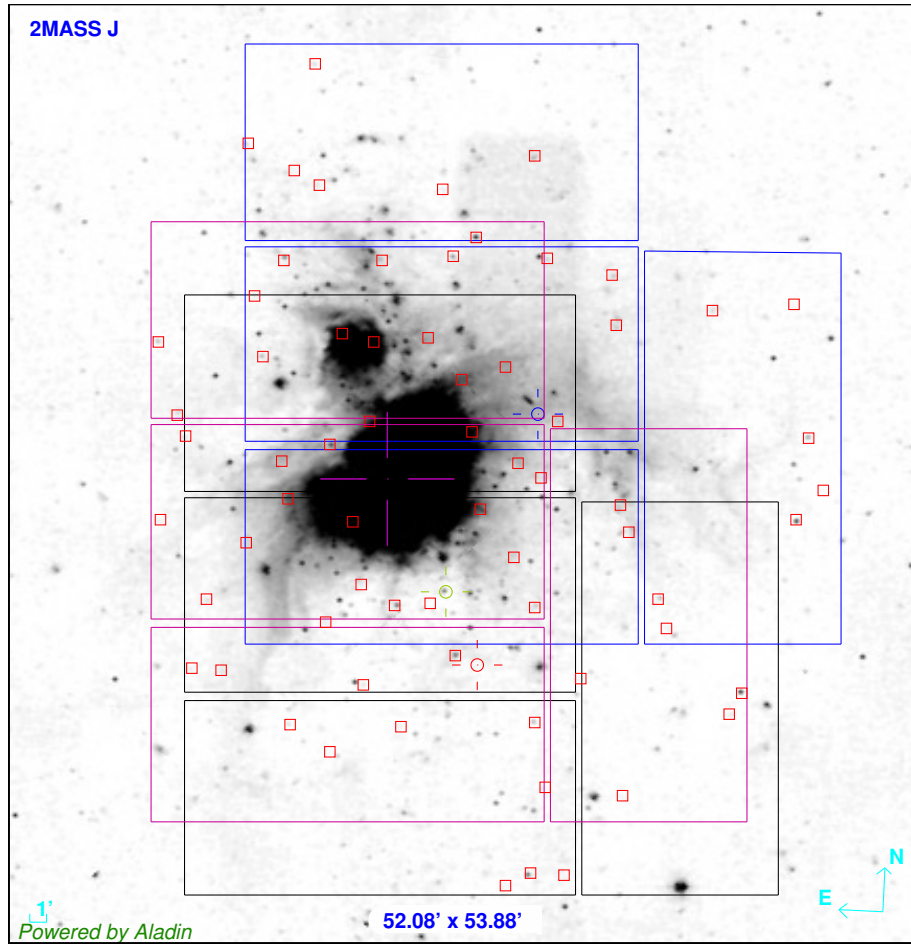


Figure 4.3: 2MASS J-band image of the Orion Nebula Cluster region with my three INT WFC fields of view overlaid. Fields 1, 2 and 3 are represented by black, blue and purple CCD mosaics respectively. The positions of stars simultaneously monitored using the AF2/WYFFOS spectrograph are marked with red squares.

Table 4.3: Filters and exposure times used for each of the cycled INT pointings

Filter	λ_{central} Å	FWHM Å	Exposure time sec
<i>U</i>	3630	638	100
<i>g</i>	4846	1285	20
<i>r</i>	6240	1347	10
H α	6568	95	100
n_{6800}	6800	92	100
<i>i</i>	7743	1519	10

4.3.2 Image reduction and optimal photometry

Bias subtraction, linearity correction, flat-field correction and bad-pixel masking were performed as described in Section 3.2.2. Band specific twilight flat frames were constructed using frames from each of 11 morning and evening flat field observations taken over the course of the 7 observing nights so that any outlier frames could be rejected through median combination. Due to its short exposure time, the i band observations were not subject to de-fringing as the predicted fringe amplitude based on analysis of library INT fringe frames was only ≈ 1 ADU count.

The data were analysed using the `CLUSTER` software package described in detail by Naylor et al. (2002), Burningham et al. (2003) and Jeffries et al. (2004). Deep images for each field were created using the individual n_{6800} images. This deep frame was then used for object detection and the catalogues for each field were merged to create a single large ‘master catalogue’ in which each star had its own unique ID number. The Two Micron All Sky Survey (2MASS; Cutri et al. 2003) was used to provide an astrometric solution for the deep catalogue. Deep frames were then constructed for each individual filter and field using a median stack of the 10 frames with the best seeing and transparency conditions. These deep frames were searched to detect object positions and to provide a reference for measurement of pointing offsets in the individual frames. The astrometric solution (again using 2MASS) and the photometry were both found to be improved by calculating positions and frame offsets on a filter by filter basis, rather than using a single colour for the positions. This is probably (at least in part) due to the relatively low number of detected stars in the U , g and $H\alpha$ filters. The IDs of the objects found in the individual field and filter catalogues were then corrected through astrometric matching to agree with those in the master catalogue. List-driven optimal photometry was then performed on the individual frames, providing a flux for each object. The fluxes were then ‘profile corrected’, a process that is analogous to ‘aperture correction’ in aperture photometry (see Section 4.3.3). The photometric measurements were then adjusted for any difference in the airmass and transparency for each frame, by determining a relative transparency correction from bright but unsaturated stars.

An additional statistical uncertainty was added to each measurement at this stage to ensure that the distribution of reduced chi-squared (χ^2_ν) for all stars was independent of signal-to-noise ratio and close to unity. Mean χ^2_ν is greater than unity in all filters due to the intrinsic variability of the majority of stars in the field. The additional uncertainty ranged from 0.007 to 0.02 mag and reflects errors in the flat-field and profile corrections.

4.3.3 Profile correction

A spatially varying profile correction was calculated so that I could combine data for each star from different fields. The profile correction was also essential so that I could calibrate the photometry using standard star observations. Profile corrections are usually calculated by fitting low order polynomial functions that vary as a function of position on the CCD for a sample of bright unsaturated stars. Unfortunately, the high optical depth of the background OMC-1 molecular cloud resulted in a paucity of well distributed bright unsaturated stars in each field, particularly in the U , g and $H\alpha$ bands. Profile-corrections were instead derived by a semi-empirical model that as-

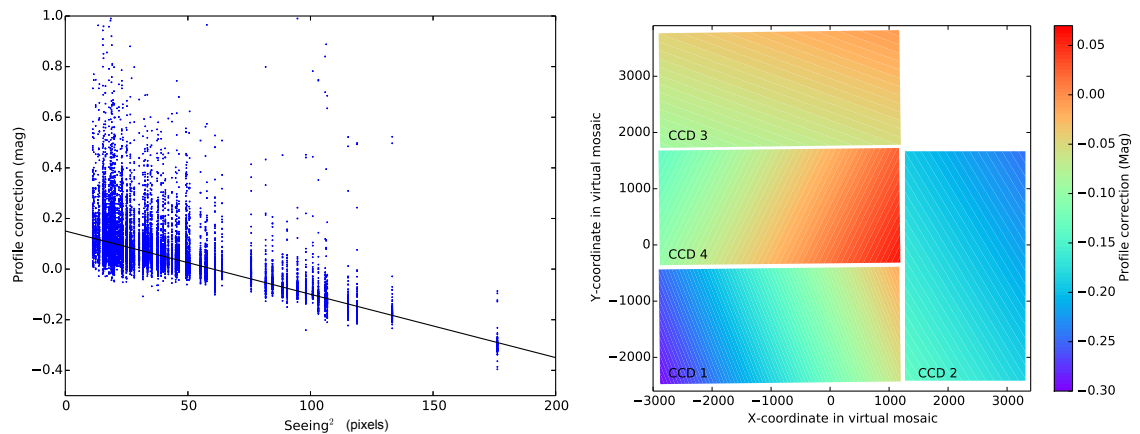


Figure 4.4: The two principal elements of the profile correction model for the g band photometry. Left panel: The relation between the square of the seeing (in pixels) and the measured profile correction for all bright, unsaturated stars in all g band frames. The blue points represent the difference in measured magnitude for a given star in a given frame using optimal and large-aperture (10 pixel radius) photometry. The linear fit (solid black line) shows the derived relation of $-0.002501 \text{ mag/arcsec}^2$. This seeing component is removed prior to the subsequent fitting of tilts and radial aberrations. Right panel: The ‘tilted plane’ components of the four CCD chips in the camera.

sumed the profile correction was caused by modification of the point-spread-function (PSF) by a combination of the seeing, CCD non-coplanarity and tilt, plus radially dependent optical aberrations. The optimal photometry was compared with aperture photometry (with an aperture radius of 10 pixels) of all bright unsaturated stars in all exposures and in all fields. The combination of these measurements provided a much larger sample over which to fit than using individual frames alone. The parameter which made the largest contribution to the profile correction is the seeing. Fortunately the profile correction shows a strong linear relationship with the square of the seeing, and combination of all of the data allowed this term to be fitted and corrected. Fig. 4.4 shows the linear relationship between the square of the seeing and the profile correction in the g filter. The squared dependence is to be expected as PSF errors are likely to be 2D in nature.

Once the effect of the seeing was measured and corrected, residual profile corrections were then fitted assuming that the PSF was being spread due to inclination of the CCDs with respect to the focal plane (documented¹ as being up to $20 \mu\text{m}$) and optical aberrations. The optical aberrations are assumed to act radially about the optical axis and be caused by a combination of field-curvature and coma. These model elements are also illustrated in Figure 4.4.

4.3.4 Correction of lightcurve systematics

Despite the care taken to prevent field-to-field errors in the reduction, some systematic offsets were seen between lightcurves for the same star measured in different fields. Typically the offsets were $\lesssim 0.1 \text{ mag}$. These resulted from flat-field errors caused by scattered light in twilight flat frames and residual errors in the profile correction, possibly due to physical effects that were not accounted

¹http://http://www.ing.iac.es/Engineering/detectors/ultra_wfc.htm

for in the empirical model.

To assess and correct these offsets, I compared lightcurves for each star taken in different fields. First I selected the highest quality lightcurve for each star as a reference, based on highest mean flux and minimum χ^2 deviation. I then measured the nightly offset between the lightcurve for each field and the reference. A χ^2 analysis showed that the nightly offsets were statistically indistinguishable from a single offset over all nights for each field for a given star. Thus each star had a single correction applied for each field that normalised the lightcurves together onto the baseline of its highest quality lightcurve. Where poor quality or lack of data meant that the offset could not be confidently determined, no correction was applied and the lightcurve flagged.

4.3.5 Absolute calibration of photometry

Five standard star fields in the *SDSS* ‘stripe 82’ were observed at a variety of airmasses throughout the night of the 10th of November. Conditions on that night were photometric. These fields were particularly suitable as Bell et al. (2012) presented a catalogue of over 10 000 main sequence stars in these fields with *U*, *g*, *r*, *i* and *z* photometry that is calibrated in the INT WFC system (note: not the *SDSS* system). Comparison of stars that matched between my data and Bell et al. (2012) was used to calculate magnitude zero-points and extinction terms for the *U*, *g*, *r* and *i* filters.

The standard star fields had not previously been observed using the narrow-band n_{6800} and $H\alpha$ filters. Tim Naylor provided predicted narrowband magnitudes for the standard stars based on their broad-band colours and theoretical models. This was achieved by first predicting $r - i$, $r - H\alpha$ and $r - n_{6800}$ colours for main sequence stars in the mass range 0.1 - 7 M_{\odot} using interior models by Siess et al. (2000) and atmospheres by Allard et al. (2011). Fig. 4.5 shows the derived relations. These models were used to predict $r - H\alpha$ and $r - n_{6800}$ for the standard stars using their measured $r - i$ colour. $H\alpha$ and n_{6800} magnitudes were then found by subtracting the predicted colours from the *r* band magnitudes. Comparison between the predicted narrowband magnitudes and those measured in the standard field observations allowed zero-points and extinction terms to be calculated.

The final photometric catalogue for the ONC was generated by combining the magnitudes and colours for each star from all observations made on the night of the 10th of November. These were then corrected for the mean airmass of the observations (using the standard star coefficients) to give the final colours and magnitudes. All magnitude zero-points are calibrated in the AB system.

4.3.6 Spectroscopic observations

Spectroscopic observations were made using AF2/WYFFOS with the R1200R grating and the Red+4 detector. This provided a spectral range of $\approx 1500 \text{ \AA}$ at a resolution of $R \approx 3500$. The spectra were centered at $\approx 7000 \text{ \AA}$ and covered a wavelength range that included $H\alpha$, the Li doublet at 6708 \AA and several sets of TiO bands. Pairs of science exposures were bracketed by observations of a B0.5V ‘telluric standard’ star (θ^1 Ori D). The smooth and featureless spectrum of the B0.5V star allowed me to measure the strength of atmospheric (telluric) absorption (caused

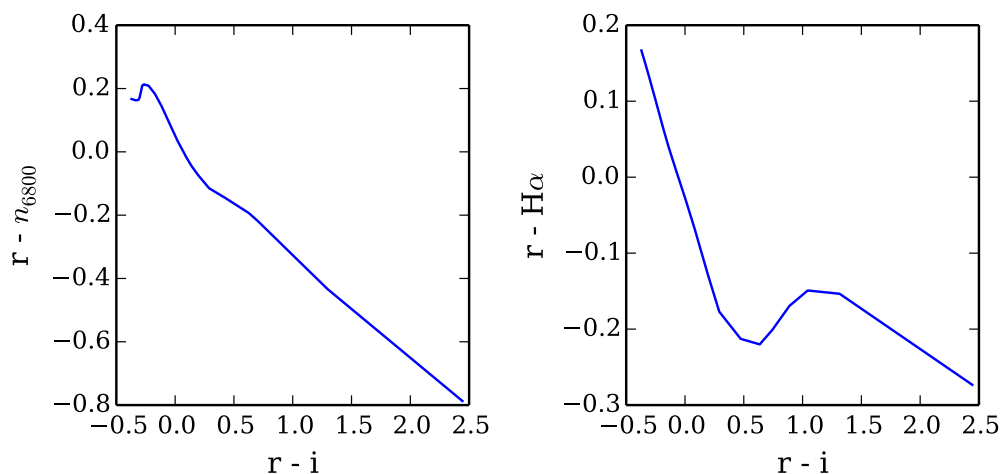


Figure 4.5: Theoretical relations for $r - i$ vs. $r - H\alpha$ and $r - i$ vs. $r - n_{6800}$ derived for main sequence stars in the mass range $0.1 - 7 M_{\odot}$. Interior models are from Siess et al. (2000) and atmospheres are from Allard et al. (2011).

by the presence of molecules such as O_2 and H_2O) as a function of wavelength and thus correct for these in the target spectra. Differences in air-mass between observations of the targets and the telluric standard star were minimised through regular observation of the standard throughout the night. This was important as any difference in airmass between target and standard gives rise to two main problems. Firstly the correction of telluric absorption features will be incorrect as the line depths vary as a function of airmass. Secondly, when flux calibrating, the airmass difference will apply a smooth error to the flux calibrated data which mimics the atmospheric Rayleigh and Mie scattering. The scattering losses are corrected in the target spectra by multiplying the atmospheric transmission function derived for La Palma by King (1985) by the difference in airmass between the target observation and its telluric calibration frame. A histogram of the differences in airmass between all target and telluric standard star observations is shown in Fig. 4.6. The mean difference in airmass is 0.047.

The exposure time for each observation was 900 seconds. This exposure time was shorter than ideal for some of the fainter stars in the sample. However it had the advantage of minimising contamination from cosmic ray artefacts and also allowed for regular measurement of telluric stars, thus improving the removal of telluric lines. Spectra for the fainter stars in the sample which achieved lower SNR in individual frames could be improved by stacking several consecutive observations together. On the nights of the 12th and 13th of November four observations were made of regions of sky offset from the target positions by 3 arcsec to the N, S, E and W. A mean of these ‘offset-sky’ spectra were later used to estimate and subtract the contamination in the target spectra caused emission from the nebula.

Bias and dark frames were observed on each night. Observations of neon and mercury arc lamp spectra were made several times per night. Comparison of these spectra with spectra line catalogues were used to provide wavelength calibration. Both a tungsten lamp and the smoothly illuminated dawn sky were observed on each night to provide ‘flat-field’ spectra.

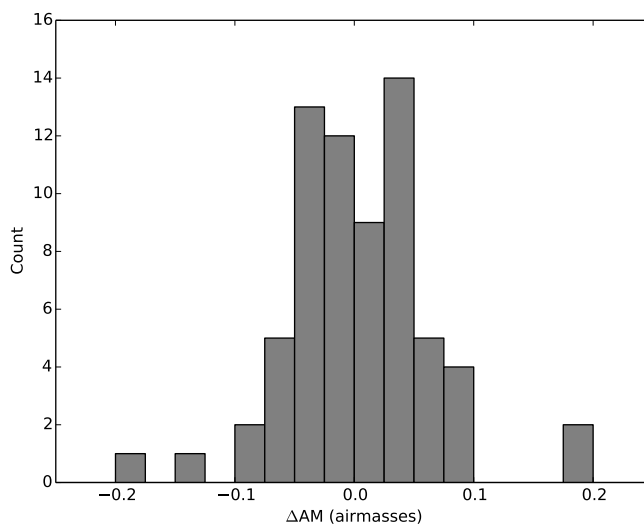


Figure 4.6: Histogram of airmass differences between target and telluric star observations for the entire set of spectra. The mean of the modulus of the difference in airmass is 0.047.

4.3.7 Reduction and wavelength calibration

All frames were bias corrected using a median stack of 10 bias frames taken throughout the week. Target and telluric spectra were flat-fielded to remove pixel sensitivity variations by dividing target spectra by tungsten lamp spectra. Sky-flat frames were used to trace the fibre positions on the CCD and a standard extraction was performed using routines originally developed by Mukai (1990).

The neon lamp spectra provide many strong lines for wavelength calibration blueward of 7000\AA . The mercury lamp spectra complement these well by providing many strong calibration lines redward of 7000\AA . However, a technical failure prevented the use of the neon lamp on the nights of 10th and 11th of November. For these nights, nebular emission lines ([O I] 6300.2\AA , [N II] 6548.1\AA , [N II] 6583.6\AA , [S II] 6717.0\AA) within the science exposures were used to supplement the mercury arcs and provide wavelength calibration. Cosmic ray removal was performed via a sigma-clipping routine, based on the rms flux variability characterised as a function of wavelength for each star.

4.3.8 Flux calibration and removal of night-sky and nebular contamination

A model was created that simultaneously corrected for atmospheric absorption and provided a relative flux calibration. The high temperature of the B0.5V telluric standard spectrum renders it intrinsically smooth, exhibiting no metal lines in the wavelength region of interest. Thus any absorption features observed in the region of H_2O or O_2 atmospheric bands are faithful measurements of these features. Despite being free of metal lines, the B0.5V standard does exhibit strong hydrogen and helium absorption lines. To construct the calibration model I removed the H and He lines in each observed B0.5V spectrum through a spline interpolation. I then divided each target spectrum by the closest (in time) instance of the calibration model to remove atmospheric absorption features.

A spectrophotometric model of a B0.5V star was then created by median combining B0V and B1V spectra from the catalogue of Pickles (1998) calibrated in units of f_ν ($\text{erg s}^{-1} \text{cm}^{-2} \text{Hz}^{-1}$). All spectra in this study are calibrated in f_ν , to allow for direct comparison with the photometric measurements which are calibrated in the f_ν based AB magnitude system. This allows them to be plotted together on the same axes to create a combined spectral-energy-distribution (SED) for each star at each epoch.

The spectrophotometric model was reddened based on its broad band colours (Ducati 2002) and the reddening law of Cardelli et al. (1989). This model was then smoothed by fitting a power law function (which describes the Rayleigh-Jeans tail of such a hot spectrum well) thus removing the H and He lines as well as residual noise. The target spectrum was then multiplied by the spectrophotometric model, resulting in a flux calibrated target spectrum. Sky fibres and offset sky exposures were also fluxed by multiplying by the same spectrophotometric model.

A model night sky spectrum was created for each exposure by median combining all of the placed sky fibre spectra from that exposure. Nebular emission is spatially variable and so is subtracted separately. Thus in the model night sky spectra, the nebular lines were removed by interpolation. The appropriate night sky spectrum was then subtracted from each target spectrum. Nebular contamination was modelled for each star by first subtracting the appropriate night sky spectrum (which was created as described for target spectra) from the offset sky spectra for each star. The four offset sky spectra for each star were then median combined to create a nebular spectrum for each star. A scaling for the nebular spectrum was then calculated for each exposure based on the ratio of the nebular line strengths in the placed sky fibres compared with the offset sky nebular model for the same placed sky fibres. A mean of the corrections calculated for the 22 placed sky fibres was determined for each exposure and this factor was used to scale all nebular spectra in a given exposure. The appropriate scaled nebular spectra were then subtracted from the spectrum for each star at each epoch.

At this stage the target spectra were roughly flux calibrated and corrected for non-stellar contamination but were still affected by seeing and transparency losses. The final flux calibration was performed by calculating the mean flux (weighted by the filter transmission function) in the spectrum over the n_{6800} bandpass for each observation. The flux measured in the n_{6800} photometry at the closest epoch to the spectrum was then divided by the mean flux calculated within the spectrum to create a normalisation factor. Any spectrum that did not have a photometric measurement within 15 minutes was rejected as the validity of the flux calibration would be uncertain. The entire spectrum was then multiplied by the normalisation factor to create a final flux-calibrated spectrum. Examples of flux calibrated spectra are shown in Fig 4.7. An example of a single epoch combined photometric and spectroscopic SED for a single star is shown in Fig. 4.8. The reduced datasets described in this chapter form the basis for the analysis in Chapters 5 to 9.

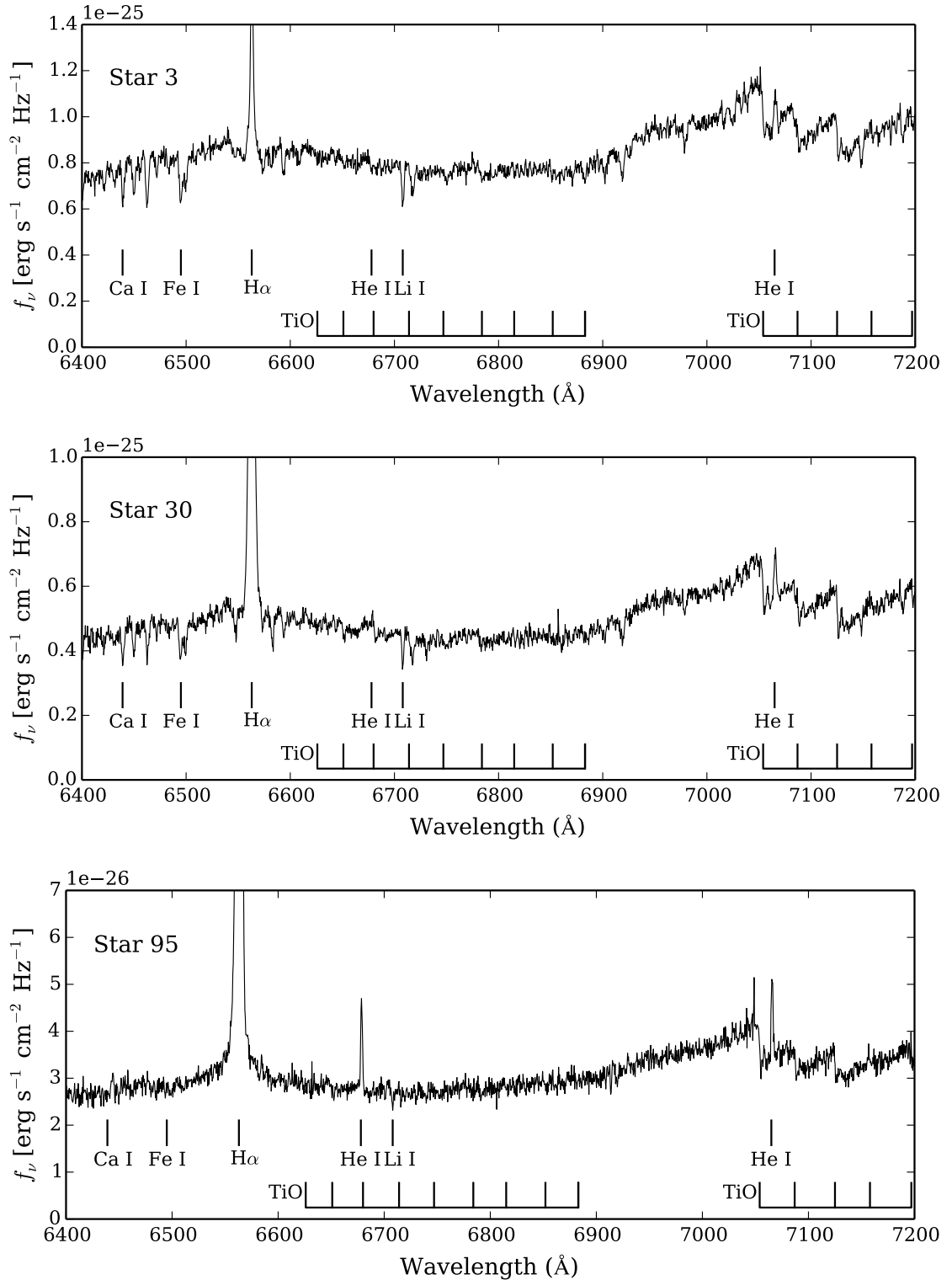


Figure 4.7: Examples of individual (single epoch) spectra collected using AF2/WYFFOS. Spectra are flux calibrated using n_{6800} photometry. Important atomic and molecular lines are labeled. All stars display the presence of lithium, evidence of their youth. Star 95 shows weak photospheric absorption lines, broad H α emission and strong He I emission, all indicators of accretion.

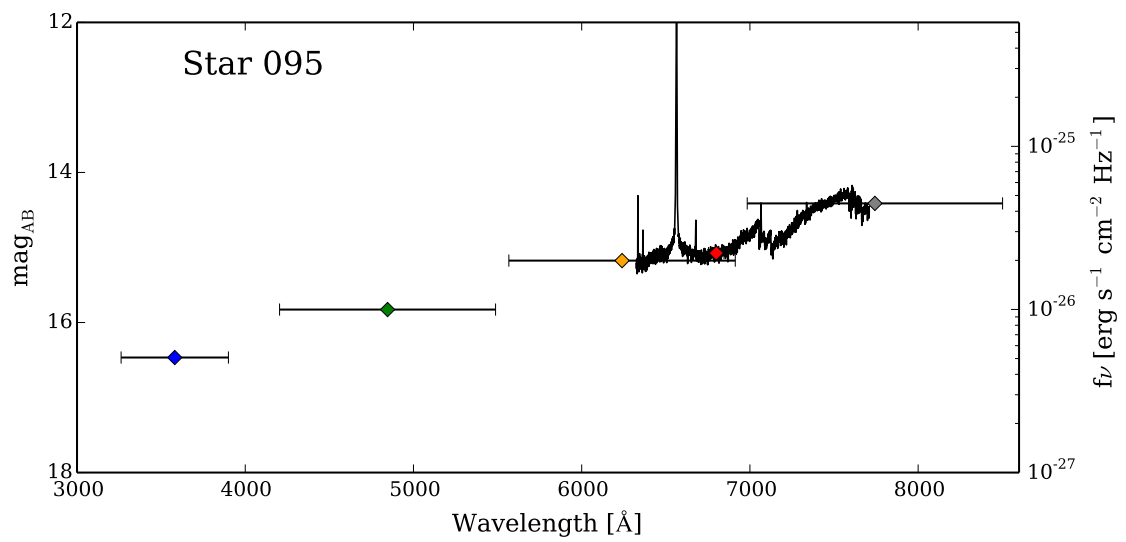


Figure 4.8: An example of a composite photometric/spectroscopic SED for star 95 at a single epoch. The (coloured) diamonds are photometric measurements in U , g , r , n_{6800} and i bands. the (black) solid line is the spectrum. The horizontal error bars on the photometric points indicate the nominal bandwidth of the filters.

Chapter 5

Young star multi-colour photometric variability

5.1 Introduction

Young stars have long been known to be time-variable at all wavelengths, from x-rays to the infrared (e.g. Joy 1945; Montmerle et al. 1983; Bouvier et al. 1993; Herbst et al. 1994; Burningham et al. 2005; Morales-Calderón et al. 2011; Cody et al. 2014; Rice et al. 2015). The impact of this variability on the spread in luminosity of the pre-main-sequence locus in CMDs is unclear, particularly in very young regions such as the ONC where a high fraction ($80 \pm 5\%$ according to Haisch et al. 2001) of stars still have dusty circumstellar discs. A two-epoch study of Cep OB3b and σ Ori by Burningham et al. (2005) found that variability was insufficient to explain the age spreads observed, however these clusters are likely to be older than the ONC (Mayne & Naylor 2008; Bell et al. 2013) and have disc fractions below 35%, significantly lower than the ONC (Allen et al. 2012; Hernández et al. 2007).

I show in Chapter 3 that YSO optical variability ‘saturates’ on timescales of ~ 1 week, so this seven night study provides an opportunity to study the full extent of variability in the CMD for a very young cluster. I have performed this analysis in the $g, g - i$ CMD as this (and the similar $V, V - I$) are often used for determining the ages and age-spreads of young stellar populations by comparison with pre-main-sequence isochrone models (e.g. Hillenbrand et al. 1995; Hillenbrand 1997; Mayne et al. 2007; Bell et al. 2013).

5.2 Variability in $g, g - i$

To study the effect of photometric variability on CMD position, I have taken each of the spectroscopic target stars and calculated its g and $g - i$ magnitudes at all available epochs throughout the seven nights of observations. The number of fields that a star appeared in and the quality of the photometry determined how many CMD position epochs there were for each star. Photometry was only used when both the g and i magnitudes were flagged ‘clean’ and had $S/N > 10$. For each g magnitude measurement, I found the closest i magnitude measurement in the lightcurve

and rejected any pairings with time differences > 60 minutes. Fig. 5.1 shows the results for a small subset of stars from the sample. It is immediately clear from these plots that photometric variability is able to move the position of a star very significantly in the CMD. A variety of behaviour is observed, some of which is consistent with motion along extinction vectors, indicating temporal variation in the line-of-sight column density of dust (e.g. star 40 in Fig. 5.1). The rapid timescale on which these changes occur indicate that the extinction changes are most likely to be occurring close to the star, and are perhaps associated with the inner regions of the circumstellar disc. Variability is also seen in many stars which infrared studies indicate do not have an optically thick disc circumstellar disc. For these stars, the amplitude of the magnitude and colour changes implicate cool spots as the source of the variability. Typically in these cases (e.g. star 6 in Fig. 5.1) an increase in brightness is correlated with a blue-ward shift in colour. This behaviour is well known from previous studies of spots on T Tauri stars (e.g. Bouvier et al. 1986b). Beyond these simple cases, a wide variety of phenomena appear to move stars across the CMD in many different ways. A motion that is similar to extinction but ‘flatter’ is often observed, particularly for stars fainter than the principal PMS locus. A clear example of this behaviour is shown by star 14 in Fig. 5.1. I shall later explore the idea that this behaviour is linked with changes in accretion luminosity. This hypothesis is tested further using the spectroscopic data in Chapter 8. Furthermore, some stars show behaviour which initially appears difficult to explain. For example, star 10 in Fig. 5.1 shows variability in g in excess of 2 mag, and the increase in luminosity corresponds to a reddening of the star. This system does not appear in any literature to be an eclipsing binary system, and indeed within this dataset there is no indication that this is the case. The data (including spectroscopic veiling measurements) indicate that the most likely explanation is that this star is an ‘AA Tau analogue’ (Bouvier et al. 1999; Alencar et al. 2010) and that at high inclination the equatorial regions of the star are occulted by orbiting circumstellar material. Hot, blue regions of the photosphere that are associated with accretion may lie close to the high-latitude magnetic poles and thus escape occultation along our line of sight. This would explain the colour, magnitude and spectroscopic changes observed. This star was not however identified by Morales-Calderón et al. (2011) who used $3.6\mu\text{m}$ lightcurves collected using the *Spitzer* space telescope to identify some AA Tau analogue stars in the ONC.

5.2.1 Variability trends

Using the photometric variability data for the entire population, I have searched for correlation between variability and location in the CMD or other physical parameters such as accretion and discs.

Fig. 5.2 compares the variability in the $g, g - i$ plane with CMD position. The variability for each star has been characterised by finding the mean CMD position for each star and fitting a linear least-squares-fit to its locus of positions in this plane as a function of time. The length of the line represents the rms displacement along the variability vector with respect to the mean position for that star. The points are coloured to show whether they are in the accreting, non-accreting disc-bearing or discless samples identified in Chapter 8. Discless stars in this case are those that are not found to show an infrared excess by Megeath et al. (2012) and also have a membership probability

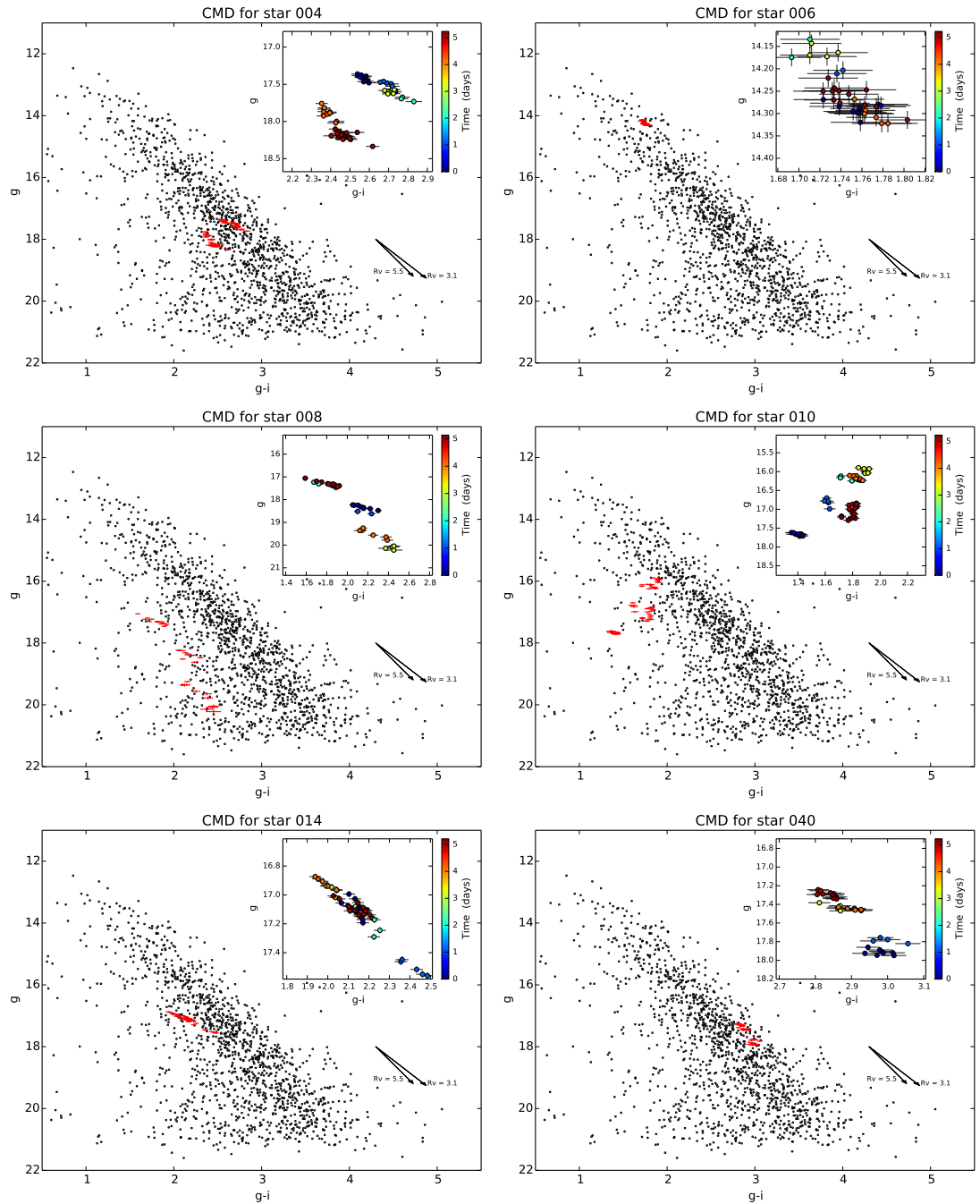


Figure 5.1: g , $g - i$ colour-magnitude diagrams for a selection of target stars showing how their position varies in CMD space over the course of one week. The black points are the mean colours and magnitudes for all stars with clean photometry in this study. The red (grey) points are the positions at different epochs for the target star in question. The inset is a close-up of the positions of the target star, coloured to represent the epoch and highlighting the photometric uncertainties. Extinction vectors corresponding to $A_V = 1.0$ are shown for $R_V = 3.1$ and 5.5 . A range of movement is seen in this diagram, the physical nature of this is investigated in later sections of this thesis.

Table 5.1: Derived parameters for CMD variability for stars in the ONC. Each parameter has a mean value quoted with its standard error. The standard deviations of each parameter across the samples are also shown.

Classification	$\langle \text{vectorlength} \rangle$	σ vector length	$\langle \text{grad} \rangle$	σ grad	$\langle \Delta g \rangle$	σg
Discless	0.085 ± 0.007	0.112	0.96 ± 0.05	0.76	0.057 ± 0.005	0.080
Non-accreting disc-bearing	0.092 ± 0.004	0.065	1.21 ± 0.06	0.90	0.062 ± 0.003	0.055
Accreting disc-bearing	0.145 ± 0.008	0.106	1.17 ± 0.06	0.81	0.098 ± 0.006	0.086

> 95% from Hillenbrand (1997). For the vast majority of stars, a linear fit to the variability in the CMD plane is a good approximation of their behaviour, see examples in Fig. 5.1 and Appendix A.

Table 5.1 summarises the population-level mean vector lengths, gradients and g band variability. It is immediately apparent in this analysis that the accreting population exhibits significantly greater variability in the CMD than the non-accreting disc-bearing or discless populations (see Fig. 5.3). It is also apparent that the variability vectors do not lie parallel to either the reddening vectors or the pre-main-sequence locus. This indicates that the causes of the variability are not simply variations in extinction (although this may play a role) and that variability will act to broaden the pre-main-sequence locus. Broadening of the locus will add an apparent spread in age that is not real. The measured gradients indicate that the accreting stars exhibit variability in CMD space that is ‘flatter’ than the reddening vector and acts to move stars blueward away from the PMS locus more effectively than for non-accreting disc-bearing stars. The gradients for discless stars are even flatter than the accretors, although their relatively low amplitudes limit the spreading effect about the PMS locus. It is curious that whilst the amplitude of the variability is similar between the non-accreting disc-bearing stars and the discless stars, the discless variability is much ‘flatter’, perhaps alluding to a reduced influence from the much steeper extinction vector.

5.3 What contribution does variability make to the ‘age spread’ in the $g, g - i$ diagram for the ONC?

5.3.1 Motivation

In Chapter 8 I will show that accretion luminosity can spread the positions of pre-main-sequence stars in the CMD, emulating a spread in age. This effect appears to be the dominant source of luminosity spread for accreting stars, however for the remaining non-accreting stars (both with and without discs) there remains a luminosity spread that is broader than can be explained simply by binarity and photometric measurement uncertainties. Photometric variability has long been cited as a potential source of luminosity spread (e.g. Hartmann 2001), in the next section I examine whether that variability could be responsible for luminosity spread that is observed in the non-accreting stars.

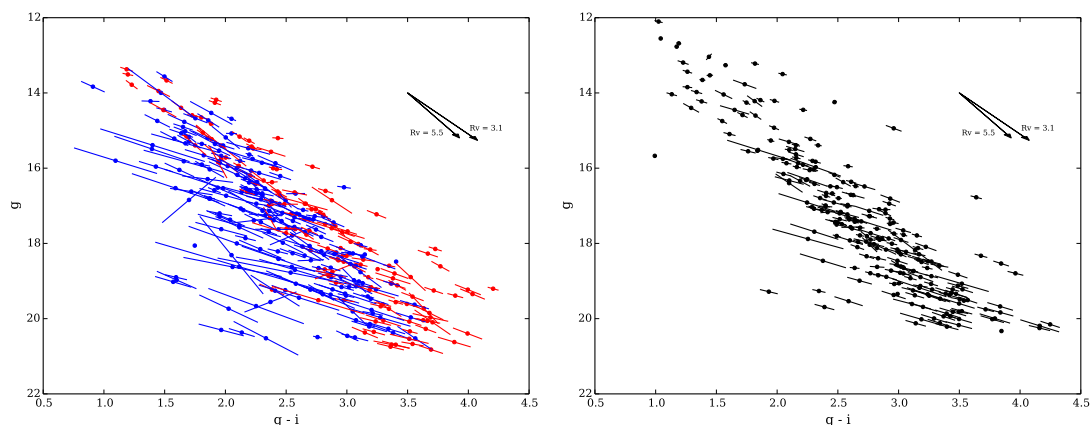


Figure 5.2: A comparison of variability vectors for disc-bearing (left panel) and discless (right panel) stars in the ONC. Each circular data point marks the mean g , $g - i$ position for a given star. The line running through each data point is a linear fit through the variability locus for that star. The length of the line represents the rms variability with respect to the mean position. The points are coloured to show whether they are identified as being in the ‘accreting disc-bearing’ (blue), ‘non-accreting disc-bearing’ (red) or ‘discless’ samples as identified in Chapter 8. The discless sample only shows stars which have membership probabilities $> 95\%$ from Hillenbrand (1997).

5.3.2 Analysis

The dataset provides temporally well-sampled photometric measurements for 411 non-accreting stars in the ONC, 59 of which have *Spitzer* detected discs. These non-accreting stars all have membership probabilities $> 95\%$ in Hillenbrand (1997).

To test whether the observed CMD spread is explained by variability, I have assumed that the cluster is truly co-eval, created a synthetic sample of single and binary stars that fits the mean PMS locus and then displaced these model stars by an amount based on the variability observed in the real data from this study. Comparison of this variability-broadened synthetic population with the real data tells us how much spread can be attributed to photometry variability. This method implicitly includes the effects of photometric uncertainty. This method is very similar to that employed by Burningham et al. (2005), though in that study all stars (including accretors) were included.

I modelled the intrinsic pre-main-sequence locus as a linear relation between $1.5 < g - i < 3.5$. Within this range the linear assumption appears true and the real pre-main-sequence is densely populated for effective comparison. Stars with $g - i < 1.5$ are close to the radiative-convective gap (Mayne et al. 2007) and the density of stars available for fitting is significantly reduced. Stars with $g - i > 3.5$ are getting close to the sensitivity limit in g such that faint objects are not detected, hence potentially skewing the analysis. The linear fit to the PMS was calculated by dividing the real CMD into 0.25 mag wide bins in $g - i$ and calculating a mean magnitude for each bin, iteratively clipped at 1.5σ until no further stars were rejected. The sigma clipping reduced the impact of extreme stars. The binned magnitudes were then least-squares-fit with a straight line described by the function

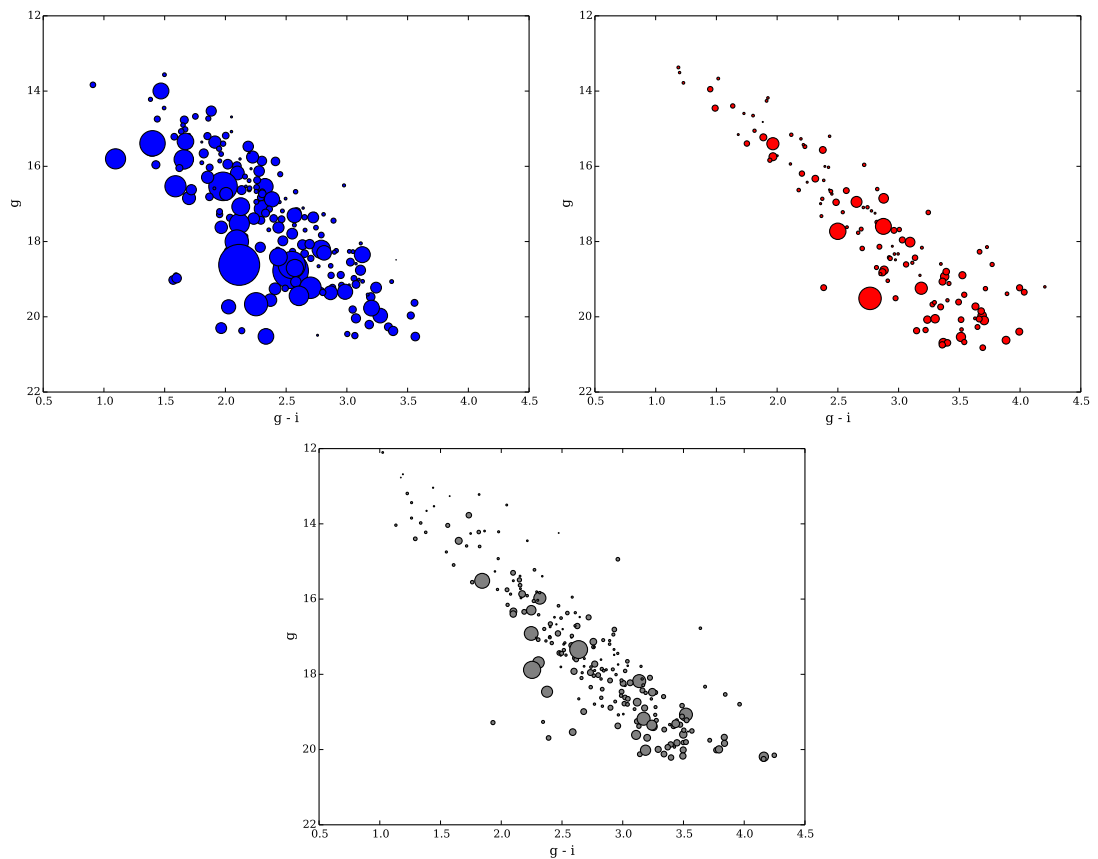


Figure 5.3: The amplitude of the variability vectors shown in Fig 5.2 are presented for the accreting (top left), non-accreting disc-bearing (top right) and discless (lower middle) stars as a function of CMD position. The diameter of each symbol corresponds linearly with the length of the variability vector in Fig 5.2. In addition to the CMD position differences between the populations, it is clear that the accreting population exhibits significantly greater variability. The non-accreting disc-bearing and discless populations are indistinguishable.

$$g = 3.125(g - i) + 9.027. \quad (5.1)$$

This linear fit is shown in the left panel of Fig. 5.4, compared with the real data. A number of synthetic stars (equal to the number of real stars in the sample) were then generated with a uniform distribution in $g - i$ and a magnitude defined by the PMS locus function. Stars were then randomly assigned to a binary population (assuming a binary fraction of 0.5) and given a magnitude randomly selected from a uniform distribution between the single-star sequence and the ‘single-star sequence + 0.75 mag’ corresponding to equal-mass binaries. The single-stars plus binaries model population may be seen in the centre panel of Fig. 5.4, compared with the real data.

Each synthetic star in the model population was then displaced by an amount corresponding to real variability in the dataset using the following process. Firstly the synthetic star was matched to the star closest in mean magnitude in the real data. A point was then randomly selected from the lightcurve of the matched real star. The difference in magnitude and colour between this lightcurve point and the mean for the real star was calculated. This is the variability-induced CMD displacement for the real star about its mean position. The calculated displacement was then applied to the synthetic star. This process was applied to all synthetic stars. The catalogue of stars from which variability was measured contained only non-accreting stars. The variability broadened synthetic population may be seen in the right panel of Fig. 5.4, compared with the real data. To compare the spread in the real and synthetic populations I then calculated the difference in $g - i$ colour between all stars (real and synthetic) and the model locus at each star’s given magnitude. Fig. 5.5 compares histograms of the deviations about the mean locus for the real and synthetic data sets.

It is immediately clear from Fig. 5.5 that the variability-broadened model sequence does not describe the full spread that is seen in the real pre-main-sequence population. To quantify the discrepancy I calculated the rms deviation in $g - i$ for the real and synthetic populations. The rms of the real data, $\Delta(g - i) = 0.376$ mag. The rms of the synthetic data, $\Delta(g - i)_{\text{var}} = 0.114$. As sources of luminosity spread may be assumed to combine in an additive manner

$$\Delta(g - i) = \sqrt{[\Delta(g - i)_{\text{var}}]^2 + [\Delta(g - i)_{\text{Other}}]^2}, \quad (5.2)$$

where $\Delta(g - i)_{\text{Other}}$ is the spread caused by unknown sources other than binarity, variability and photometric uncertainty. It then follows that

$$\Delta(g - i)_{\text{Other}} = \sqrt{[\Delta(g - i)]^2 - [\Delta(g - i)_{\text{var}}]^2}, \quad (5.3)$$

and using the measured values of these parameters

$$\Delta(g - i)_{\text{Other}} = 0.358, \quad (5.4)$$

so the fraction of the CMD spread that can be attributed to variability f_{var}

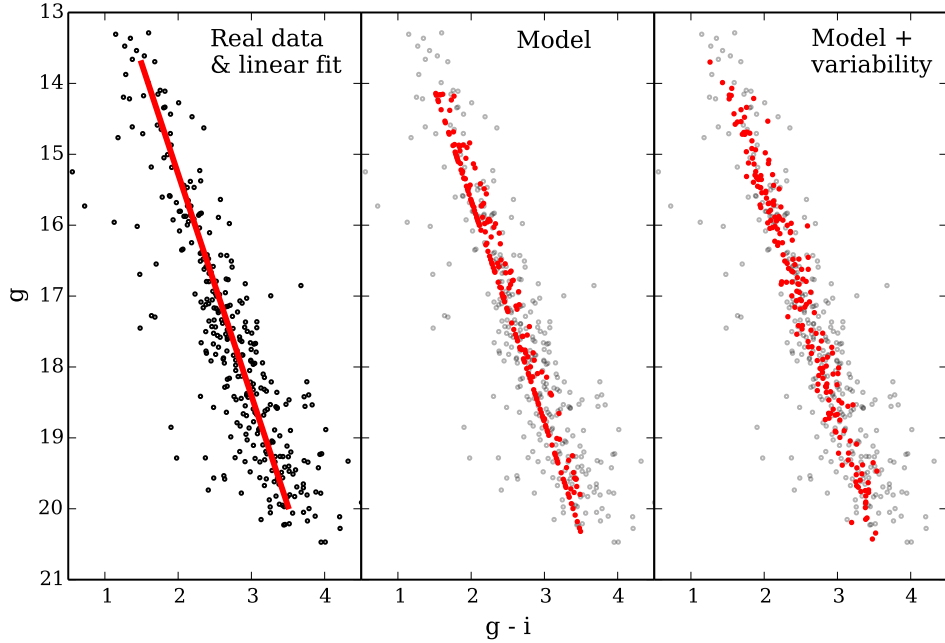


Figure 5.4: The synthetic model population, constructed and compared with the real data for the ONC. The left panel shows the real ONC data (black circles) overlaid with the model locus (red line). The central panel shows a synthetic model population of stars with binary fraction 0.5 displaced equally about the model locus (red dots). The real data is compared (grey dots). The right panel shows the synthetic population dispersed by the variability measured from my real lightcurve data (red dots) and compared with the real data (grey dots). It is clear that the spread in the model population which simulates the effects of binarity, variability and photometric uncertainties is insufficient to explain the full luminosity spread in the data.

$$f_{\text{var}} = \frac{\Delta(g-i)_{\text{var}}}{\Delta(g-i)_{\text{var}} + \Delta(g-i)_{\text{Other}}} = 0.24. \quad (5.5)$$

Thus only $\sim 1/4$ of the CMD spread that is seen appears to be due to variability or measurement uncertainties when the effects of accretion luminosity (and its intrinsic variability) are removed. This is strong evidence to support the findings of Jeffries (2007) who conclude that intrinsic radius spreads (of a factor 2-3) are present in the ONC.

A comparison was made between the deviation in g from the locus described in Equation 5.1 for each star. The measured deviations were compared with literature $v \sin i$ and period data to investigate whether any correlation was present. No correlations were seen.

5.4 Summary

The ages for individual YSOs (in contrast to population studies) are also often calculated based on their position relative to model isochrones in the colour-magnitude diagram. (e.g. Palla & Stahler 2000; Drake et al. 2005; Güdel et al. 2007). These derived ages often have a significant influence

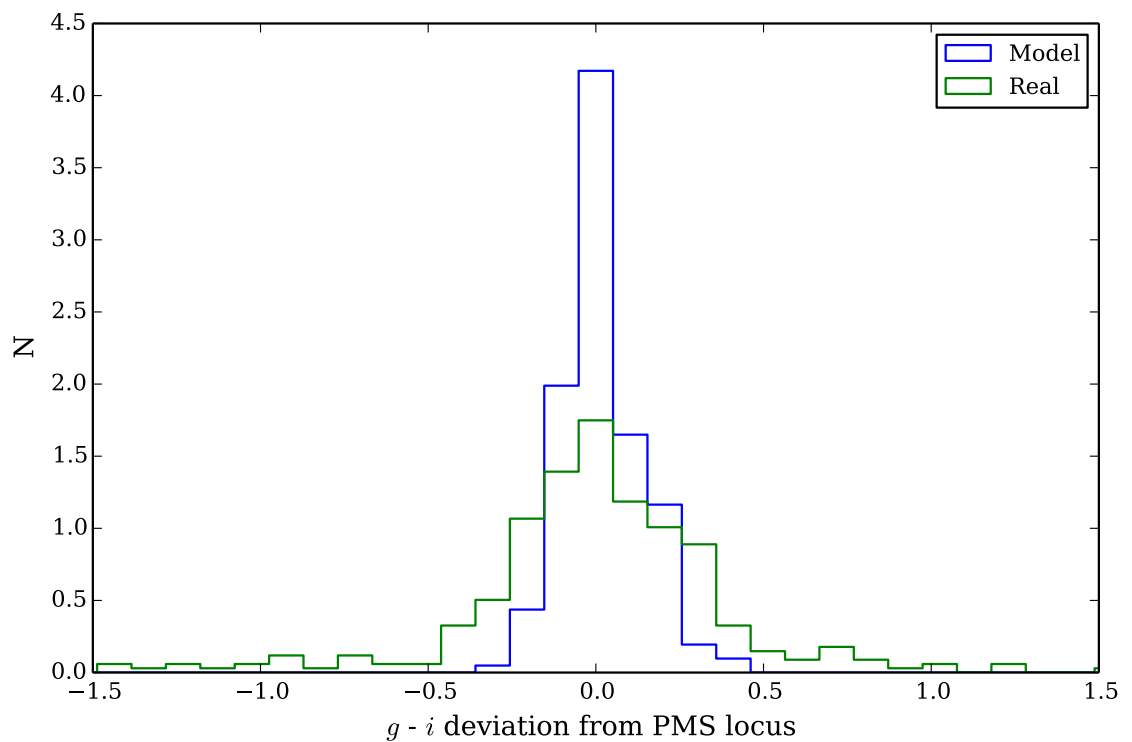


Figure 5.5: Histograms to show the spread in $g - i$ present in the model (blue) and real (green) CMD data for the ONC. Each histogram is constructed by binning the deviations in $g - i$ shown for all stars in a sample about the model PMS locus. The real data is clearly spread more widely than the model dataset, implying that a source of spread is present in addition to the binarity, variability and photometric variability modelled in this analysis.

on the conclusions drawn about other astrophysically important parameters such as the formation time for planets or dispersal time for circumstellar discs (Boss et al. 1989). The variability that is displayed by young stars in this study shows that an age derived for an individual star based on its CMD position in single epoch photometry must be considered highly uncertain, particularly for accreting stars. Ensemble ages for a given star forming region will be more robust as the error on the mean stellar locus will be far more weakly influenced by variability.

The spread in luminosity caused by variability, binarity and photometric uncertainty has been shown to be insufficient to explain the luminosity spread that is seen in non-accreting stars. This implies that other mechanisms may be responsible, or that there is indeed an intrinsic spread in age in a given star-forming region. Additional sources of luminosity spread that are unrelated to age may include imperfect extinction correction or spot-induced radius variations (Jackson & Jeffries 2014).

Chapter 6

Dust within the inner regions of YSO discs

6.1 Introduction

Grain-grain collisions in circumstellar discs around young stars represent the first stage of planet formation (Beckwith et al. 2000). These collisions are thought to be much more frequent than in the interstellar medium (ISM) and allow dust grains to grow beyond the sub-micron sizes characteristic of the ISM. Despite its importance in the process of planet-building, observational data on how fast grain-growth occurs around young stars and what the distribution of grain sizes might be within the disc is sparse and contradictory.

The only observational metric of dust grain sizes is through the wavelength dependence of extinction measurements. Grain growth is expected to increase the opacity at long wavelengths and decrease the opacity at short wavelengths. The opacity is likely to become completely grey (constant with wavelength) as the grain size becomes much larger than the wavelengths in question. Throop et al. (2001) estimated grain sizes in the outer regions (> 350 AU) of a resolved circumstellar disc in Orion by comparing the opacity of the disc against the background nebular emission at $H\alpha$ and Paschen- α wavelengths. They found that the extinction appeared ‘grey’ to a level of $\sim 5\%$. This suggests that grains are larger than $\sim 5\mu\text{m}$, 25 to 50 times larger than typical ISM grains. Shuping et al. (2004) used Brackett- α measurements to refine this result, concluding that grains slightly larger than $\sim 4\mu\text{m}$ were present. Ricci et al. (2010) model observed mm-wavelength SEDs for 21 isolated disc-bearing stars in Taurus. They conclude that grain growth occurs quickly in YSOs, perhaps even during the protostellar stage, and present evidence that mid-plane grain sizes have reached sizes of 1mm. In contrast, Watson & Stapelfeldt (2004) observe light scattered by the disc of HH30 and compare these observations with models of disc geometry and grain size. They conclude that the dust opacity in the scattering layers of the outer parts of the disc of HH30 is not grey between 0.44 and $2.04\mu\text{m}$, however it is less chromatic than in the ISM. This suggests that moderate grain growth has occurred but that small grains still dominate the visible and near-infrared opacity. This result and others at wavelengths where the disc is optically thick are not able to observe dust within the mid-plane of the disc. Thus grain growth may be underestimated,

particularly if larger grains preferentially settle toward the mid-plane.

As these previous studies have relied on resolving the disc to perform their measurements, they are limited by instrument resolution to studying the outer regions. It is not clear whether dust grains within the inner regions of the disc differ from those of the outer regions and whether this has any impact on the formation of planetary systems. However, McGinnis et al. (2015) suggest that dust grain growth has occurred within the inner regions of YSO discs based on the infrared colour evolution of photometry of stars apparently exhibiting occultation by inner disc dust in NGC 2264.

As well as understanding the evolution of dust grains in the disc, the colour dependence of disc-extinction is important to the study of the evolution of young stars. Very often the photometry of young stars is corrected for the effects of extinction and reddening before conclusions are drawn about important astrophysical parameters (e.g. Hillenbrand 1997; Mayne et al. 2007; Bell et al. 2013; De Marchi et al. 2013). The photometric corrections are based on models of interstellar extinction measured along sight-lines within the Galactic plane (e.g. Cardelli et al. 1989; Fitzpatrick 1999) where the chromatic dependence of the extinction is defined by

$$R_V = \frac{A_V}{E(B - V)} \quad (6.1)$$

where A_V is the extinction in V and $E(B - V)$ is the difference in extinction between the B and V bands. A value of $R_V \approx 3.1$ is that typically adopted when dereddening young stars, however the direct measurements of circumstellar disc dust opacity indicate that this value is most-likely too low for extinction in high inclination YSOs. If we under-estimate R_V , the effect is to underestimate the luminosity of young stars when correcting for extinction based on measured colour-excess.

There is strong evidence that the inner discs of YSOs exhibit significant vertical structure (Bouvier et al. 2003; Alencar et al. 2010; Morales-Calderón et al. 2011; Cody et al. 2014). Material within the inner disc orbits close to the star (\lesssim few stellar radii) with near-Keplerian velocity. In systems that are viewed at high inclination, orbiting vertical structures occult the star, causing the observed flux to rise and fall on timescales of a few days.

Multi-wavelength simultaneous photometry and spectroscopy provides a unique way of probing the opacity (and hence dust grain sizes) within these occulting inner-disc regions. By selecting disc-bearing stars which show variability in their SED which is unrelated to changes in accretion luminosity or cool spots (constrained using the spectroscopic time-series data), I can measure the wavelength dependence of opacity changes in the inner disc dust.

6.2 Extinction driven variables as probes of inner-disc dust

6.2.1 Selection of purely extinction variability stars

To identify a set of stars that exhibit variability which is simply driven by changes in extinction, I compare the equivalent width (EW) of the TiO band at 7050Å (EW_{TiO}) with the n_{6800} flux at every available epoch over the seven nights of observations. If the brightness of the star is varying due to

changes in the accretion luminosity then I would expect to see changes in the veiling of the spectral lines that correlate with the changes in brightness. If instead, the veiling remains constant as the brightness of the star changes, then the variability mechanism is most likely to be occultation of the star by material within the circumstellar disc.

Fig. 6.1 shows plots of n_{6800} flux against EW_{TiO} for four stars from my sample which show significant brightness changes at constant EW_{TiO} . In contrast Fig. 6.2 shows the same parameters plotted for two stars that exhibit brightness changes due to accretion (verified through changes in U band excess) and cool-spots (verified through lack of a circumstellar disc) respectively. The four stars identified as varying in brightness at constant equivalent width also show variability in the $U - g$, $g - i$ diagram that is consistent with motion along extinction vectors. It is not inconceivable that some residual accretion luminosity changes may be present within the lightcurves of these stars, however the effects of these luminosity changes must be present at a level $< 4\%$ (see Section 6.2.2) except in the case that accretion changes are extremely well correlated with changes in the extinction. Also, in Chapter 5 I show that the accretion luminosity vectors in the g , $g - i$ CMD are quite similar in gradient to that of the extinction vectors. Thus, a low level of accretion luminosity contamination will simply amount to a small systematic error that under-estimates the derived R_V . As shown in Section 6.2.3, this has little effect on the conclusion that grain-growth is occurring within the inner disc.

6.2.2 Analysis of variability in the SED

The multi-colour photometric time series described in Chapter 4 allowed me to construct a six-band multi-epoch photometric SED time-series that covered the wavelength range $\sim 0.36 - 0.77 \mu\text{m}$. Thus I could study how the optical SED for each star varied over the seven nights of observations. Each single epoch SED for a given star was constructed by taking a point in the r lightcurve, finding the closest photometric measurement in each of the other bands and combining them into a single SED. All of the measurements for a given single epoch SED were made within 0.5 hour of the r measurement and most were made within < 10 minutes.

To identify the most important spectral contributors to the SED variability, I applied a principal component analysis (PCA) to the SED time series. PCA identifies the smallest set of independent spectra (that must be added to the mean spectrum) that account for the observed variance in the time-series. The first step was to calculate the mean spectrum $\langle S \rangle$ and subtract it from the individual SEDs. Next I computed the covariance matrix of the SED time series and determined the eigenvectors (E_i) and eigenvalues (Λ_i) of the covariance matrix. Components were then sorted by eigenvalue, and the contribution of each component to the overall variability was determined by $\Lambda_i / \sum \Lambda_i$ where $\sum \Lambda_i$ is the sum of the eigenvalues for all components.

Individual spectra $S(t)$ are re-constructed as

$$S(t) \approx \langle S \rangle + c_0(t)E_0 + c_1(t)E_1 + \dots + c_i(t)E_i \quad (6.2)$$

where the series is truncated to include only components that contribute significantly above the noise level. $c_i(t)$ is the projection of the principal component onto the individual $S(t) - \langle S \rangle$.

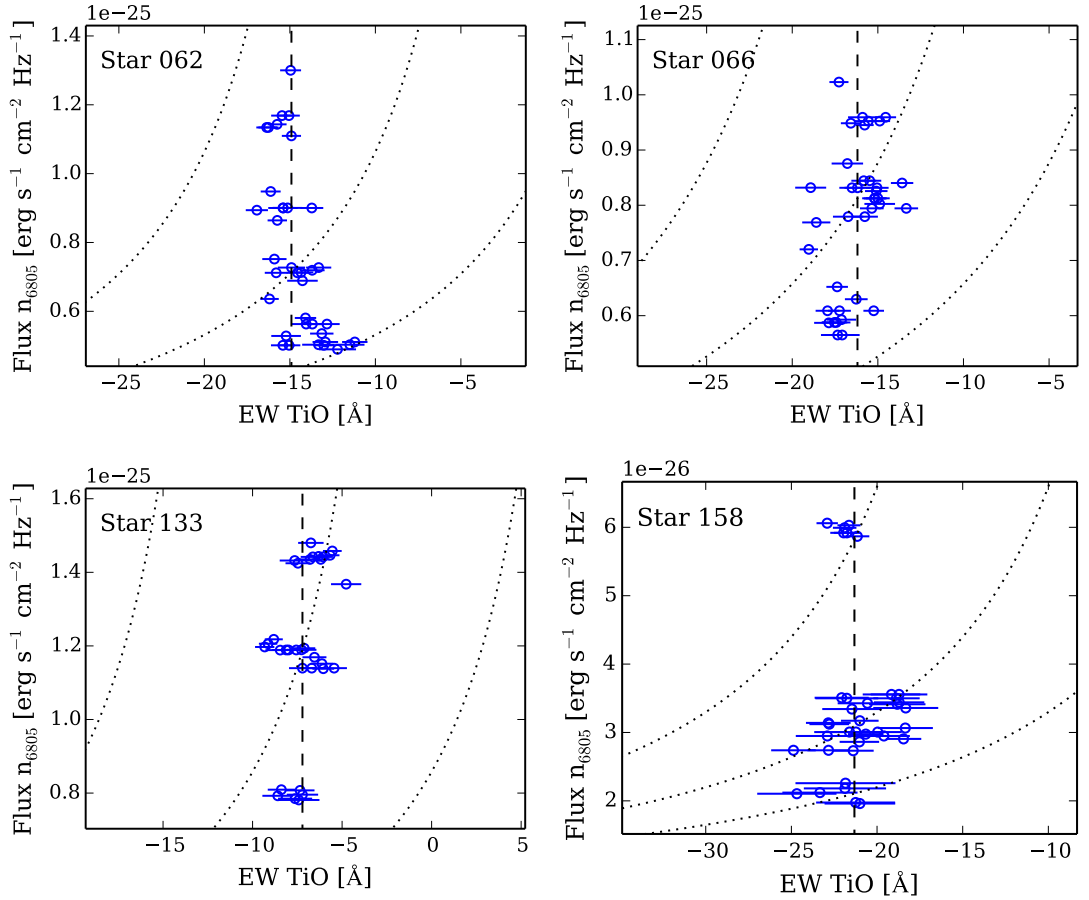


Figure 6.1: n_{6800} flux plotted against EW_{TiO} for four stars which show flux variability without apparent changes in the EW of the photospheric lines. The blue points are the measurements for the star at epochs over 7 nights of observations. The black dotted lines are vectors along which the star should move if the line EW was ‘veiled’ by an amount corresponding to the change in flux in the n_{6800} band. As these stars move vertically in this plot, the flux changes that we see are likely to be driven by occultation/extinction of the star rather than changes in the accretion luminosity or cool-spot coverage. Fig 6.2 shows the equivalent plot for two stars which show photometric modulation that is attributed to changes in accretion luminosity and cool spots.

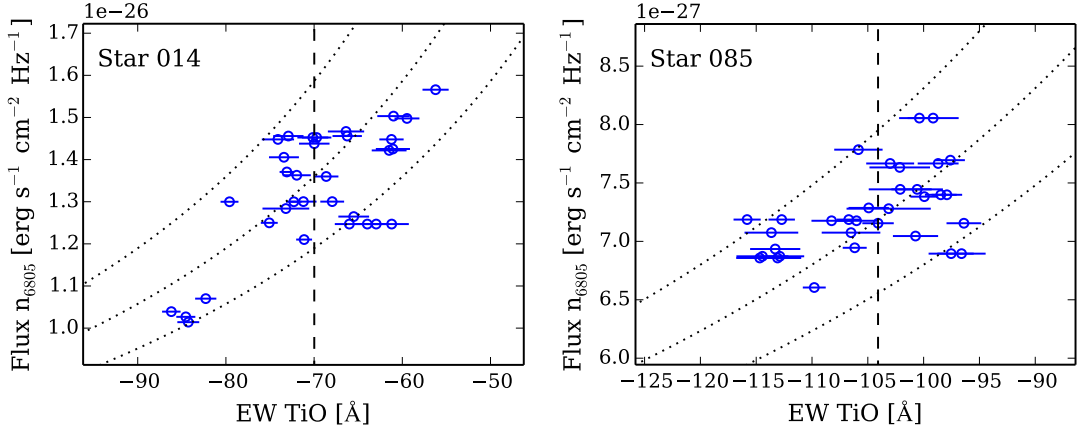


Figure 6.2: For comparison with Fig. 6.1, the same data is plotted for a star that shows significant accretion luminosity changes (left panel) and brightness changes that are attributed to change in cool-spot area (right panel). They are clearly distinguishable from the stars in 6.1 as they show significant changes in EW_{TiO} as the n_{6800} flux varies. The black dotted lines are vectors along which the star should move if the line EW was ‘veiled’ by an amount corresponding to the change in flux in the n_{6800} band.

Table 6.1: Key parameters for stars which show variability in extinction. A_i is that measured in Chapter 7 at a single epoch and varies from this value. Spectral types are from Hillenbrand et al. (2013). The fraction of the SED variability described by the FPC is shown in column 6. In all of these stars, the variability due to the FPC is dominant, comprising $> 96\%$ of the variability observed.

Star ID	RA hh mm ss.ss	Dec dd mm ss.s	A_i mag	Spectral type	First PC fraction %
62	05 35 52.76	-05 12 59.0	0.25±0.25	K5-K6	98.7
66	05 35 46.12	-05 10 51.8	0.25±0.25	K7	97.5
133	05 34 19.54	-05 30 19.9	1.10±0.25	K5	96.8
158	05 35 12.21	-05 30 32.9	2.10±0.25	M0.5	98.5

For the four extinction modulated stars, just one principal component is required to reconstruct $> 96\%$ of the variability in the SED time-series. This strongly implies that just a single physical phenomenon is changing the luminosity of the star and the constant equivalent width of the photospheric TiO lines is strong evidence that the variability is unrelated to changes in accretion luminosity or cool spots. The first principal component (FPC) for each of the four stars are compared with their mean SEDs in Fig. 9.7. The fraction of the variability that the FPCs describe are shown in Table. 6.1.

6.2.3 Measurement of R_V

To determine the wavelength dependence of the extinction, the mean scaled FPC for each star was divided by its mean spectrum to derive the extinction curve. To eliminate the possibility of variability due to seeing, chromospheric activity or wind emission spuriously influencing the result

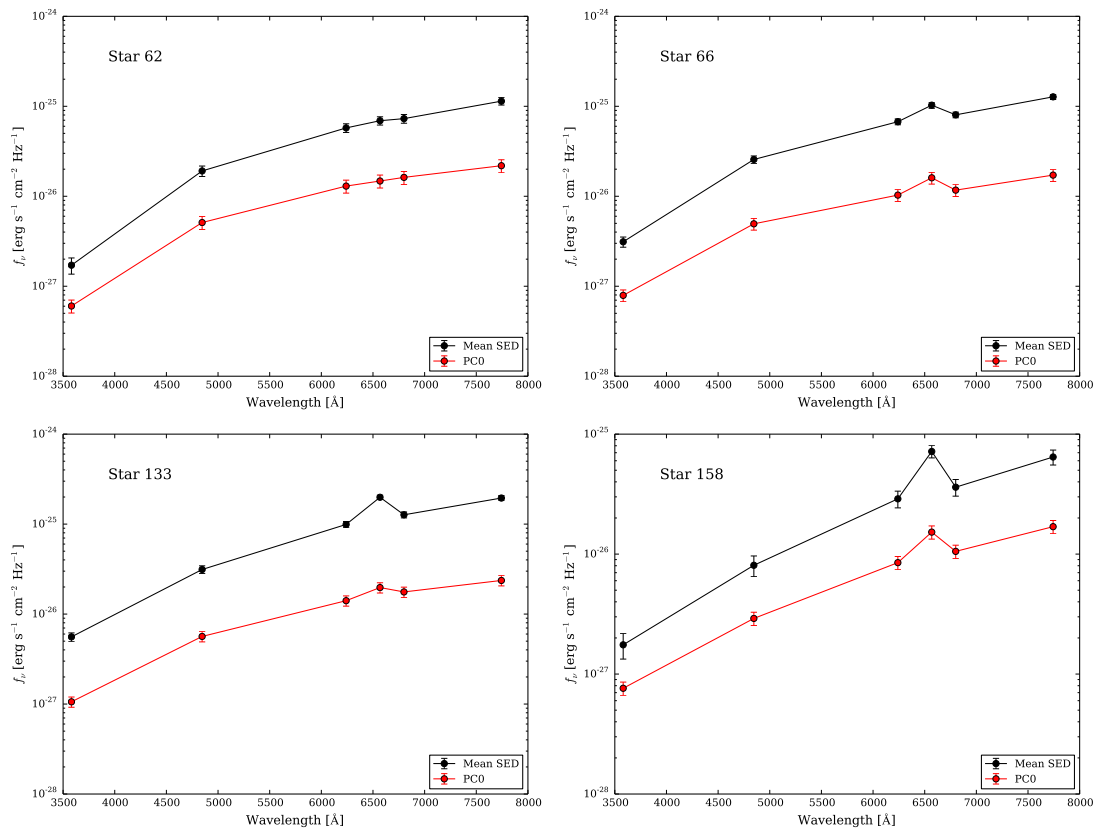


Figure 6.3: The mean spectrum (black) compared with the FPC (red) for each of the ‘extinction’ driven variable stars. In each case the FPC has been scaled by its mean amplitude from the seven nights of observations. The FPCs describe almost all of the variability ($> 96\%$) for each star. Each FPC also appears to be essentially a scaled version of the mean spectrum, supporting the assertion that extinction changes are driving the variability in these stars.

I have not included the $H\alpha$ photometry in this analysis. Both the mean spectrum and the FPC will be reddened by the ISM between the star and the observer, however by dividing one by the other, this effect is cancelled and any chromatic dependence is associated with a change in extinction that has occurred on the timescale of hours or days.

To compare the extinction curves for each star against those published for the ISM, the curves were normalised at the effective wavelength of the V filter ($\approx 5500\text{\AA}$). Fig. 6.4 shows the normalised extinction curves with ISM models from Cardelli et al. (1989). On comparison with the models, it is immediately clear that the extinction for the stars is ‘greyer’ than that of the ISM. To quantify this, I have calculated R_V for each star. As the definition of R_V is based on the Johnson B and V filters (Bessell 1990), I have predicted the extinction A_V and A_B in these filters. I did this by performing a simple linear interpolation between my extinction measurements which are made at the effective wavelengths of the INT WFC filters. I then calculated R_V as per Equation 6.1. The measured values are shown in Table 6.2. It is possible that increases in extinction that are highly correlated with increases in accretion luminosity (particularly U band) could bias this measurement toward a higher value of R_V . Whilst this is possible it appears unlikely, as changes in veiling should be observed if changes in accretion luminosity were occurring. Changes in veiling are not seen, implying that changes in accretion luminosity are small.

The wavelength dependence of the extinction ranges from $R_V = 5.03$ to 8.26 . Thus the circumstellar material being probed imparts a smaller colour dependent extinction than is typical for the ISM ($R_V \approx 3.1$). This implies that typical grain size distribution is greater than that the 10^{-3} to $1\mu\text{m}$ distribution modelled for the ISM by Weingartner & Draine (2001). This range of R_V values also indicates that whilst dust grain-growth has occurred within the disc environment, the typical grain size appears to be smaller than the $\sim 5\mu\text{m}$ grains found in the outer disc by Throop et al. (2001). In practice, we are looking at a distribution of grain sizes and the behaviour observed would be well modelled by simply increasing the fraction of grains larger than $1\mu\text{m}$ compared with the ISM.

Table 6.2: Derived extinction parameters for ‘variable extinction’ stars. A_V and A_B are found by linear interpolation of extinctions in the INT WFC filters. Note that all of the R_V values are ‘greyer’ than that typically adopted for the ISM ($R_V \approx 3.1$).

Star ID	ΔA_V	$\Delta E(B - V)$	R_V
62	0.240	0.039	6.11
66	0.174	0.035	5.03
133	0.163	0.020	8.26
158	0.308	0.044	7.02

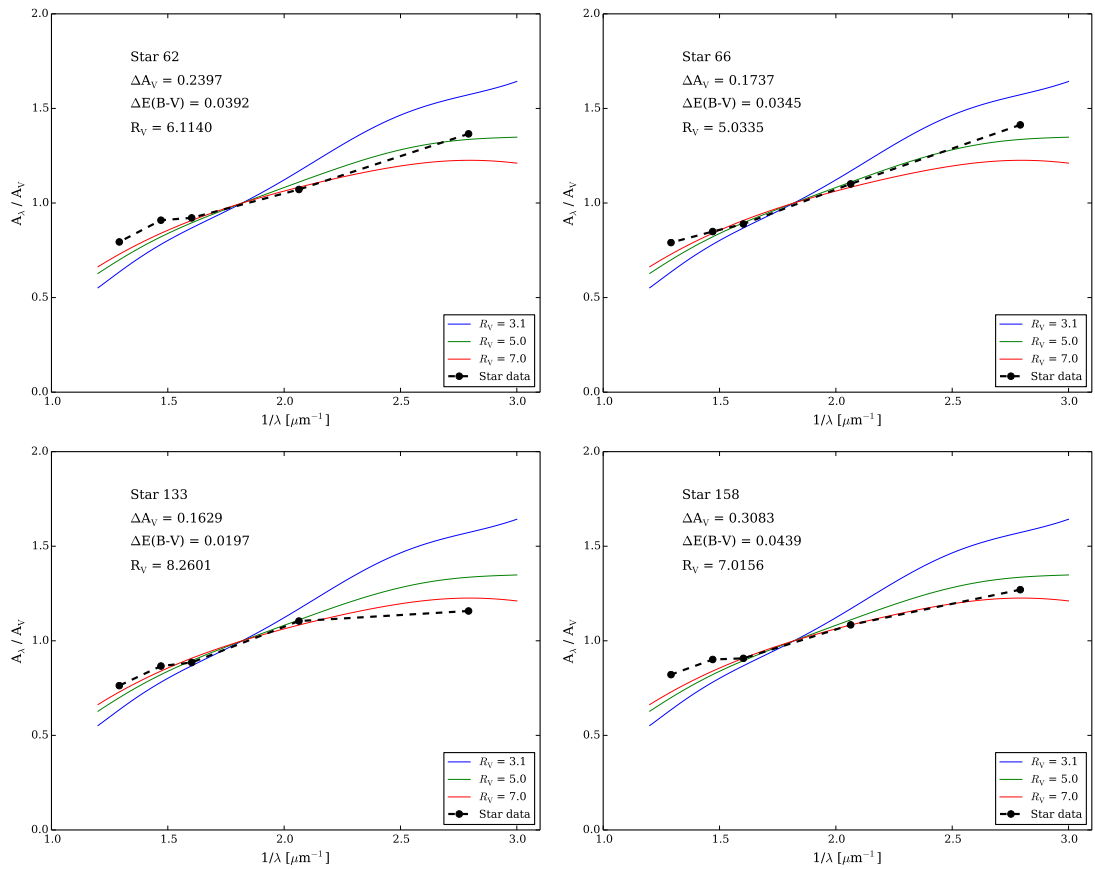


Figure 6.4: Normalised extinction curves for the YSO variability are compared with ISM models. The black points are the extinction curves calculated for each star, coloured lines are models of extinction from Cardelli et al. (1989), using $R_V = 3.1, 5.0$ and 7.0 . It is clear that the circumstellar extinction is ‘greyer’ than that typically seen in the ISM, implying that grain growth has occurred.

6.3 Discussion

6.3.1 The location of the extinguishing material

The short timescale of the extinction changes that are studied strongly imply that their origin is within the inner regions of the circumstellar disc. Alencar et al. (2010) studied photometric variability in NGC 2264 and found that $28 \pm 6\%$ of disc-bearing stars show photometric fading consistent with periodic dust obscuration of the photosphere. Periods between 2 and 15 days were found, the peak of the distribution being at ~ 5 days. They interpreted these results as being due to quasi-stable vertical structures within the inner disc, orbiting at close to Keplerian velocity, analogous to the well studied AA Tau system.

If the extinction events that I have observed are due to AA Tau type phenomena, then given the typical range of orbital periods observed and assuming Keplerian orbital motion about stars with mass $0.1 < M_{\star} < 2.0M_{\odot}$, one can simply calculate the likely range of orbital radii over which this material must occur. Fig. 6.5 shows the orbital radius dependence (in R_{\odot}) of period and stellar mass in a Keplerian system. In the case of extinction in an AA Tau analogue system, the material will most likely lie between 5 and $30 R_{\odot}$ (0.02 - 0.14 AU) from the star.

It may be that the extinction changes that I have studied are not actually related to the AA Tau phenomenon and may instead be due to clumps of material located above the surface of the disc within regions further from the star. The size of these clumps is constrained by the magnitude and rate at which the variability occurs. I see flux changes of order two that occur on timescales of a single night. For a clump to appreciably attenuate the star (along our line of sight) and assuming that the clump is much closer to the star than it is to the observer, it must have a linear size (along the orbital velocity vector) that is of the order of the diameter of the star. For the change in flux to occur on timescales of a single day, we can infer the limit on the radial position of the clump within the disc through a dynamical argument. The orbital velocity of disc material reduces as the radial disc position increases by

$$V = \sqrt{\frac{GM_{\star}}{r}}. \quad (6.3)$$

Where M_{\star} is the mass of the star, G is the universal gravitational constant and r is the orbital radius. The minimum line-of-sight crossing velocity for material occulting the star is

$$V_{min} \approx \frac{2R_{\odot}}{\Delta t}. \quad (6.4)$$

So the upper-limit on the orbital radius of clump material that could cause the extinction changes that we see is

$$r \lesssim \frac{GM_{\star}\Delta t^2}{4R_{\odot}^2}. \quad (6.5)$$

Fig. 6.6 shows Equation 6.3 plotted for stars with masses of 0.1, 0.5, 1.0 and $2.0 M_{\odot}$. The orbital velocity is calculated to a radius of 1000 AU. The minimum orbital velocity that is possible to occult the star in 1 day is calculated using Equation 6.4 and is also compared in Fig. 6.6. This

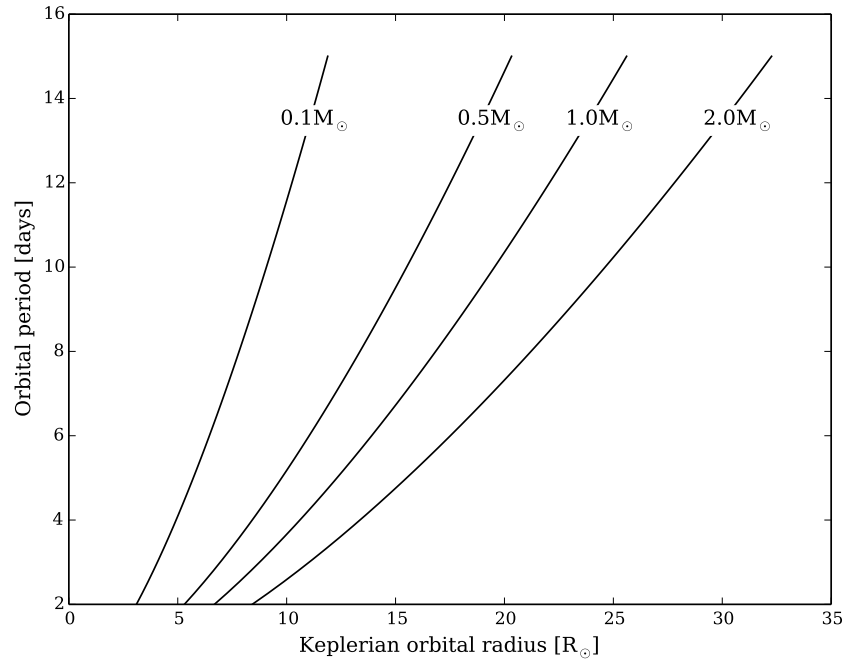


Figure 6.5: Calculated orbital radii of material in Keplerian orbits about stars with mass 0.1, 0.5, 1.0 and 2.0 M_{\odot} as a function of period. The radii calculated are typical of quasi-static structures in the inner-discs of ‘AA Tau analogue’ systems found in NGC 2264 by Alencar et al. (2010).

places limits on the maximum radial distance of clumps that could be causing the extinction that is seen. The radial distance must be less than ~ 20 AU for a star of $1M_{\odot}$ and less than ~ 1.5 AU for a star of $0.1M_{\odot}$. These limits are conservative as the radius of a $1M_{\odot}$ star is assumed to be $\sim 1R_{\odot}$. In reality a PMS star will be of a larger radius than its equivalent main-sequence dwarf, thus the minimum velocity limit will be higher and the outer orbital radius limit will be smaller. The inner radial limit of extinction measurements made by Throop et al. (2001) and Shuping et al. (2004) are ≈ 350 AU.

The extinction measurements made in this study are for dust that must be at least 1 - 2 orders of magnitude closer to the star than those made by resolved imaging studies. However, the further away from the star that we consider these extinguishing clumps to be, the less likely it is that we are able to observe them as the required inclination and range of possible inclinations becomes much smaller. Thus, by a probabilistic argument, it is more likely that we are observing extinction by AA Tau like structures than more distant clumps at up to 20 AU from the star.

6.3.2 Grain growth

R_V values of between 5.03 and 8.26 are measured for extinction within the central regions of four YSO discs. This suggests that moderate grain growth has occurred but that grains are smaller than the $4\text{-}5 \mu\text{m}$ grains found by Throop et al. (2001) and Shuping et al. (2004) in the outer disc. It is not possible to tell whether the grain-growth within the inner regions has been inhibited in some way by the intense radiation from the star or by particle collisions, or whether smaller grains are present due to reprocessing of material during accretion outbursts (Ábrahám et al. 2009).

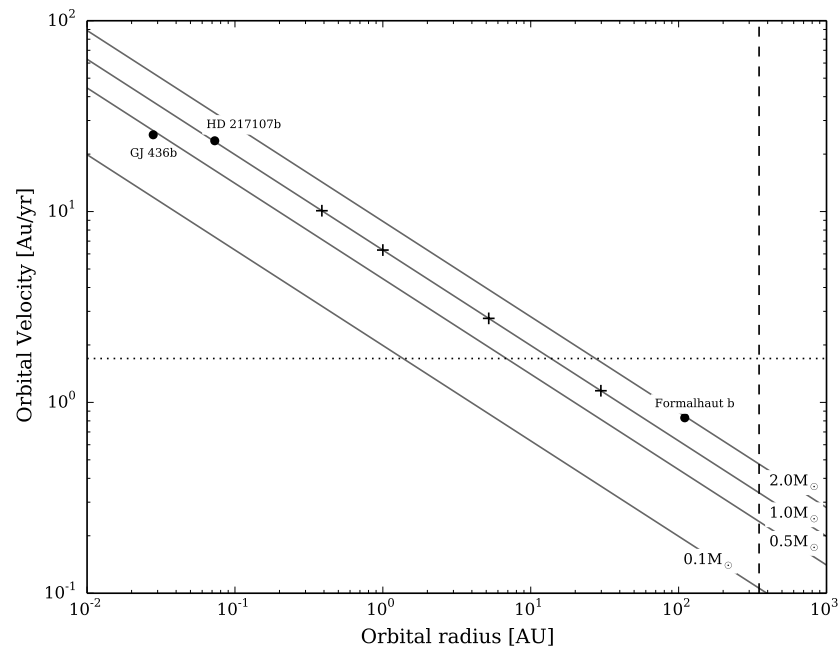


Figure 6.6: The Keplerian velocity of material orbiting stars of mass 0.1, 0.5, 1.0 and 2.0 M_{\odot} as a function of orbital radius (black solid lines). The black dotted line shows the lower limit of orbital velocity required to occult a star of radius $1R_{\odot}$ in 1 day. The dotted line places upper limits on the orbital radius of clumps that could provide the variable extinction that I measure in Section 6.2.3. For comparison Mercury, Earth, Jupiter and Neptune (black crosses) and some extra-solar planets (labelled black circles) are shown. The inner radius of the measurement by Throop et al. (2001) of outer disc dust is shown by the black dashed line, indicating the regions probed in this study are between 1 and 2 orders of magnitude closer to the star.

If this dust is indeed located within AA Tau like warped disc structures, the implications for the mechanism of grain growth are profound. Models of YSO discs suggest that the ‘snow line’ (the radius beyond which temperatures are low enough for the formation of icy materials) is of the order of an AU or greater (Sasselov & Lecar 2000; Kennedy & Kenyon 2008; Martin & Livio 2012). In the ISM, the mechanism that is invoked to explain differences in observed values of R_V is the addition of icy mantles on the surface of dust grains (Draine 2003). Within the snow line of YSO discs it is too hot for such icy mantles to form, thus the implication is that the grain growth observed here must be due to genuine coagulation of small dust grains to form larger grains. This view is supported by the observations of McGinnis et al. (2015) who detect a difference in infrared extinction slopes (the ratio $A_{4.5\mu\text{m}}/A_R$) between inner disc dust in AA Tau analogues in NGC 2264 and that seen in the ISM. In the ISM, the infrared extinction slope is quite insensitive to R_V . The discrepancy in $A_{4.5\mu\text{m}}/A_R$ might therefore imply that in YSO discs, not only are the small grains growing and hence influencing the optical extinction, but that a new population of grains have formed at the large end of the size spectrum, beyond that normally seen in the ISM.

6.3.3 Photometric extinction correction

When correcting the magnitudes of stars for the effects of extinction, models usually assume $R_V \approx 3.1$. If however, a significant fraction of the extinction for a given star is due to material in the circumstellar environment rather than the ISM, the findings of this study indicate that the R_V value should be higher. If R_V is systematically underestimated, then the extinction-corrected luminosity of the star will also be underestimated. This would lead to a spurious radius determination and CMD or Hertzsprung-Russell diagram derived ages would be over-estimated.

For the four extinction variable stars in this study, I can put some limits on the fraction of the extinction that results from both the ISM and the circumstellar environment as the overall extinction has been estimated using spectral fitting in Chapter 7. The mean extinction change due to occulting inner-disc material has been calculated by multiplying the FPC i flux measurement by the mean FPC amplitude from the seven nights of observations. As the mean extinction change is a deviation from the mean spectrum and occurs in a positive and negative sense at some point in the lightcurve, the peak-to-peak inner-disc extinction is twice the mean extinction change.

Table 6.3 compares the inner-disc extinction peak-to-peak amplitude (in the i filter) with spectroscopically derived A_i values from Chapter 7. For two stars, the overall extinctions can be entirely explained by the inner-disc circumstellar material. For the other two stars, $\approx 25\%$ of the observed extinction can be attributed to inner-disc circumstellar material, the rest being due to the ISM or material within the outer reaches of the circumstellar environment.

The key outcome here is that for all stars in the sample, approximately 0.25 to 0.5 mag of extinction in i is due to the circumstellar material rather than the ISM. Stars with relatively low absolute extinctions will therefore have their A_i systematically over-estimated if it is based on colour excess using $R_V = 3.1$.

If we use the R_V dependent extinction model of Cardelli et al. (1989), de-reddening an extinction of $A_i = 0.25$ using $R_V = 3.1$ rather than $R_V = 7.0$ leads to an under-estimate of the V band magnitude of 0.05. If the circumstellar extinction component is $A_i = 0.5$, the error becomes

Table 6.3: Comparison of the spectroscopically derived A_i with the Peak-to-peak inner-disc extinction for the four ‘extinction variable’ stars. For stars 62 and 66, the overall extinction for the star can be entirely explained by the circumstellar material. For stars 133 and 152, approximately 25% of the observed extinction can be attributed to inner circumstellar material, the rest being due to the ISM or the outer circumstellar regions.

Star id	Single epoch spectroscopic A_i [mag]	Peak-to-peak inner-disc A_i [mag]
62	0.25 ± 0.25	0.38 ± 0.2
66	0.25 ± 0.25	0.28 ± 0.14
133	1.10 ± 0.25	0.24 ± 0.14
158	2.10 ± 0.25	0.5 ± 0.28

0.1 mag in V .

6.4 Summary

Dust grain-growth is the first step toward building planets. Grain-grain collisions within circumstellar discs are thought to grow the grains toward the size where gravitational forces can begin to assemble planetary cores. Previous studies have shown that dust grains present in the outer regions of YSO discs ($\gtrsim 350$ AU from the star) are 25-50 times larger than those in the ISM (Throop et al. 2001) and Shuping et al. (2004). Recently, McGinnis et al. (2015) has made the first suggestion that larger grains are present within the inner regions of YSO discs and that dust evolution has an impact on the wavelength dependence of circumstellar extinction. I have identified four stars which show significant variability in their photometric SED whilst maintaining constant equivalent width in photospheric TiO spectral lines. The obvious interpretation of this behaviour is that the variability is due to variable extinction along the line-of-sight to the star. Comparison with stars known to show variability due to accretion and cool spots as well as the similarity between the variability SED and the mean SED support the ‘extinction change only’ explanation for their variability. A principal component analysis shows that for each of these four stars, $> 96\%$ of the variability can be explained by the addition of a single additional spectral component. The normalised ratio of the first principal component to the mean spectrum for each star cancels the effect of ISM reddening and allows the estimation of the chromatic dependence of the variable extinction (R_V). R_V values are found to range from 5.03 - 8.26. This is significantly less wavelength dependent than typical values for the ISM. This indicates that dust grains are larger than those in the ISM and that grain-growth is occurring, however the wavelength dependence indicates that some small grains must still be present.

The location of the material causing the variable extinction is determined from dynamical arguments to be < 20 AU from the central star (assuming $M_\star = 1 M_\odot$). In reality, it is likely that it is much closer. If these stars are similar to AA Tau type stars (which Alencar et al. 2010, found to be common in NGC 2664), the dust causing the variable extinction is likely to be $< 30 R_\odot$ from the star. Either way, the dust is 1-2 orders of magnitude closer to the star than the larger grains

(and ‘greyer extinction’) found by Throop et al. (2001) and Shuping et al. (2004).

Extinction of at least $A_i \sim 0.25 - 0.5$ mag is found to be caused by circumstellar dust in the four YSO systems. As R_V is found to be greater for this material than that assumed in ISM models, extinction corrected V magnitudes will tend to be systematically under-estimated by 0.05 - 0.1 mag for the four stars in this sample. If circumstellar extinction of this nature is common, it is likely that measurements of stellar luminosity are under-estimated by 5-10% for many disc-bearing stars, with resulting underestimates of radius and over-estimates of age in the H-R diagram.

Chapter 7

Spectral typing, extinction and veiling estimates for spectroscopic target stars

7.1 Introduction

Subsequent chapters in this thesis use the data described in Chapter 4 to understand the accretion luminosity for young stars in the ONC. To perform these analyses, it is important that fundamental parameters such as intrinsic photospheric colours, magnitudes, extinctions and veiling are well defined. The spectra presented in this study for 67 ONC stars provide a powerful means to define these parameters accurately for a representative sub-set of the population.

In accreting stars, veiling is often seen and reduces the equivalent widths of photospheric lines. This veiling is principally caused by accretion luminosity, although there is evidence that an additional source of veiling is present at wavelengths greater than $\sim 6000 \text{ \AA}$ which cannot be explained by accretion shock models (Fischer et al. 2011). The veiling at 7000 \AA is typically between 0.1 and 1, however in extreme cases it can be several times larger than the photospheric emission (Hartigan et al. 1995; Fischer et al. 2011).

Hillenbrand (1997) and Hillenbrand et al. (2013) provide catalogues of spectral types, T_{eff} and extinctions for large (> 1000) numbers of stars in the ONC based on spectral indices from low-resolution ($R \sim 1000$) spectra. These spectral type catalogues make no estimate of the contamination from optical veiling emission and thus the spectral type estimates (based on absorption line depths) are systematically biased toward earlier classifications in accreting stars. As an example, Hillenbrand (1997) states that an M2 star veiled with $r_{5800\text{\AA}} = 1$ would appear to be M0.5 and $r_{5800\text{\AA}} = 5$ makes it appear as a K6 star. A similar bias is present in the catalogue of spectral types by Da Rio et al. (2009) which are derived from narrowband-photometry of TiO bands. This bias affects the subsequent determination of T_{eff} , A_V and H-R diagram derived age and mass.

The combined effect of veiling and reddening on the photometric colours of accreting stars is both significant and degenerate. With photometry alone it is impossible to robustly define the veiling and extinction without recourse to theoretical models which are known to be incorrect for late-type PMS stars (see Bell et al. 2012, and references therein). Instead I have measured the optical veiling for the accreting stars in this sample through comparison of the target spectra with

non-accreting PMS template spectra. The higher resolution ($R \approx 3000$) of my spectra compared with Hillenbrand (1997) and Hillenbrand et al. (2013) aids in the precision of this task. 21 of the 67 spectroscopic targets are discless stars and almost all of these show no signatures of accretion in their photometric colours. As these stars are likely to be broadly co-eval and of similar metallicity and surface gravity to other stars in the ONC, they provide an ideal template sample.

Once a set of appropriate spectral type templates was established it was possible to perform a fitting procedure which allowed the measurement of intrinsic $g - i$, extinction (A_{6800}) and veiling (r_{6800}) at 6800\AA . In Section 7.2 I show how template stars were selected and correct for the effects of extinction and reddening of the templates. In Section 7.3 I describe the fitting procedure. In Section 7.4 I present the results.

7.2 Discless templates

7.2.1 De-reddening of template stars - the TiO bandhead index vs. $g - i$ for discless stars.

The spectra collected for the discless template stars were first corrected for extinction and reddening so that the template photometry and spectra represent the intrinsic SED of the stellar photospheres. To achieve this I defined a relationship between the intrinsic de-reddened $g - i$ colours of the template stars and the strength of a temperature sensitive spectral index. My sample is biased toward late-K and M stars. TiO is an effective temperature diagnostic in this temperature range (e.g. Cruz & Reid 2002; Slesnick 2007) so the spectral index chosen was the ratio of flux in a continuum region ($7005 - 7035\text{\AA}$) to the flux in a temperature sensitive TiO absorption band ($6750 - 6900\text{\AA}$). This spectral index is similar to that employed by Herczeg & Hillenbrand (2014) for nearby T Tauri stars. Spectral indices are essentially unaffected by extinction and flux calibration errors, providing the continuum and absorption bands used are similar in wavelength.

To avoid adding uncertainty through employing colour - T_{eff} relations, I have chosen to derive a direct relationship between the temperature sensitive spectral index and the observed de-reddened $g - i$ colour. As I simply wish to link an accreting star to its intrinsic photospheric colours via the non-accreting templates, a direct estimate of T_{eff} is not necessary.

The discless template stars are scattered throughout the ONC and the patchy nature of the interstellar material in the region mean that they have a variety of extinctions. Fortunately a proportion of the sample have very low extinctions. This allowed the relation between TiO spectral index and intrinsic $g - i$ to be derived from stars that have little or no reddening affecting their photospheric colours. I identified the low extinction templates by selecting stars with $A_V < 0.05$ from Hillenbrand (1997). As these stars were unaffected by accretion or discs, these extinction estimates should be robust. Fig. 7.1 shows the spectral index plotted against $g - i$ for all of the template stars. A second order polynomial fit has been made to the positions of the low extinction templates. This polynomial was used to predict the $g - i$ colours of stars based on their measured spectral index. Stars with extinctions > 0.05 exhibit a $g - i$ excess (dotted lines) which was assumed to stem from extinction reddening. Assuming an extinction colour-excess $E(B - V) = 3.1$, the measured reddenings allowed $A_{6800\text{\AA}}$ to be calculated. A correction was then made to

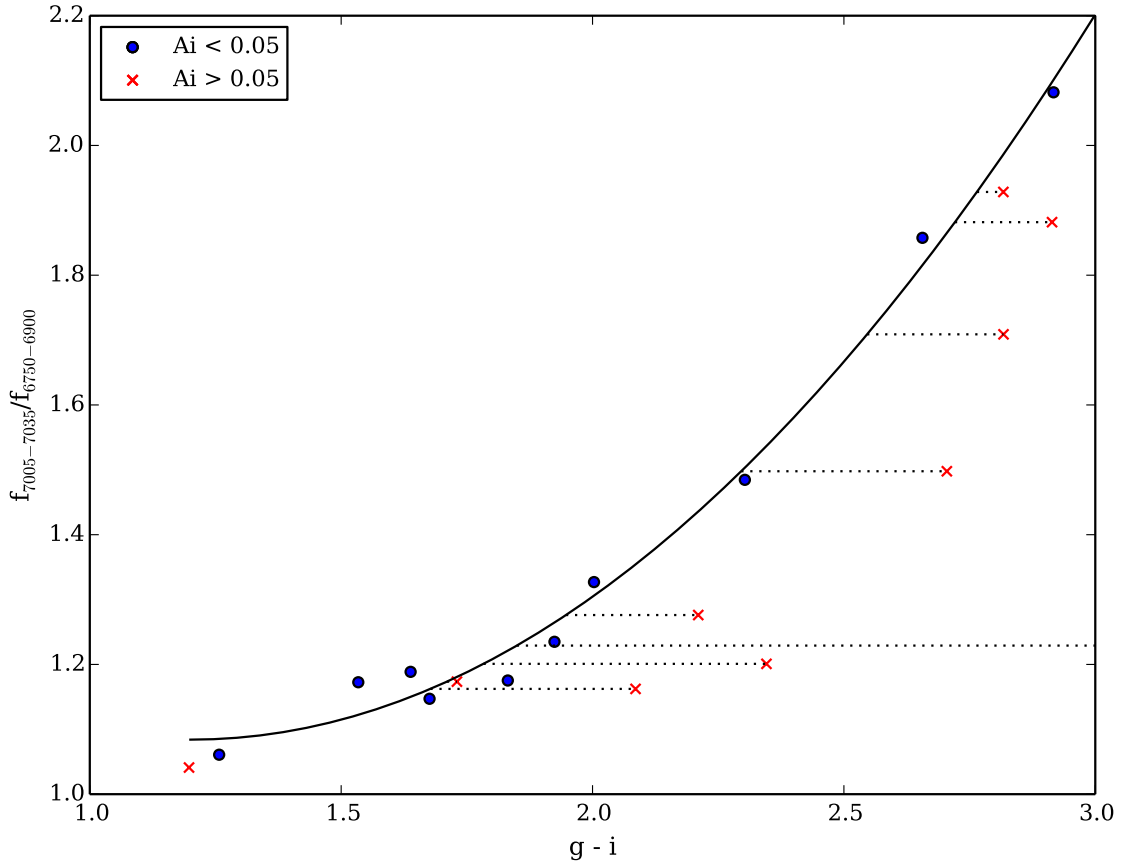


Figure 7.1: Relationship between TiO spectral index and measured $g - i$ for discless template stars. The (blue) circles are stars with $A_V < 0.05$ according to Hillenbrand (1997). The black line is a second order polynomial fit to these points. The (red) crosses are stars with $A_V > 0.05$. The dashed lines are the measured $g - i$ colour excesses which are attributed to extinction-reddening. Stars which show a $g - i$ excess are corrected for extinction and reddening using the wavelength dependent extinction relation of Fitzpatrick (1999).

the photometry of the extinguished stars (using the derived extinctions) to bring them back to their intrinsic magnitudes in all bands using the wavelength dependent extinction relation derived by Fitzpatrick (1999).

7.2.2 Rejection of anomalous templates

Of the 21 discless stars, 11 were rejected for use in template fitting for the following reasons.

- Signs of accretion were seen in the photometric colours of two stars.
- Five stars had spectral index < 1.1 and hence fell outside of the usable range of the index.
- Three stars had spectral gradients which were inconsistent with their spectral index derived colours, indicating binarity or incorrect extinction correction.
- One star had low membership probability based on proper motion measurements.

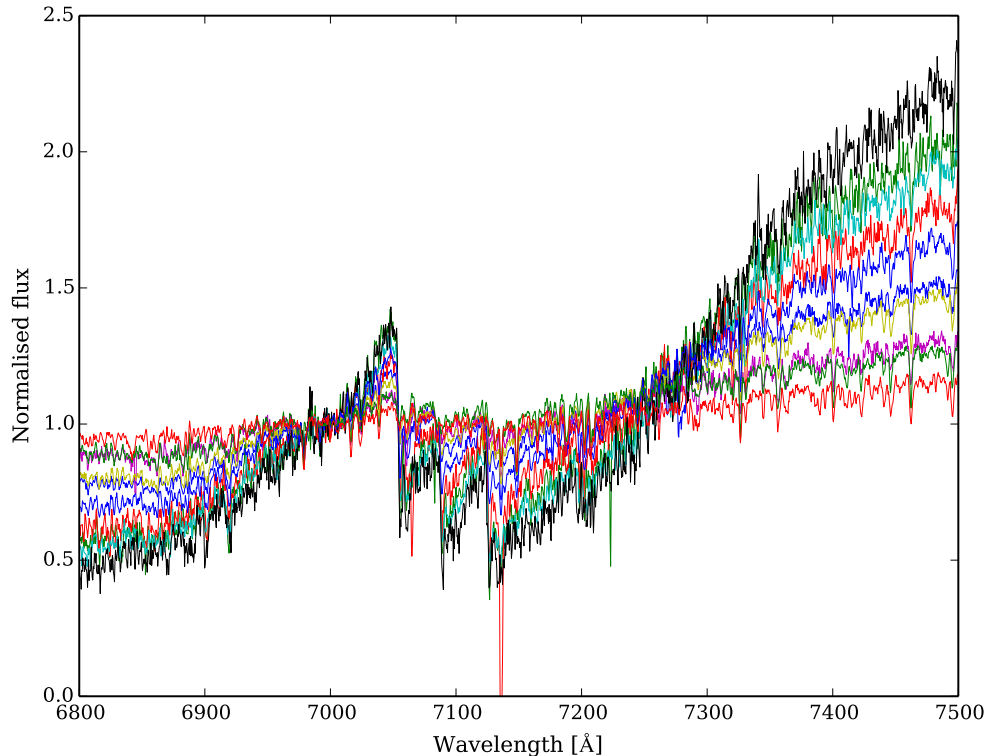


Figure 7.2: The spectra of the selected discless template stars are shown, corrected for reddening and normalised to 1.0 at 7000\AA . The correlation between the depth of TiO absorption bands with the gradient of the spectra (increasing with reducing T_{eff}) is clear. The range of spectra shown here correspond to $1.26 < (g - i)_0 < 3.06$.

The spectra selected for the final template set are shown in Fig. 7.2. They have been corrected for the effects of extinction and for clarity have been normalised to a flux of 1.0 at 7000\AA . The 10 spectra selected have $1.26 < (g - i)_0 < 3.06$.

The location of the template stars within the $g, g - i$ CMD is shown in Fig. 7.3. The templates have been corrected for the effects of extinction and reddening based on the spectroscopic analysis. The photometry is calculated using measurements taken over six consecutive nights, thus the effects of variability will be ‘averaged’ over a timescale that is commensurate with (and in some cases longer than) the rotation period. Despite this, the templates show a scatter in g of approximately ± 0.5 mag about a linear locus. This luminosity spread is probably real, consistent with other studies of the ONC (e.g. Hillenbrand 1997; Da Rio et al. 2009) and is possibly due to the spread in stellar radii identified by Jeffries (2007).

7.3 Deriving the fundamental parameters

The objective of the fitting procedure was to determine the $g - i$ colour, veiling and extinction for the accreting and disc-bearing stars within the ONC sample. Although I was unable to directly

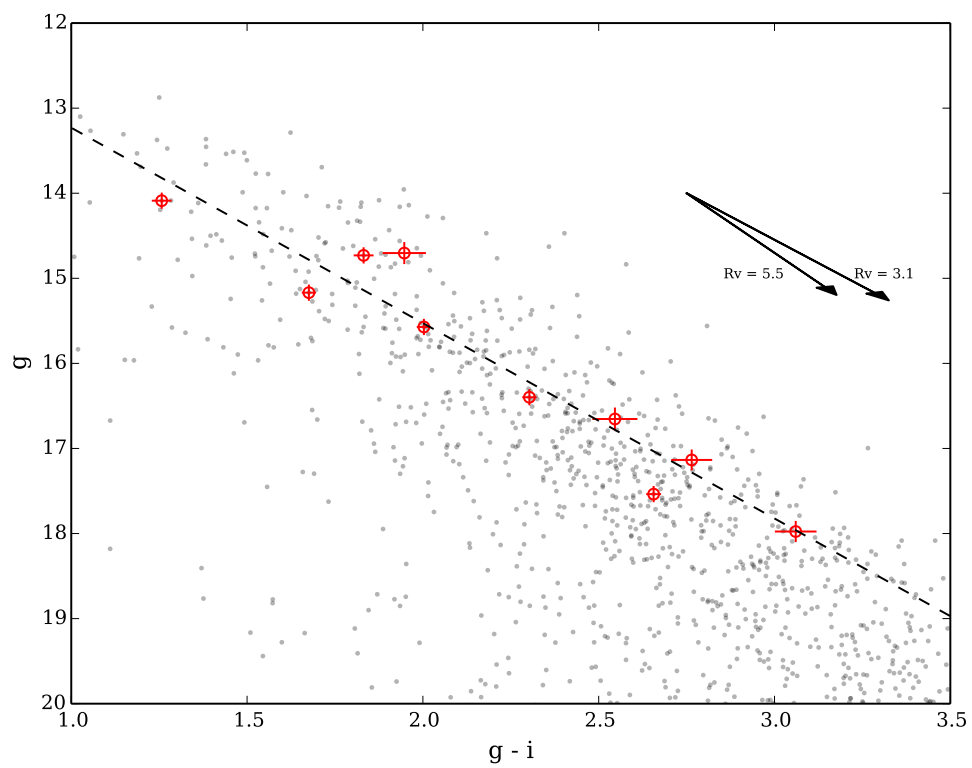


Figure 7.3: $g, g - i$ colour-magnitude diagram showing the positions of the template stars (red circles) compared with the rest of the ONC population (grey dots). The templates have been corrected for the effects of extinction and reddening, based on their spectroscopic TiO index. The black dashed line is a linear fit to the template stars.

measure the intrinsic $g - i$ colour for the accreting and disc-bearing targets, I was able to find the closest spectral-match template by using a fitting procedure that measures the difference between target and template spectra. The de-reddened SED of the best-fit template should closely match the intrinsic photospheric SED of the target. An uncertainty in the estimated $g - i$ for the target is caused by the discrete nature of the template colours, however the wide and reasonably dense sampling in $g - i$ means these uncertainties are typically < 0.15 .

A important by-product of this fitting process is the measurement of the veiling flux in the accreting stars. In addition, as the spectra in this study are accurately flux-calibrated, I was also able to use the depths of the spectral lines to estimate the extinction to the target.

All target and template spectra were mean-stacks of all spectra collected for each star throughout the 7 nights of observations. Typically each comprises ≈ 50 spectra with a combined exposure time of ≈ 12.5 hours.

7.3.1 Fitting procedure

The fitting procedure simultaneously fits for spectral template, extinction and veiling. The initial step in the fitting procedure was to correct all templates and targets to a common reference radial velocity scale so that spectral features matched in wavelength. The fitting procedure then employed a two part model, constructed using three free parameters. Firstly a template spectrum (as described in Section 7.2) was selected and then scaled in flux by an amount corresponding to an extinction $A_{6800\text{\AA}}$ to create a model. The extinction scaling is wavelength dependent and defined by the relation from Fitzpatrick (1999). The model was then subtracted from the target spectrum to leave a residual which was assumed to be the veiling spectrum. I varied the template and the extinction applied and examined the residuals using a χ^2 test performed between the residuals and (290\AA boxcar average) smoothed versions of themselves.

The extinctions were sampled in the range $-0.5 < A_i < 4.0$ at a resolution of 0.1. Sampling of negative extinctions seems at first-glance unphysical, however the intrinsic luminosity spread in the templates (shown in Fig. 7.3) means that it is possible for a target star to be brighter than its template. This does not mean that the spectral type derived is incorrect, instead it is simply that the target star has a larger radius than the template. In the fitting analysis the A_i derived is not actually simply an extinction term but is the extinction to the target minus the magnitude difference caused by any discrepancy in radius. This will add an uncertainty to the derived reddening of the target, however for the spectral fitting this effect will be small and will only be seen as a small additional gradient on the residual. As the added gradient is very smooth (and small due to the limited wavelength range) it will not influence the χ^2 statistic or the outcome of the fitting process. In Chapter 9 it will be shown that the uncertainty in the reddening caused by the luminosity spread has some effect on the photometric SED.

Fitting was performed over the range $6800 - 7420 \text{\AA}$ as this allowed the fitting to be driven by molecular bands of TiO, CaH and VO as well as numerous singly-ionised metal lines. The combination of these lines, plus the intrinsic spectral slope allowed the χ^2 test to distinguish between spectral templates, even under the presence of veiling and extinction. Two short wavelength regions were omitted for the calculation of χ^2 . The first ($7062 < \lambda < 7070 \text{\AA}$) is a strong He I

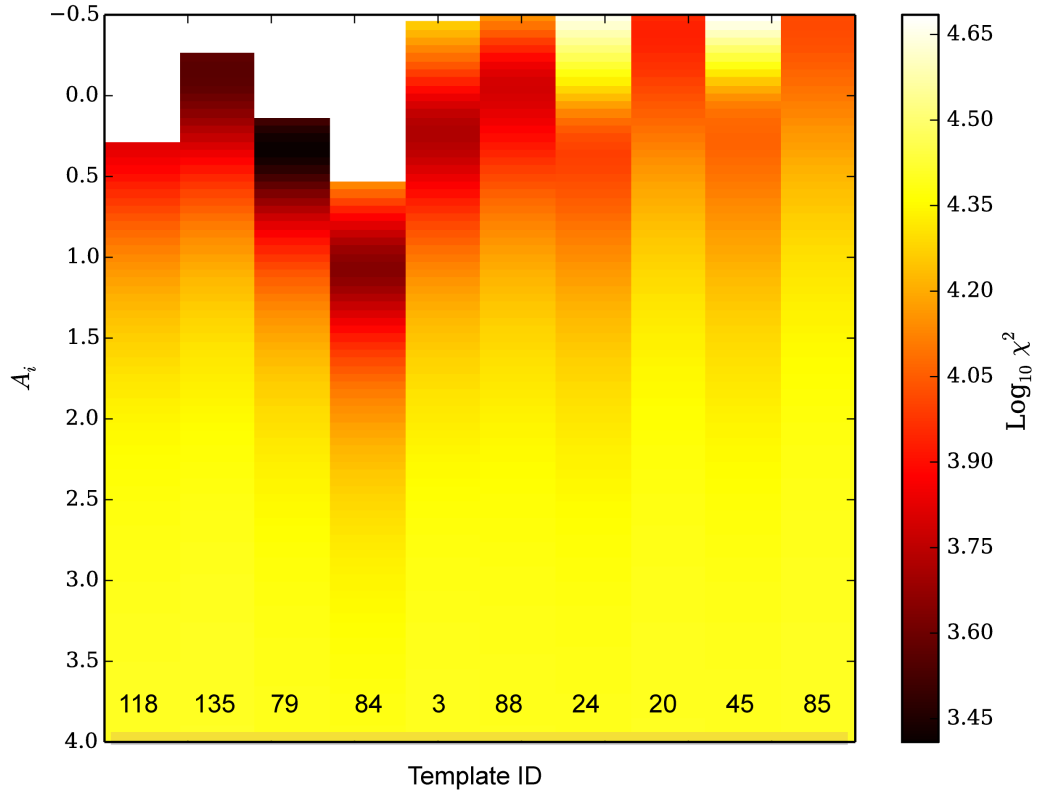


Figure 7.4: A grid of values showing the χ^2 fitting statistic as a function of template and extinction, (A_i) for one example star in my sample (Star 50). The y-axis shows the iterative step in A_i running from -0.5 (top) to 4.0 (bottom). The x-axis corresponds to the template number, running from hotter (left) to cooler (right). White areas show regions of the χ^2 space that return negative veiling, an un-physical situation that rules them out of the fitting. The colour scaling corresponds to $\log_{10}\chi^2$. Visually this reduces the contrast between good and poor fits, however it is necessary to illustrate the large range of χ^2 values returned. The best-fit solution in this case is template 79 ($g - i = 1.83$), $A_i = 0.3$ and a veiling flux at 6805\AA of $1.41 \times 10^{-25} \text{ erg cm}^{-2} \text{ s}^{-1} \text{ Hz}^{-1}$.

line that is associated with both accretion emission and nebular contamination. The second ($7132 < \lambda < 7140 \text{\AA}$) is the strong forbidden line [Ar III] from nebular emission. The effect of varying the smoothing length was assessed, it became clear that smoothing lengths significantly shorter than that employed resulted in insensitivity to large molecular-band features as these could be ‘smoothed’ in the residual without penalty in χ^2 . The expectation is that the veiling is essentially thermal emission and thus should be smooth, thus a longer smoothing length is preferable.

An example of the χ^2 grid returned for an accreting star is shown in Fig. 7.4. The colour corresponds to the χ^2 value derived for each parameter combination. Obvious minima are seen for several of the templates, corresponding to different values of A_i . In this case the best solution is $g - i = 1.83$, $A_i = 0.3$ giving an $r_{6805} = 1.41 \times 10^{-25} \text{ erg cm}^{-2} \text{ s}^{-1} \text{ Hz}^{-1}$. The value of A_i at which minimum χ^2 occurs is seen to be variable between templates. This is the result of the intrinsic luminosity scatter already discussed. Examples of ‘best-fit’ solutions for two accreting stars and two non-accreting disc-bearing stars are shown in Fig. 7.5.

As a verification of this technique, the discless template stars were tested using the same procedure, albeit without allowing them to use their own spectrum as the template. The ‘best-fit’

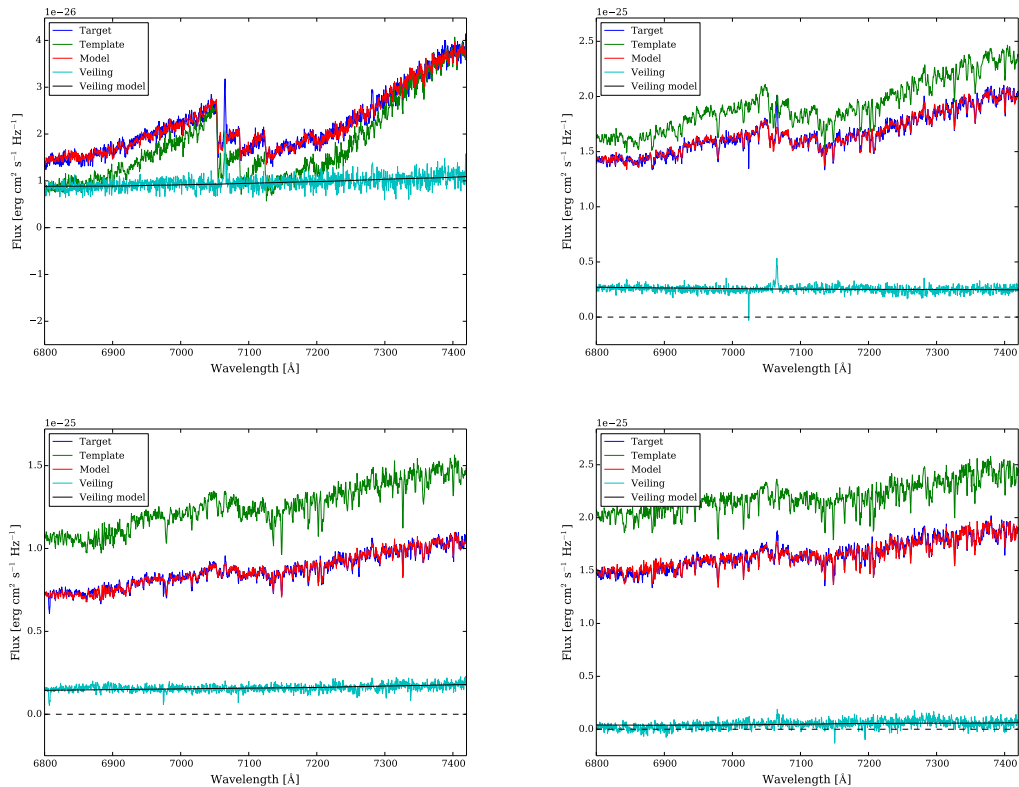


Figure 7.5: ‘Best-fitting’ models of template, extinction and veiling for four target stars. The dark blue line is the target spectrum, the green line is the best-fit template spectrum. The light-blue line is the residual (assumed to be the accretion spectrum) and the black line is the boxcar smoothed residual against which χ^2 is measured. The red line is the complete model spectrum, comprising the extinguished template plus the smoothed accretion spectrum. The top two panels show stars which show optical veiling and also show accretion luminosity excess in their photometry (left panel - star 14, right panel - star 50). The lower two panels show stars with discs which do not have photometric excesses consistent with accretion (left panel - star 62, right panel - star 155).

parameters consistently returned the nearest blue-ward template in $g - i$, albeit with a slightly reduced value of A_i and a small veiling correction that allowed the line fluxes to scale correctly. The error in A_i and addition of spurious veiling contribution was an expected and correct outcome as the fits were not allowed to use their own spectra as a template and thus the closest match (without negative veiling contribution) was that of a slightly hotter star with a small veiling contribution and reduced extinction.

7.4 Results

The spectral fitting analysis was performed for a sample of 31 stars in two categories. The first category analysed was stars identified as having optical photometric accretion signatures (see Section 8.3). The second sample was a group of stars identified by Megeath et al. (2012) as having circumstellar discs but that did not show signs of accretion in their optical photometry. Table 7.1 shows A_i , intrinsic $g - i$ of the closest match template and the veiling flux in the n_{6805} filter derived for each of these stars.

7.5 Summary

To provide a basis for further analysis in this thesis, basic parameters such as intrinsic SED, extinction and optical veiling must be known, at least for a representative sub-set of the stellar population. To achieve this, a sample of ONC members without discs were selected as photospheric templates to then use in measuring the veiling and extinction of stars exhibiting discs and accretion.

For low-extinction discless stars a relation was derived between the $g - i$ photometric colours and a spectroscopic index that was dependent on the depth of a temperature sensitive TiO band. This allowed the accurate measurement of intrinsic colours of the discless photospheric templates through the extinction-independent spectral index. This subsequently allowed the photospheric templates to be corrected for extinction.

The templates were then used to construct a model that comprised a photospheric template, an extinction and a smooth optical veiling spectrum. The model was compared with the target spectrum and the ‘goodness-of-fit’ was measured using a χ^2 statistic. Iteration of the free-parameters and examining the resulting χ^2 allowed the estimation of best fit intrinsic parameters for the accreting and disc-bearing stars. This process was conducted without any recourse to theoretical models which could have introduced systematic errors. The use of templates from the ONC population also mitigated biases in fitted parameters that could stem from differences in metallicity, surface gravity and age. The results of the fitting procedure are presented in Table 7.1 and are used in later chapters of this thesis.

Table 7.1: Best-fit parameters determined for stars with discs in the ONC based on the spectroscopic fitting procedure. The last column defines the accretion status of each star based on U band and $H\alpha$ excess flux found in Chapter 8. ‘acc’ denotes accreting stars, ‘non-acc’ denotes non-accreting stars.

Star id	A_i (mag)	Template $g - i$	Veiling flux at 6805Å $\text{erg cm}^{-2} \text{s}^{-1} \text{Hz}^{-1}$	r_{6800}	Accretion status
8	3.4	85	8.88×10^{-28}	4.62	acc
10	1.15	135	2.40×10^{-26}	1.43	acc
14	0.35	85	8.84×10^{-27}	1.30	acc
23	1.75	20	1.19×10^{-26}	3.47	acc
26	0.75	85	2.85×10^{-27}	0.36	acc
30	0.15	88	1.68×10^{-26}	0.47	acc
49	-0.1	135	4.20×10^{-26}	0.48	acc
50	0.3	79	2.70×10^{-26}	0.28	acc
58	-0.3	135	3.52×10^{-26}	0.23	non-acc
62	0.55	135	1.44×10^{-26}	0.25	non-acc
66	0.55	135	1.26×10^{-27}	0.02	non-acc
77	0.85	20	5.25×10^{-26}	6.97	acc
90	0.0	88	9.95×10^{-27}	0.37	acc
92	2.3	79	5.87×10^{-27}	0.45	non-acc
95	0.35	20	2.43×10^{-26}	2.03	acc
98	2.2	118	5.22×10^{-28}	0.03	non-acc
104	0.6	118	8.71×10^{-28}	0.01	non-acc
121	0.3	88	1.80×10^{-27}	0.08	acc
127	0.85	135	1.85×10^{-26}	0.86	acc
130	0.4	135	1.76×10^{-27}	0.24	acc
133	1.1	118	2.22×10^{-26}	0.87	acc
137	-0.5	118	0.0	0.0	non-acc
139	1.4	79	1.02×10^{-26}	0.29	non-acc
143	0.6	135	5.53×10^{-26}	1.51	acc
150	0.25	20	1.02×10^{-27}	0.10	non-acc
152	-0.1	20	1.17×10^{-26}	0.75	acc
153	-0.3	20	8.98×10^{-27}	0.83	acc
155	0.3	118	4.00×10^{-27}	0.02	non-acc
158	2.1	79	4.39×10^{-27}	0.38	acc

Chapter 8

How does accretion affect the colours of young stars?

8.1 Introduction

Studies such as those by Hillenbrand (1997), Palla & Stahler (1999) and Da Rio et al. (2010b) have used the well populated CMD of the ONC to estimate the age, star forming chronology and mass function for the cluster. Whilst it is not the purpose of this study to re-visit the age and apparent age spread question, a critical analysis of the properties of stars as a function of CMD position may help us to understand the limitations of these previous studies and help us to interpret their findings. Isochrone fitting for age analysis typically assumes that all stars are fully visible (except for a correction for inter-stellar extinction) and that their colours and magnitudes, measured at a single epoch are characteristic of their ‘immaculate’ photospheres and provide a reliable proxy for T_{eff} and L_{bol} respectively. In reality, we know that T Tauri stars are messy, violent objects, where surface temperature variations, accretion structures and circumstellar material act to alter the light that our telescopes receive from the star.

This multi-band study provides an opportunity to explore the intrinsic properties of T Tauri stars and compare them with position within the CMD. In this chapter I principally focus on the effect of accretion luminosity. It has long been known that accreting T Tauri stars exhibit excess blue luminosity which is associated with thermalisation of kinetic energy from in-falling accreting material. Bertout et al. (1988) first proposed that truncation of the circumstellar disc and channeling of the accreting material may lead to localised heating of the photosphere. Rotation of the star then modulates the blue emission that we observe along our line of sight. As a result, excess flux in U is an effective tool for identifying accreting PMS stars (e.g. Rebull et al. 2000; Rigliaco et al. 2011; Venuti et al. 2014).

Accretion luminosity is not considered in PMS models, yet hot continuum contributions many times brighter than the photosphere have been observed from veiling measurements in T Tauri stars. Stout-Batalha et al. (2000) found that a hot-continuum flux 6.1 times brighter than the photosphere was present at 6000 Å in RW Aur.

In this chapter I present my colour-magnitude diagram for the ONC. I then identify accret-

ing stars using ultra-violet and line-emission indicators and investigate whether accretion luminosity affects the position of stars in CMD space.

8.2 The $g, g - i$ colour-magnitude diagram

A $g, g - i$ colour magnitude diagram of all stars in the observed fields is shown in Fig. 8.1. Isochrones and evolutionary tracks are overlaid, constructed from the models of Bell et al. (2014), using a distance modulus of 7.96 and mean $E(B - V) = 0.4$ (Mayne & Naylor 2008). The ONC lies in front of the dense OMC-1 molecular cloud which Scandariato et al. (2011) found to exhibit $A_V \geq 6$ and up to $A_V \approx 30$ in regions close to the core of the cluster. This effectively removes almost all background galactic stellar contamination from our photometric sample.

In common with previous surveys by Hillenbrand (1997) and Da Rio et al. (2010b), the cluster population appears to stretch across an age range of > 100 Myr. Many stars appear to be so faint that they fall well below the zero-age main-sequence. The huge luminosity spread at a given $g - i$ colour is clearly incompatible with simple theoretical PMS models.

A foreground population of galactic field-stars is likely to be present, however the comparatively nearby nature of the ONC means that contamination from such sources is relatively low. A proper-motion study by Jones & Walker (1988) concluded that $\approx 90\%$ of stars within 20 arc-min of the ONC are cluster members. I rejected foreground stars by using only high-probability members identified by Hillenbrand (1997). Membership probabilities are calculated based on proper-motions, extinction, spectral line emission, variability, and infrared excess. Alves & Bouy (2012) find that a foreground PMS population with age $\approx 4 - 5$ Myr exists in front of the ONC, centred around NGC 1980 which lies ≈ 30 arc-min to the south of the Trapezium stars. They estimate that this foreground population may contribute 10-20% of the PMS stars observed in the ONC and will bias estimates of age and age-spread. Whilst this foreground population is important in determination of the age of the cluster, it has little effect on my analysis of T Tauri variability, simply contributing an extra source of young-stars to study

8.3 Identifying accreting stars

I have used two photometric tools to identify accreting stars in the sample, U band excess and $H\alpha$ line-emission excess. I have also compared the relation between these two parameters to check for consistency and be sure that identified stars really are accreting.

Before I could determine an excess in either of these quantities, I needed to predict the flux that I expected in these bands for a PMS star without any accretion signature. Broad-band fluxes predicted by PMS atmosphere models do not generally agree well with observations, particularly in U (see Da Rio et al. 2010b). In addition, accretion related $H\alpha$ line-emission is thought to originate from flows of optical thin material falling onto the star from the circumstellar disc. As a result, emission line fluxes are not predicted by PMS models. Thus to predict the expected U and $H\alpha$ fluxes I defined a PMS locus in both the $U - g, g - i$ plane and the $r - H\alpha, r - i$ plane using an empirical fit to non-accreting young stars. To be sure that the stars that I used for determining the

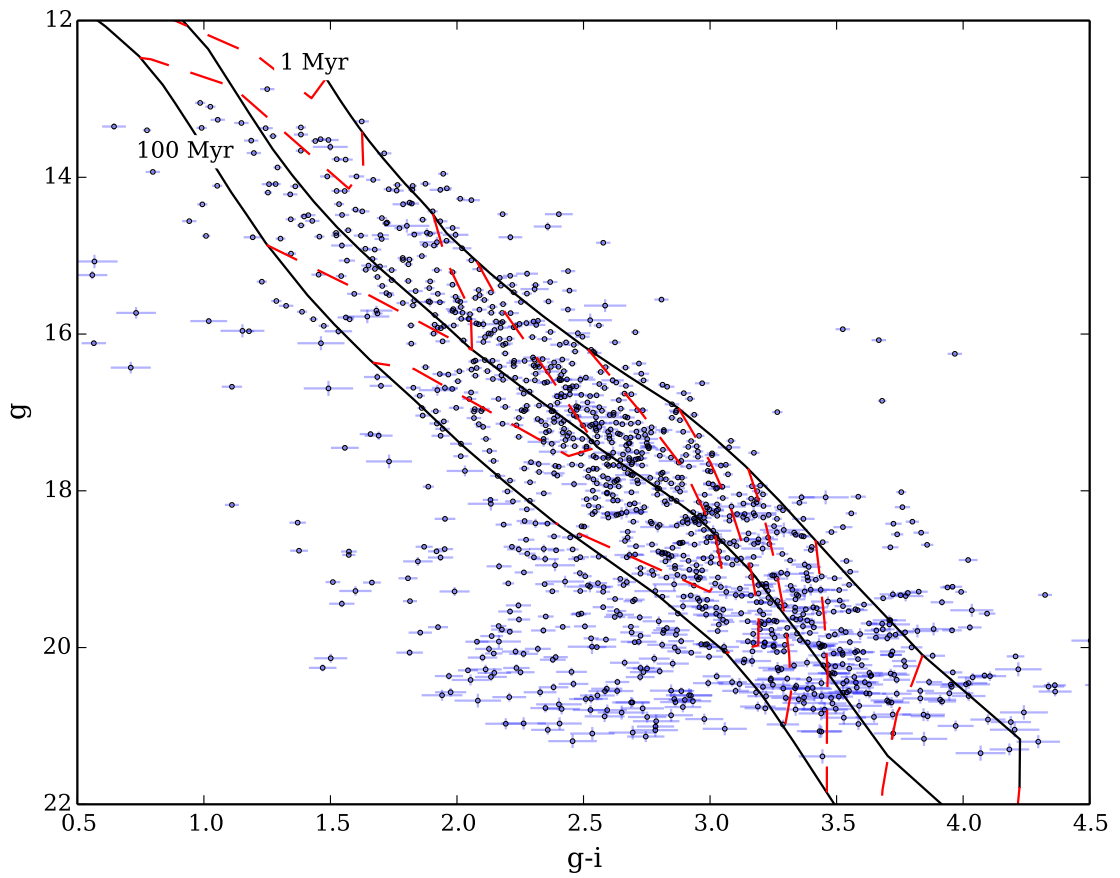


Figure 8.1: $g, g - i$ CMD of all stars in our field of view with clean photometry (unflagged and $S/N \geq 10$). The black (solid) lines show 1, 10 and 100 Myr isochrones from the models of Bell et al. (2014). Red (dashed) lines show (from right to left) evolutionary tracks for single stars of mass 0.1, 0.2, 0.3, 0.4, 0.5, 0.6, 0.8, 1.0, 1.5 and $2.0 M_{\odot}$. The sample is limited at the faintest g magnitudes by S/N and at the brightest magnitudes by saturation.

PMS locus are genuine members of the cluster and that their colours are not modified by accretion, discs or extinction, I identified candidate stars in the main catalogue that

- have no associated mid-infrared (disc) excess identified by Megeath et al (2012);
- have low extinctions from Hillenbrand (1997), $0 < A_V < 1.0$;
- have small photometric uncertainties (< 0.1 mag and unflagged) in all bands;
- and are EITHER known ONC members (Hillenbrand (1997) membership probability $\geq 98\%$) OR are periodic variables identified in the flanking fields by Rebull (2001).

These cuts yield a catalogue containing 262 candidates that I will refer to as the ‘non-accreting discless stars’. Even using these cuts, it is clear that some of the selected stars exhibit excess emission in U or $H\alpha$. These are possibly stars with unusually active chromospheres or have incorrectly measured fluxes due to imperfect subtraction of the nebular background, which in some regions of the ONC is both bright and highly structured. This contamination is more prevalent in U , so the empirical fitting process is staged so that I can use the ‘cleaner’ $H\alpha$ excess measures to remove contamination from the U band fitting.

8.3.1 $H\alpha$ emission line excess

The $r - H\alpha$, $r - i$ colour-colour diagram may be used to identify $H\alpha$ emission-line objects such as young stars and estimate the flux within the $H\alpha$ line (e.g. Drew et al. 2005; Barentsen et al. 2011). Fig. 8.2 shows the data for the non-accreting discless sample (with photometry that is unflagged and has $S/N > 10$ in r, i and $H\alpha$) plotted in this plane. Accreting stars exhibit $r - H\alpha$ colours that are brighter in $H\alpha$ than the non-accreting population at a given $r - i$ colour and hence are easy to identify once I have empirically defined the locus for non-accreting PMS stars.

To fit the non-accreting PMS locus, the non-accreting discless stars were binned in groups of 20 in $r - i$, and each bin had a median $r - H\alpha$, and $r - i$ colour determined. The $r - H\alpha$ colour was subject to a $2\text{-}\sigma$ clipping routine to reduce the influence of the outlying stars with significant $H\alpha$ excess or extinction. The median values were then fitted using a quadratic function to define the locus of non-accreting stars. The locus for non-accreting stars is defined by the function

$$r - H\alpha = -0.0951(r - i)^2 + 0.6697(r - i) - 0.0644. \quad (8.1)$$

An excess $r - H\alpha$ was then calculated with respect to this function for each of our target stars. It should be noted that the photometry has not been subject to any dereddening, however as Fig. 8.2 shows, the extinction vectors in this plane lie almost parallel to the PMS locus and hence do not significantly affect the calculated excess in $r - H\alpha$.

An offset was then defined which corresponds to the non-accreting locus plus an $r - H\alpha$ excess corresponding to an equivalent width of 10\AA . The excess added is that calculated for dwarfs by Barentsen et al. (2011). This 10\AA ‘buffer’ allows for particularly active non-accreting stars and is a traditional (if perhaps slightly arbitrary) cut used between accretors and non-accretors. Forty

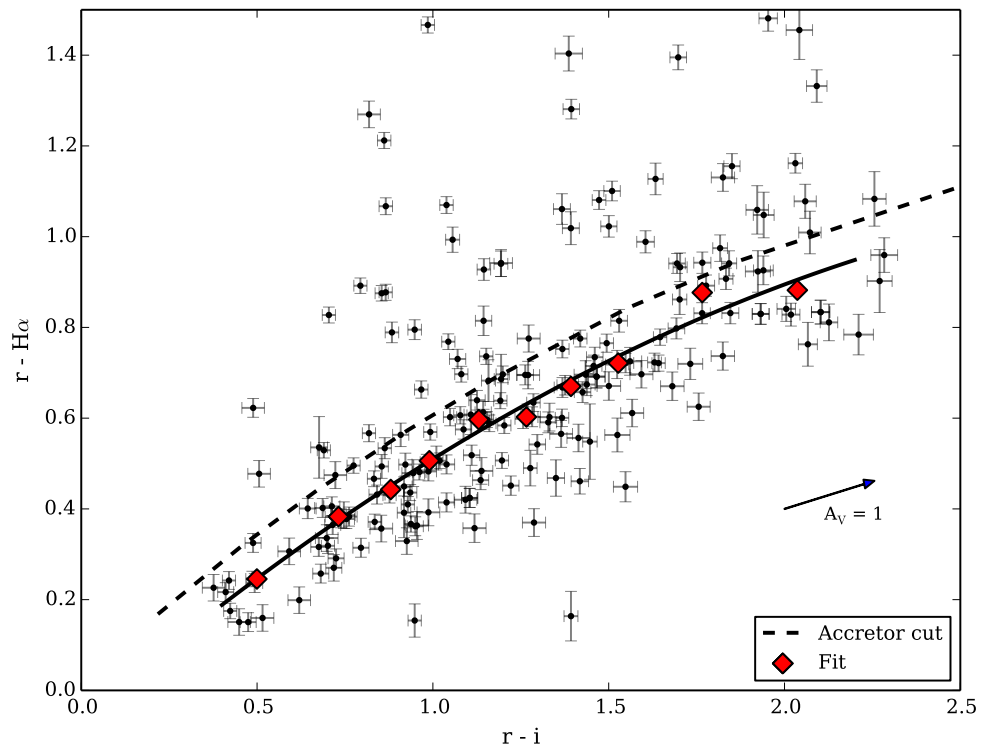


Figure 8.2: $r - i$, $r - H\alpha$ colour-colour plot for stars that are likely members of the ONC and that do not exhibit Mid-IR evidence of an accretion disc. Black points (with error-bars) are all stars in the sample. Red (light grey) diamonds are the median colours in 20 star wide bins in $r - i$. A 2σ clipping routine has been applied in $r - H\alpha$ to reduce the influence of the few contaminating stars that exhibit $H\alpha$ excess or strong extinction. The solid line is a quadratic function fitted to the median colour points and defines the locus for non-accreting stars. A (dashed) line shows the expected $r - H\alpha$ excess corresponding to an equivalent width of 10 \AA above the non-accreting locus.

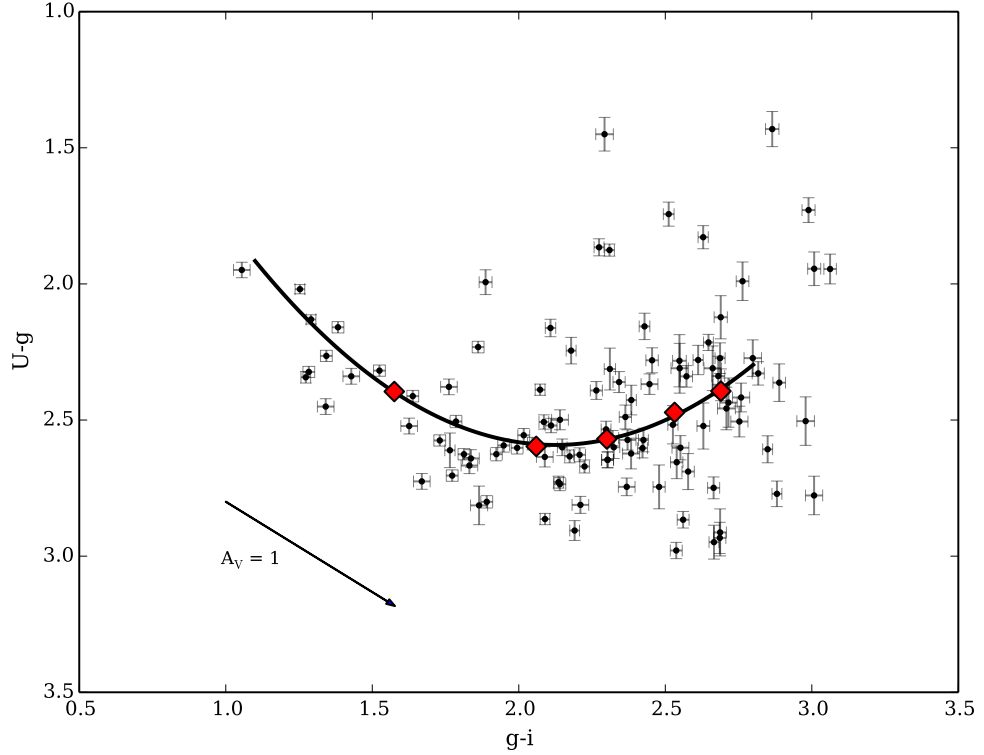


Figure 8.3: $U - g$, $g - i$ colour-colour plot for stars that are likely members of the ONC and that do not exhibit mid-IR evidence of an accretion disc or evidence of active accretion via $H\alpha$ excess. Black points (with error-bars) are all stars in the sample. Red (light grey) diamonds are the median colours in 20 star wide bins in $g - i$. The solid line is a quadratic function fitted to the median colour points and defines the locus for non-accreting stars.

eight stars in the non-accreting discless sample exhibit $r - H\alpha$ above the 10 \AA contour and thus are suspected accretors. These stars are rejected from further analysis in characterising non-accreting PMS fluxes, thus reducing the sample to 214 stars.

8.3.2 Ultraviolet excess

Fig 8.3. shows the remaining non-accreting discless sample plotted in the $U - g$, $g - i$ colour-colour diagram. Using the same method as the analysis in Section 8.3.1, I calculated a PMS locus in $U - g$, $g - i$. The locus was fit using a quadratic defined by the function

$$U - g = -0.6445(g - i)^2 + 2.738(g - i) - 0.3164, \quad (8.2)$$

this model appears to fit the data well in the range $1.1 < g - i < 2.8$. Outside of this range the model will overestimate the photospheric U flux and lead to an underestimate of the U excess for a given star. For the purposes of this investigation, this is acceptable as our final objective is to identify accreting stars and an underestimate of U excess at the extremes of our sample would

simply mean that some weak accretors were not identified. The $U - g$ excess was then calculated for each star by subtracting the model $U - g$ at the correct $g - i$ for each star from its measured $U - g$ colour.

8.3.3 Comparison of accretion diagnostics

My objective is to robustly identify stars that are accreting in the ONC. To be sure that stars identified are bone-fide accretors, I compare the $H\alpha$ and U excesses measured both for stars with and without *Spitzer* identified circumstellar discs. As accretion is essentially impossible without a reservoir of material in an orbiting disc, I can use the discless population to define thresholds in the $H\alpha$ and U excesses that correspond to accretion, and thus remove contamination caused by chromospheric activity.

Fig. 8.4 shows the measured $U - g$ excess plotted against $r - H\alpha$ excess for discless (left panel) and disc-bearing (right panel) stars. This plot clearly shows that the presence of $H\alpha$ emission is strongly correlated with U excess, a correlation that has attracted much previous study (e.g. Hartigan & Kenyon 2003; Dahm 2008; Herczeg & Hillenbrand 2008; Sicilia-Aguilar et al. 2010). A small fraction of stars violate this correlation by showing an excess in either $U - g$ or $r - H\alpha$ alone. Those which show an excess in $U - g$ but not $r - H\alpha$ are mostly foreground main-sequence stars of higher T_{eff} than the PMS population. These stars have a low-probability of membership in Hillenbrand (1997). Stars which show an excess in $r - H\alpha$ but not $U - g$ are most likely highly-reddened accreting objects. The reddening vector that influences the colours of these stars may be seen in Fig. 8.4.

To determine colour-cuts for accreting stars I calculated the mean and standard deviation in $U - g$ and $r - H\alpha$ excesses for the discless population. These results are shown in Table 8.1. The mean values in both colours are very close to zero, indicating that the PMS loci defined in Sections 8.3.1 and 8.3.2 are robust. The 1σ thresholds in the non-accreting stars has been adopted as a nominal cut in both $U - g$ and $r - H\alpha$. However to be identified as an accretor, the star must exhibit colours that lie above these thresholds in both indices. To be considered in further analysis as a non-accretor, a star must fall below the thresholds in both indices. Fig. 8.4 shows the derived thresholds against the discless and disc-bearing populations. The quadrants corresponding to the defined accreting and non-accreting samples are labelled. Any stars which fall into the other two quadrants (i.e. fall above the accretion threshold in one colour only) are of ambiguous nature and thus are rejected from all further analysis. The stars for which I have collected spectra as part of this study are highlighted in Fig. 8.4. It is clear that I have good sampling over the full range of accretion behaviour in the spectroscopic sample. Fig 8.5 shows a $U - g$, $g - i$ colour-colour plot showing the positions of the accreting and non-accreting samples. It is clear that the accretors show significant U band excess.

It should be noted that this analysis indicates the presence of a significant population of stars which have *Spitzer* identified circumstellar discs but that fall within the non-accreting region of the diagram. A population of thick-disc stars without optical accretion indicators was noted by Teixeira et al. (2012) in NGC 2264, comprising $\approx 15\%$ of the population.

There is also an intriguing population of stars that are identified as discless stars within

Table 8.1: Mean colour excess and 1σ limits for all discless stars in our sample

Colour	Mean excess (non-discs)	1σ limit
$U - g$	0.03	-0.395
$r - H\alpha$	-0.028	0.146

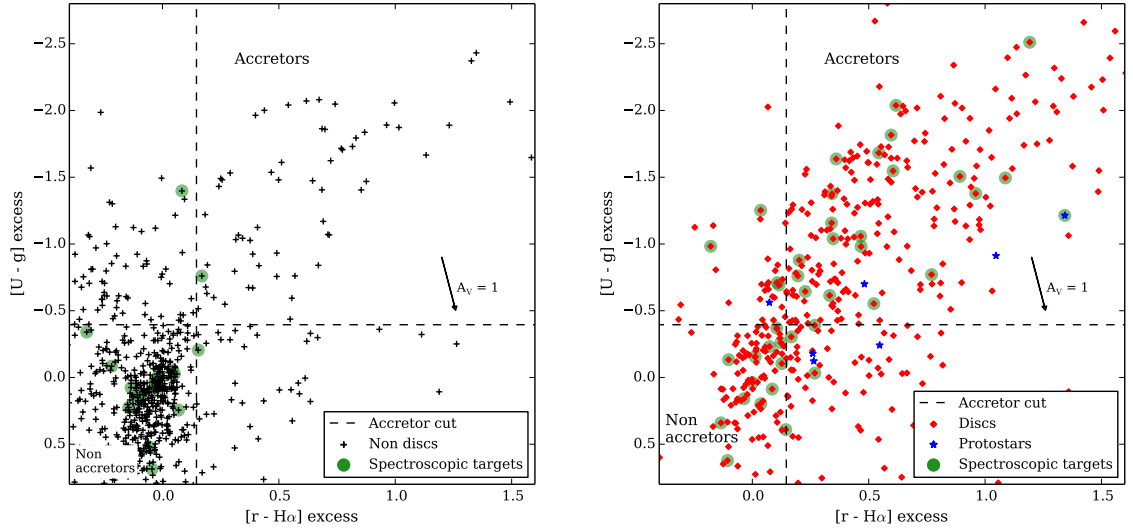


Figure 8.4: $U - g$ excess plotted against $r - H\alpha$ excess for the discless stars (left panel) and disc-bearing stars (right panel) identified by Megeath et al. (2012). The correlation between U excess and $H\alpha$ is strong, although scatter about this correlation is ≈ 1 mag in either colour. The dotted lines show the adopted cuts made to identify accreting stars. The upper right quadrant is the accreting star population. The lower left quadrant is the non-accreting sample. The other two quadrants contain stars with ambiguous accretion status. The green points highlight stars for which spectral time-series were collected. An extinction vector corresponding to $R_V = 3.1$ is shown.

the *Spitzer* sample, that appear to exhibit optical accretion signatures. This is not the first time that such stars have been identified, Littlefair et al. (2004) observed stars in ρ Oph that appear to exhibit spectroscopic accretion signatures without associated near-infrared excess.

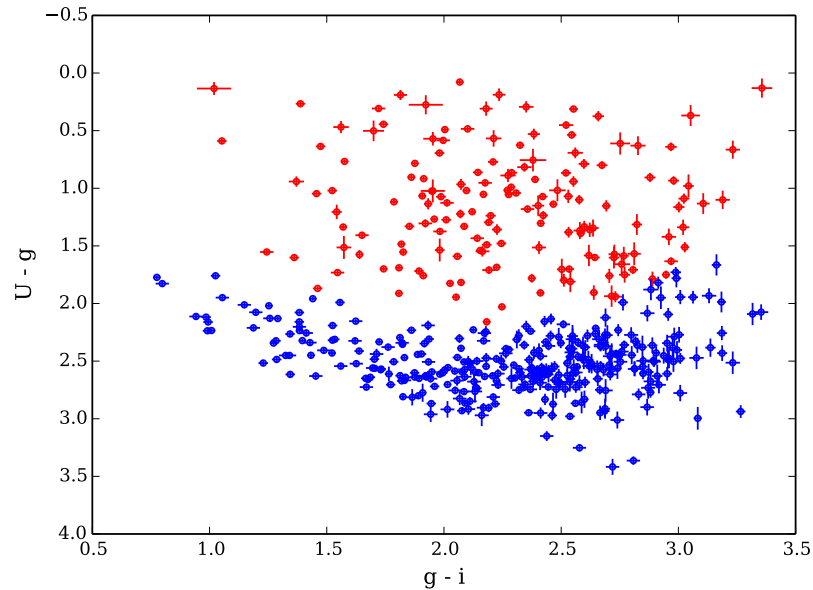


Figure 8.5: A $U - g$, $g - i$ plot comparing the positions of the accreting (red) and non-accreting (blue) samples. The accreting stars show significant excess in U compared with the non-accreting stars.

8.4 Accretion induced luminosity spreads in the CMD

Fig. 8.6 shows g , $g - i$ colour magnitude diagrams that compare the distributions of stars within the three sample groups. It is immediately clear that the accreting population is both more spread in CMD space than the other populations and also shows a bulk offset in the sense that the population appears older against the isochrones. Whilst the non-accreting disc-bearing stars and the discless stars appear to cluster between the 1 and 10 Myr isochrones, the accreting stars spread as far blueward as the 100 Myr isochrone and beyond. This finding provides strong evidence that accretion luminosity is responsible for much of the apparent ‘age spread’ that we see in optical colour magnitude diagrams.

It is also notable that the non-accreting disc-bearing population does not show significant luminosity shift or spread beyond that seen in the discless population. This implies that extinction caused by the disc or remaining accreting envelope must move stars in the CMD in a direction that is broadly consistent with the interstellar reddening vector. As that vector lies almost parallel to the PMS, little spread about the isochrones is induced.

The fact that non-accreting disc-bearing stars are not spread blue-ward in a manner similar to the accretors implies that the spread that we see in the accreting stars is caused by the accretion luminosity itself (or directly related phenomenon) and is not simply caused by the presence by the circumstellar-discs.

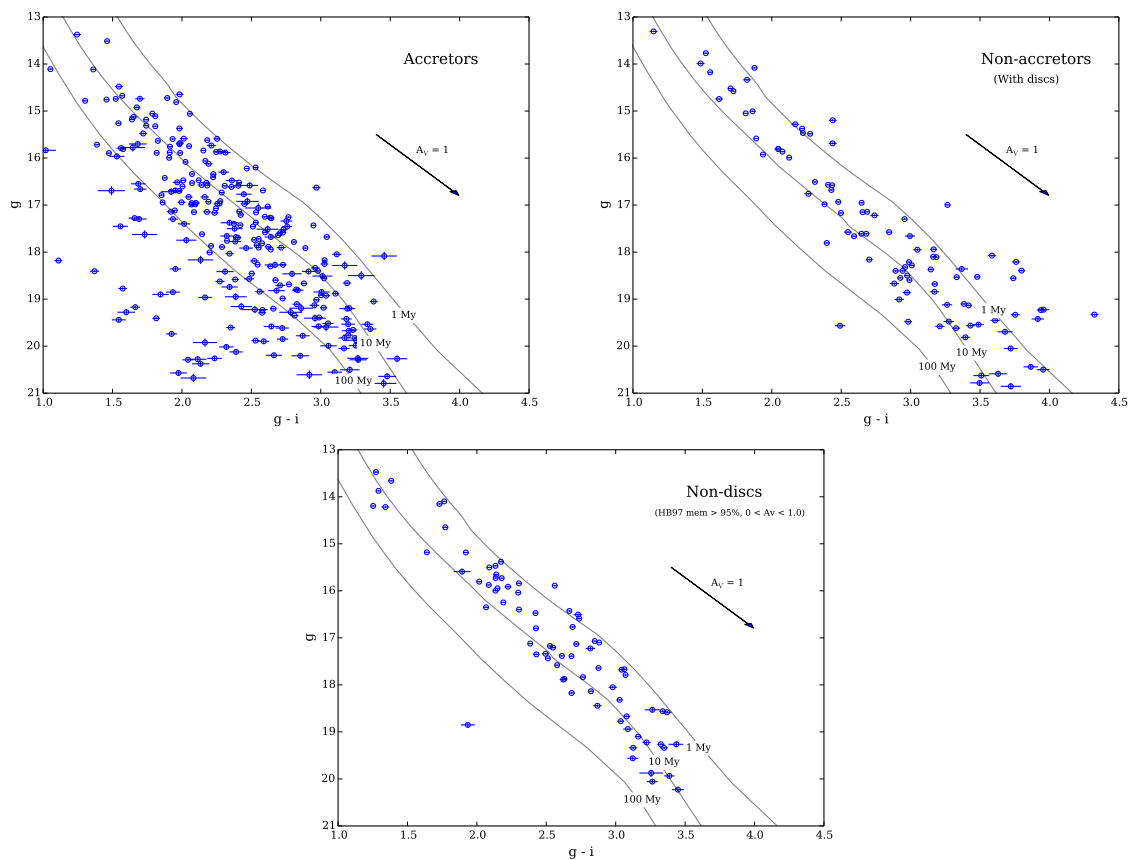


Figure 8.6: $g, g-i$ colour magnitude diagrams showing the samples containing only accreting stars (upper left), non-accreting disc-bearing stars (upper right) and discless stars (lower). The discless sample comprises stars with membership probability $> 95\%$ and $A_V < 1.0$ in Hillenbrand (1997). All stars in these diagrams have photometry which is unflagged and has $S/N > 10$ in both g and i .

8.5 What is the physical mechanism for this blueward shift?

Whilst it is clear that some mechanism linked to the accretion process is causing stars to be shifted either blueward or downward in the CMD, it is not clear what this process might be. Possible theories might include enhanced ‘grey’ extinction associated with circumstellar material in accreting stars or a contribution from accretion luminosity that has a spectrum that is bluer than the stellar photosphere.

8.5.1 ‘Grey’ extinction

Populations of stars that fall below the main population in the CMD have previously been explained by invoking a geometric argument, whereby disc-bearing systems are observed at high inclination so that the outer regions of the flared circumstellar disc cause high levels of extinction on the central star along our line-of-sight. Guarcello et al. (2010a) suggest this as the explanation for the faint-blue population in NGC 6611. In Chapter 2 I found three anomalously faint stars in the ONC that were associated with edge-on disc systems in *Hubble* space telescope images or high extinction. Theoretical models also support the notion that a population of high inclination stars should appear obscured by their own discs, this effect being more pronounced for Brown Dwarfs which may exhibit proportionally greater disc scale-heights (Walker et al. 2004; Mayne & Harries 2010).

Whilst undoubtedly this scenario occurs in star-forming regions, two pieces of evidence suggest that this is not the dominant mechanism behind the faint/blue stars in the CMD. Firstly the non-accreting disc-bearing population in our study does not show a similar fraction of faint/blue stars as the accreting population. Fig. 8.7 compares *Spitzer* IRAC photometry of the non-accreting and accreting disc-bearing populations. The left panel of Fig. 8.7 is a histogram of the two samples which compares the slope of the SED between 3.6 and 8.0 μm . This index (α IRAC) was defined by Lada et al. (2006) and used to empirically classify the density and structure of circumstellar discs. Whilst it appears that the non-accreting discs have a systematically lower value of α IRAC, both populations peak strongly within the ‘thick disc’ regime. Virtually no stars in either sample fall into the anaemic disc or naked photosphere categories. Thus if the discs are apparently so similar in structure for both populations, it seems unlikely that the presence of the disc is responsible for the faint/blue CMD positions of the accreting stars. Secondly, De Marchi et al. (2013) analyses models of flared discs around T Tauri stars and shows that geometric obscuration effects can only be responsible for a few percent of faint stars, a far lower number than is seen in the ONC or NGC 6611.

8.5.2 Accretion luminosity

To investigate whether accretion luminosity can cause PMS stars to move blue-ward in the CMD, I have used spectral types and extinctions measured for the spectroscopic stars in Chapter 7. For each of the accreting stars with spectra, I have taken the de-reddened photometric magnitude and colour of the best-fitting spectroscopic template star and have applied the extinction and reddening (assuming $R_V = 3.1$) that was measured for the accreting star. The resulting ‘extincted template’

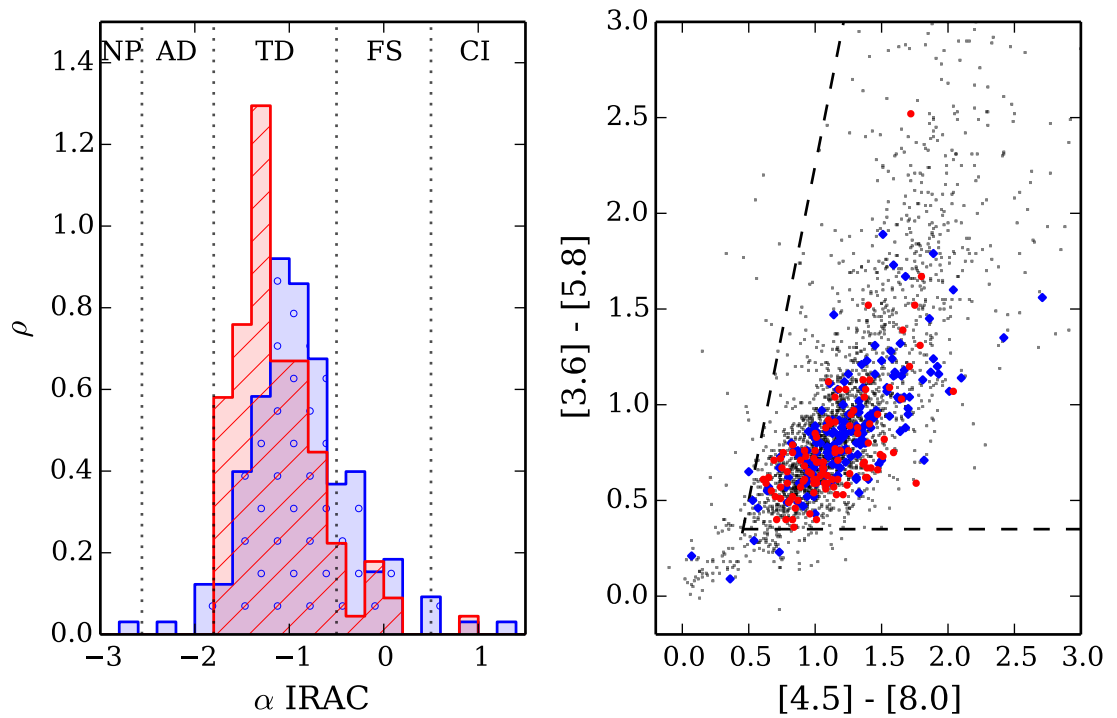


Figure 8.7: A comparison of the non-accreting disc-bearing and accreting disc-bearing stars based on *Spitzer* IRAC colours. A histogram (left panel) compares the α IRAC index for the accreting (blue-dotted) and non-accreting (red-hatched) stars. The histograms are normalised as a probability distribution function so that the area under the curve equals one. The vertical dotted lines denote the empirical disc classifications of Lada et al. (2006). NP: Naked photosphere, AD: Anaemic disc, TD: Thick disc, FS: Flat spectrum, CI: Class I. The right panel shows a *Spitzer* colour-colour diagram with the limit defined by Gutermuth et al. (2009) to classify Class II YSOs. Circles (red) denote non-accreting disc-bearing stars, Diamonds (blue) denote accreting disc-bearing stars. Faint (black) dots denote all stars in Cep OB3b with *Spitzer* photometry. Data from Megeath et al. (2012).

shows the position in the CMD that represents the photospheric colours plus extinction for the accreting star. The vector between the extinguished template and the mean CMD position of the accreting star corresponds to the accretion luminosity contribution (albeit also extinguished by an amount equal to that experienced by the photosphere). Examples of this process are shown in Fig. 8.8.

As the spectroscopic templates used are at discrete values of $g - i$, the colour of the intrinsic photosphere for the accreting star has an uncertainty corresponding to half of the spacing in $g - i$ between the templates. The templates used also show what appears to be an intrinsic luminosity scatter of up to ≈ 0.5 mag (see Chapter 7). Thus the CMD position of the accretion subtracted and extinction-corrected target is defined by the green box which incorporates these uncertainties. The spectroscopic extinction measurement is derived by comparing the fluxes in photospheric lines. Thus it is actually the sum of the extinction plus radius discrepancy between the two stars. As the radius discrepancy is accounted for within the extinction estimate, the uncertainty in magnitude of the extinguished template becomes small when the extinction is applied. Conversely the uncertainty in $g - i$ grows because the uncertainty in the intrinsic colour and magnitude of the accreting star photosphere combine to add extra uncertainty to the absolute extinction and hence the reddening too. The error box for the extinguished template is shown by the blue region.

The remaining vector required to move the star from the extinguished template position to the mean measured CMD position cannot be explained by extinction, binarity or photometric uncertainties. This vector is attributed to accretion luminosity. 21 stars in the sample have spectra that allow this analysis to be performed. The accretion vectors for all of these stars are compared in Fig. 8.9 and are consistent in explaining the blue-ward dispersion of the accreting stars. In Chapter 9 I show that in most accreting stars the SED of the accretion luminosity is consistent with that of a black body with a temperature between 5000 and 10000 K. Thus these vectors appear consistent with expectations based on models such as those by Calvet & Gullbring (1998). Fig 8.10 shows that lengths of the vectors in CMD space are broadly consistent with the veiling measured for each star.

8.6 Discussion

8.6.1 Ages of young star-forming regions

Much of the previous work to understand the age spread within the ONC has been performed within the Hertzsprung-Russell (H-R) plane rather than the CMD. Da Rio et al. (2010b) is the most comprehensive study to-date and derives values for T_{eff} using either low-resolution spectra or TiO sensitive narrowband photometry. L_{bol} is calculated using V and I band photometry and empirically derived bolometric corrections. Corrections for accretion luminosity, extinction and distance are also made. The conversion into the H-R plane appears to mitigate the direct correlation between accretor status and CMD position, a result shown by Jeffries et al. (2011) when comparing H-R diagram ages of stars in the ONC with and without discs. Despite this, there still remains a luminosity spread at a given T_{eff} that has no observationally confirmed cause.

For the ONC the accretion driven spread of stars in CMD space has relatively little effect

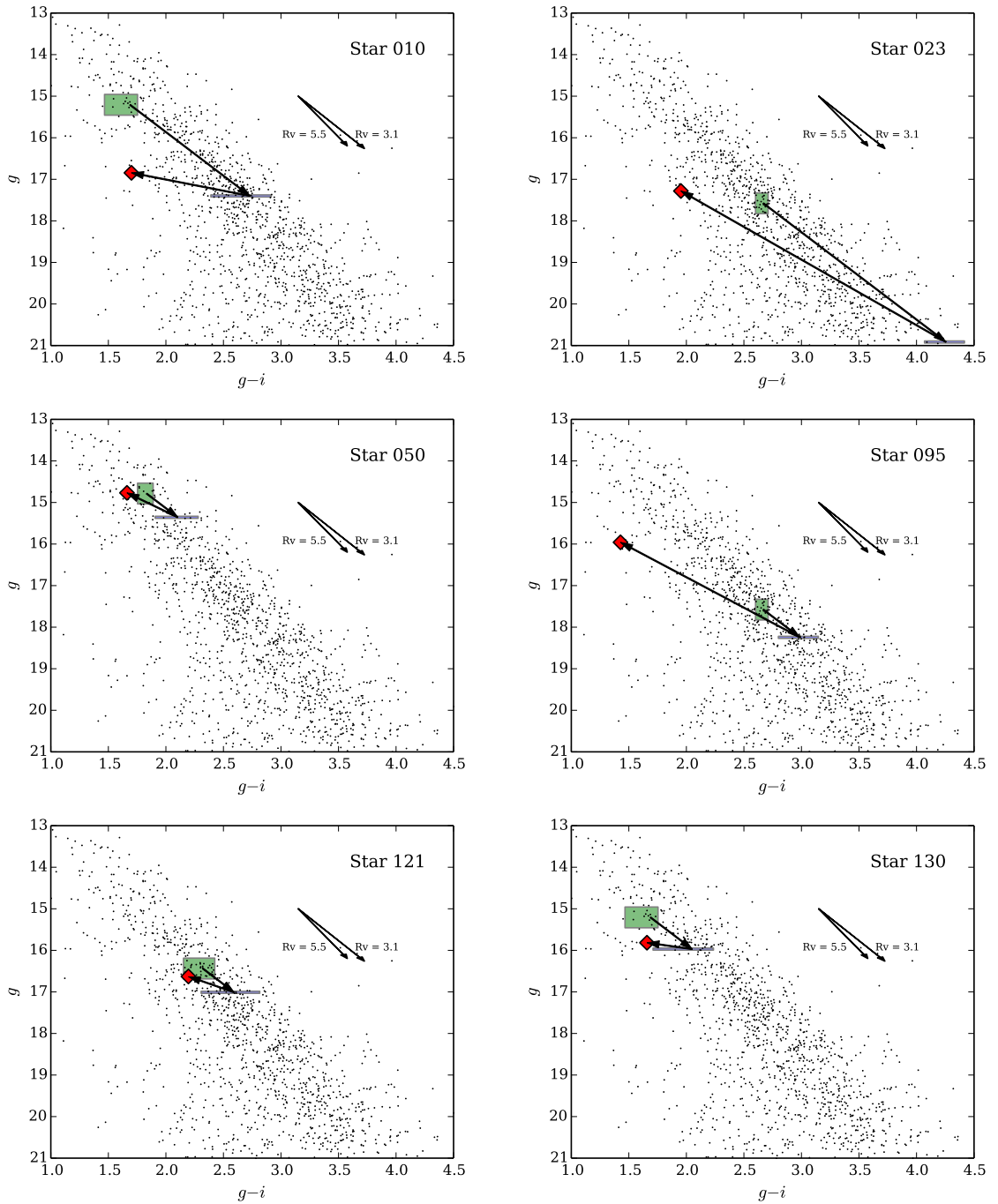


Figure 8.8: g , $g-i$ CMDs for accreting stars with spectra. For each accreting star the CMD position of the best-fit template star found in Chapter 7 is shown by the green box. The bounds of the green box are defined by the discrete colours of the template stars and their intrinsic luminosity spread. The extent of the green box defines the region in which we should find the intrinsic ‘photosphere only’ position for the accreting star. The blue box is the region in which a star within the green box will reside once its photospheric colours have been subject to extinction and reddening corresponding to the spectroscopically measured extinction of the accreting star. The red diamond is the mean CMD position for the accreting star. Extinction and accretion-luminosity vectors are shown with black arrows.

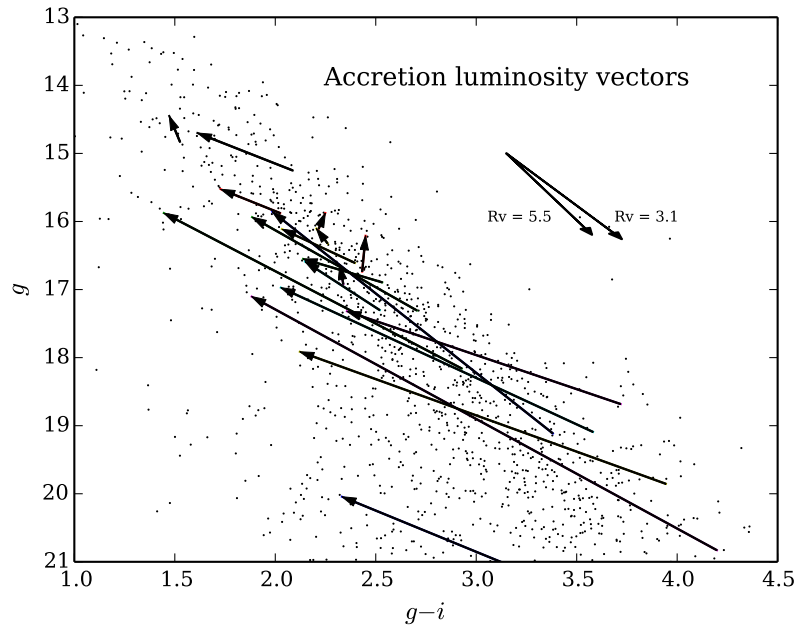


Figure 8.9: Accretion luminosity vectors calculated for all accreting stars within the spectroscopic sample (black arrows) compared with the CMD (black dots). The picture shown is clear, accretion luminosity moves stars blue-ward in the CMD, spreading stars away from the PMS locus. Extinction vectors corresponding to $A_V = 1$ are shown for comparison.

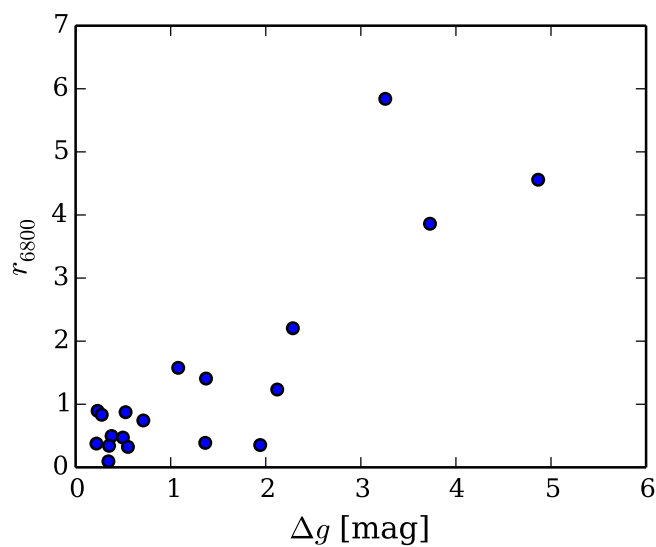


Figure 8.10: A comparison of accretion induced g band magnitude changes with mean values of veiling at 6800 \AA for the accreting stars.

on studies of its age and age-spread as there are comprehensive catalogues of stellar spectral types (Da Rio et al. 2010b; Hillenbrand et al. 2013). This is a situation that almost unique to the ONC. In contrast, most star forming regions are studied only using photometrically derived colour-magnitude diagrams, because of the prohibitive amount of telescope-time that is required to establish spectroscopically derived catalogues (e.g. Prisinzano et al. 2005; Mayne et al. 2007; Guarcello et al. 2010b; Bell et al. 2013). In light of the bias that accretion luminosity is shown to apply to both the apparent age and age-spread, studies that simply use photometry to derive these parameters should be treated with caution in very young regions with heavily accreting stars.

One notable example where accretion luminosity may explain an anomalously blue population of young stars is in NGC 6611. Guarcello et al. (2010a) find a population of stars with infrared excess that have colours much bluer than the bulk of the PMS population seen in this region. Comparison of the SEDs of these ‘blue with excess’ (BWE) stars with models by Robitaille et al. (2006) lead Guarcello et al. (2010a) to conclude that accretion luminosity can only be responsible for a small fraction of the BWE objects. Importantly though, the models of Robitaille et al. (2006) treat accretion luminosity with the models of Calvet & Gullbring (1998). Observations of near-infrared veiling by Fischer et al. (2011) as well as photometric measurements of accretion spectra in this study add weight to the argument that accretion luminosity might actually be on-average cooler and redder than these models suppose (see Chapter 9). This may explaining the poor χ^2 fitting statistics achieved by Guarcello et al. (2010a) for the BWE stars against the accreting SED models.

Other regions where this effect may be important include NGC 6530 where Damiani et al. (2006) find a population of stars with near-infrared excesses distributed closer to the ZAMS in $V, V - I$ colour-magnitude diagrams than the bulk of the X-ray identified members.

8.6.2 Angular momentum evolution

Littlefair et al. (2011) showed that a correlation exists between rotation rate and position in CMDs whereby stars which lie above an empirically determined pre-main sequence locus rotate more rapidly than stars which lie below this sequence. The result was confirmed in four young clusters, Cep OB3b, NGC 2264, NGC 2362 and the ONC. This is an unexpected and curious result as low-mass stars broadly evolve downward in the CMD as they contract along Hayashi tracks (Hayashi 1961) toward the ZAMS. Angular momentum conservation implies that we expect to see rotational rates increasing as one moves downward in the CMD. The high-resolution spectroscopic study of 74 K-M stars in four young associations by Scholz et al. (2007) determine that angular momentum conservation is indeed observed at ages > 5 Myr. At younger ages, angular momentum regulation is primarily explained by disc-locking theories, where magnetic field lines connect the star to the disc, forcing synchronous rotation between the star and the inner regions of the disc (e.g. Koenigl 1991; Bouvier et al. 1997).

The correlation that I see in Section 8.4 explains the Littlefair et al. (2011) results, as we would expect to see the accreting (and hence disc-locked) slowly rotating stars shifted bluewards in the CMD by contaminating accretion luminosity. To confirm that the effect that I see in Section 8.4 is not only limited to the ONC, Fig. 8.11 shows CMDs of Cep OB3b split into disc-bearing and

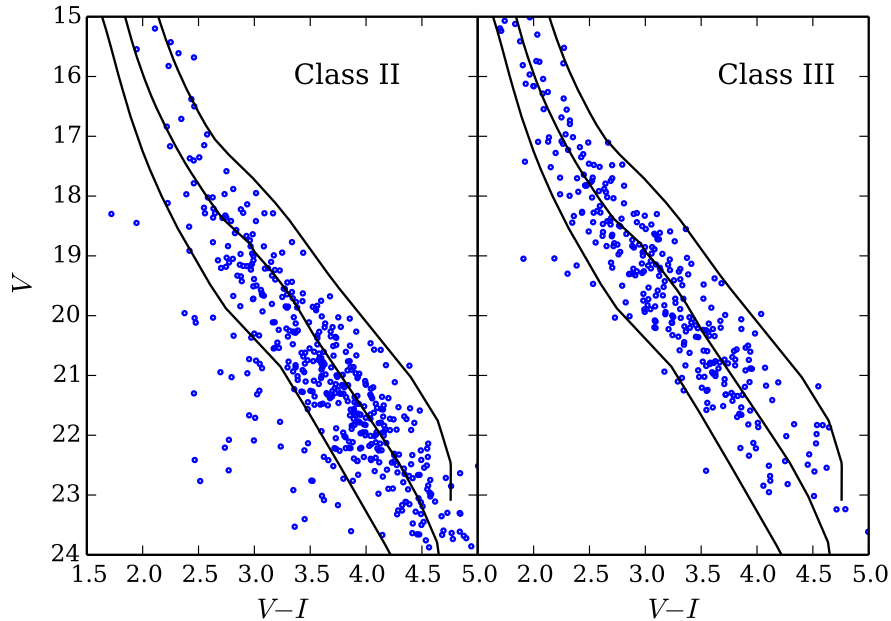


Figure 8.11: A comparison of $V, V - I$ CMDs for YSOs in Cep OB3b. Disc-bearing stars (left panel) are identified from *Spitzer* colours, Discless stars (right panel) are identified using *Spitzer* colours and X-ray flux (Allen et al. 2012). Optical photometry is from Mayne et al. (2007), as used in the Littlefair et al. (2011) study.

discless stars using classifications by (Allen et al. 2012). The disc-bearing stars are clearly shifted blueward when compared with the discless population. This effect is also seen in young stars in Taurus (Rees et al. *in-prep*). Littlefair et al. (2011) invoke several scenarios involving differences in accretion history to explain their result. The observations presented here do not rule-out such mechanisms, however their occurrence is not required to reconcile the observations with theory.

8.6.3 Correlations between Lithium depletion and apparent age

Palla et al. (2007) present results showing six stars in the ONC which appear to exhibit lithium depletion ages > 10 Myr in conjunction with H-R diagram ages that appear similar. They cite these as evidence for an older ‘evolved’ population of stars existing with the younger main population in the ONC. Closer inspection of these stars indicate that the reason for their high apparent H-R diagram and lithium ages may be accretion luminosity.

In Fig. 8.12 I show the position of these six stars in the CMD and in the $U - g, g - i$ colour-colour diagram. In the CMD it is clear that 5 of the six stars are shifted blue-ward from the PMS locus, indicating either old age or increased accretion luminosity. Their positions within the colour-colour diagram are particularly revealing in that all of the stars show a very large U excess, indicating that they are some of the most extreme accreting objects in the ONC. The fact that they show such large U excesses and thus very high accretion rates is unlikely to be compatible with stars that are > 10 Myr old.

Palla et al. (2007) determine H-R diagram ages based on T_{eff} and L_{bol} from Hillenbrand

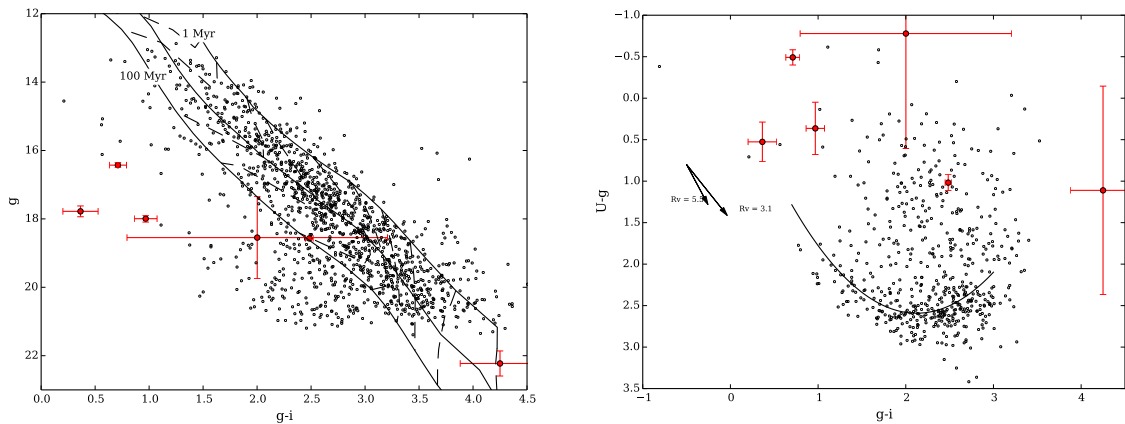


Figure 8.12: $g, g - i$ CMD (left panel) and $U - g, g - i$ colour-colour diagram (right panel) of the six stars identified in Palla et al. (2007) (red points) as having H-R diagram and/or lithium derived ages > 10 Myr. The CMD shows these stars compared with the general ONC population (black dots) and isochrones at 1, 10 and 100 Myr from Bell et al. (2014). In the colour-colour diagram, these stars are compared with the general ONC population (black dots) and the empirically defined PMS locus. The position of these stars in the colour-colour diagram implies that they have a large U excess and hence are heavily-accreting objects.

(1997). As discussed in Section 8.6.1 analysis of stellar ages using H-R diagrams will partly mitigate the effects of accretion luminosity, however high levels of accretion luminosity will make stars appear older in H-R space than they should. Thus, because of the extreme U excess shown, the Palla et al. (2007) stars are highly likely to have systematically over-estimated T_{eff} and thus appear erroneously older against model isochrones.

The lithium derived ages are not immune from the problems of high veiling either. Palla et al. (2007) account for the effects of veiling in the 6708\AA lithium line by assuming that the veiling spectrum is locally smooth and estimating its magnitude by comparing the equivalent widths of nearby metal lines (Ni 6643\AA , Fe 6663\AA , V 6625\AA) with those in unveiled templates. As is suggested in Chapter 9 and by Gahm et al. (2008) and Petrov et al. (2011), the assumption that the optical veiling is a smooth continuum breaks down at high accretion rates as line-emission adds to the smooth thermal component. The curves of growth of different species will then ‘infill’ spectral lines by different amounts, rendering the lithium-abundance measurement highly suspect. Whilst the smooth continuum assumption is generally reasonable at low accretion rates, the extreme veiling suggested by the position of the Palla et al. (2007) stars in the right panel of Fig. 8.12 renders their lithium derived ages highly uncertain.

8.7 Summary

The ages of PMS populations are often estimated by comparing the positions of stars against model isochrones within the CMD (e.g. Prisinzano et al. 2005; Mayne et al. 2007; Guarcello et al. 2010b; Bell et al. 2013). I have identified accreting stars in the ONC from their optical emission, and have compared the $g, g - i$ CMD position of the accreting stars with those of non-accreting disc-bearing and discless members. The population of accreting stars shows a significant blueward

shift, compared with the non accreting stars. If naively measuring the age of this population by comparison with PMS isochrones, one might conclude that the accreting stars are older than the non-accreting stars. This effect would cause the age of heavily accreting (and likely the youngest) stellar populations to be systematically over-estimated compared with (potentially older) more weakly accreting populations. The accreting stars also show a greater luminosity spread than the non-accretors. The similarity in CMD positions of the non-accreting disc-bearing and discless populations show that the presence of a disc does not by itself contribute to a shift in CMD position. Spectroscopic analysis of 21 accreting stars shows that this blue-ward shift is driven by accretion luminosity along vectors that cut across the PMS locus.

This result may explain three outstanding problems in star-formation. Firstly, populations of apparently ‘older’ stars in young regions such as NGC 6611 and NGC 6530 lie blue-ward of the main PMS population and the close to the ZAMS. These stars may conceivably be explained as a population of heavily accreting stars that have had their colours modified by accretion luminosity. A comprehensive spectroscopic survey or a photometric U survey might determine whether this is the case.

Secondly, Littlefair et al. (2011) found a correlation between rotation rate and position in the CMD whereby fainter stars rotate more rapidly than brighter stars. This may simply be explained by the slowly-rotating disc locked accreting stars being displaced blue-ward of the PMS locus by their accretion luminosity. The implication of this is that no recourse to models of luminosity spreads caused by episodic accretion is required.

Finally, a small subset of stars in the ONC are found by Palla et al. (2007) to have H-R diagram and lithium ages > 10 Myr, and are used to argue that star-formation has been occurring in the ONC for longer than this time. I find that this subset of stars are some of the most heavily accreting objects in the entire ONC population. Accretion luminosity is shown to bias spectroscopic estimates of T_{eff} (using TiO band indices) toward hotter photospheric temperatures. At a given luminosity, this makes a star look older than it really is. Accretion luminosity in stars with extremely high accretion rates has also been shown to preferentially ‘fill’ some spectral lines with emission, rendering estimates of veiling and hence element abundance highly uncertain. The result of this is to make H-R diagram or lithium ages estimated from spectroscopic analyses of heavily veiled stars highly uncertain and most-likely significantly overestimated.

Chapter 9

Comparing accretion diagnostics and exploring the nature of veiling

9.1 Introduction

Whilst theoretical models of accretion luminosity (e.g. Calvet & Gullbring 1998) approximate the observed veiling in YSOs at UV and blue wavelengths (Gullbring et al. 2000) they often fail to match observations of veiling in the red and near-IR for many stars (e.g. Folha & Emerson 1999; Cieza et al. 2005; Edwards et al. 2006; Fischer et al. 2011). This is an important problem, as either it means that the accretion luminosity models are wrong, or that there is an additional source of veiling at longer wavelengths (beyond $\approx 6000 \text{ \AA}$) that is currently unidentified. It may be that the red and near-IR excess emission is entirely unrelated to the accretion signature on the stellar surface. This is a conclusion that is postulated by Fischer et al. (2011), who suggest that emission from optically thin gas from within the dust-sublimation radius of the disc may be responsible. McClure et al. (2013) suggest that instead the red and near-IR excess is the result of emission from dust at the inner edge and surface of the disc. Ingleby et al. (2013) further suggest a composite accretion luminosity model where hot, low filling-factor accretion spots are combined with cooler, high filling-factor regions. This latter model is inspired by models of unstable accretion flows which suggest that accretion-shock heated regions may be distributed over a much larger fraction of the star than is normally supposed. Uncertainty in the source of the veiling at red wavelengths is problematic as many authors use measurements of veiling to predict accretion rates (see Hartigan et al. 1991; White & Basri 2003; White & Hillenbrand 2004, and Section 1.4.3). These predictions rely on estimating bolometric corrections for the accretion luminosity based on the theoretical models. If accretion luminosity is in fact more distributed and cooler than typically thought, these models will over-estimate the accretion rates. Also, if the veiling emission is from a source that is unrelated to the accretion luminosity, accretion rates will once again be over-estimated.

In this chapter, I use my simultaneous spectroscopy and photometry to investigate time variability in the relationship between the three main accretion metrics, U band flux, $H\alpha$ flux and veiling at $\approx 7000 \text{ \AA}$. I then characterise the excess luminosity over the range $\approx 3500 - 8000 \text{ \AA}$ for a sample of accreting stars and use temporal variability to investigate whether the red excess is

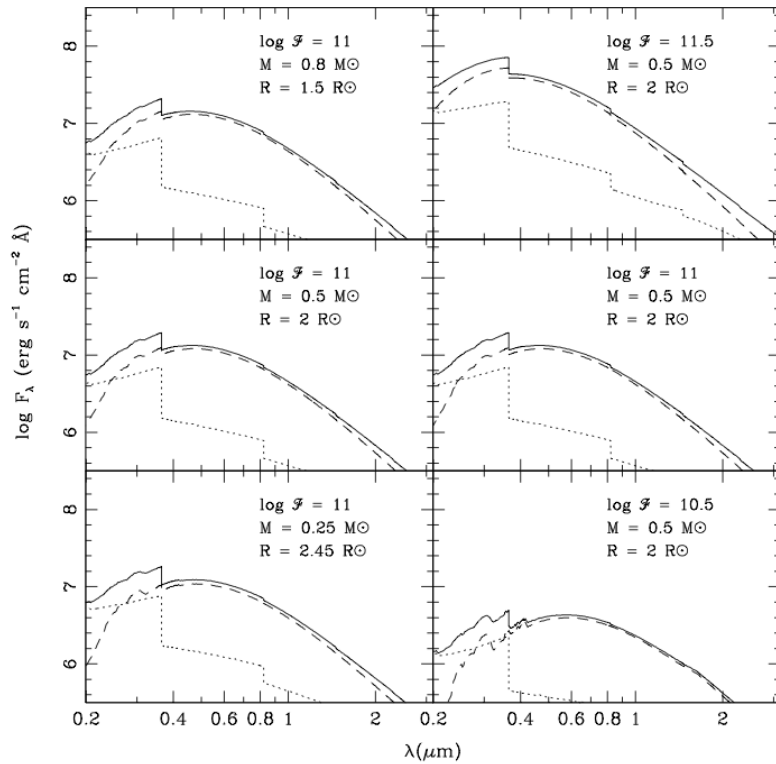


Figure 9.1: The accretion luminosity models of Calvet & Gullbring (1998) for a selection of stellar masses, radii and accretion energy fluxes \mathcal{F} . The dotted line is optically thin emission from the preshock (plus attenuated post-shock emission), the dashed line is the emission from the heated photosphere, and the solid line is the total emission.

physically linked to that seen in the range 3500 - 5000 Å.

9.2 The accretion luminosity model

The ‘benchmark’ model of accretion luminosity that is typically used in studies of young stars is that by Calvet & Gullbring (1998). This model (shown in Fig. 9.1) describes the accretion luminosity as an optically thick thermal emission spectrum from the heated photosphere below the shock combined with optically thin emission from the preshock and attenuated postshock regions. The optically thin emission dominates at wavelengths shorter than the Balmer discontinuity at 3646 Å. The heated photosphere is modelled as a discrete region at the foot of the accretion column with temperature $T \approx 6000 - 10\,000$ K and covering an area of 0.1 - 1 % of the star.

9.3 Comparison of accretion diagnostics

Measurement of U band excess luminosity is thought to be the most robust diagnostic for accretion rates in YSOs (see Section 1.4). However extinction by both interstellar dust and the atmosphere of the Earth as well as contamination by nebular emission and poor observing conditions can make U band photometric observations difficult, time-consuming and imprecise. Thus measures of

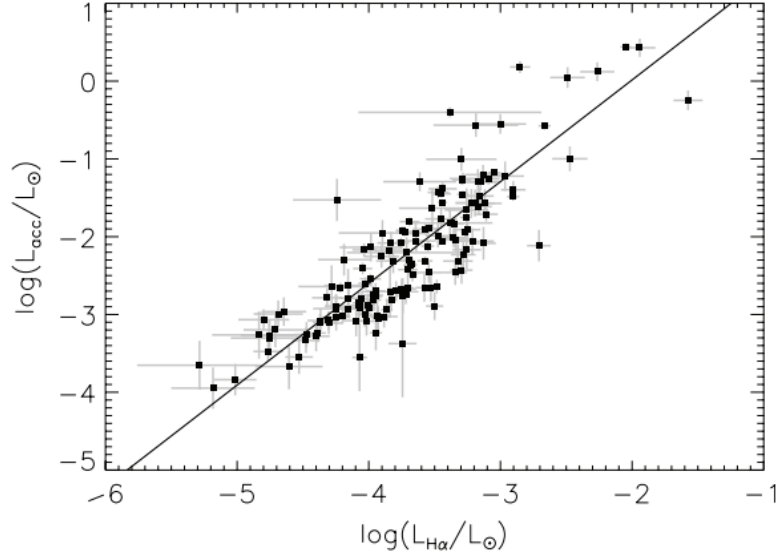


Figure 9.2: Empirical relation between L_{acc} and $L_{\text{H}\alpha}$. From: Manara et al. (2012)

accretion rate that rely on other diagnostics such as $\text{H}\alpha$ emission or photospheric veiling are often used instead. The simultaneous observations of YSOs made in this study using spectroscopy and U and $\text{H}\alpha$ narrowband photometry offer an excellent and possibly unique opportunity to directly compare these techniques and comment on their degree of agreement and efficacy as accretion rate diagnostics.

9.3.1 U band flux vs. $\text{H}\alpha$

Ingleby et al. (2013) show that the relation between U band excess emission and $\text{H}\alpha$ is much more clearly defined if we consider the flux in the $\text{H}\alpha$ line rather than its equivalent width. Thus for large surveys, where flux calibration of large numbers of spectra would be difficult and time consuming, $\text{H}\alpha$ narrowband photometry is most effective as an accretion rate estimation tool. Manara et al. (2012) define an empirical function linking the luminosity in the $\text{H}\alpha$ emission line ($L_{\text{H}\alpha}$) and the total accretion luminosity (L_{acc})

$$\log\left(\frac{L_{\text{acc}}}{L_{\odot}}\right) = (1.31 \pm 0.03) \log\left(\frac{L_{\text{H}\alpha}}{L_{\odot}}\right) + (2.63 \pm 0.13), \quad (9.1)$$

using photometric data from Da Rio et al. (2009). The fit to the data is shown in Fig.9.2. Similar relations have been described by Herczeg & Hillenbrand (2008), Barentsen et al. (2011), and Ingleby et al. (2013).

Whilst the relation appears robust, there is a scatter of ≈ 1 dex in L_{acc} at a given $L_{\text{H}\alpha}$, which corresponds to an uncertainty of similar magnitude in estimates of \dot{M} . This scatter may be caused by time-variable extinction (as extinction corrections are usually made based on single epoch measurements) or by changing viewing geometry of the different emitting regions. I have investigated how much of this spread is due to time variable processes, allowing an assessment of

how closely coupled these diagnostics are in a given star. Fig 9.3 compares U band excess flux with $H\alpha$ excess flux for the 15 stars in the spectroscopic accreting disc-bearing sample that have suitable high quality photometry in U and $H\alpha$. The $H\alpha$ and U bands fluxes shown are the excess remaining once the expected photospheric continuum contribution had been subtracted. This was achieved by predicting the continuum flux in the $H\alpha$ and U bands using the relations derived in Chapter 8 (Equations 8.1 and 8.2) and subtracting the continuum contributions from the measured fluxes at each epoch.

The data show that most stars vary in a manner that is not consistent with a monotonic relation between U excess and $H\alpha$ excess. Variability in U that is not matched by variability in $H\alpha$ appears to be the most common behaviour (e.g. Stars 10, 26, 158) although changes in $H\alpha$ at constant U are seen (e.g. Stars 50, and 95). Without performing any statistical analysis, it is immediately apparent that the variability seen in Fig. 9.3 is able to explain the ≈ 1 dex scatter that we see in the relation between L_{acc} and $L_{H\alpha}$.

It is pertinent to consider physical mechanisms which might explain this behaviour. The U band excess is principally thought to result from discrete and inhomogeneously distributed hot-spots on the surface of the star. Much of the $H\alpha$ excess is thought to originate from infalling material above the surface of the star with perhaps some contribution from wind emission. Thus it would appear that modulation in the U excess that is independent of the $H\alpha$ excess could be due to changes in the area of these structures that are visible as the star rotates. Even if the hot-spots and accretion flows are physically associated (the former being formed by the impact of the latter), the spots on the surface will rapidly move in and out of view as the star rotates, whereas the vertical extent of accretion columns as well as their quasi-transient nature might make them visible for different parts of the rotation cycle. In addition, the hot regions may exhibit strong $H\alpha$ absorption features (as seen in main-sequence stars with spectral types of approximately F0 and earlier), thus modulating the integrated $H\alpha$ flux for the star which also includes contributions from the chromosphere and an extended wind or outflows.

9.3.2 U band flux and veiling

I have measured the veiling at $\approx 7000\text{\AA}$ as a function of time for stars within the accreting disc-bearing sample. I wished to evaluate how well changes in the accretion veiling correlate with time-domain changes in the observed U band excess flux. Unlike $H\alpha$ emission, the veiling continuum is often assumed to arise from the same physical regions as the U band excess, so we might expect a better correlation between these parameters than we see between U band excess and $H\alpha$.

The veiling measurements were made by using the best fitting discless templates found for each star in Chapter 7. The veiling measurement process was performed between 7000 and 7200 \AA and used the same fitting procedure as that described in Section 2.4.2. Individual spectra with SNR < 10 per 0.4 \AA pixel were rejected from the fitting process. Veiling measurements were matched to their (temporally) nearest U band excess measurement. Measurements that could not be matched to a U band excess measurement within a limit of 0.5 hours were rejected, as variability in U would add uncertainty to the flux measurement. The U band measurements have their predicted photospheric component subtracted using the method described in Section 9.3.1, leaving just the

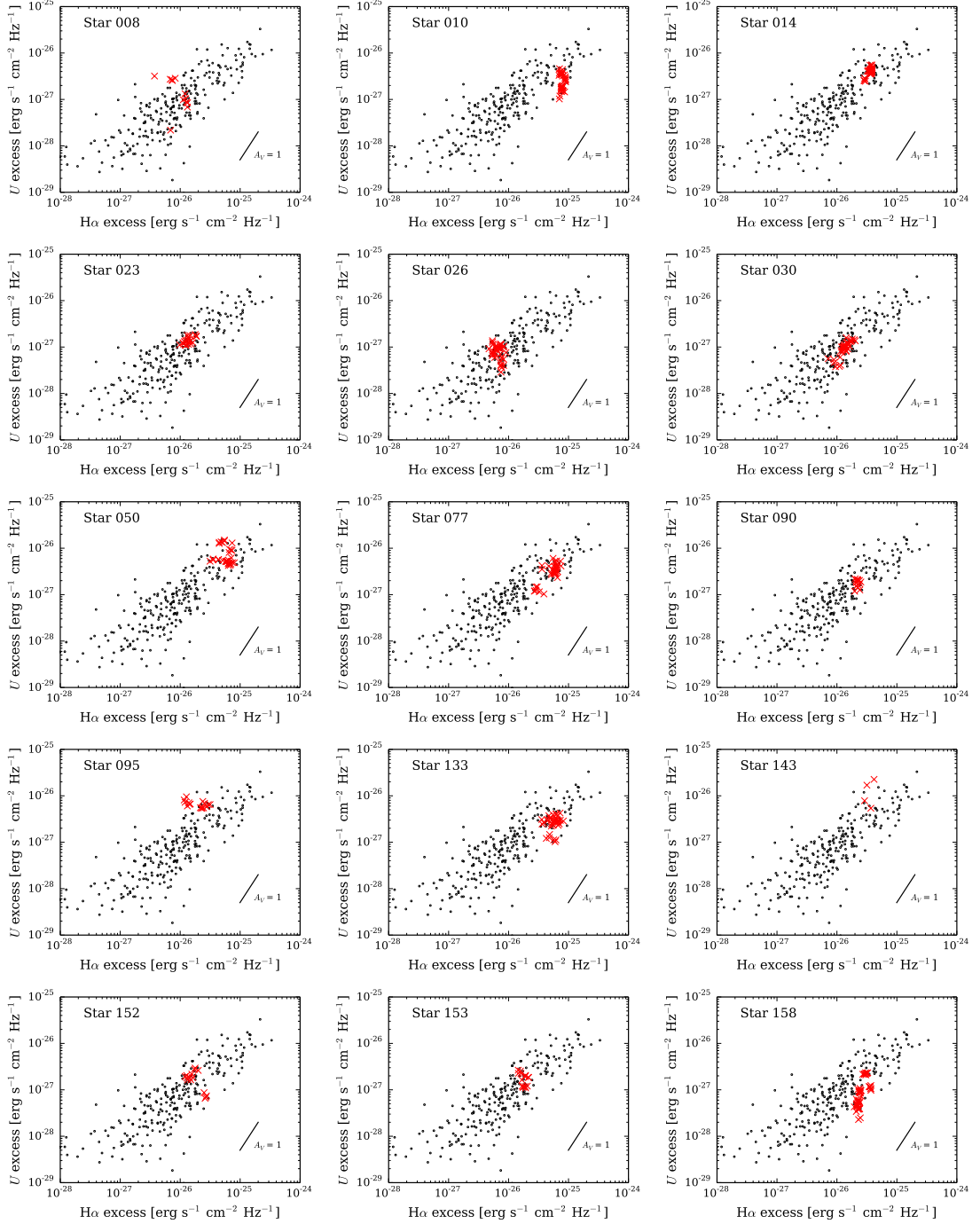


Figure 9.3: A comparison of $H\alpha$ and U band excess fluxes as a function of time for accreting disc-bearing stars in the spectroscopic sample. The (red) crosses show measurements made at different epochs over the seven nights for a given star. The black circles are mean measurements (over the seven nights) for all available stars in the ONC dataset. The spread seen in the black circles is comparable to the spread seen in single epoch data by Manara et al. (2012). An extinction vector corresponding to $A_V = 1$ is shown. No correction for extinction has been made.

excess. Fig. 9.4 compares the measured veilings with the U band excess for the same 15 accreting disc-bearing stars that were shown in Fig. 9.3.

The relationship between the two parameters appears in a few cases to behave as we might expect. Stars 14 and 23 appear to show variability which shows a linear relationship (within uncertainties). Thus in these cases, the measurements of the veiling might be expected to describe the U flux. Conversely, other stars show changes in U flux that appear to be uncorrelated with the veiling (e.g. Stars 10, 133 and 158). These probably indicate that changes in extinction or possibly additional sources of veiling are present, that mask the true accretion luminosity. For many stars, I see a combination of correlated and uncorrelated behaviours. It is notable that in some stars, significant changes in veiling appear to occur at approximately constant U excess (e.g. Stars 26, 50 and 158). It is possible that this behaviour is the result of a fortuitous combination of increasing extinction combined with increasing accretion luminosity. However, given how common this behaviour appears to be, this explanation seems unlikely. Changes in veiling that do not correspond to changes in U excess might be evidence for variability in an additional veiling source, such as emission from the disc, or cool distributed accretion luminosity that only weakly contributes to the U band flux. Either way, it appears that predicting L_{acc} from bolometrically corrected veiling flux measurements appears difficult for many stars.

9.4 Analysis of correlation between U excess and veiling

To further understand the nature of the luminosity excess and explore the temporal behaviour of veiling at 7000 \AA , in what follows I use the simultaneous photometric and spectroscopic data to estimate the mean SED of the luminosity excess across the optical bands for the accreting stars. This has allowed me to do two things. Firstly, I have compared the mean SED of the excess emission to the variability seen in the total SED of the star. Thus I could determine whether simple changes in the magnitude of the luminosity excess were driving the observed variability or whether other mechanisms such as extinction changes were responsible. Where the SED variability behaviour was shown to be explained by changes in the magnitude of a single excess spectrum, it suggested that the excess was produced through a single physical mechanism and the excess SED allowed me estimate the temperature of the source.

I also wished to investigate whether the excess luminosity appears different in nature between the stars where changes in the U excess and the veiling are correlated and those where little correlation is seen. To do this, I have selected two samples that represent stars exhibiting a monotonic relation between U excess and the veiling and stars that do not show any relation. These have been selected based on a Spearman's rank correlation test which measures how well the relationship between two variables can be described using a monotonic function whilst assuming no prior knowledge about the expected distribution of the data. The stars selected in the 'correlated' sample all have a 'p-value' (which describes the likelihood that a correlation is seen by chance from a random uncorrelated sample) of < 0.001 . Stars in the 'uncorrelated' sample have p-values > 0.2 . Table 9.1 lists the sample of 'correlated' stars, Table 9.2 lists the sample of stars which show no evidence of correlation.

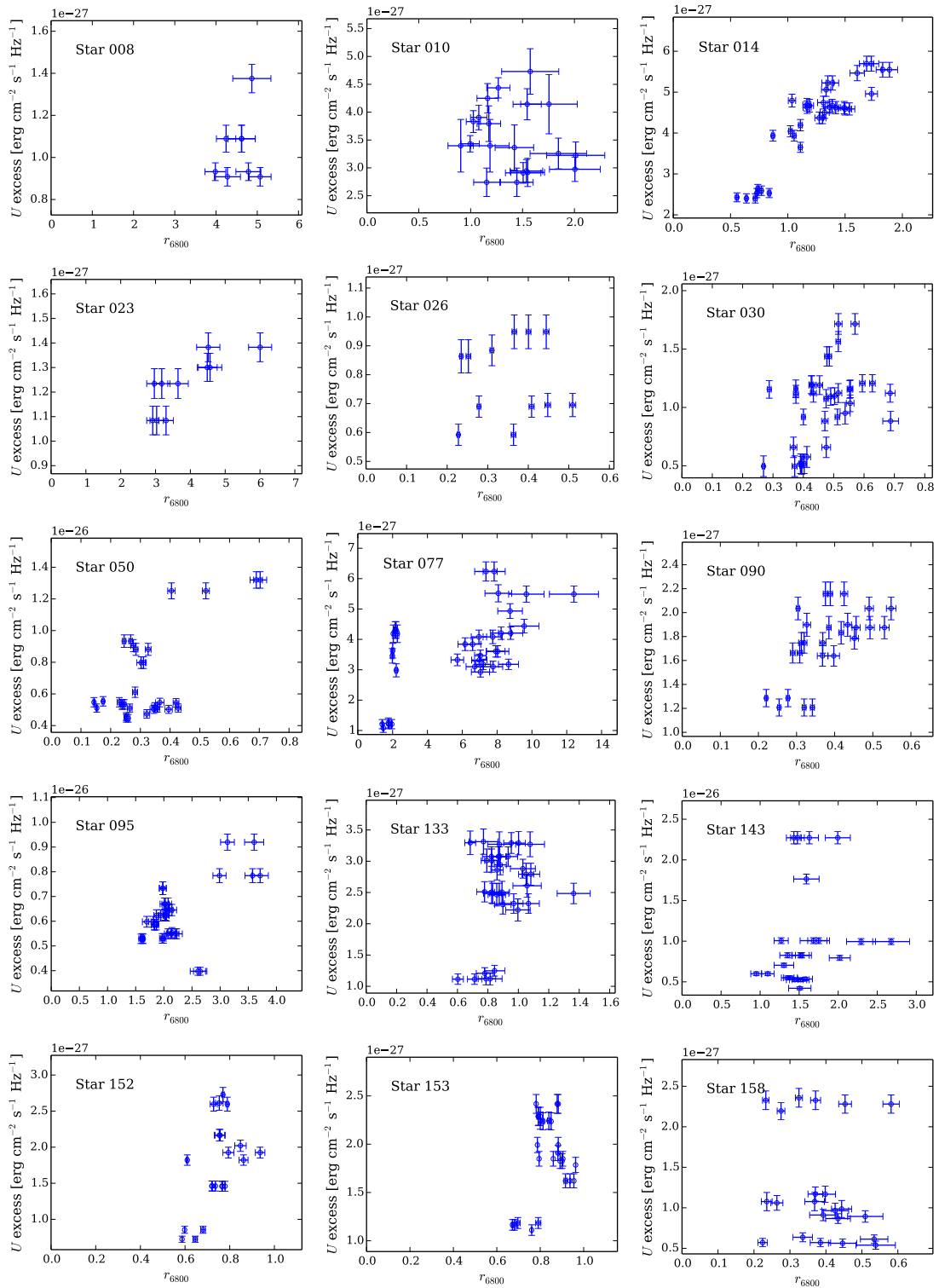


Figure 9.4: A comparison of veiling and U band excess fluxes as a function of time for accreting disc-bearing stars in the spectroscopic sample. The points show measurements made at different epochs over the seven nights for a given star. Changes in extinction will move points vertically in this diagram. No correction for extinction has been made.

Table 9.1: Key parameters for stars showing correlated U excess and veiling behaviour

Star id	$\langle A_i \rangle$ (mag)	$\langle r \rangle$
14	0.35	1.23
23	1.75	3.86
77	0.85	5.84
90	0.0	0.38

Table 9.2: Key parameters for stars showing uncorrelated U excess and veiling behaviour

Star id	$\langle A_i \rangle$ (mag)	$\langle r \rangle$
10	1.15	1.41
26	0.75	0.35
133	1.1	0.90
153	0.0	0.83
158	2.1	0.39

9.4.1 Measurement of the luminosity excess spectrum

To measure the excess luminosity in accreting stars, I compare the photometric SED measured for each accreting star with that of its ‘best-fit’ photospheric template that I found through the spectroscopic analysis in Chapter 7. The spectroscopic analysis also provided a measurement of the mean extinction at 6800 \AA (A_{6800}) for each accreting star. This was achieved by measuring the ratio of flux in the photospheric lines of the template spectrum to the flux in the photospheric lines of the accreting target star. The reciprocal of this ratio, converted into magnitudes is the extinction A_{6800} .

The first step in measuring the excess luminosity for each star is to take the photometrically measured SED of the ‘best-fit’ (low extinction) photospheric template and then apply the extinction that is measured for the target star. The resulting SED is assumed to represent the accreting star without any excess emission. The extinction that is applied has $R_V = 3.1$. There is evidence that R_V may actually be greater than this in the circumstellar environment around young stars (see Chapter 6), however we have no independent method of measuring this parameter in stars where the accretion luminosity is variable. Thus the template SED has an additional uncertainty after application of the extinction which is calculated by applying the extinction with an alternative value of $R_V = 6.0$.

The discless template stars appear to show an intrinsic scatter in radius. This is shown by the luminosity scatter seen in Fig. 7.3 and is supported by earlier work by Jeffries (2007). The spread in radius does not affect their validity as spectral templates ($\log g$ differences are too small to be of consequence), it does however have an impact on the estimate of A_{6800} , as a contribution to the difference in the flux within the lines between template and accreting star may stem from radius difference rather than simply the extinction. The result is that uncertainty in the radius

of the template star adds an additional uncertainty in the extinction A_{6800} . Hence the predicted magnitudes in filters other than the 6800 Å narrowband incur an additional uncertainty which is the product of the uncertainty in A_{6800} and the chromatic component of the extinction. This additional uncertainty is calculated and is shown in all SEDs assuming an intrinsic rms scatter in luminosity of 0.3 magnitudes, this corresponds to $\approx 12\%$ in radius (see Section 7.2). Fig. 9.5 compares the predicted photospheric SEDs with their measured SEDs for the 15 stars in the accreting star sample. In all stars, the extinguished template SEDs have smaller fluxes in all bands than the observed SEDs for the accreting targets. Excess emission is seen in all stars, particularly (as expected) at bluer wavelengths.

The next step was to subtract the photospheric template SED from the accreting star SED, revealing the excess in each band. The resulting excess SED for each star was then corrected to remove the effects of extinction and reddening based on the measured A_{6800} to reveal the intrinsic SED of the excess emission. As this extinction correction is applied using an R_V value that is the same as that used when reddening the templates, the uncertainty on the SED of the luminosity excess caused by uncertainty on R_V largely cancels, rendering uncertainty in R_V unimportant. Thus, the uncertainty on the final excess luminosity SED is driven by the uncertainty on the template radii, A_{6800} and photometric uncertainties (of which the latter two are typically small in comparison).

Fig. 9.6 shows the derived luminosity excess SEDs for the sample of accreting stars. It is clear that the SEDs show significant differences both in magnitude and colour dependence. Fig. 9.6 also compares the luminosity excess to simple black-body models with temperatures of 5000 K, 7500 K, 10 000 K and 50 000 K. In some cases the luminosity excess flux appears to agree reasonably well with that of a simple black-body (e.g. Stars 10, 23 and 30). However, some stars (e.g. 90, 152 and 153) show a general trend in the luminosity excess that is too bright in the redder bands to be explained by models which employ small (as fraction of the stellar surface) spots with temperatures > 5000 K. This suggests that either another source of excess emission exists that is much redder than the accretion luminosity, or that the accretion luminosity is (at least in-part) cooler than is typically assumed.

9.4.2 Comparing the luminosity excess with SED time-variability

I have characterised temporal changes in the SEDs for the accreting stars using a principal component analysis (PCA) that is identical to that described in Section 6.2.2. For the 15 accreting stars analysed in this chapter, the number of principal components required to reconstruct $> 95\%$ of the variability in the SED time-series is either one (for 10 stars) or two (for 5 stars). This implies that just one or two phenomena dominate their broad-band variability. The first principal component (which describes the largest fraction of their variability) for each of these stars is shown in Fig. 9.7 and is compared with the excess luminosity that I measured for each star in Section 9.4.1. The first principal component spectrum has in each case been scaled by its mean flux over the seven nights of observations. In Fig. 9.7 the excess luminosity has not been corrected for extinction and reddening so that it can be directly compared with the results of the PCA.

For four stars (14, 23, 77 and 95) the similarity between the first principal component and

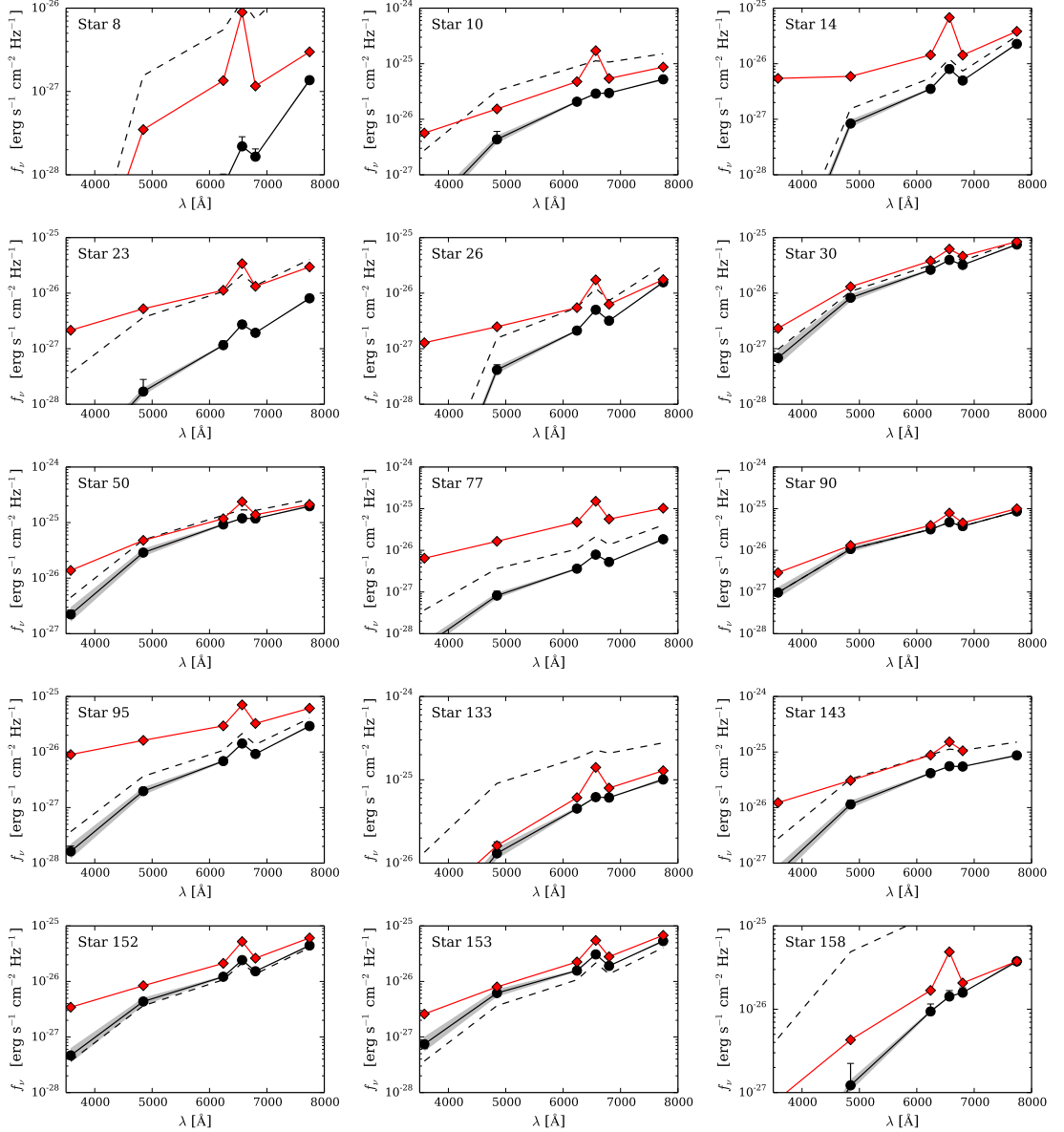


Figure 9.5: A comparison of intrinsic photospheric SEDs with observed SEDs for accreting stars. The dashed black line is the extinction-free best-fit photospheric template SED found for each star using the spectroscopic analysis in Chapter 7. The (black) circles represent the template after application of the extinction measured for each accreting star in the spectroscopic analysis. Uncertainties on the template SED caused by uncertainties in the adopted value of R_V are indicated by the black error bars, which are computed assuming $R_V = 6$ rather than the nominal $R_V = 3.1$. Where error bars are not visible, they are smaller than the markers. The (grey) shaded region represents the uncertainty on the photospheric SED due to uncertainty on the intrinsic radius of the templates. The (red) diamonds represent the measured SED for each accreting star. The peak in the SEDs at 6568\AA is the flux measurement in the narrow-band $H\alpha$ filter.

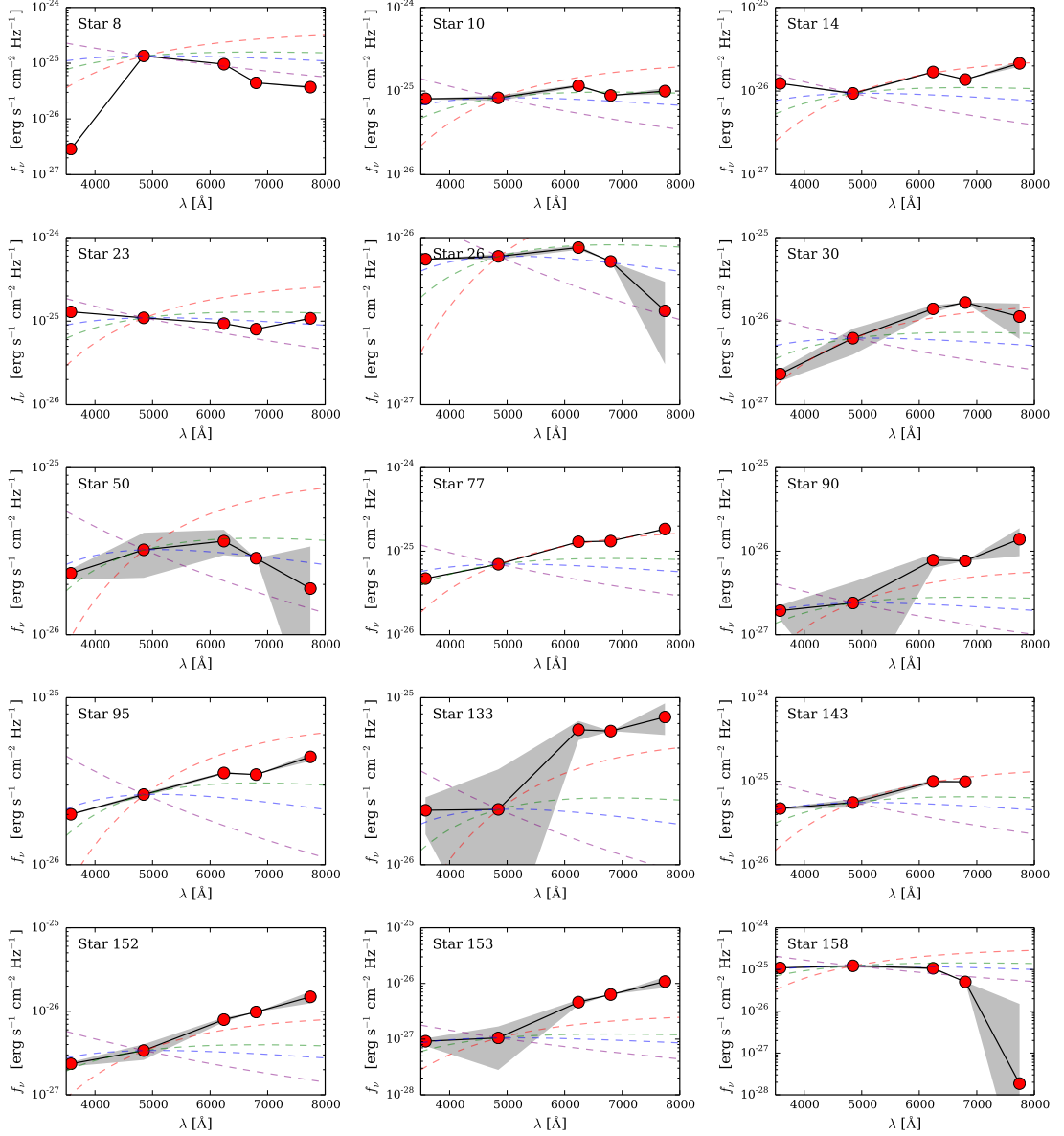


Figure 9.6: The luminosity excess flux calculated as a function of wavelength for 15 accreting stars in the ONC (red circles). The grey shaded region shows the uncertainty on the excess. The dashed lines show black-body functions with temperatures of 5000 K, 7500 K, 10000 K and 50000 K, normalised to the data at the wavelength of the g band. The excess in the narrowband $H\alpha$ filter is omitted as it is likely that multiple sources of non-thermal flux are present and thus any measurement of luminosity excess is considered unreliable.

the excess luminosity is remarkable. This similarity implies that the temporal changes that we see in the SEDs over the seven nights are driven by the same mechanism that is responsible for the excess luminosity. For other stars the correlation is not so clear. In three stars (8, 90 and 143) the variability and the luminosity excess do agree well, except for in the the *U* band and $H\alpha$. This might imply that variability is driven by emission from ‘hot’ spots on the surface which are not correlated with Balmer emission. For the remaining eight stars, the relationship between the variability and the luminosity excess is not clear. This implies that other mechanisms (or combinations) are responsible.

9.4.3 Comparing stars with ‘correlated’ and ‘uncorrelated’ *U* band excess and veiling behaviour

Two samples of stars were selected in Section 9.4 which showed correlated and uncorrelated variability in *U* band excess and veiling.

The ‘correlated’ stars

The analysis has shown that three of the four stars with strong correlation between *U* band excess and veiling are also highly veiled ($1.23 < \langle r \rangle < 5.84$), and display variability in the PCA that is dominated by a single SED which is almost identical to their calculated excess luminosity spectrum (Stars 14, 23 and 77). Thus it seems highly likely that for these stars the variability is dominated by changes in the magnitude of accretion luminosity. Each of these stars shows an excess that appears to be hotter than a 5000K black-body, consistent with a Calvet & Gullbring (1998) model. The fourth star in this sample (Star 90) appears to behave somewhat differently. It shows variability in PCA that is redder than its mean luminosity excess. The mean luminosity excess also appears to be quite red when compared with black body models in Fig. 9.6, apparently displaying a temperature cooler than 5000K. As this cool excess appears to be correlated with its *U* band excess, this star is a candidate for high filling-factor ‘cool’ accretion like that described by Ingleby et al. (2013).

The ‘uncorrelated’ stars

Stars within the uncorrelated sample show a range of luminosity excess colours ranging from very blue (e.g. Star 26) to very red (e.g. Star 133). The SED variability in PCA is slightly more consistent across the sample, showing a first principal component that is almost always slightly redder than the luminosity excess (Star 133 being the exception to this). The typical veiling in this sample is considerably lower than that seen in the ‘correlated’ sample ($0.35 < \langle r \rangle < 1.41$). The combination of behaviours observed indicate that perhaps the variability in four of these stars (Stars 10, 26, 133 and 153) are driven by changes in extinction. It is possible also that the presence of cool spots may contribute to the modification of the SED, although the strong temperature dependence of the flux contribution ($L \propto T^4$) will limit the influence of spots that are significantly cooler than the primary photosphere.

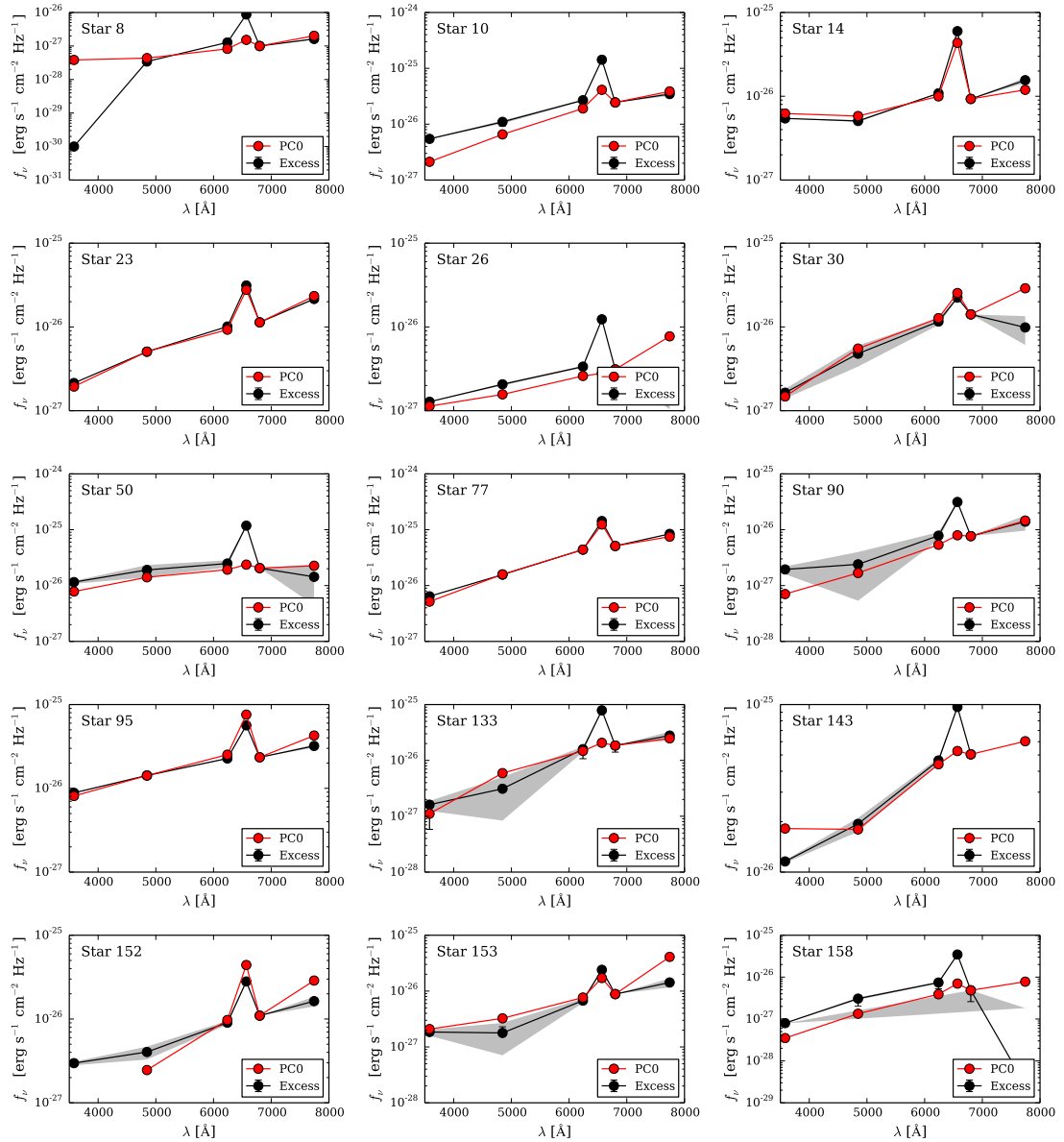


Figure 9.7: Comparison of photometric SED variability with the excess luminosity for accreting stars. The black points show the measured luminosity excess. The red points show the first principal component. The excess luminosity SED had been normalised to the variability SED at the n_{6800} wavelength to allow for comparison.

Table 9.3: Estimated stellar masses and accretion rates for stars with extracted excess luminosity SEDs.

Star id	Template mass (M_{\odot})	Accretion rate ($M_{\odot}\text{yr}^{-1}$)
8	0.18	3.2×10^{-8}
10	0.78	1.6×10^{-8}
14	0.18	5.5×10^{-9}
23	0.37	3.1×10^{-8}
26	0.18	3.4×10^{-9}
30	0.56	1.8×10^{-9}
49	0.78	3.6×10^{-9}
50	0.72	5.7×10^{-9}
77	0.37	2.5×10^{-8}
90	0.56	9.5×10^{-10}
95	0.37	8.1×10^{-9}
127	0.78	9.9×10^{-9}
130	0.78	2.2×10^{-9}
133	1.15	5.3×10^{-9}
143	0.78	1.2×10^{-8}
152	0.37	1.4×10^{-9}
153	0.37	7.5×10^{-10}
158	0.72	2.0×10^{-8}

The behaviour exhibited by star 133 is curious and indicates that a red source of excess is appearing within the system that is uncorrelated with U band excess emission. This may be evidence for the presence of ‘warm’ disc emission similar to that suggested by Fischer et al. (2011) or McClure et al. (2013).

9.5 Mass accretion rates

I have estimated accretion rates for the accreting stars using Equation 1.10. L_{acc} has been estimated by integrating the luminosity excess across all bands. R_{\star} and M_{\star} are estimated from the $g-i$ colour of the best-fitting template, using the semi-empirical models of Bell et al. (2014) adopting interior models by Dotter et al. (2008) and an age of 3 Myr. Fig 9.3 shows the estimated stellar masses and the accretion rates derived. The range of rates measured agrees well with those measured for stars in the ONC by Manara et al. (2012).

9.6 Summary

Accretion rates in YSOs are typically estimated using either measurements of excess luminosity at UV or $H\alpha$ wavelengths beyond that expected for simple photospheric models, or the presence of continuum emission that ‘veils’ spectra lines. I have provided an analysis of the time-variability of these measures and show that the ~ 1 dex spread in predicted L_{acc} for a given $L_{H\alpha}$ can be explained

by decoupling of these parameters due to viewing geometry effects. The clear conclusion from this is that estimates of L_{acc} from either L_U or $L_{H\alpha}$ will be significantly improved by time-averaging several measurements made over a significant fraction of the rotational period of the star.

The relation between U band flux and veiling at wavelengths around 7000\AA also appears to be significantly variable, particularly at low veiling fractions where significant variability is seen in the veiling with apparently constant U band excess. The variability in the relationship between U band flux and $H\alpha$ flux is perhaps not surprising as the sources of the luminosities are different, but the apparent lack of strong correlation between U band flux and veiling is more difficult to explain as the emission is often considered to be from the same ‘hot-spots’ on the surface of the star. The clear conclusion from this analysis is that in most stars the veiling at 7000\AA is not a good measure for the calculation of the accretion rate.

Current theoretical models of accretion onto YSOs do not adequately explain the strength of veiling that is observed in all stars at 7000\AA . I have examined the excess luminosity in 15 accreting YSOs and have shown that in highly veiled stars, the excess luminosity is well explained by accretion luminosity models such as that by Calvet & Gullbring (1998). However, I have identified two stars which exhibit an excess of cool (or red) emission which may be consistent with models of large cool accretion regions and contamination from the inner region of the disc respectively.

Chapter 10

Long-timescale high-amplitude variability

10.1 Introduction

In Chapter 3 I show that YSO variability generally lies within well defined limits on timescales from 1 minute to ≈ 10 years. At a population level, there does not appear to be a significant increase in variability on any timescale that is longer than a few days. This appears to agree with the results of studies of smaller numbers of stars (e.g. Grankin et al. 2007; Costigan et al. 2012). These observations are at odds with theories that suggest that accretion rates might change significantly on timescales much longer than the rotation period of the star. Dramatic increases in accretion rate are predicted due to gravitational instability within the outer disc (Vorobyov & Basu 2005, 2015) and within shielded regions of the inner disc (Armitage et al. 2001). The evolution and migration of giant planets may also cause large scale accretion outbursts (Nayakshin & Lodato 2012). These ‘episodic’ accretion theories and observational support for them are described in detail in Section 1.5.

The dataset that is described in Chapter 3 contains ≈ 700 disc-bearing YSOs in Cep OB3b, that have been photometrically monitored in the i band for ≈ 10 years. With this sample it is reasonable to believe that we might be sensitive to accretion variability events that occur on timescales of up to ~ 10000 years. If accretion or other variability events occur on timescales less than this, and cause changes with amplitudes greater than that seen on days timescales, then they should be detectable in a structure function analysis.

One long-timescale high accretion rate object is already known in Cep OB3b. V733 Cep (also known as Persson’s star) was found to appear in (Palomar Sky Survey) POSS II images taken in 1984, but was absent in POSS I images taken in 1953 (Persson 2004). Reipurth et al. (2007) performed an investigation of this object using $1 - 4\mu\text{m}$ spectroscopy and concluded that it was a FUor that had erupted between the two POSS epochs. Since 1994, the star has shown a very slow decline in luminosity, consistent with other observed FUors (Peneva et al. 2010). In this chapter, I have further studied the evolution of V733 Cep and have shown that it exhibits previously unobserved deep ‘fading’ events. I have also analysed long-timescale structure functions for the

rest of the YSO population in Cep OB3b and have identified three new variable stars which exhibit variability behaviour that is similar to known EXor variables.

10.2 The evolution of V733 Cep

In this study V733 Cep ($\alpha = 22\ 53\ 46.544$, $\delta = +62\ 34\ 58.24$, J 2000.0) corresponds with source 2-336 in the numbering system of Littlefair et al. (2010). A CCD image of V733 Cep taken by Reipurth et al. (2007) shows a nebulous star of $R \approx 17.3$ apparently located at the edge of a cavity in the L1216 cloud. Infrared *Spitzer* photometry indicates the presence of infrared excess corresponding to a Class II source (see Fig. 10.14). Optical spectroscopy shows a well-defined Li 6708 Å line. Blueshifted absorption in the H α and Na D lines indicates the presence of a massive fast wind. An infrared 1-4 μm spectrum of V733 Cep shows strong water vapor features, very similar to those seen in FU Ori. Assuming an intrinsic energy distribution similar to that of FU Ori, V733 Cep has a luminosity of about $135 L_{\odot}$ (Reipurth et al. 2007).

I have constructed the lightcurve of V733 Cep based on all *i* band observations described in Chapter 3. Often FUor stars have been seen to be broadly stable in luminosity in their outburst states, however in these data V733 Cep shows what appears to be a strong fade during the period 2004-2005. It recovers from this fade by ~ 2 magnitudes in *i* over ≈ 3 years before fading back to 2004 levels. This behaviour is seen both in my data and that collected by the *IPHAS* and *SDSS* surveys. The lightcurve and example images of the star are shown in Fig 10.2. A much smaller (but apparently similar in nature) fade is seen in 2009 by Peneva et al. (2010). In my 2013 epoch data the star again appears to be in a faint state. *U, g, r, i, z* photometry of the star was collected by the *SDSS* in 2003 and then by Bell et al. (2013) in 2007 at epochs which corresponds with a change in brightness of ~ 0.5 mag. The colour evolution of the SED appears to be colour-neutral.

The deep fading behaviour that I see in V733 Cep is similar to that seen in the FUor candidate V582 Aur (Semkov et al. 2013). Whether this behaviour is due to time-variable extinction or a reduction in accretion rate back toward pre-outburst levels is unclear. Further photometric and spectroscopic monitoring is required to answer this question. The photometry collected in this study is combined with all available literature data to show the long-term evolution of the lightcurve (Fig. 10.3).

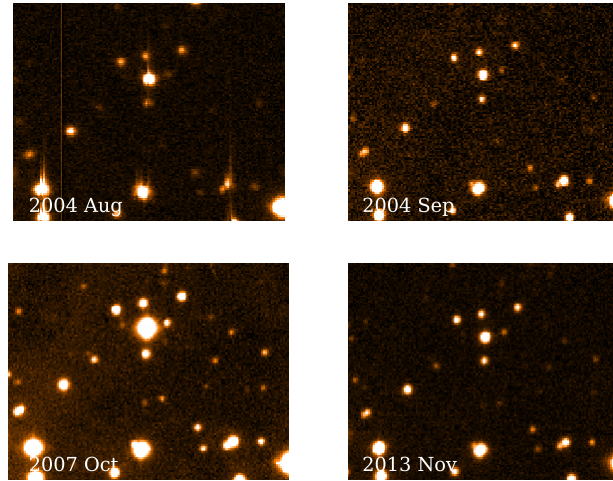


Figure 10.1: INT WFC images of V733 Cep (star 2-336) taken using the i filter. Image scale is $0.333 \text{ \AA pixel}^{-1}$. Upper left and right are taken in August and September 2004. Lower left was taken in 2007 and lower right in 2013. The brightening event detected in the photometry is clearly evident.

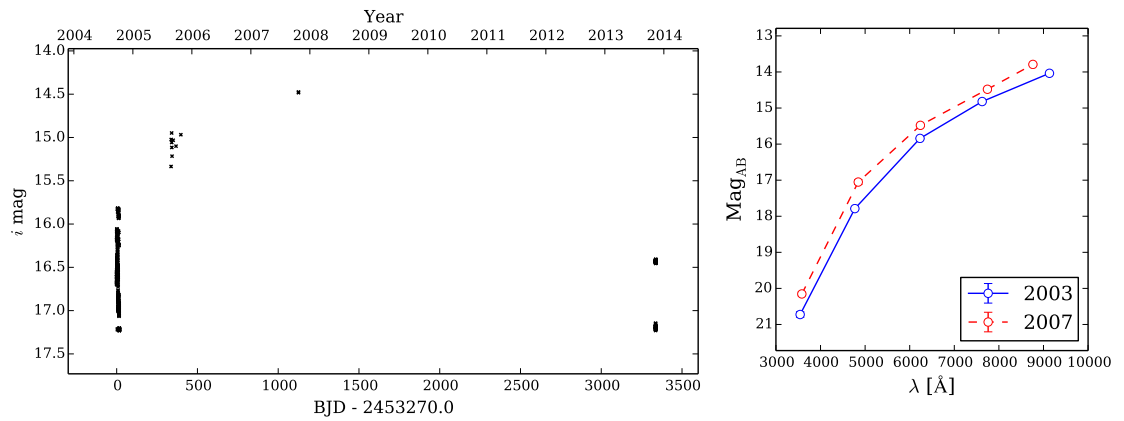


Figure 10.2: The INT lightcurve (left panel) and SED (right panel) for V733 Cep (star 2-336). The SEDs are from the *SDSS* and Bell et al. (2013), taken in 2003 and 2007 respectively.

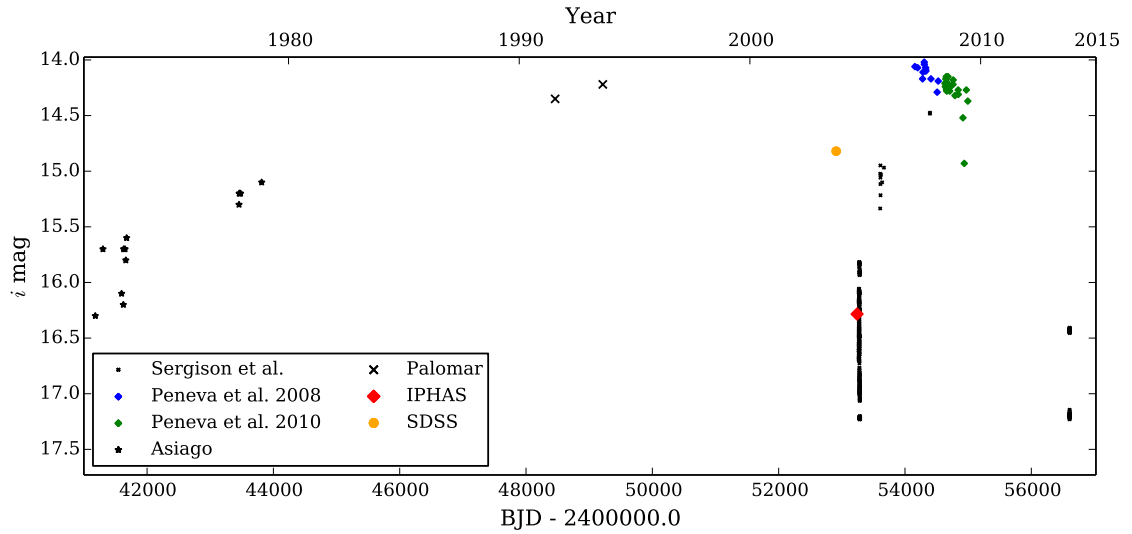


Figure 10.3: Long-term lightcurve for V733 Cep (star 2-336). Data is compiled from Reipurth et al. (2007); Peneva & Semkov (2008); Abazajian et al. (2009); Peneva et al. (2010); Barentsen et al. (2014). Measurements made by Abazajian et al. (2009), Barentsen et al. (2014) and this study use a *SDSS* based filter bandpass which adds an additional systematic error of ≈ 0.3 magnitudes when compared with photometry using the Johnson/Cousins filter systems of the other observers. It is clear though that the large amplitude of variability seen means that this systematic does not have any impact on conclusions drawn from these observations.

10.3 Detection of long-timescale variables

Fig. 10.4 shows the region of a combined structure function for disc-bearing stars where long-period, high variability-amplitude stars would be seen. Five stars fall above the one magnitude rms line in bins where $\tau > 1$ year (note that all stars appear at each time-lag). On inspection of the raw images, one of these appears to be a false-alarm, the photometry appears compromised by very close proximity to the edge of a CCD. Another of these is V733 Cep which I have already discussed. The other three appear to be bone-fide long-timescale variables which warrant further analysis to determine their nature. No stars showed any increase in variability on years-timescales in the discless sample. All four long-timescale variables are located close to the two ‘cores’ of the Cep OB3b cluster. Their locations are shown in Fig 10.5 compared with that of the disc-bearing population. The identification numbers used to refer to the stars are the CCD and star-id numbers from Littlefair et al. (2010).

Images and lightcurves for each of the three new long-timescale variables are shown in Figures 10.6 - 10.11. For each star a sequence of images are shown at different epochs. The lightcurve is also shown for each star. Finally, the optical SED at two epochs (2003 and 2007) are shown based on photometry from the *Sloan Digital Sky Survey* (Abazajian et al. 2009) and Bell et al. (2013).

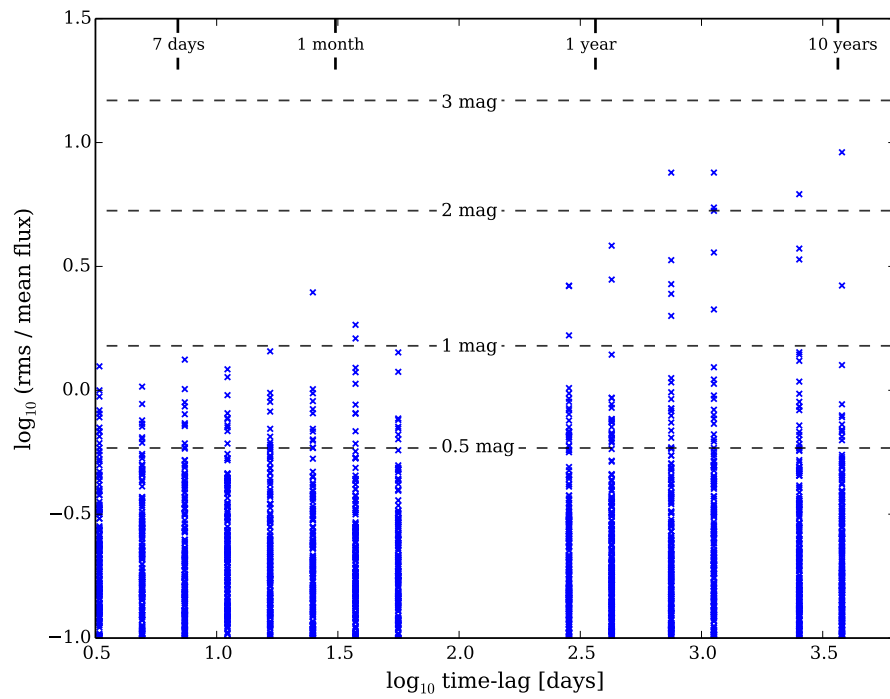


Figure 10.4: Close-up of the region of the combined structure function where stars may show long-timescale variability in excess of that seen on rotation timescales. The blue crosses are individual points in the structure functions of all stars in the disc-bearing sample. On timescales $\gtrsim 1$ year, a few stars exhibit variability that is greater than that seen on timescales of a few days where variability saturates for most disc-bearing stars.

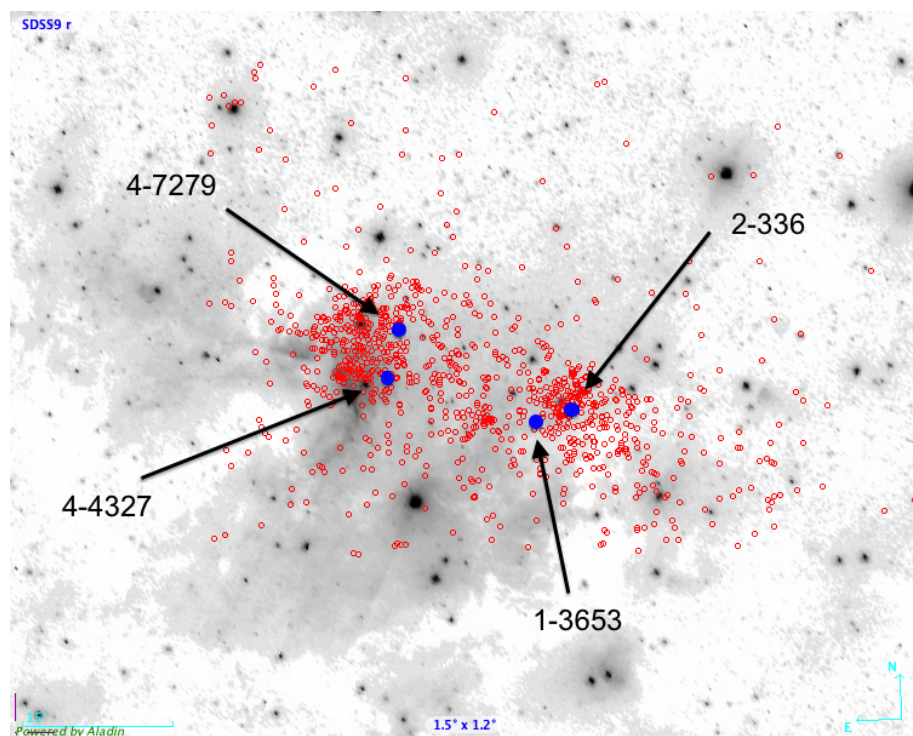


Figure 10.5: *SDSS* r-band image showing the locations of the disc-bearing YSOs identified by Allen et al. (2012) (red circles). The blue points show the location of the four high-amplitude variables identified in Section 10.3. Star 2-336 is V733 Cep. Image created using *Aladin* (Bonnarel et al. 2000).

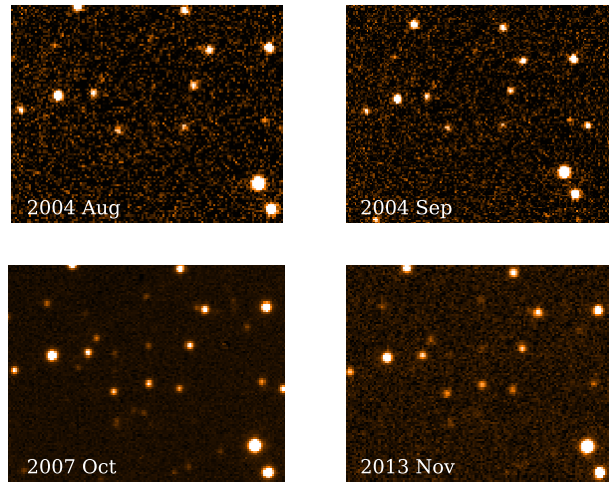


Figure 10.6: INT WFC images of star 1-3653 taken using the i filter. Image scale is $0.333 \text{ \AA pixel}^{-1}$. Upper left and right are taken in August and September 2004. Lower left was taken in 2007 and lower right in 2013. The brightening event detected in the photometry is clearly evident.

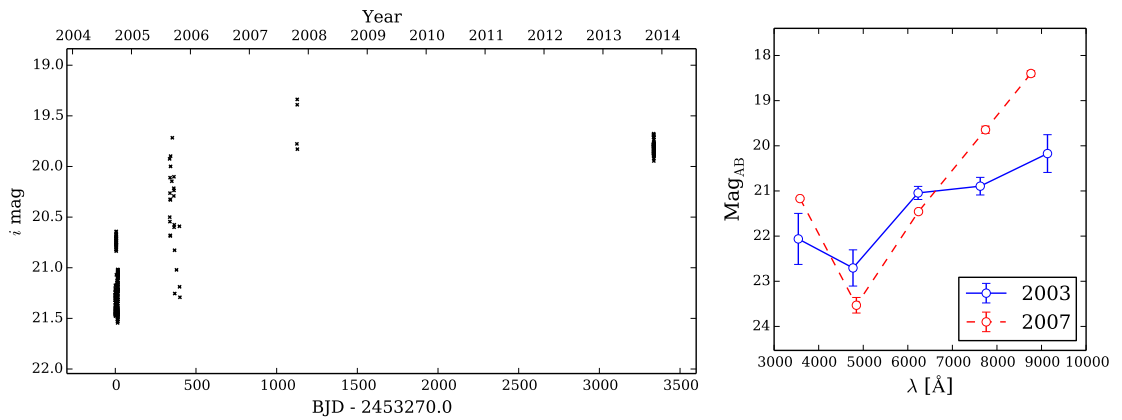


Figure 10.7: Lightcurve (left panel) and u, g, r, i, z , photometric SED (right panel) for star 1-3653. The SEDs are from the *SDSS* and Bell et al. (2013), taken in 2003 and 2007 respectively.

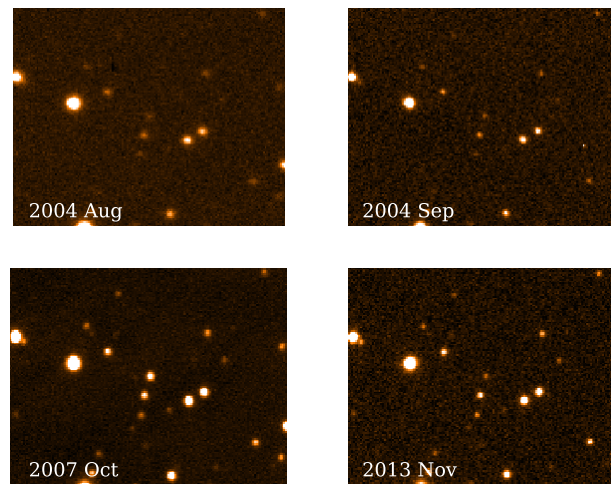


Figure 10.8: Images of star 4-4327. Details as per Fig. 10.6. The bright phase in 2007 is evident compared with the other epochs.

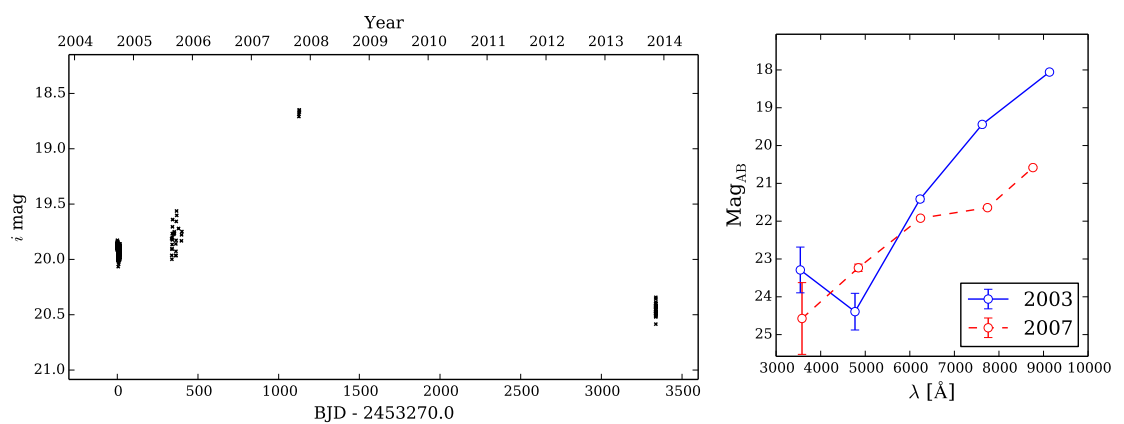


Figure 10.9: Lightcurve (left panel) and SED (right panel) for star 4-4327. Details as per Fig. 10.7.

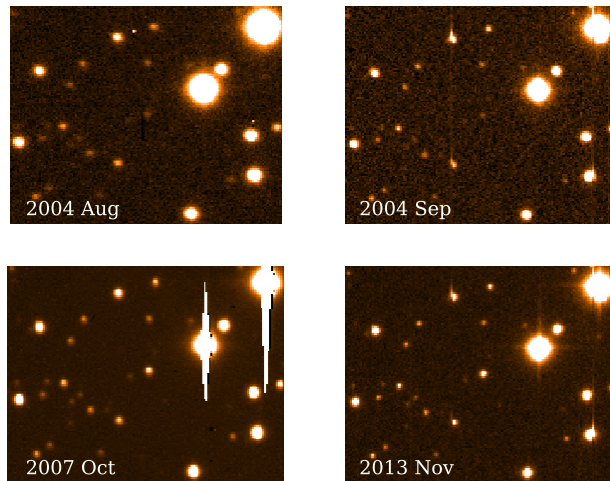


Figure 10.10: Images of star 4-7279. Details as per Fig. 10.6. The 2007 and 2013 epochs clearly show the star in a brighter state.

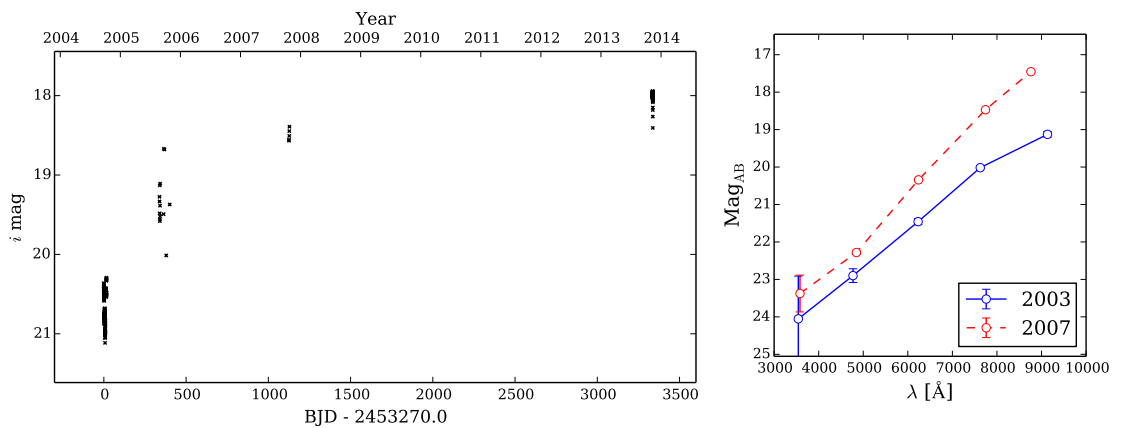


Figure 10.11: Lightcurve (left panel) and SED (right panel) for star 4-7279. Details as per Fig. 10.7.

Star 1-3653

$\alpha = 22\ 54\ 15.955$, $\delta = +62\ 33\ 43.80$, (J 2000.0).

The lightcurve shows a 1.8 magnitude brightening in i , most of which occurred in ≈ 3 years. It then shows a ≈ 0.25 mag fade before the measurements taken in 2013. The SED appears to show the star getting redder as it brightens in i . It apparently shows excess flux in the U band at both epochs, this effect strengthening whilst brightening in i .

Star 4-4327

$\alpha = 22\ 56\ 25.705$, $\delta = +62\ 38\ 28.96$, (J 2000.0).

The lightcurve shows a brightening and then a fade, with a peak-to-peak amplitude of ≈ 1.75 magnitudes. Data collected in 2003 by the *SDSS* shows the star to be two magnitudes brighter in i than at the peak of the lightcurve in 2007. Thus it appears to be coming down from a previously much brighter phase, dropping by ≈ 4 magnitudes over the 10 years between 2003 and 2013. Whilst in its brighter phase, it appears to be redder than when fainter. There is however indication that the flux in U increases at the bright epoch.

Star 4-7279

$\alpha = 22\ 56\ 16.467$, $\delta = +62\ 43\ 01.68$, (J 2000.0).

The lightcurve shows a rapid brightening between 2004 and 2007, followed by a slow rise to 2013. The overall increase is the largest of the four stars at ≈ 2.7 mag. Whilst in its brighter phase, it appears to be redder than when fainter. The large errors at both epochs preclude comment on U flux behaviour.

10.3.1 What is causing the extreme variability in these stars?

The variability in CMD space for the long-timescale variables is shown in Fig. 10.13. Whilst the INT WFC camera photometric system is intended to be similar to the *SDSS* system, slight differences in the filter bandpasses, instrument throughput and detector response mean that magnitudes cannot be compared directly (see Bell et al. 2012, for details). Thus I have derived transforms to convert the 2007 INT WFC photometry into the *SDSS* system. The transforms have been derived in each filter by selecting 182 PMS members (taken from Bell et al. 2013) and comparing their magnitudes in the *SDSS* and INT WFC systems (see Fig. 10.12). The zero-point corrections found are $g_{\text{WFC}} - g_{\text{SDSS}} = -0.253$, $i_{\text{WFC}} - i_{\text{SDSS}} = -0.035$ and $z_{\text{WFC}} - z_{\text{SDSS}} = 0.078$.

Photometry for the four long-timescale variables at the 2003 and 2007 epochs (*SDSS* and transformed Bell et al. 2013, respectively) is plotted along with the *SDSS* photometry for all stars in Fig. 10.13. CMDs in $i, g - i, i, i - z$ and $g, g - i$ are shown. V733 Cep appears several magnitudes brighter than the other long-timescale variable stars and its movement in CMD space is blueward when brightening, similar to that observed in stars with variable extinction. The three new long-timescale variables exhibit behaviour that is broadly similar to each other in the $i, g - i$ and $i, i - z$ CMDs. Brightenings in the i band are accompanied by very large red-ward colour changes. Notably, in the $g, g - i$ CMD, two stars (1-3653 and 4-4327) exhibit variability vectors that are very

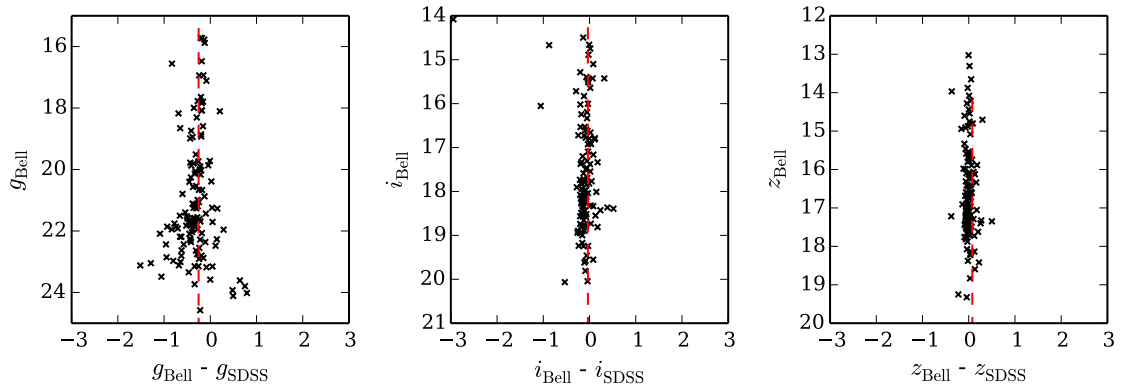


Figure 10.12: Zero point corrections between photometry in the INT WFC system and *SDSS* for 182 PMS stars from Bell et al. (2013).

similar in direction to that seen in accreting stars in Chapter 8, albeit with much larger amplitudes. Fig. 10.14 shows a *Spitzer* colour-colour diagram illustrating how the mid-IR SED compares for each of the long-timescale variables. Again, V733 Cep appears to be different from the new variables which apparently sit together in a region close to the border between Class II and Class I sources. The difference in CMD behaviour and *Spitzer* colours imply that V733 Cep is a distinctly different object from the new long-timescale variables.

The new variables show optical colours that are much fainter or bluer than typical PMS stars when in their *i* band faint phase. Chapter 8 of this thesis shows that accreting stars have colours that are systematically bluer than non-accreting stars. This, in combination with high-levels of circumstellar extinction may explain the colours and magnitudes of these objects when in their faint phase. In their *i* band bright phase, these three stars become significantly redder. Each object displays a 2 - 3 magnitude change in *i* between the faint and bright state.

This combination of behaviour suggests that they are candidate EXor type erupting objects. EXors (Named after the prototype EX Lup) are PMS stars which exhibit optical and near-IR outbursts with durations of 1-2 years that have been explained by significant increases in accretion rate (Hartmann & Kenyon 1996; Zhu et al. 2009). The mid-IR SEDs of known EXors span the Class I/II divide symmetrically, with a peak in the ‘Flat-spectrum’ category (Giannini et al. 2009). This agrees with the *Spitzer* colours of these three EXor candidates.

Some studies of young eruptive stars suggest that the flux changes of these systems are due to the combination of two effects of comparable amplitude. An intrinsic brightening is related to the appearance of new accretion-driven emission, whilst at the same time dust-clearing reduces the extinction along the line of sight (e.g. Reipurth & Aspin 2004; Kun et al. 2011b). Lorenzetti et al. (2012) explain the reddening of the source during outburst by an increase in emission from dust within the inner disc which is heated by the increased accretion luminosity originating from the surface of the star. Two of the three stars (1-3653 and 4-4327) show a corresponding excess of flux in *U* during their *i* band bright phase, further supporting their candidacy as accretion-powered eruptive stars. Fig. 10.15 shows photometry of 7 known EXor candidates and illustrates how their magnitudes and colours change between quiescence and outburst. In common with the three

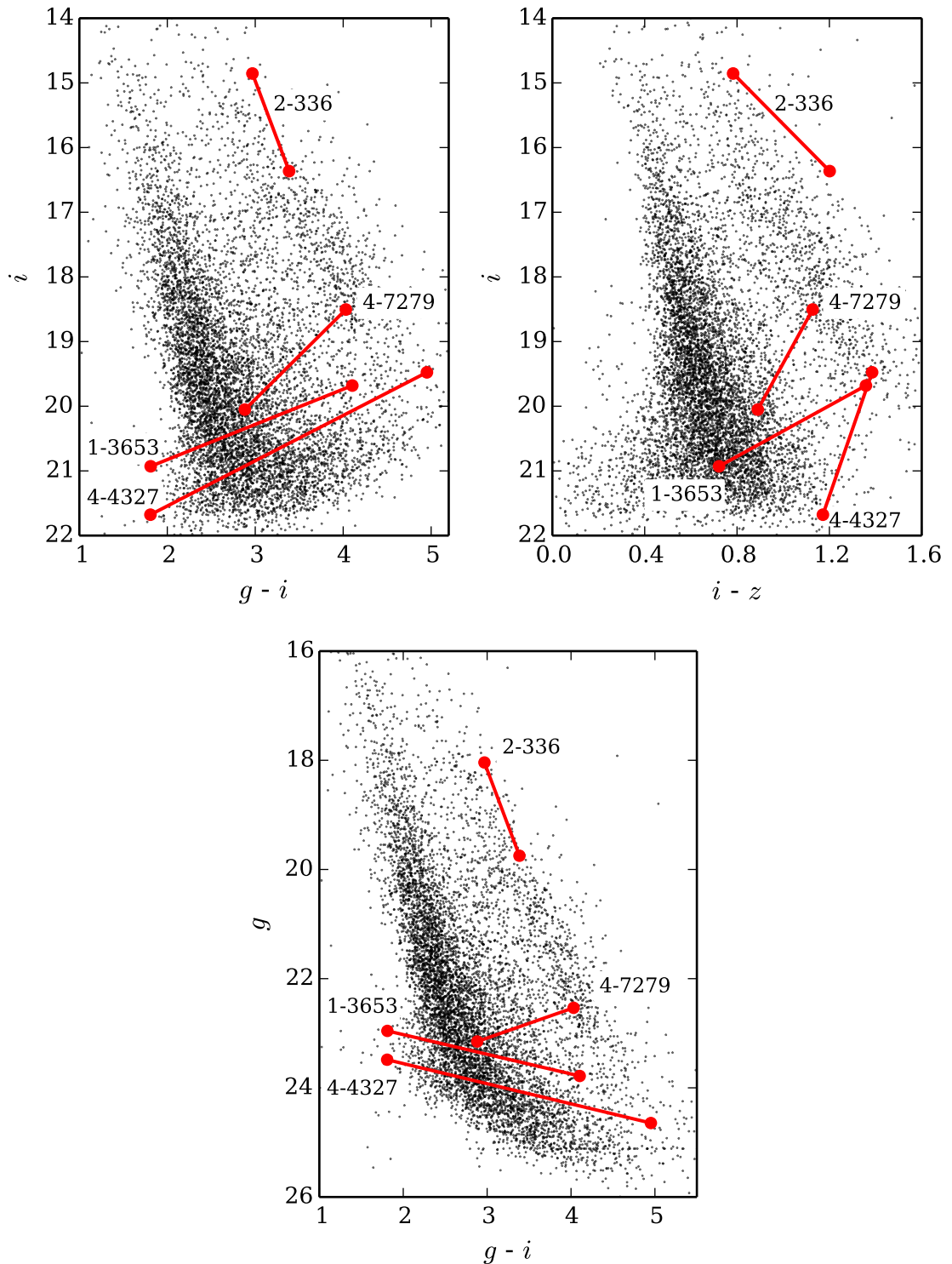


Figure 10.13: *SDSS* $i, g - i$ (left), $i, i - z$ (right) and $g, g - i$ (lower), CMDs of Cep OB3b. Black points are all stars within the INT field of view that appear in the *SDSS*. The four long-timescale variables have two epochs of photometry plotted (red points connected with lines) taken from observations in 2003 and 2007 showing how they move in CMD space. Numbers correspond to ccd number and ID for each star.

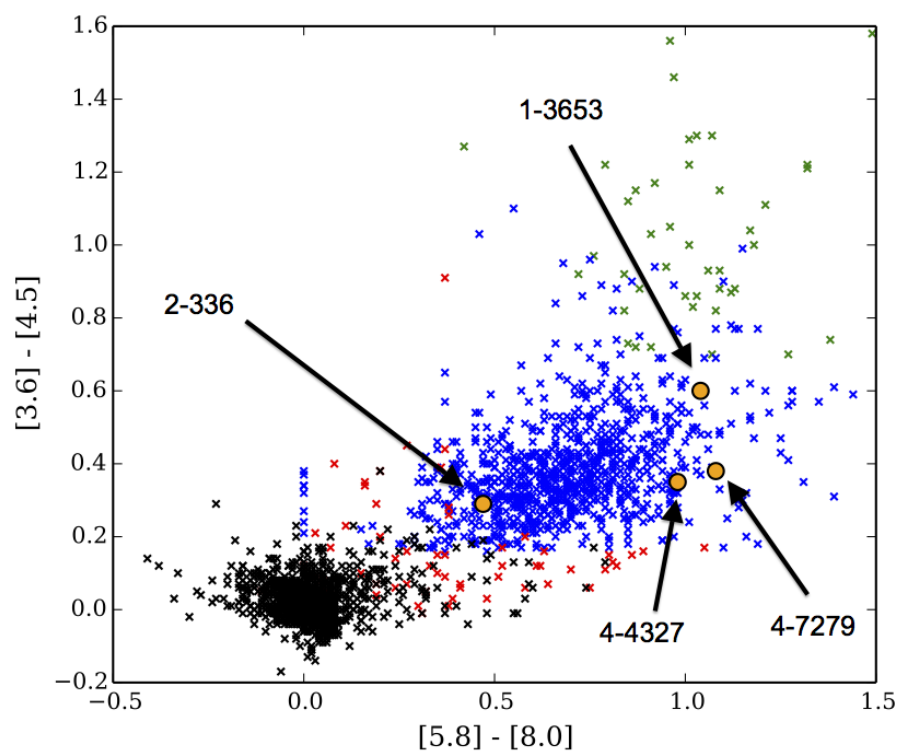


Figure 10.14: A *Spitzer* colour-colour diagram comparing the mid-IR SEDs of the long-timescale variables (yellow dots) with the Cep OB3b population. Star 2-336 is the FUor candidate V733 Cep. Green crosses are Class I YSOs (embedded protostars), blue crosses are Class II YSOs (disc-bearing), black crosses are Class IIIs (discless). The red crosses are ‘transition-disc’ objects. Photometry from Allen et al. (2012).

new Cep variables (Fig. 10.13) some are very faint or blue in quiescence when compared with the PMS. Four of the stars also show a broadly redward colour evolution when brightening. Lorenzetti et al. (2012) suggests that the temperature of heated circumstellar dust will determine the colour evolution.

10.4 Summary

In the disc-bearing sample, four stars exhibit significant variability on timescales longer than rotational timescales. Three stars appear to show brightening events which appear consistent with EXor outbursts with amplitudes between 1.75 and 2.7 magnitudes. A fourth star is a pre-identified FUor candidate (V733 Cep) which in this study appears to show deep fade events which may be indicative of extinction changes or may be an indication of the cessation of the FUor outburst. Further study of these stars is required to provide a more robust characterisation of their behaviour. The four long-timescale variables comprise $\approx 0.5\%$ of the disc-bearing sample. If the long-timescale variability is driven by accretion change related events that all disc-bearing stars undergo, these four events occurring in the sample of ≈ 700 stars over the observing interval of 10 years implies that a given star might exhibit a similar event on average every ≈ 2000 years. If this phenomenon does not randomly occur in all stars but instead repeatedly occurs in a few stars, the quiescent phase for most stars will be longer. This appears to agree well with the outburst intervals predicted by the models of Vorobyov & Basu (2005) and Vorobyov & Basu (2015). Notably though those models were for stars up to an order of magnitude younger than the likely age of Cep OB3b.

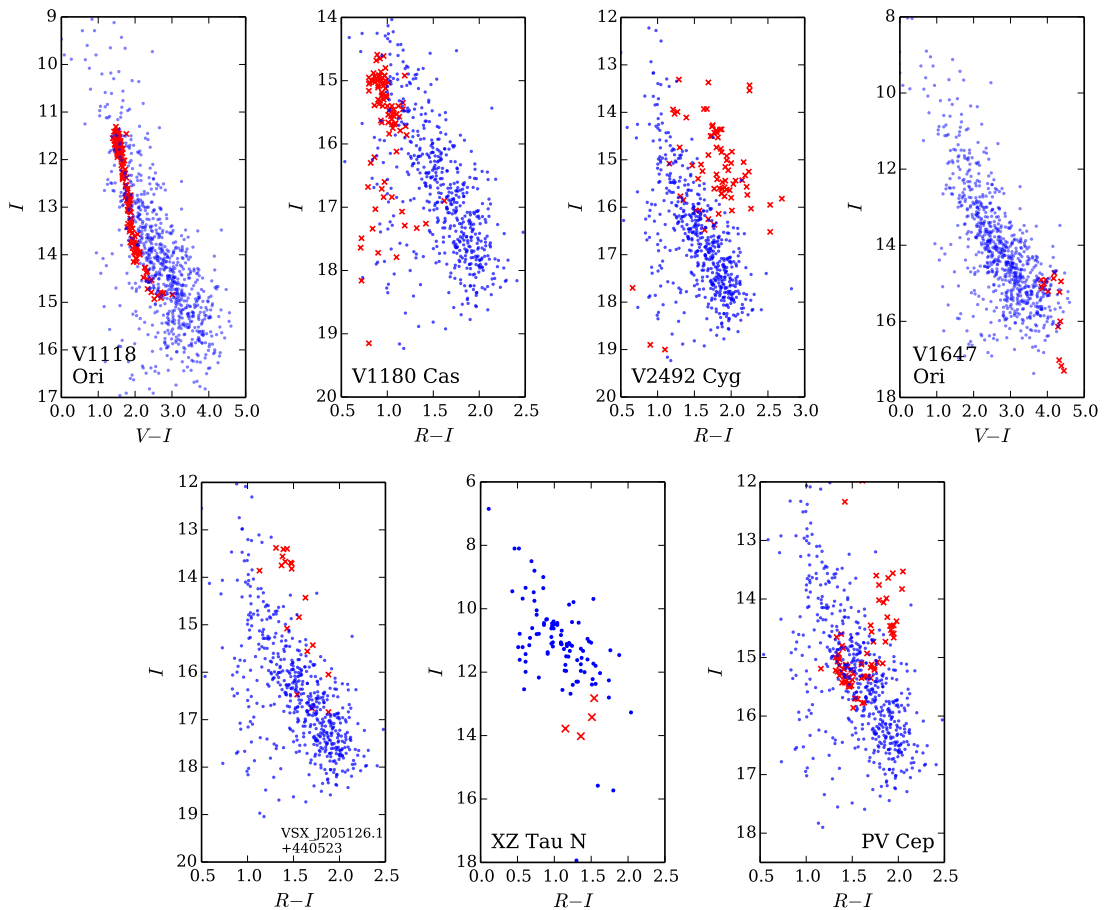


Figure 10.15: Photometry of previously studied EXOrs from the literature. The crosses (red) are photometry of the EXOr candidate showing the brightness and colour evolution from quiescence to outburst. The stars V1118 Ori and V1647 Ori are compared with V , $V - I$ photometry of the ONC by Hillenbrand (1997). XZ Tau N is compared with photometry of Taurus by Kenyon & Hartmann (1995). The other stars do not have available photometry of associated star forming regions so they are compared with photometry of Cep OB3b from Littlefair et al. (2010) which have been corrected to the distance modulus of each EXOr. The (blue) ‘plus’ symbols are PMS members in the associated regions. In Cep OB3b photometry these are those identified by Bell et al. (2013). EXOr Data are from Audard et al. (2010) [V1118 Ori], Kun et al. (2011a) [V1180 Cas], Kóspál et al. (2013) [V2492 Cyg], Kóspál et al. (2011) [VSX J205126.1+440523], Coffey et al. (2004) [XZ Tau N], Kun et al. (2011b) [PV Cep].

Chapter 11

Conclusions and Future work

11.1 Conclusions

The aim of this thesis was defined in the introduction as

Aim: *To explore poorly understood behaviours that are seen in colour-magnitude diagrams of young star forming regions and use this new information to characterise the physical processes that occur in the formation and evolution of young stars.*

If we are to make use of CMDs as useful diagnostics of the underlying physical properties of young stars, it is important to understand the various physical phenomena that we observe and understand their effects on the position of stars in the CMD. It is also crucial that any limitations and potential biases are fully understood. In this section I outline the principal findings of my research and frame them in the context of optical CMDs.

11.1.1 Photometric variability

It has long been known that variability driven by several different physical mechanisms causes some luminosity spread at a given colour in optical CMDs (e.g. Burningham et al. 2005). However, the detailed characterisation of variability that is performed in Chapters 3 and 5 of this thesis place strong constraints on their magnitudes and the timescales on which the contributions are made. I outline my key findings on variability in the following paragraphs, ordered by increasing timescale.

‘Minutes’ timescale variability

On timescales $\lesssim 15$ minutes, almost no variability is detected (at levels greater than $\approx 0.2\%$) in the i band for a sample of ≈ 700 disc-bearing stars in Cep OB3b. Variability on these timescales is predicted by some accretion shock models, resulting from cooling instabilities in magnetically confined post-shock gas. These results suggest that this variability it is either very weak or not present. It may be that the emission from the accretion shock is simply too hot to contribute significantly in the i -band, or it may be that the quasi-periodicity that is predicted in the oscillation of the shock-front is in some way disrupted (e.g. Matsakos et al. 2013). Alternatively, it may be

that all of the gas in the shock region is optically thin and thus any quasi-periodic emission from the shock-heated gas is emitted in the Balmer continuum and lines.

Two discless stars do show variability on minutes timescales, these are individual events that appear to be ‘flare’-like activity. Given the sample and observing parameters detailed in Chapter 3, these two flare events imply a flare rate of 0.0036 ± 0.0014 per hour (roughly 1 every 12 days per star). In the sample of two flare events seen in Cep OB3b, the duration of the brightenings range from ≈ 10 minutes to 1 hour. The amplitudes of these events are 0.6 and 0.25 magnitudes respectively.

‘Hours to days’ timescale variability

On hours to days timescales the optical variability in most stars is well described by a simple power law

$$a \propto f^{-k} \quad (11.1)$$

where a is the amplitude of the variability, f is the frequency (in days^{-1}) and k is the power law exponent. This power law is valid up to a certain timescale (t_{max}) at which point the variability amplitude reaches a plateau and does not increase any further. Whilst as expected, the disc-bearing stars show greater variability amplitudes than the discless stars it is notable that the other key parameters, the variability timescale and power spectrum exponent are remarkably similar. Disc-bearing and discless YSOs, exhibit median values of k of 0.85 ± 0.02 and 0.95 ± 0.03 respectively. t_{max} is found to be 1.50 ± 0.07 days and 1.41 ± 0.10 days for disc-bearing and discless stars respectively. The quoted uncertainties are the standard error on the median. In the structure function analysis this timescale was found to correspond to approximately 1/4 of the rotational timescale of stars with literature periods. This implies that the magnitude of the variability is driven by the physics of the underlying process, but that the timescales are instead driven by geometric effects. The stars with the the highest amplitude variability in all bands are those that exhibit strong accretion related excess emission in U and $H\alpha$. Accreting stars often appear to vary in the CMD along lines that correspond to changes in accretion luminosity.

Burningham et al. (2005) performed an analysis of the impact of variability on positions of stars in the CMD. In Chapter 5, I performed a similar analysis, however I was able to remove the influence of the accretion driven variability. Even stars with no accretion show a spread, and of that, only a quarter of their spread is explained by variability.

Variability on timescales longer than the rotational period.

Four disc-bearing stars (approximately 0.5% of the disc-bearing sample) in Cep OB3b show extreme variability on timescales of years. One known example of the FUor class is present which in this study shows large amplitude variability which may be related to deep extinction events. The position of this FUor in the CMD both in its bright and faint states is not inconsistent with other PMS stars in the cluster. The three other long-timescale variables exhibit broadband optical photometric variability and mid-IR SEDs which are constant with EXor accretion-driven outbursting

stars. These stars are previously unknown EXor candidates. The CMD behaviour of these stars is extreme, and in their i band faint states they fall several magnitudes below the PMS locus. Their CMD behaviour is very different to the short-timescale accretion driven variability seen in Chapter 5, as brightening events are accompanied by a large redward change in colour. Thus the mechanism for these luminosity changes appear entirely different to those seen on shorter timescales. If the long-timescale variability is driven by episodic accretion events that all disc-bearing stars see, then these four events occurring in the sample of ≈ 700 disc-bearing stars over the observing interval of 10 years implies that a given star might exhibit a similar event on average every ≈ 2000 years. For the EXor candidates, these long-timescale changes have a dramatic effect on their CMD position. However their small numbers mean that the overall impact on the CMDs of young associations is small.

The combined effect of variability of the CMD

It is clear from this analysis that variability on timescales of the rotational period and shorter will add a significant spread in luminosity at a given colour. As a result a considerable uncertainty will be present on age estimates of individual stars that are calculated by comparison with PMS models. The magnitude of this uncertainty will depend on the age of the star forming region, becoming more significant in older populations as the isochrones bunch closer together. This problem is particularly acute in accreting stars as their variability is considerably greater than in non-accreting stars. However, it should be noted that the ages of ensembles of stars will be unaffected due to the random temporal nature of this short to medium term variability.

Conversely, long-timescale variability in EXor accreting outbursters will place PMS members in a part of the CMD where they might be interpreted as being much fainter or older than they really are. This is probably due to a combination of excess accretion luminosity and very high (possibly colour neutral) extinction.

11.1.2 Other physical processes that influence CMDs of young stars

The conclusions described so far provide a detailed description of the variability behaviour of young stars and their impact on the CMD. However, it is clear that there are further significant physical mechanisms that affect the positions of YSOs in the CMD. The remaining sections describe the investigation of these mechanisms and summarise what we can learn from them about YSO systems.

Accretion histories

In Chapter 2, I showed that the spread in luminosity seen at a given T_{eff} in the ONC and NGC2264 could not be explained by episodic accretion at high-rates occurring within the protostellar phase of YSO evolution. Models predict that early lithium depletion should accompany any intrinsic radius change that is caused by episodic accretion at high rates (Baraffe & Chabrier 2010). However, our failure to find any lithium depletion in the sample of 168 stars observed in the ONC and NGC 2264 places limits on cold accretion models. Burst accretion rates of $\dot{M} \geq 5 \times 10^{-4} M_{\odot} \text{ yr}^{-1}$ must occur

in less than 0.5 % of $0.3 \leq M_{\star} \leq 1.9 M_{\odot}$ stars. Analysis of accretion luminosity in Chapter 8 shows that five stars in the ONC which were previously identified as depleted in lithium (by Palla et al. 2007) were almost certainly simply subject to extremely high accretion veiling that is hard to correct. Thus it appears that CMDs are not a useful diagnostic for study of the accretion histories of YSOs.

Inner disc dust and extinction correction

Extinction by dust within the inner regions of YSO discs was investigated in Chapter 6 and was shown to differ from that seen in the ISM. Typically the wavelength dependence of the extinction is seen to be of order $R_V \approx 5 - 8$, compared with the value of $R_V \approx 3.1$ that is typically adopted in the literature for sight-lines within the galactic plane (e.g. Cardelli et al. 1989; Fitzpatrick 1999). The interpretation of this observation is that grain growth has occurred. The location of this material within the ‘snow line’ implies that refractory grains have actually coalesced rather than simply gaining an ice mantle which is thought to be the cause of grain growth in the ISM (Draine 2003). This is evidence for the beginning of planetary formation.

The effect of the high value of R_V on the CMD is to add additional uncertainty to photometric measurements that have been corrected for the effects of extinction. For example, for a star where a contribution of $A_V = 0.5$ comes from circumstellar dust, if the R_V value of 3.1 was used then the V magnitude will be under-estimated by ≈ 0.1 mag. This would lead to an under-estimate of stellar luminosity of $\approx 10\%$. As extinction contributions from the inner disc are likely to be significantly different depending on the structure and inclination of the disc, this effect will add a spread in magnitude to the photometry. As good statistics on the number and distribution of these parameters does not exist, it is impossible to quantify the effect on an ensemble of stars in the CMD, however it is likely that this effect is smaller than luminosity spreads caused by other mechanisms described in this thesis. In Chapter 2, I discuss some stars which appear to be viewed at high inclinations and thus are significantly more faint than the PMS locus due to occultation of the star by their disc. There is little evidence from the main variability analysis that this is a common scenario.

Accretion luminosity

In Chapter 8, I showed that the dominant factor in the luminosity spread seen in CMDs of young associations appears to be contamination by accretion luminosity. Stars which exhibit significant excess flux in optical accretion indicators such as the U band or $H\alpha$ are significantly displaced in CMD space. The direction of the displacement vector derived by analysis of the spectroscopic sample is a significant blueward shift in colour accompanied by a modest brightening in the $g, g-i$ CMD. The gradient of the accretion luminosity vector is typically less than the PMS locus, resulting in a luminosity spread (or more accurately a colour spread) as stars are displaced blueward below the PMS locus.

This effect is not seen in disc-bearing stars that do not exhibit excess in U or $H\alpha$. Curiously, the influence of accretion on CMD position was investigated by Littlefair et al. (2011) and

no evidence found for the influence of accretion luminosity. Unfortunately, this study only considered stars with measured rotation periods, which significantly biased the sample against accreting objects. Also the study focussed on only the brightest ($I \gtrsim 14$) stars in the ONC and NGC 2264. However as models calculated by Da Rio et al. (2010b) show, the colours of the brighter (and hence hotter) stars will be far less affected by accretion luminosity than cooler PMS members.

Whilst we can see that accretion luminosity systematically changes photometric colours in a broadly consistent manner in the CMD, it is impossible to predict the intrinsic colours of accreting stars with photometric data alone. In Chapter 9, I extracted the underlying accretion luminosity spectrum for 15 accreting stars and showed that the colour temperature of the emission excess is not consistent across the sample. Thus to quantify the effect of accretion luminosity on CMD positions, large numbers of moderate resolution spectra would be required.

It is pertinent to consider whether accretion luminosity may systematically bias estimates of PMS ages that are calculated through comparison of ensembles of stars with model isochrones (e.g. Mayne et al. 2007; Guarcello et al. 2010a; Bell et al. 2013). The evidence from this study suggests that indeed a bias toward older ages may exist in the youngest clusters where larger populations of accreting stars still exist. A simple mitigation for this would be to exclude disc-bearing stars from the analysis, or alternatively to use indicators such as U or $H\alpha$ excess to exclude accreting objects. This is only likely to be a significant issue for lower mass objects in the very youngest clusters, as beyond $\gtrsim 5$ Myr the stellar populations are dominated by discless stars and the discs that do remain exhibit dramatically reduced accretion rates.

To fully assess the effect of accretion on stellar colours, luminosities and structure, precise metrics of accretion rate are required. In Chapter 9, I showed that both U and $H\alpha$ flux vary independently by ≈ 1 dex on timescales shorter than the rotation period of the star. This implies that single epoch measurements of these parameters will add an uncertainty of ≈ 1 dex on the derived accretion rate. The decoupled behaviour of these two accretion rate diagnostics is most probably a viewing geometry effect. The key message from this is that accretion rates derived from either U or $H\alpha$ excess should be calculated from a mean of several photometric measurements, separated by significant fractions of the rotation period of the star.

The relation between U band flux and veiling at wavelengths around 7000\AA also appears to be significantly variable, particularly at low veiling fractions where variability is seen in the veiling with apparently constant U band excess. The clear conclusion from this analysis is that in most stars, the veiling at 7000\AA is not a good measure for the calculation of the accretion rate. Through examination of the excess luminosity in 15 accreting YSOs, I have shown that in highly veiled stars, the excess luminosity is well explained by accretion luminosity models such as those of Calvet & Gullbring (1998). However two stars within my sample exhibit an excess of cool (or red) emission which may be consistent with models of large cool accretion regions or contamination from the inner region of the disc.

Other mechanisms

Despite providing a detailed characterisation of phenomena that influence the positions of YSOs in the CMD, there exists some residual luminosity spread at a given T_{eff} that cannot be explained

by variability on any timescale, extinction uncertainties or accretion luminosity. This is best illustrated by the CMD of the discless spectroscopic template stars shown in Figure 7.3. These stars have had any variability averaged by the seven nights of observations, they exhibit no disc or optical accretion indicators and their (intrinsically small and ISM driven) extinctions have been corrected using spectroscopically derived measurements. Despite this, they appear to show an intrinsic luminosity discrepancy of up to ± 0.5 magnitudes in g about an empirically defined locus.

Jeffries (2007) measured a spread in radii for stars in the ONC. However in that study no correction is made for the effects of accretion, whereas in my data I have managed to remove the potentially significant effects of accretion luminosity. The fact that a luminosity dispersion remains is strong evidence toward their being a further mechanism that is adding luminosity dispersion within the cluster. Star-spots are such a candidate mechanism. Star-spots that are cooler than the surrounding photosphere, are thought to be ubiquitous in pre-MS stars (Jackson & Jeffries 2012), and the lower luminosity of the cooler regions may potentially reduce the luminosity of the star. In main-sequence stars, the need to radiate the energy from the core causes the presence of spots to drive an increase in radius, in brown dwarfs it instead reduces their luminosity and slows their contraction (Chabrier et al. 2007). Fully convective pre-MS stars will most likely behave in a similar way to brown dwarfs, with varying spot fractions driving a scatter in luminosity. In addition, the presence of high fractions of spot coverage is predicted to slow the contraction and progress of the star down Hayashi tracks (Jackson & Jeffries 2014). This effect, seen across an entire coeval population may lead to a systematic under-estimate of the age of the cluster.

11.2 Further work

11.2.1 Exploring ‘old’ stars in young clusters

Populations of apparently ‘older’ stars are found amongst younger populations of PMS stars in some very young regions such as NGC 6611 and NGC 6530 (Prisinzano et al. 2005; Guarcello et al. 2010a). The evidence for their older age is that they lie blueward of the main PMS population and close to the ZAMS. These stars may conceivably be explained as a population of heavily accreting stars that have had their colours modified by accretion luminosity in a similar manner to that seen in the ONC. A comprehensive spectroscopic survey or a deep photometric U band survey is required to determine whether this is the case.

11.2.2 Searching for ‘minutes’ timescale accretion shock variability

The results of the variability analysis in Chapter 3 were very clear that minute timescale variability was not present to sub-percent levels. Given the predictions made by theory, this was a challenging result. This result agrees with previous smaller scale studies by Drake et al. (2009) and Günther et al. (2010) who looked at X-ray and optical variability respectively. One explanation is that the photosphere at the base of the accretion streams (where the accretion energy is thermalised) has a cooling timescale that is long compared to the timescale of the accretion instabilities. As a result, the variability in the observed optically thick emission would most likely be of little use

in probing the dynamics of the much more transient accretion flows themselves. However, the thermal timescale of the optically thin accretion flows is thought to be of order minutes. So if the optically thin flows either reprocess the accretion luminosity, or as the above models suggest are responsible for it, it is likely that emission from these regions will be uniquely sensitive to any high frequency changes in the accretion process. Considering the temperatures involved and the observational limits, the obvious solution to this problem is to look for high frequency variability in the U band which is sensitive to changes in the optically thin Balmer continuum emission, shortward of 4000\AA . A robust and comprehensive search for minute-timescale variability in the Balmer continuum emission has been performed. Time-series U -band observations of stars in the ONC with a cadence of 1 minute were made in 2014 using the *Canada France Hawaii* Telescope and its *MegaCam* wide field camera. These data are yet to be analysed but will tell me whether variability is present on timescales between 1 minute and 1 hour in Balmer continuum emission. Identification of U band variability on minute timescales would allow me to measure parameters that constrain accretion models and to learn about the dynamics, homogeneity and shock physics of the infalling material. Conversely, a null result might be even more important as it would imply much smoother accretion processes than currently predicted and challenge theorists to explain how accretion occurs without the expected strong variability.

11.2.3 Long-timescale episodic accretion

On timescales of years and longer there is a significant contradiction between theory and observations of YSO variability. The dramatic increases in accretion rate that models of disc instability and planet formation predict should be seen as episodic outbursts in the lightcurves of YSOs. The current statistics on this kind of behaviour are sparse and subject to many biases, rendering them poor for characterising the frequency and nature of such outbursts.

The recent launch of GAIA (Eyer et al. 2013), with observations of the entire sky every ≈ 30 days for five years offers an outstanding opportunity to study a large sample of YSOs. Furthermore, as an optical survey it is biased towards older systems in their planet-forming epoch (ages $\approx 5\text{Myr}$) when compared to IR surveys. Although GAIA will tell us that an object has changed in brightness, it will not tell us why. In addition to accretion-rate changes, variable obscuration also produces variability in YSOs. It is crucial, therefore, that the GAIA data is complemented by ground-based follow-up observations that will measure changes in accretion rate that occur during these events. I have been allocated time on the Liverpool Telescope to perform such observations. These data will allow me to determine the duty cycle and accretion rate amplitudes of a large sample of YSO accretion burst events. Over $\sim 10^4$ known YSOs are within the range of GAIA, but an order of magnitude more will be detectable in outburst. Given the fraction of outbursting stars seen in Chapter 10, a significant number (perhaps 5 - 50 per year) of outbursting stars should be detected. Thus, a unique window exists to undertake a statistical study of accretion variability events that occur with duty-cycles of $\sim 10^4$ and perhaps up to $\sim 10^5$ years, whilst the planets are forming. Importantly, this information would allow me to determine whether most of a star's mass is accreted smoothly over long timescales or instead in shorter episodic bursts between quiescent periods. This information will feed back into theory and allow us to improve our understanding

of the structure of circumstellar discs, with important implications for the planet formation and migration occurring within.

11.2.4 The effect of spots on PMS evolution

To test whether star-spots significantly change the luminosity of pre-MS stars, I have collected medium resolution (VLT/GIRAFFE) spectra for a sample of K-type discless YSOs in two clusters of different ages and dispersions in luminosity. I intend to measure the spot coverages for these stars and compare them with position in the CMD. Magnetically active K-stars are sufficiently hot that their photospheres should be free of TiO absorption, however their cool-spots mimic M-star atmospheres with their distinctive TiO bands. By modelling their total spectrum as the sum of template K-type and M-type stars, the spot area and temperature is recovered (Neff et al. 1995). I observed discless stars as they are still contracting toward the main sequence but have very little spectral contamination from circumstellar discs and accretion, though the technique is robust against contaminating accretion flux (Webb et al. 2002).

A significant correlation between luminosity (at a given colour) and spot coverage would offer strong support to the idea that star-spots are responsible for some luminosity spread and could potentially affect pre-MS ages. If instead, large areas of spot coverage are ubiquitous across all stars in the pre-MS, it might mean that clusters appear considerably younger (as a fraction of their nominal ages) than their true age. Finally, if we find a systematic difference in spot coverage between the cluster of different ages, it would imply that the correction to the ages is itself age dependent.

Bibliography

- Abazajian, K. N., Adelman-McCarthy, J. K., Agüeros, M. A., et al. 2009, *ApJS*, 182, 543
- Ábrahám, P., Juhász, A., Dullemond, C. P., et al. 2009, *Nature*, 459, 224
- Alencar, S. H. P. & Basri, G. 2000, *AJ*, 119, 1881
- Alencar, S. H. P., Teixeira, P. S., Guimarães, M. M., et al. 2010, *A&A*, 519, A88
- Allard, F., Homeier, D., & Freytag, B. 2011, in *Astronomical Society of the Pacific Conference Series*, Vol. 448, 16th Cambridge Workshop on Cool Stars, Stellar Systems, and the Sun, ed. C. Johns-Krull, M. K. Browning, & A. A. West, 91
- Allen, T. S., Gutermuth, R. A., Kryukova, E., et al. 2012, *ApJ*, 750, 125
- Alves, J. & Bouy, H. 2012, *A&A*, 547, A97
- Anders, E. & Grevesse, N. 1989, *Geochim. Cosmochim. Acta*, 53, 197
- Andre, P., Ward-Thompson, D., & Barsony, M. 1993, *ApJ*, 406, 122
- Armitage, P. J., Livio, M., & Pringle, J. E. 2001, *MNRAS*, 324, 705
- Audard, M., Stringfellow, G. S., Güdel, M., et al. 2010, *A&A*, 511, A63
- Babcock, A. & Weaver, W. B. 2000, in *Bulletin of the American Astronomical Society*, Vol. 32, American Astronomical Society Meeting Abstracts, 1414
- Ballesteros-Paredes, J. & Hartmann, L. 2007, *RMexAA*, 43, 123
- Bally, J., O'Dell, C. R., & McCaughrean, M. J. 2000, *AJ*, 119, 2919
- Baraffe, I. & Chabrier, G. 2010, *A&A*, 521, A44
- Baraffe, I., Chabrier, G., Allard, F., & Hauschildt, P. H. 1998, *A&A*, 337, 403
- Baraffe, I., Chabrier, G., Allard, F., & Hauschildt, P. H. 2002, *A&A*, 382, 563
- Baraffe, I., Chabrier, G., & Gallardo, J. 2009, *ApJL*, 702, L27
- Baraffe, I., Vorobyov, E., & Chabrier, G. 2012, *ApJ*, 756, 118
- Barentsen, G., Farnhill, H. J., Drew, J. E., et al. 2014, *MNRAS*, 444, 3230

- Barentsen, G., Vink, J. S., Drew, J. E., et al. 2011, *MNRAS*, 415, 103
- Barentsen, G., Vink, J. S., Drew, J. E., & Sale, S. E. 2013, *MNRAS*, 429, 1981
- Bary, J. S. & Petersen, M. S. 2014, *ApJ*, 792, 64
- Bate, M. R. 2011, *MNRAS*, 417, 2036
- Baxter, E. J., Covey, K. R., Muench, A. A., et al. 2009, *AJ*, 138, 963
- Beckwith, S. V. W., Henning, T., & Nakagawa, Y. 2000, *Protostars and Planets IV*, 533
- Bell, C. P. M. 2012, PhD thesis, University of Exeter
- Bell, C. P. M., Naylor, T., Mayne, N. J., Jeffries, R. D., & Littlefair, S. P. 2012, *MNRAS*, 424, 3178
- Bell, C. P. M., Naylor, T., Mayne, N. J., Jeffries, R. D., & Littlefair, S. P. 2013, *MNRAS*, 434, 806
- Bell, C. P. M., Rees, J. M., Naylor, T., et al. 2014, *MNRAS*, 445, 3496
- Bergin, E. A., Hartmann, L. W., Raymond, J. C., & Ballesteros-Paredes, J. 2004, *ApJ*, 612, 921
- Bertout, C. 2000, *A&A*, 363, 984
- Bertout, C., Basri, G., & Bouvier, J. 1988, *ApJ*, 330, 350
- Bessell, M. S. 1990, *PASP*, 102, 1181
- Bessell, M. S., Castelli, F., & Plez, B. 1998, *A&A*, 333, 231
- Biazzo, K., Melo, C. H. F., Pasquini, L., et al. 2009, *A&A*, 508, 1301
- Bildsten, L., Brown, E. F., Matzner, C. D., & Ushomirsky, G. 1997, *ApJ*, 482, 442
- Blitz, L., Fukui, Y., Kawamura, A., et al. 2007, *Protostars and Planets V*, 81
- Bonnarel, F., Fernique, P., Bienaymé, O., et al. 2000, *A&AS*, 143, 33
- Boss, A. P., Morfill, G. E., & Tscharnuter, W. M. 1989, *Models of the formation and evolution of the solar nebula*, ed. S. K. Atreya, J. B. Pollack, & M. S. Matthews, 35–77
- Bouvier, J., Alencar, S. H. P., Boutelier, T., et al. 2007, *A&A*, 463, 1017
- Bouvier, J., Bertout, C., Benz, W., & Mayor, M. 1986a, *A&A*, 165, 110
- Bouvier, J., Bertout, C., & Bouchet, P. 1986b, *A&A*, 158, 149
- Bouvier, J., Cabrit, S., Fernandez, M., Martin, E. L., & Matthews, J. M. 1993, *A&A*, 272, 176
- Bouvier, J., Chelli, A., Allain, S., et al. 1999, *A&A*, 349, 619
- Bouvier, J., Covino, E., Kovo, O., et al. 1995, *A&A*, 299, 89

- Bouvier, J., Forestini, M., & Allain, S. 1997, *A&A*, 326, 1023
- Bouvier, J., Grankin, K. N., Alencar, S. H. P., et al. 2003, *A&A*, 409, 169
- Bouvier, J., Matt, S. P., Mohanty, S., et al. 2014, *Protostars and Planets VI*, 433
- Buckle, J. V., Drabek-Maunder, E., Greaves, J., et al. 2015, *MNRAS*, 449, 2472
- Burningham, B., Naylor, T., Jeffries, R. D., & Devey, C. R. 2003, *MNRAS*, 346, 1143
- Burningham, B., Naylor, T., Littlefair, S. P., & Jeffries, R. D. 2005, *MNRAS*, 363, 1389
- Burrows, C. J., Stapelfeldt, K. R., Watson, A. M., et al. 1996, *ApJ*, 473, 437
- Calvet, N. & Gullbring, E. 1998, *ApJ*, 509, 802
- Cardelli, J. A., Clayton, G. C., & Mathis, J. S. 1989, *ApJ*, 345, 245
- Carlsson, M., Rutten, R. J., Bruls, J. H. M. J., & Shchukina, N. G. 1994, *A&A*, 288, 860
- Castelli, F. & Kurucz, R. L. 2004, *ArXiv Astrophysics e-prints*
- Chabrier, G., Gallardo, J., & Baraffe, I. 2007, *A&A*, 472, L17
- Chambers, J. 2010, in *Exoplanets*, ed. S. Seager, 297–317
- Chelli, A., Carrasco, L., Mújica, R., Recillas, E., & Bouvier, J. 1999, *A&A*, 345, L9
- Choi, P. I. & Herbst, W. 1996, *AJ*, 111, 283
- Cieza, L. A., Kessler-Silacci, J. E., Jaffe, D. T., Harvey, P. M., & Evans, II, N. J. 2005, *ApJ*, 635, 422
- Clarke, C. J. 2007, *MNRAS*, 376, 1350
- Cody, A. M., Stauffer, J., Baglin, A., et al. 2014, *AJ*, 147, 82
- Coffey, D., Downes, T. P., & Ray, T. P. 2004, *A&A*, 419, 593
- Contreras Peña, C., Lucas, P. W., Froebrich, D., et al. 2014, *MNRAS*, 439, 1829
- Correnti, M., Paresce, F., Aversa, R., et al. 2012, *Ap&SS*, 340, 263
- Costigan, G., Scholz, A., Stelzer, B., et al. 2012, *MNRAS*, 427, 1344
- Cruz, K. L. & Reid, I. N. 2002, *AJ*, 123, 2828
- Cutri, R. M., Skrutskie, M. F., van Dyk, S., et al. 2003, *VizieR Online Data Catalog*, 2246, 0
- Da Rio, N., Gouliermis, D. A., & Gennaro, M. 2010a, *ApJ*, 723, 166
- Da Rio, N., Robberto, M., Soderblom, D. R., et al. 2009, *ApJS*, 183, 261
- Da Rio, N., Robberto, M., Soderblom, D. R., et al. 2010b, *ApJ*, 722, 1092

- Dahm, S. E. 2008, *AJ*, 136, 521
- Dahm, S. E. & Simon, T. 2005, *AJ*, 129, 829
- Damiani, F., Prisinzano, L., Micela, G., & Sciortino, S. 2006, *A&A*, 459, 477
- D'Angelo, C. R. & Spruit, H. C. 2012, *MNRAS*, 420, 416
- D'Antona, F. & Mazzitelli, I. 1994, *ApJS*, 90, 467
- Davies, C. L., Gregory, S. G., & Greaves, J. S. 2014, *MNRAS*, 444, 1157
- de Jong, T., Boland, W., & Dalgarno, A. 1980, *A&A*, 91, 68
- De Marchi, G., Panagia, N., Guarcello, M. G., & Bonito, R. 2013, *MNRAS*, 435, 3058
- de Vries, W. H., Becker, R. H., & White, R. L. 2003, *AJ*, 126, 1217
- Dobbs, C. L. & Bonnell, I. A. 2007, *MNRAS*, 376, 1747
- Dobbs, C. L., Bonnell, I. A., & Pringle, J. E. 2006, *MNRAS*, 371, 1663
- Dodin, A. V. & Lamzin, S. A. 2012a, *Astronomy Letters*, 38, 649
- Dodin, A. V. & Lamzin, S. A. 2012b, *ArXiv e-prints*
- Donati, J.-F., Bouvier, J., Walter, F. M., et al. 2011, *MNRAS*, 412, 2454
- Donati, J.-F., Gregory, S. G., Alencar, S. H. P., et al. 2012, *MNRAS*, 425, 2948
- Donati, J.-F., Gregory, S. G., Alencar, S. H. P., et al. 2013, *MNRAS*, 436, 881
- Donati, J.-F., Jardine, M. M., Gregory, S. G., et al. 2007, *MNRAS*, 380, 1297
- Dotter, A., Chaboyer, B., Jevremović, D., et al. 2008, *ApJS*, 178, 89
- Draine, B. T. 2003, *ARA&A*, 41, 241
- Drake, J. J., Ratzlaff, P. W., Laming, J. M., & Raymond, J. 2009, *ApJ*, 703, 1224
- Drake, J. J., Testa, P., & Hartmann, L. 2005, *ApJL*, 627, L149
- Drew, J. E., Greimel, R., Irwin, M. J., et al. 2005, *MNRAS*, 362, 753
- Ducati, J. R. 2002, *VizieR Online Data Catalog*, 2237, 0
- Dutrey, A., Guilloteau, S., Duvert, G., et al. 1996, *A&A*, 309, 493
- Edwards, S., Fischer, W., Hillenbrand, L., & Kwan, J. 2006, *ApJ*, 646, 319
- Edwards, S., Hartigan, P., Ghandour, L., & Andrulis, C. 1994, *AJ*, 108, 1056
- Elmegreen, B. G. 2000, *ApJ*, 530, 277

- Elmegreen, B. G. 2007, *ApJ*, 668, 1064
- Enoch, M. L., Evans, II, N. J., Sargent, A. I., & Glenn, J. 2009, *ApJ*, 692, 973
- Eyer, L., Holl, B., Pourbaix, D., et al. 2013, *Central European Astrophysical Bulletin*, 37, 115
- Feigelson, E. D. & Montmerle, T. 1999, *ARA&A*, 37, 363
- Fendt, C. 2007, in *IAU Symposium*, Vol. 243, *IAU Symposium*, ed. J. Bouvier & I. Appenzeller, 265–276
- Fernandez, M. & Eiroa, C. 1996, *A&A*, 310, 143
- Fűrész, G., Hartmann, L. W., Szentgyorgyi, A. H., et al. 2006, *ApJ*, 648, 1090
- Fischer, W., Edwards, S., Hillenbrand, L., & Kwan, J. 2011, *ApJ*, 730, 73
- Fitzpatrick, E. L. 1999, *PASP*, 111, 63
- Flaccomio, E., Damiani, F., Micela, G., et al. 2002, in *Astronomical Society of the Pacific Conference Series*, Vol. 277, *Stellar Coronae in the Chandra and XMM-NEWTON Era*, ed. F. Favata & J. J. Drake, 155
- Flaccomio, E., Micela, G., Sciortino, S., et al. 1999, *A&A*, 345, 521
- Folha, D. F. M. & Emerson, J. P. 1999, *A&A*, 352, 517
- Gahm, G. F., Loden, K., Gullbring, E., & Hartstein, D. 1995, *A&A*, 301, 89
- Gahm, G. F., Walter, F. M., Stempels, H. C., Petrov, P. P., & Herczeg, G. J. 2008, *A&A*, 482, L35
- Gammie, C. F. 2001, *ApJ*, 553, 174
- Getman, K. V., Feigelson, E. D., Grosso, N., et al. 2005, *ApJS*, 160, 353
- Giannini, T., Lorenzetti, D., Elia, D., et al. 2009, *ApJ*, 704, 606
- Grankin, K. N., Melnikov, S. Y., Bouvier, J., Herbst, W., & Shevchenko, V. S. 2007, *A&A*, 461, 183
- Greene, T. P. & Lada, C. J. 2000, *AJ*, 120, 430
- Greene, T. P., Wilking, B. A., Andre, P., Young, E. T., & Lada, C. J. 1994, *ApJ*, 434, 614
- Guarcello, M. G., Damiani, F., Micela, G., et al. 2010a, *A&A*, 521, A18
- Guarcello, M. G., Micela, G., Peres, G., Prisinzano, L., & Sciortino, S. 2010b, *A&A*, 521, A61
- Güdel, M., Briggs, K. R., Arzner, K., et al. 2007, *A&A*, 468, 353
- Guenther, E. & Ball, M. 1998, in *Astronomical Society of the Pacific Conference Series*, Vol. 154, *Cool Stars, Stellar Systems, and the Sun*, ed. R. A. Donahue & J. A. Bookbinder, 1701

- Guenther, E. & Hessman, F. V. 1994, in *Astronomical Society of the Pacific Conference Series*, Vol. 62, *The Nature and Evolutionary Status of Herbig Ae/Be Stars*, ed. P. S. The, M. R. Perez, & E. P. J. van den Heuvel, 132
- Gullbring, E., Calvet, N., Muzerolle, J., & Hartmann, L. 2000, *ApJ*, 544, 927
- Gullbring, E., Hartmann, L., Briceño, C., & Calvet, N. 1998, *ApJ*, 492, 323
- Günther, H. M., Lewandowska, N., Hundertmark, M. P. G., et al. 2010, *A&A*, 518, A54
- Gutermuth, R. A., Megeath, S. T., Myers, P. C., et al. 2009, *ApJS*, 184, 18
- Gutermuth, R. A., Myers, P. C., Megeath, S. T., et al. 2008, *ApJ*, 674, 336
- Haisch, Jr., K. E., Lada, E. A., & Lada, C. J. 2001, *ApJL*, 553, L153
- Hartigan, P., Edwards, S., & Ghandour, L. 1995, *ApJ*, 452, 736
- Hartigan, P., Hartmann, L., Kenyon, S., Hewett, R., & Stauffer, J. 1989, *ApJS*, 70, 899
- Hartigan, P. & Kenyon, S. J. 2003, *ApJ*, 583, 334
- Hartigan, P., Kenyon, S. J., Hartmann, L., et al. 1991, *ApJ*, 382, 617
- Hartmann, L. 1998, *Accretion Processes in Star Formation*, ed. Hartmann, L.
- Hartmann, L. 2001, *AJ*, 121, 1030
- Hartmann, L., Ballesteros-Paredes, J., & Bergin, E. A. 2001, *ApJ*, 562, 852
- Hartmann, L., Calvet, N., Gullbring, E., & D'Alessio, P. 1998, *ApJ*, 495, 385
- Hartmann, L., Cassen, P., & Kenyon, S. J. 1997, *ApJ*, 475, 770
- Hartmann, L. & Kenyon, S. J. 1996, *ARA&A*, 34, 207
- Hartmann, L., Zhu, Z., & Calvet, N. 2011, *ArXiv e-prints*
- Hatchell, J., Fuller, G. A., Richer, J. S., Harries, T. J., & Ladd, E. F. 2007, *A&A*, 468, 1009
- Hawkins, M. R. S. 2002, *MNRAS*, 329, 76
- Hayashi, C. 1961, *PASJ*, 13, 450
- Henney, W. J. & O'Dell, C. R. 1999, *AJ*, 118, 2350
- Heney, L. G., Lelevier, R., & Levée, R. D. 1955, *PASP*, 67, 154
- Herbig, G. H. 1958, *Ricerche Astronomiche*, 5, 127
- Herbig, G. H. 1962, *Advances in Astronomy and Astrophysics*, 1, 47
- Herbig, G. H. 1977, *ApJ*, 217, 693

- Herbig, G. H. 2007, *AJ*, 133, 2679
- Herbig, G. H. 2008, *AJ*, 135, 637
- Herbst, W., Bailer-Jones, C. A. L., Mundt, R., Meisenheimer, K., & Wackermann, R. 2002, *A&A*, 396, 513
- Herbst, W., Herbst, D. K., Grossman, E. J., & Weinstein, D. 1994, *AJ*, 108, 1906
- Herczeg, G. J. & Hillenbrand, L. A. 2008, *ApJ*, 681, 594
- Herczeg, G. J. & Hillenbrand, L. A. 2014, *ApJ*, 786, 97
- Hernández, J., Calvet, N., Briceño, C., et al. 2007, *ApJ*, 671, 1784
- Hillenbrand, L. A. 1997, *AJ*, 113, 1733
- Hillenbrand, L. A., Hoffer, A. S., & Herczeg, G. J. 2013, *AJ*, 146, 85
- Hillenbrand, L. A., Meyer, M. R., Strom, S. E., & Skrutskie, M. F. 1995, *AJ*, 109, 280
- Hollenbach, D. & Salpeter, E. E. 1971, *ApJ*, 163, 155
- Hollenbach, D. J., Yorke, H. W., & Johnstone, D. 2000, *Protostars and Planets IV*, 401
- Horne, K. 1986, *PASP*, 98, 609
- Hosokawa, T., Offner, S. S. R., & Krumholz, M. R. 2011, *ApJ*, 738, 140
- Hughes, P. A., Aller, H. D., & Aller, M. F. 1992, *ApJ*, 396, 469
- Ingleby, L., Calvet, N., Herczeg, G., et al. 2013, *ApJ*, 767, 112
- Irwin, J., Hodgkin, S., Aigrain, S., et al. 2007, *MNRAS*, 377, 741
- Jackson, R. J. & Jeffries, R. D. 2014, *MNRAS*, 441, 2111
- Jeans, J. H. 1902, *Royal Society of London Philosophical Transactions Series A*, 199, 1
- Jeffries, R. D. 2007, *MNRAS*, 381, 1169
- Jeffries, R. D., Littlefair, S. P., Naylor, T., & Mayne, N. J. 2011, *MNRAS*, 418, 1948
- Jeffries, R. D., Naylor, T., Devey, C. R., & Totten, E. J. 2004, *MNRAS*, 351, 1401
- Jeffries, R. D., Oliveira, J. M., Barrado y Navascués, D., & Stauffer, J. R. 2003, *MNRAS*, 343, 1271
- Jeffries, R. D., Oliveira, J. M., Naylor, T., Mayne, N. J., & Littlefair, S. P. 2007, *MNRAS*, 376, 580
- Johns-Krull, C. M. 2007, *ApJ*, 664, 975

- Johnstone, D., Hollenbach, D., & Bally, J. 1998, *ApJ*, 499, 758
- Jones, B. F. & Walker, M. F. 1988, *AJ*, 95, 1755
- Joy, A. H. 1945, *ApJ*, 102, 168
- Kastner, J. H., Huenemoerder, D. P., Schulz, N. S., Canizares, C. R., & Weintraub, D. A. 2002, *ApJ*, 567, 434
- Kawaguchi, T., Mineshige, S., Umemura, M., & Turner, E. L. 1998, *ApJ*, 504, 671
- Kennedy, G. M. & Kenyon, S. J. 2008, *ApJ*, 673, 502
- Kenyon, S. J. & Hartmann, L. 1995, *ApJS*, 101, 117
- Kenyon, S. J., Hartmann, L., Hewett, R., et al. 1994, *AJ*, 107, 2153
- Kenyon, S. J., Hartmann, L. W., Strom, K. M., & Strom, S. E. 1990, *AJ*, 99, 869
- Kenyon, S. J., Kolotilov, E. A., Ibragimov, M. A., & Mattei, J. A. 2000, *ApJ*, 531, 1028
- King, J. R. 1998, *AJ*, 116, 254
- Koenigl, A. 1991, *ApJL*, 370, L39
- Koenigl, A. & Pudritz, R. E. 2000, *Protostars and Planets IV*, 759
- Kóspál, Á., Ábrahám, P., Acosta-Pulido, J. A., et al. 2013, *A&A*, 551, A62
- Kóspál, Á., Ábrahám, P., Acosta-Pulido, J. A., et al. 2011, *A&A*, 527, A133
- Kraus, S., Hofmann, K.-H., Malbet, F., et al. 2009, *A&A*, 508, 787
- Kun, M., Szegedi-Elek, E., Moór, A., et al. 2011a, *ApJL*, 733, L8
- Kun, M., Szegedi-Elek, E., Moór, A., et al. 2011b, *MNRAS*, 413, 2689
- Kurosawa, R., Harries, T. J., & Symington, N. H. 2006, *MNRAS*, 370, 580
- Kurosawa, R. & Romanova, M. M. 2013, *MNRAS*, 431, 2673
- Lada, C. J. 1987, in *IAU Symposium*, Vol. 115, *Star Forming Regions*, ed. M. Peimbert & J. Jugaku, 1–17
- Lada, C. J., Muench, A. A., Luhman, K. L., et al. 2006, *AJ*, 131, 1574
- Lada, C. J. & Wilking, B. A. 1984, *ApJ*, 287, 610
- Lamm, M. H., Bailer-Jones, C. A. L., Mundt, R., Herbst, W., & Scholz, A. 2004, *A&A*, 417, 557
- Lanza, A. F. 2010, in *IAU Symposium*, Vol. 264, *IAU Symposium*, ed. A. G. Kosovichev, A. H. Andrei, & J.-P. Rozelot, 120–129

- Larson, R. B. 1969, *MNRAS*, 145, 271
- Littlefair, S. P., Naylor, T., Harries, T. J., Retter, A., & O'Toole, S. 2004, *MNRAS*, 347, 937
- Littlefair, S. P., Naylor, T., Mayne, N. J., Saunders, E., & Jeffries, R. D. 2011, *MNRAS*, 413, L56
- Littlefair, S. P., Naylor, T., Mayne, N. J., Saunders, E. S., & Jeffries, R. D. 2010, *MNRAS*, 403, 545
- Lodato, G. & Clarke, C. J. 2004, *MNRAS*, 353, 841
- Lomb, N. R. 1976, *Ap&SS*, 39, 447
- Lorenzetti, D., Antonucci, S., Giannini, T., et al. 2012, *ApJ*, 749, 188
- Machida, M. N., Inutsuka, S.-i., & Matsumoto, T. 2006, *ApJL*, 647, L151
- Machida, M. N., Inutsuka, S.-i., & Matsumoto, T. 2010, *ApJ*, 724, 1006
- MacLeod, C. L., Ivezić, Ž., Sesar, B., et al. 2012, *ApJ*, 753, 106
- Manara, C. F., Robberto, M., Da Rio, N., et al. 2012, *ApJ*, 755, 154
- Martin, R. G. & Livio, M. 2012, *MNRAS*, 425, L6
- Martin, R. G., Lubow, S. H., Livio, M., & Pringle, J. E. 2012, *MNRAS*, 423, 2718
- Martin, S. C. 1996, *ApJ*, 470, 537
- Matsakos, T., Chièze, J.-P., Stehlé, C., et al. 2013, *A&A*, 557, A69
- Mayne, N. J. 2010, *MNRAS*, 408, 1409
- Mayne, N. J. & Harries, T. J. 2010, *MNRAS*, 409, 1307
- Mayne, N. J. & Naylor, T. 2008, *MNRAS*, 386, 261
- Mayne, N. J., Naylor, T., Littlefair, S. P., Saunders, E. S., & Jeffries, R. D. 2007, *MNRAS*, 375, 1220
- McClure, M. K., Calvet, N., Espaillat, C., et al. 2013, *ApJ*, 769, 73
- McGinnis, P. T., Alencar, S. H. P., Guimarães, M. M., et al. 2015, *A&A*, 577, A11
- McNamara, B. J. 1976, *AJ*, 81, 845
- McQuillan, A., Aigrain, S., & Mazeh, T. 2013, *MNRAS*, 432, 1203
- Megeath, S. T., Gutermuth, R., Muzerolle, J., et al. 2012, *AJ*, 144, 192
- Ménard, F. & Bertout, C. 1999, in *NATO Advanced Science Institutes (ASI) Series C*, Vol. 540, *NATO Advanced Science Institutes (ASI) Series C*, ed. C. J. Lada & N. D. Kylafis, 341

- Mendoza V., E. E. 1966, *ApJ*, 143, 1010
- Menten, K. M., Reid, M. J., Forbrich, J., & Brunthaler, A. 2007, *A&A*, 474, 515
- Meyer, M. R., Backman, D. E., Weinberger, A. J., & Wyatt, M. C. 2007, *Protostars and Planets V*, 573
- Mohanty, S., Basri, G., & Jayawardhana, R. 2005, *Astronomische Nachrichten*, 326, 891
- Montmerle, T., Koch-Miramond, L., Falgarone, E., & Grindlay, J. E. 1983, *ApJ*, 269, 182
- Morales-Calderón, M., Stauffer, J. R., Hillenbrand, L. A., et al. 2011, *ApJ*, 733, 50
- Mukai, K. 1990, *PASP*, 102, 183
- Muzerolle, J., Calvet, N., & Hartmann, L. 2001, *ApJ*, 550, 944
- Muzerolle, J., Hartmann, L., & Calvet, N. 1998, *AJ*, 116, 2965
- Muzerolle, J., Hillenbrand, L., Calvet, N., Briceño, C., & Hartmann, L. 2003, *ApJ*, 592, 266
- Natta, A., Testi, L., & Randich, S. 2006, *A&A*, 452, 245
- Nayakshin, S. & Lodato, G. 2012, *MNRAS*, 426, 70
- Naylor, T. 2009, *MNRAS*, 399, 432
- Naylor, T., Totten, E. J., Jeffries, R. D., et al. 2002, *MNRAS*, 335, 291
- Neff, J. E., O'Neal, D., & Saar, S. H. 1995, *ApJ*, 452, 879
- O'dell, C. R. & Wong, K. 1996, *AJ*, 111, 846
- Orlando, S., Sacco, G. G., Argiroffi, C., et al. 2010, *A&A*, 510, A71
- Palla, F., Randich, S., Flaccomio, E., & Pallavicini, R. 2005, *ApJL*, 626, L49
- Palla, F., Randich, S., Pavlenko, Y. V., Flaccomio, E., & Pallavicini, R. 2007, *ApJL*, 659, L41
- Palla, F. & Stahler, S. W. 1999, *ApJ*, 525, 772
- Palla, F. & Stahler, S. W. 2000, *ApJ*, 540, 255
- Palla, F. & Stahler, S. W. 2002, *ApJ*, 581, 1194
- Paltani, S. 1999, in *Astronomical Society of the Pacific Conference Series*, Vol. 159, BL Lac Phenomenon, ed. L. O. Takalo & A. Sillanpää, 293
- Parsamian, E. S. & Mujica, R. 2004, *Astrophysics*, 47, 433
- Peneva, S. P. & Semkov, E. H. 2008, *Bulgarian Astronomical Journal*, 10, 29
- Peneva, S. P., Semkov, E. H., Munari, U., & Birkle, K. 2010, *A&A*, 515, A24

- Persson, R. 2004, *IAU Circ.*, 8441, 2
- Petrov, P. P., Gahm, G. F., Stempels, H. C., Walter, F. M., & Artemenko, S. A. 2011, *A&A*, 535, A6
- Pflamm-Altenburg, J. & Kroupa, P. 2007, *MNRAS*, 375, 855
- Pickles, A. J. 1998, *PASP*, 110, 863
- Pinsonneault, M. 1997, *ARA&A*, 35, 557
- Press, W. H. 1978, *Comments on Astrophysics*, 7, 103
- Prisinzano, L., Damiani, F., Micela, G., & Sciortino, S. 2005, *A&A*, 430, 941
- Rebull, L. M. 2001, *AJ*, 121, 1676
- Rebull, L. M., Hillenbrand, L. A., Strom, S. E., et al. 2000, *AJ*, 119, 3026
- Rebull, L. M., Makidon, R. B., Strom, S. E., et al. 2002, *AJ*, 123, 1528
- Rebull, L. M., Stauffer, J. R., Megeath, S. T., Hora, J. L., & Hartmann, L. 2006, *ApJ*, 646, 297
- Reipurth, B. 1990, in *IAU Symposium*, Vol. 137, *Flare Stars in Star Clusters, Associations and the Solar Vicinity*, ed. L. V. Mirzorian, B. R. Pettersen, & M. K. Tsvetkov, 229–251
- Reipurth, B. & Aspin, C. 2004, *ApJL*, 606, L119
- Reipurth, B., Aspin, C., Beck, T., et al. 2007, *AJ*, 133, 1000
- Reipurth, B., Pedrosa, A., & Lago, M. T. V. T. 1996, *A&AS*, 120, 229
- Rhode, K. L., Herbst, W., & Mathieu, R. D. 2001, *AJ*, 122, 3258
- Ricci, L., Testi, L., Natta, A., et al. 2010, *A&A*, 512, A15
- Rice, T. S., Reipurth, B., Wolk, S. J., Vaz, L. P., & Cross, N. J. G. 2015, *ArXiv e-prints*
- Rieke, G. H. & Lebofsky, M. J. 1985, *ApJ*, 288, 618
- Rigliaco, E., Natta, A., Randich, S., Testi, L., & Biazzo, K. 2011, *A&A*, 525, A47
- Robitaille, T. P., Whitney, B. A., Indebetouw, R., Wood, K., & Denzmore, P. 2006, *ApJS*, 167, 256
- Romanova, M. M., Kulkarni, A. K., & Lovelace, R. V. E. 2008, *ApJL*, 673, L171
- Romanova, M. M., Long, M., Lamb, F. K., Kulkarni, A. K., & Donati, J.-F. 2011, *MNRAS*, 411, 915
- Romanova, M. M., Ustyugova, G. V., Koldoba, A. V., & Lovelace, R. V. E. 2002, *ApJ*, 578, 420

- Romanova, M. M., Ustyugova, G. V., Koldoba, A. V., & Lovelace, R. V. E. 2012, *MNRAS*, 421, 63
- Rucinski, S. M., Matthews, J. M., Kuschnig, R., et al. 2008, *MNRAS*, 391, 1913
- Rucinski, S. M., Zwintz, K., Hareter, M., et al. 2010, *A&A*, 522, A113
- Sacco, G. G., Argiroffi, C., Orlando, S., et al. 2008, *A&A*, 491, L17
- Sacco, G. G., Randich, S., Franciosini, E., Pallavicini, R., & Palla, F. 2007, *A&A*, 462, L23
- Sasselov, D. D. & Lecar, M. 2000, *ApJ*, 528, 995
- Saunders, E. S., Naylor, T., Mayne, N., & Littlefair, S. P. 2009, *MNRAS*, 397, 405
- Scandariato, G., Robberto, M., Pagano, I., & Hillenbrand, L. A. 2011, *A&A*, 533, A38
- Scargle, J. D. 1982, *ApJ*, 263, 835
- Scholz, A., Coffey, J., Brandeker, A., & Jayawardhana, R. 2007, *ApJ*, 662, 1254
- Scholz, A., Froebrich, D., & Wood, K. 2013, *MNRAS*, 430, 2910
- Scholz, A., Xu, X., Jayawardhana, R., et al. 2009, *MNRAS*, 398, 873
- Semkov, E. H., Peneva, S. P., Munari, U., et al. 2013, *A&A*, 556, A60
- Sergison, D. J., Mayne, N. J., Naylor, T., Jeffries, R. D., & Bell, C. P. M. 2013, *MNRAS*, 434, 966
- Shu, F., Najita, J., Ostriker, E., et al. 1994, *ApJ*, 429, 781
- Shull, J. M. & Beckwith, S. 1982, *ARA&A*, 20, 163
- Shuping, R. Y., Bally, J., Morris, M., & Throop, H. 2004, in *Astronomical Society of the Pacific Conference Series*, Vol. 324, *Debris Disks and the Formation of Planets*, ed. L. Caroff, L. J. Moon, D. Backman, & E. Praton, 218
- Sicilia-Aguilar, A., Henning, T., & Hartmann, L. W. 2010, *ApJ*, 710, 597
- Siess, L., Dufour, E., & Forestini, M. 2000, *A&A*, 358, 593
- Simonetti, J. H., Cordes, J. M., & Heeschen, D. S. 1985, *ApJ*, 296, 46
- Slesnick, C. L. 2007, *PASP*, 119, 1205
- Smith, N., Bally, J., Licht, D., & Walawender, J. 2005, *AJ*, 129, 382
- Stassun, K. G., Mathieu, R. D., Mazeh, T., & Vrba, F. J. 1999, *AJ*, 117, 2941
- Stauffer, J., Cody, A. M., Baglin, A., et al. 2014, *AJ*, 147, 83
- Stout-Batalha, N. M., Batalha, C. C., & Basri, G. S. 2000, *ApJ*, 532, 474

- Tan, J. C., Krumholz, M. R., & McKee, C. F. 2006, *ApJL*, 641, L121
- Teixeira, P. S., Lada, C. J., Marengo, M., & Lada, E. A. 2012, *A&A*, 540, A83
- Throop, H. B., Bally, J., Esposito, L. W., & McCaughrean, M. J. 2001, *Science*, 292, 1686
- Tout, C. A., Livio, M., & Bonnell, I. A. 1999, *MNRAS*, 310, 360
- Uzawa, A., Tsuboi, Y., Morii, M., et al. 2011, *PASJ*, 63, 713
- van Hamme, W. 1993, *AJ*, 106, 2096
- Vazquez-Semadeni, E., Passot, T., & Pouquet, A. 1996, *ApJ*, 473, 881
- Venuti, L., Bouvier, J., Flaccomio, E., et al. 2014, *A&A*, 570, A82
- Viallet, M. & Baraffe, I. 2012, *ArXiv e-prints*
- Vogel, S. N. & Kuhi, L. V. 1981, *ApJ*, 245, 960
- Vorobyov, E. I. & Basu, S. 2005, *ApJL*, 633, L137
- Vorobyov, E. I. & Basu, S. 2015, *ArXiv e-prints*
- Walker, C., Wood, K., Lada, C. J., et al. 2004, *MNRAS*, 351, 607
- Walker, M. F. 1972, *ApJ*, 175, 89
- Watson, A. M. & Stapelfeldt, K. R. 2004, *ApJ*, 602, 860
- Webb, N. A., Naylor, T., & Jeffries, R. D. 2002, *ApJL*, 568, L45
- Weingartner, J. C. & Draine, B. T. 2001, *ApJ*, 548, 296
- White, R. J. & Basri, G. 2003, *ApJ*, 582, 1109
- White, R. J. & Hillenbrand, L. A. 2004, *ApJ*, 616, 998
- Whitney, B. A., Wood, K., Bjorkman, J. E., & Wolff, M. J. 2003, *ApJ*, 591, 1049
- Wilhite, B. C., Brunner, R. J., Grier, C. J., Schneider, D. P., & vanden Berk, D. E. 2008, *MNRAS*, 383, 1232
- Wilson, C. D., Walker, C. E., & Thornley, M. D. 1997, *ApJ*, 483, 210
- Wolk, S. J., Rice, T., & Reipurth, B. 2014, in *American Astronomical Society Meeting Abstracts*, Vol. 224, *American Astronomical Society Meeting Abstracts #224*, #419.04
- Wolk, S. J., Rice, T. S., & Aspin, C. 2013, *ApJ*, 773, 145
- Yang, H. & Johns-Krull, C. M. 2011, *ApJ*, 729, 83
- Zapatero Osorio, M. R., Béjar, V. J. S., Pavlenko, Y., et al. 2002, *A&A*, 384, 937
- Zhu, Z., Hartmann, L., Gammie, C., & McKinney, J. C. 2009, *ApJ*, 701, 620

Appendices

Appendix A

The variability of spectroscopic target stars in CMD space

This appendix contains $g, g - i$ colour-magnitude diagrams for all spectroscopic target stars showing how their position varies in CMD space over the course of one week. The black points are the mean colours and magnitudes for all stars with clean photometry in this study. The red (grey) points are the positions at different epochs for the target star in question. The inset is a close-up of the positions of the target star, coloured to represent the epoch and highlighting the photometric uncertainties. Extinction vectors corresponding to $A_V = 1.0$ are shown for $R_V = 3.1$ and 5.5 . A range of movement is seen in this diagram, the physical nature of this is investigated in later sections of this thesis.

